Functional Characterisation of Aromatic L-Amino Acid Decarboxylase (AADC) Deficiency Using a Patient-Derived Dopaminergic Cell Model

A thesis submitted to University College London for the Degree of Doctor of Philosophy

Karolin Krämer

24/05/2019

UCL Great Ormond Street Institute of Child Health

Declaration of work

I, Karolin Krämer confirm that the work presented in this thesis is my own. Where information has been derived from other sources, I confirm that this has been indicated in the thesis.

Abstract

Background: Aromatic L-amino acid decarboxylase (AADC) deficiency is a severe pharmacoresistant neurological disorder due to inherited autosomal recessive loss-of-function mutations in the *DDC* gene. The resultant impairment of AADC enzyme activity severely impacts on monoamine synthesis, leading to reduced levels of dopamine and serotonin. Affected patients present with marked neurodevelopmental delay, hypotonia, oculogyric crises and autonomic dysfunction. Currently, there are few truly disease-modifying therapies.

Aims: To generate AADC patient-derived induced pluripotent stem cells (iPSC) for subsequent differentiation into midbrain dopaminergic (mDA) neurons, and to utilise this model to better define disease mechanisms and test novel therapeutic strategies.

Methods: Patient and age-matched control fibroblasts were reprogrammed into iPSC using Sendai Virus methods. A modified dual SMAD inhibition protocol was then utilised for differentiation of all iPSC lines to day 65 of maturation. The generated neuronal model was then analysed for mature mDA neuronal identity and AADC disease-specific features.

Results: iPSC lines were generated from skin fibroblasts derived from two patients with AADC deficiency. One patient harboured a homozygous missense mutation (p.R347G) and the other was a compound heterozygote for a nonsense variant (p.Arg7*) and missense mutation (p.C100S) in *DDC*. For the project two iPSC lines from one age-matched control subject were used that were previously reprogrammed in my host laboratory. Generated iPSC lines were confirmed as being truly pluripotent, then successfully differentiated into midbrain dopaminergic neurons, with characteristic neuronal morphology, expressing tyrosine hydroxylase (TH) and microtubule-associated protein 2 (MAP2). There was no evidence of neurodegeneration in the patient lines. A number of disease-specific features were identified, including significantly marked reduction of AADC enzyme activity and dysregulation of the dopaminergic system in patient mDA neurons when compared to the age-matched control. Preliminary data also shows successful lentiviral rescue of the patient-derived mDA cell model.

Conclusion: The iPSC-derived mDA neuronal model represents an ideal platform to further elucidate disease mechanisms, as well as to screen novel pharmacological agents for AADC deficiency.

Impact Statement

The aim of this work is to generate a new *in vitro* disease model of aromatic L-amino acid decarboxylase (AADC) deficiency. There is urgent clinical need for a humanised disease model, to improve disease understanding and develop novel therapies for this medically resistant, often life-limiting disorder. The model is of significant importance as, to my knowledge, it is the first reported patient-derived *in vitro* disease model of AADC deficiency. It is an excellent base to further elucidate disease mechanisms and perform drug screening to find new effective treatments. Work in this field of translational medicine has the potential to benefit patients in the longer term, by improving their quality of life and long-term survival.

Acknowledgements

I would like to thank my primary supervisor Prof. Manju A. Kurian, as well as my secondary supervisors Prof. Simon Heales and Dr. Serena Barral for their guidance and support throughout my PhD.

Also, many thanks to the Kurian research group that contributed very much to my professional and personal life.

Many thanks to family and friends who made my PhD time a lot more fun.

Many thanks to the two ICH offices 127 and 109 for cheerful moments and when there was urgent need for coffee and cake.

I would also like to thank the AADC Research Trust for funding my PhD stipend and the AADC conferences who inspired and amazed me every time.

Last but not least, I would like to thank the AADC patients and their families who never give up and always make the best out of every day.

Table of Contents

Table of Tables

Table of Figures

List of Abbreviations

3'LTR ΔU3	self-inactivating 3'long terminal repeat
3D	three-dimensional
3-OMD	3-orthomethyldopa
5'LTR	truncated 5' long terminal repeat
5-HIAA	5-hydroxyindoleacetic acid
5-HTP	5-hydroxytryptophan
AADC	aromatic L-amino acid decarboxylase
AAV-2	adeno-associated virus type 2
AAV9	adeno-associated serotype 9
AIMS	abnormal involuntary movement scale
ALDH	aldehyde dehydrogenase
ALS	amyotrophic lateral sclerosis
ANKRD46	ankyrin repeat domain 46
ATM	gene affected in Ataxia-telangiectasia
Bdnf and BDNF	brain-derived neurotrophic factor
BH_4	tetrahydrobiopterin
BPAN	beta-propeller associated neurodegeneration
cAMP	cyclic adenosine monophosphate
cDNA	complementary DNA
CMV	human cytomegalovirus immediate early promoter
CNS	central nervous system
COMT	catechol-O-methyltransferase
CpGs	CpG sites
cPPT	central polypurine tract
CSF	cerebrospinal fluid
D	dopaminergic receptor
DA	dopaminergic
DAPT	(2S)-N-[(3,5-Difluorophenyl)acetyl]-L-alanyl-2-phenyl]glycine 1,1-dimethylethyl ester
DAT	dopamine transporter
db-cAMP	N6,2′-O-Dibutyryladenosine 3′,5′-cyclic monophosphate sodium salt
DDC-GFP LV 1-04	*DDC* lentivirus treated Patient 1
DDC-GFP LV 2-01	*DDC* lentivirus treated Patient 2
DHPR	dihydropteridine reductase
DHPR	dihydropyridine receptor
DNAm	DNA methylation
DOPAC	3,4-dihydroxyphenylacetic acid
DSBs	DNA double-strand breaks
DβH	dopamine-β-hydroxylase
EB medium	embryoid body medium
EDTA	ethylenediaminetetraacetic acid
EGFP	enhanced green fluorescent protein
En1	homeobox genes engrailed 1
En2	homeobox genes engrailed 2
EtOH	ethanol
FCS	fetal calf serum

FD medium	final differentiation medium
FDOPA	6-[^{18}F] fluorodopa
Ferd3l	Fer3-like
Fgf8	fibroblast growth factor 8
FMR1	fragile X mental retardation 1
FoxA2 and FOXA2	forkhead box protein a2
FP	floor plate
GAPDH	glyceraldehyde-3-phosphate dehydrogenase
Gbx2	gastrulation brain homeobox 2
gDNA	genomic DNA
GDNF	glial cell-line derived neurotrophic factor
GFP LV 1-04	mock lentivirus treated Patient 1
GFP LV 2-01	mock lentivirus treated Patient 2
GIRK2	G-protein regulated inward-rectifier potassium 2 channel
GM2	glycospjingolipid
GPCRs	G protein-coupled receptors
GPe	globus pallidus pars externa
GPi	globus pallidus pars interna
GRID1	Glutamate Receptor Ionotropic, Delta-1
GTP	guanosine triphosphate
GTPCH	GTP cyclohydrolase
H9	human embryonic stem cell line
HDAC	histone deacetylase
hDDC	human *DDC* gene
Hes1	hairy and enhancer of Split1
hESC	embryonic stem cells
hMLO	human midbrain-like organoids
HMT	histone methyl transferase
HPLC	high-performance liquid chromatography
HRP	horseradish peroxidase
hSYN	human synapsin
hSYN	human synapsin promoter
Human BDNF	human brain-derived neurotrophic factor
Human FGF-2	human fibroblast growth factor
HVA	homovanillic acid
IGF1	insulin-like growth factor
IKBKAP	IkappaB kinase complex-associated protein gene
iNs	induced neuronal cells
iPSC	induced pluripotent stem cell
IRES	internal ribosome entry site sequence
IsO	isthmic organiser
IVS-AAA	modified U1 snRNA
IZ	intermediate zone
KCC2	K-Cl co-transporter
KI	knock in
KMT2B	lysine methyltransferase 2B
L-dopa	L-3,4-dihydroxyphenylalanine
Lmx1a	LIM homeobox transcription factor a
Lmx1b	LIM homeobox transcription factor b

LRRK2	leucine-rich repeat kinase 2
MAO	monoamine oxidase
MAOA	monoamine oxidase A
MAOI	monoamine oxidase inhibitors
MAP2	microtubule-associated protein 2
MAP2	microtubule-associated protein 2
Mash1	mouse achaete-schute homolog 1
MB-HB	midbrain-hindbrain
mDA	midbrain dopaminergic
MECP2	methyl-CpG-binding protein 2 gene
MEF	mouse embryonic fibroblasts
MO	morpholino oligonucleotides
MOI	multiplicity of infection
MSNs	medium spiny neurons
Msx1	muscle segment homeobox homolog 1
MZ	mantle zone
NAC	N-acetylcysteine
NeoR/KanR	neomycin and kanamycin antibiotic resistance
NeuN	neuronal nuclei
Ngn2	neurogenin 2
Nkx2.2	NK homeobox protein 2.2
Nkx6.1	NK homeobox protein 6.1
NPC1	niemann pick type C
NSC	neural stem cell
NSFs	N-ethylmaleimide-sensitive fusion proteins
Nurr1	nuclear receptor related 1 protein
Otx2	orthodenticle homolog 2
PanNav	voltage-gated sodium channel Nav1.1
PARK2	parkinson disease-2
PDG	pre-implantation genetic diagnosis
PDMS-2	peabody developmental motor scales-2
PEI	polyethylenimine
PINK1	PTEN induced kinase 1
Pitx3	pituitary homeobox 3
PLP	pyridoxal 5’-phosphate
PLP	pyridoxal 5’phosphate
PNMT	phenylethanolamine N-methyltransferase
POU5F1	gene of the OCT4 transcription factor
PSC	pluripotent stem cells
PTPS	6-pyruvoyltetrahydropterin synthase
qRT-PCR	real-time quantitative reverse transcription polymerase chain reaction
REST	RE-1 silencing transcription factor
RRE	Rev response element
RrF	retrorubral field
RT	room temperature
RT-PCR	reverse transcription polymerase chain reaction
SAM	S-adenosyl-methionine
SEM	standard error of mean

sEPSC	spontaneous excitatory post synaptic current
SERT	serotonin transporter
SeV	sendai virus
Shh	sonic hedgehog
SHH (compound)	recombinant modified human Sonic hedgehog C24II
Slc18a2	solute carrier family-18 member-2
Slc6a3	solute carrier family-6 member-3
SMA	alpha smooth muscle actin
SNAPs	soluble NSF attachment proteins
SNARE	SNAP receptors
SNP	single-nucleotide polymorphism
SNpc	substantia nigra pars compacta
SNpr	substantia nigra pars reticulata
SOX17	member of the SOX family of transcription factors
SR	sepiapterin reductase
STN	subthalamic nucleus
SV40pA	simian virus 40 polyadenylation signal
TAM	transaminase
TBS-T	tris buffered saline-tween
TGS	tris/glycine/SDS
TH	tyrosine hydroxylase
Top1-ccs	topoisomerase 1-DNA covalent complexes
TPH2	tryptophan hydroxylase 2
TUJ1	neuronal class III β-tubulin
VCN	vector copy number
VLA	vanillactic acid
VLA	vanillylactic
VM	ventral midbrain
VMAT2 and Vmat2	vesicular monoamine transporter 2
VTA	ventral tegmental area
VZ	ventricular zone
Wnt1	wingless-int1
WPRE	woodchuck hepatitis virus posttranscriptional regulatory element
ψ	packaging signal

Chapter 1 Introduction

1.1 Introduction to AADC Deficiency

Aromatic L-amino acid decarboxylase (AADC) has a pivotal role in brain monoamine synthesis, by converting L-3,4-dihydroxyphenylalanine (L-dopa) into dopamine and 5-hydroxytryptophan (5-HTP) into serotonin (Lovenberg, Weissbach, and Udenfriend 1962). Dopamine and serotonin are key brain neurotransmitters governing motor control, reward, affect and emotion. Dopamine is also essential for the downstream production of the catecholamines, norepinephrine and epinephrine. It is therefore not surprising that patients with AADC deficiency present with a complex neurodevelopmental syndrome characterised by abnormal motor and cognitive development with associated autonomic features.

The first human patients with AADC deficiency were published in 1990 by Hyland and Clayton. They reported monozygotic male twins presenting in infancy with abnormal eye movements consistent with oculogyric crises, hypotonia and developmental delay. Plasma AADC enzyme assay confirmed AADC deficiency in both siblings. Treatment with a monoamine oxidase inhibitor (Tranylcypromine), dopamine agonist (Bromocriptine) and the cofactor of AADC (Pyridoxine) led to significant clinical improvement. Both patients showed amelioration of tone and development of spontaneous voluntary movements. By the age of 17 months, both children had resolution of their oculogyric crises, could feed themselves from a bottle and showed better head control (Hyland et al. 1992; Hyland and Clayton 1990). Since this original disease description, 123 patients with AADC have been reported, with a wide phenotypic spectrum from virtually asymptomatic individuals to those with severe disability and neurodevelopmental delay (Himmelreich et al. 2019; Wassenberg et al. 2017).

1.2 The Human Brain: Important Motor Networks and Neurotransmitter Pathways

1.2.1 Motor Control

Motor control in humans requires the systematic regulation of movement through coordinated muscle contraction and relaxation. It is achieved through integrated function of virtually all of the major divisions of the central nervous system: multiple

cortical areas (including the primary motor area, supplementary motor area, and premotor cortex) are involved in the preparation and execution of motor commands; the cerebellum in learning and motor task coordination; the spine and brainstem in processing of sensorimotor information, as well as complex circuitry involving cortical/basal ganglia/thalamocortical and cerebellar/cortical/subcortical networks (**Figure 1-1** below). It is therefore not surprising that structural, metabolic or genetic disruption of these finely tuned pathways can cause aberrant motor control leading to reduced voluntary movement or excessive involuntary movement.

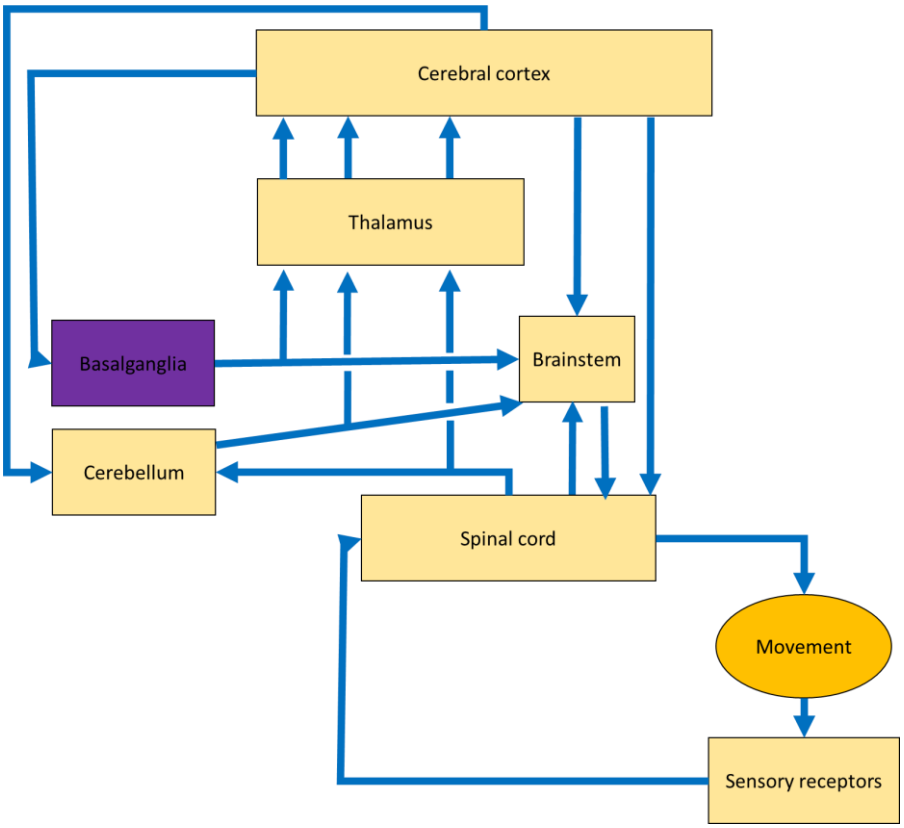

Figure 1-1: Motor control in the human brain.

The basal ganglia have a key role in movement and are involved in a number of important motor networks that govern physiological motor control. They are composed of the striatum, globus pallidus, substantia nigra and subthalamic nucleus (**Figure 1-2**).

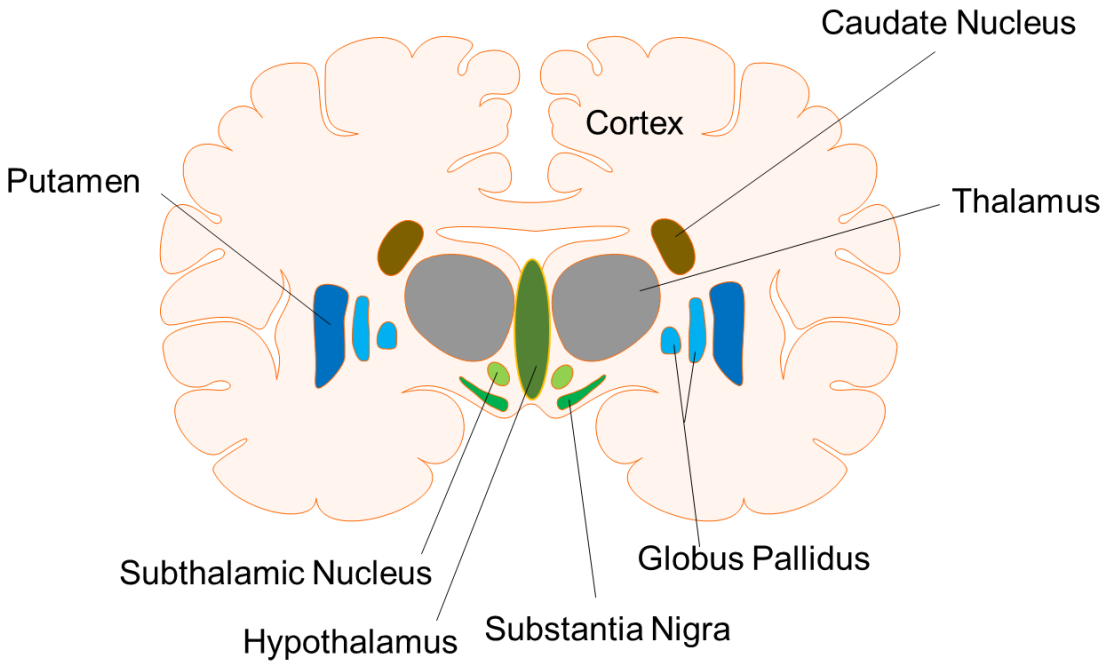

Figure 1-2: Anatomy of the basal ganglia with putamen, subthalamic nucleus, hypothalamus, substantia nigra, globus pallidus, thalamus, and caudate nucleus.

Cortical and thalamic structures project glutamatergic excitatory inputs to the striatal complex. In the striatum, medium spiny neurons (MSNs), with GABAergic output represent 95% of striatal neurons (Dubé, Smith, and Bolam 1988), but aspiny GABAergic neurons and large cholinergic interneurons are also present (Lapper and Bolam 1992). The striatum receives dopaminergic input from the substantia nigra pars compacta (SNpc) (Pickel, Chan, and Sesack 1992). Projections that are glutamatergic and dopaminergic merge onto dendritic spines from the same MSN (Bouyer et al. 1984). Striatal interneurons receive input from dopaminergic and glutaminergic neurons, synapsing to MSNs (Kawaguchi et al. 1995).

1.2.1.1 The Role of the Direct and Indirect Pathway in Motor Control

The direct and indirect pathway have a key role in motor control (Albin, Young, and Penney 1989; Calabresi et al. 2014; DeLong 1990).

In the direct pathway (**Figure 1-3 A),** cortical activation results in release of glutamate which activates MSNs of the striatum. These MSNs project to the substantia nigra pars

reticulata (SNpr), as well as the globus pallidus pars interna (GPi). As MSNs are GABAergic cells, they inhibit neurons of the SNpr which are also GABAergic. The inhibition of SNpr leads to a disinhibition of glutamatergic neurons of the thalamus. The thalamus neurons project to the cortex. The direct pathway thus results in activation of movement.

In the indirect pathway (**Figure 1-3 B)** cortical activation results in release of glutamate which activates MSNs of the striatum. The striato-pallidal MSNs project to the SNpr through the globus pallidus pars externa (GPe). The MSNs also project to the subthalamic nucleus (STN). The GPe GABAergic neurons are inhibited, which leads to disinhibition of the STN glutamatergic neurons. The activated STN neurons activate the GABAergic neurons of the SNpr. These neurons project to the thalamus and inhibit its activity, leading to a reduction of movement.

MSNs of the direct and indirect pathway express different dopaminergic receptors. D_1 dopaminergic receptors are expressed by MSNs from the direct pathway. D_2 dopaminergic receptors are expressed by MSNs from the indirect pathway. D_1 and D_2 dopamine receptors are coupled to specific G proteins which are involved in different intracellular signalling pathways. D_1 and D_2 receptor activation thus have different downstream effects (Gerfen et al. 1994; Gerfen and Surmeier 2011).

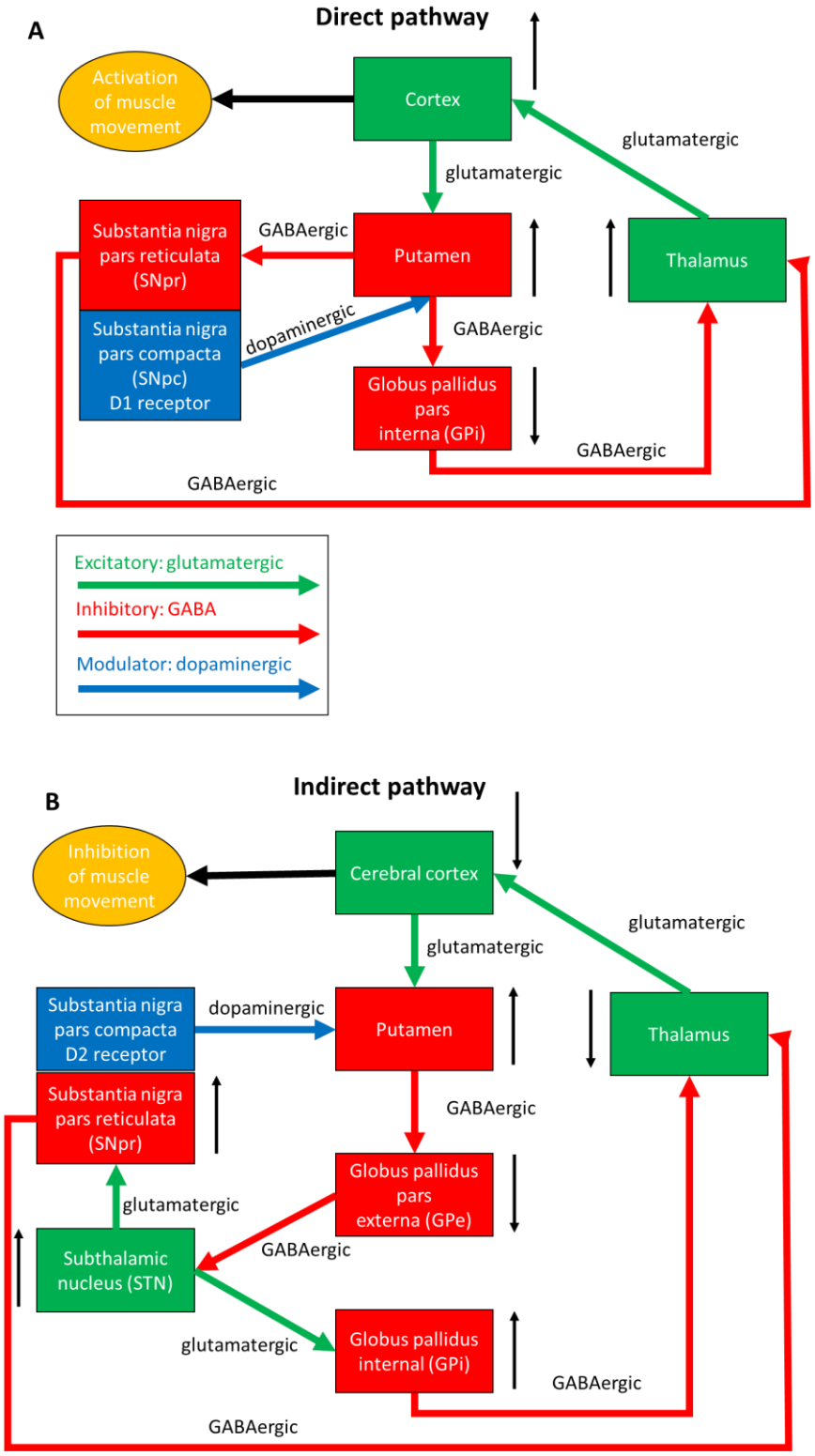

Figure 1-3: Schematic representation of the direct and indirect pathway with the cortico-basal ganglia-thalamo-cortical loop.
A shows the direct pathway. **B** shows the indirect pathway. Glutamatergic input signals are excitatory and GABAergic input signals are inhibitory. Dopamine is a modulator.

1.2.2 Role of Monoamines in the Brain

The monoamines are an important group of neurotransmitters in the central nervous system. They include the catecholamines dopamine, noradrenaline and adrenaline, as well as serotonin) (Arenas, Denham, and Villaescusa 2015). Serotonin and dopamine are produced through the monoamine synthesis pathway, and stored in serotonergic and dopaminergic neurons respectively, in the presynaptic neuron (Dahlstroem and Fuxe 1964). Both dopaminergic and serotonergic neurons project widely to other brain regions (**Figure 1-4**). The dopaminergic neurons from the ventral midbrain (VM) represent 75% of dopaminergic neurons in the adult CNS (Hegarty, Sullivan, and O'Keeffe 2013). During embryonic development, dopaminergic (DA) neurons from the ventral midbrain are produced in the floor plate area from the mesencephalon of the neuronal tube (Ono et al. 2007). Dopaminergic midbrain neurons can be found in three different cell groups: the SNpc, the ventral tegmental area (VTA), and the retrorubral field (RrF) (Arenas et al. 2015). SNpc neurons project to the dorsal striatum in the nigrostriatal pathway. SNpc neurons regulate voluntary movement (Lees, Hardy, and Revesz 2009; Toulouse and Sullivan 2008). The VTA and the RrF project to the ventral striatum and the prefrontal cortex in the mesocorticolimbic pathway. They are involved in the control of emotion and reward (Tzschentke and Schmidt 2000). Serotonin is located in 9 different types of cell bodies in the pons and midbrain, particularly in the raphe nuclei of the midbrain (Dahlstroem and Fuxe 1964). Serotonin is also thought to play a role in motor activity, and is also involved in sleep, affect, emotion, and temperature regulation (Chojnacki et al. 2016; Denoyer et al. 1989; Jacobs and Fornal 1997; Reid et al. 1968; Strasser, Gostner, and Fuchs 2016).

Further insight into the important role of these monoamines is derived from the clinical features reported in patients with dopamine and serotonin deficiency. A number of inherited primary monoamine neurotransmitter disorders are reported including (i) enzyme deficiencies resulting from defective synthesis or recycling of tetrahydriobiopterin (pterin defects) (ii) defects in monoamine synthesis (AADC and tyrosine hydroxylase deficiency) (iii) defective membrane or vesicular transport of serotonin and/or dopamine (dopamine transporter deficiency syndrome, brain dopamine-serotonin deficiency) (Ng et al. 2015). Affected patients show a number of

overlapping features, including delayed neurodevelopment, abnormal tone, movement disorders, eye movement abnormalities, gastrointestinal dysmotility, sleep disturbance and autonomic features.

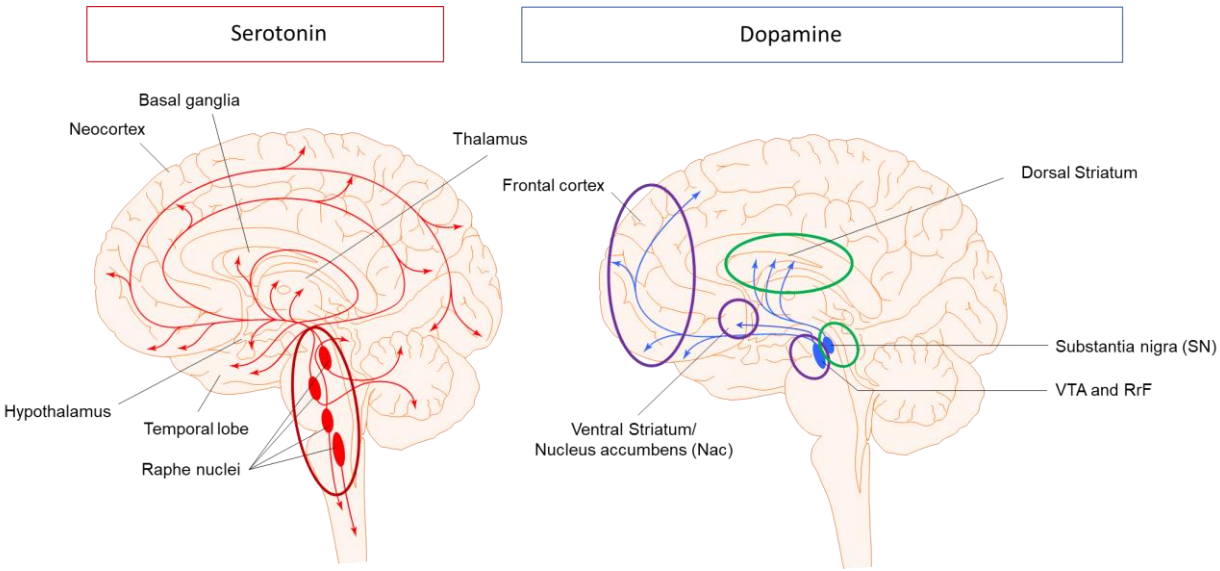

Figure 1-4: Serotonin and dopamine pathways in the brain.
Dopaminergic neurons from the SNpc project to the dorsal striatum (marked in green). Dopaminergic neurons from the VTA and the RrF project to the ventral striatum and the prefrontal cortex (marked in purple). The serotonergic projections from the raphe nuclei include regions of the sensorimotor network and default-mode network (marked in red).

1.2.3 Monoamine Synthesis and Degradation

The AADC enzyme has a key role in monoamine synthesis, converting 5-hydroxytryptophan into serotonin, and L-dopa into dopamine (**Figure 1-5**). Serotonin is synthesised in a two-step reaction. L-tryptophan is hydroxylated to L-5-hydroxytryptophan by the enzyme tryptophan hydroxylase. Tryptophan hydroxylase is dependent on the cofactor tetrahydrobiopterin (BH_4), synthesised through the pterin pathway (**Figure 1-5)** and O_2. L-5-hydroxytryptophan is finally decarboxylated to serotonin by AADC and its cofactor pyridoxal 5'-phosphate (PLP). Serotonin is metabolised to 5-hydroxyindoleacetic acid (5-HIAA) by monoamine oxidase (MAO). Serotonin is also metabolised into N-acetylserotonin and subsequently to melatonin

(Kema, de Vries, and Muskiet 2000). Dopamine is similarly synthesised in a two-step reaction from L-tyrosine. L-tyrosine, catalysed by tyrosine hydroxylase, is converted to L-dopa. Tyrosine hydroxylase is dependent on BH_4 (from the pterin pathway) and O_2. This reaction is the rate limiting step in dopamine synthesis. L-dopa then forms dopamine through decarboxylation by AADC enzyme and its cofactor PLP. Dopamine is converted in noradrenergic cells to noradrenaline by the dopamine-β-hydroxylase (DβH), using ascorbate and O_2. Noradrenaline is then methylated in adrenergic cells to adrenaline by phenylethanolamine N-methyltransferase (PNMT), which is S-adenosyl-methionine (SAM) dependent (methyl donor). The degradation of dopamine to 3,4-dihydroxyphenylacetic acid (DOPAC) is performed by MAO and aldehyde dehydrogenase (ALDH). DOPAC is then metabolised to homovanillic acid (HVA) by catechol-O-methyltransferase (COMT), which is dependent on SAM. Dopamine can also be metabolised to 3-methoxytyramine by COMT, to then be degraded to HVA by MAO and ALDH. The precursor of dopamine, L-dopa is methylated to 3-orthomethyldopa (3-OMD) by COMT. 3-OMD is then converted to vanillactic acid (VLA) by the transaminases (TAM), which depends on PLP [reviewed in (Himmelreich et al. 2019)].

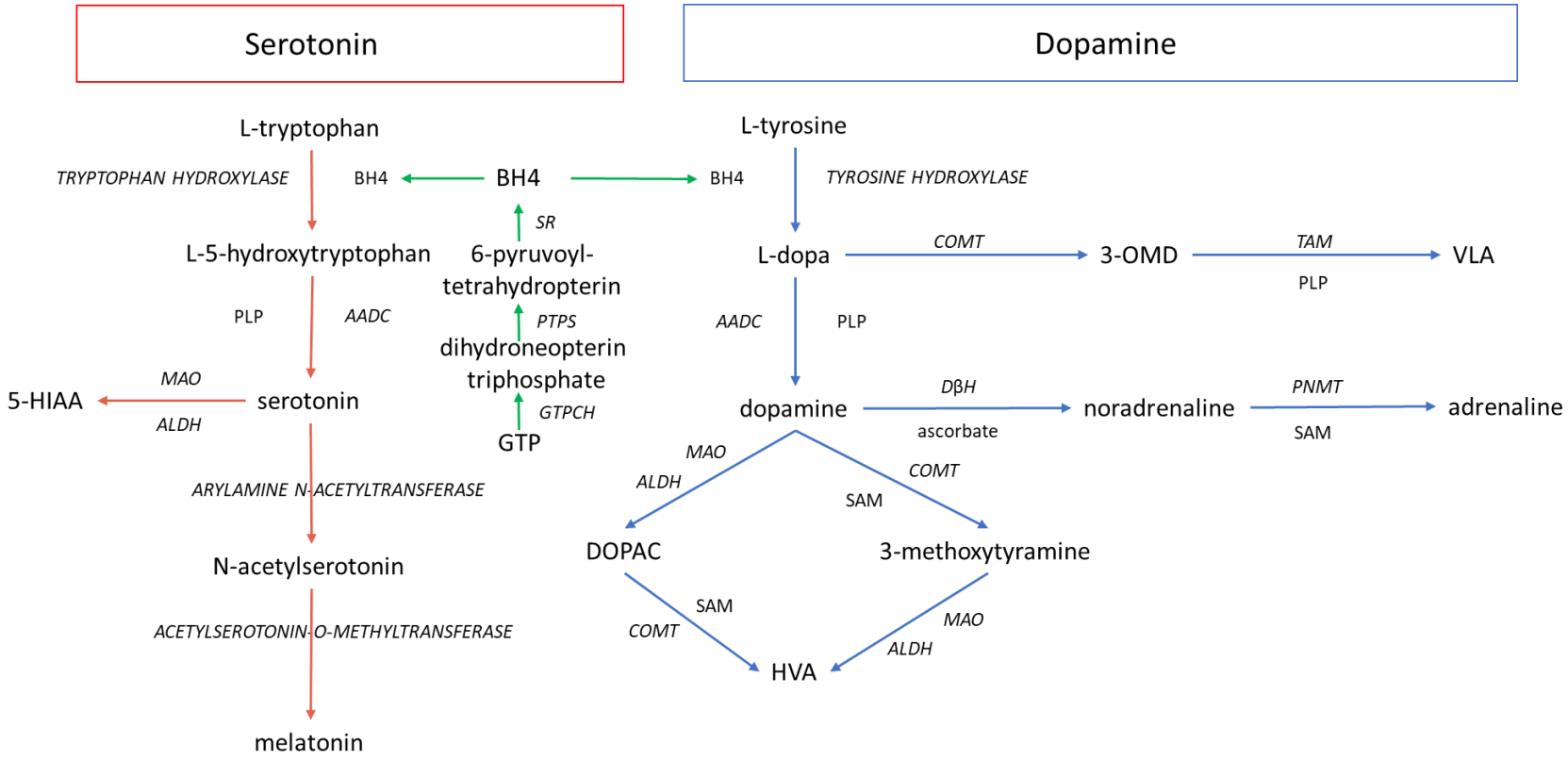

Figure 1-5: Synthesis and metabolism of serotonin and dopamine in neurons.
Figure 1-5 shows the synthesis and metabolism of BH4 (green arrows), serotonin (red arrows) and dopamine (blue arrows) in neurons. BH_4= tetrahydrobiopterin, GTP= guanosine triphosphate, GTPCH= GTP cyclohydrolase, PTPS= 6-pyruvoyltetrahydropterin synthase, SR= sepiapterin reductase, PLP= pyridoxal 5'phosphate, AADC= aromatic L-amino acid decarboxylase, ALDH= aldehyde dehydrogenase, MAO= monoamine oxidase, 5-HIAA= 5-hydroxyindoleacetic acid, L-dopa= L-3,4-dihydroxyphenylalanine, 3-OMD= 3-orthomethyldopa, VLA= vanillylactic acid, DβH= dopamine β-hydroxylase, PNMT= phenolethanolamine N-methyltransferase, SAM= S-adenosylmethionine, DOPAC= 3,4-dihydroxyphenylacetic acid, COMT= catechol-O-methyltransferase, HVA= homovanillic acid.

1.2.4 Monoamine Neurotransmission

1.2.4.1 Uptake into Synaptic Vesicles

After synthesis, dopamine and serotonin are transported from the cytoplasm by the vesicular monoamine transporter 2 (VMAT2) for packaging into synaptic vesicles in the presynaptic terminal. Monoamine uptake into the synaptic vesicles is governed by a proton gradient (Daniels and Reinhard 1988; Darchen et al. 1988) which is regulated by the vacuolar-type H^+ ATPase proton pump (Cidons and Sihrao 1989; Moriyama and Nelson 1987; Xie and Stone 1986).

1.2.4.2 Monoamine Release

Synaptic vesicles move to the active zone of the nerve terminal. The vesicles dock onto the plasma membrane and are primed for monoamine release (Südhof 2004; Wojcik and Brose 2007). The process of priming generates a protein complex to facilitate monoamine release from the synapse. SNARE complexes consist of SNAPs (soluble NSF attachment proteins), SNAREs (SNAP receptors) and NSFs (N-ethylmaleimide-sensitive fusion proteins). The SNARE complexes ensure vesicle targeting and membrane fusion (McMahon et al. 1995; Söllner et al. 1993). When an action potential depolarises the cell membrane, voltage gated Ca^{2+} channels open and generate a calcium influx into the cell. The influx induces vesicle exocytosis. Synaptotagmin proteins act as Ca^{2+} sensors for neurotransmitter release at the synapse and are also connected to the protein complex involved in membrane fusion (Geppert et al. 1994; Reim et al. 2001). After monoamine release, vesicles are endocytosed, either directly or through the endosomal pathway (Ceccarelli, Hurlbut, and Mauro 1973; Heuser and Reese 1973; Südhof 2004).

1.2.4.3 Post-Synaptic Receptor Binding

Dopaminergic neurotransmission: Released dopamine enters the synaptic cleft, and subsequently binds to dopaminergic receptors that are located either at the membrane of the post-synaptic neuron or to autoreceptors at the presynaptic membrane. Dopaminergic receptors consist of two families, the D_1-like receptor family (D_1 and D_5), and the D_2-like receptor family (D_2, D_3 and D_4) (Missale et al. 1988). Dopamine receptors are G protein-coupled receptors (GPCRs). Activation of GPCRs leads to dissociation of the G-protein from the rest of the receptor. The G-protein can then

activate intracellular effector proteins (Gilman 1987). Each GPCR is coupled to different effector proteins, with specific intracellular consequences. For example, D_1-like receptors are involved in the production of cyclic adenosine monophosphate (cAMP), whereas D_2-like receptors are involved in the inhibition of cAMP production (Kebabian and Caine 1979; Onali, Olianas, and Gessa 1984).

Serotonergic transmission: Released serotonin enters the synaptic cleft, and binds to post-synaptic serotonergic receptors, which are either G-protein coupled receptors (5-$HT_{1,2,4\text{-}7}$) (Frazer A 1999) or ligand gated ion channels (5-HT_3) (Derkach, Surprenant, and North 1989) which, similar to dopamine, activate secondary intracellular cascades leading to excitatory or inhibitory responses.

1.2.4.4 Monoamine Reuptake

Dopamine and serotonin are recycled back into the presynaptic neuron by monoamine-specific membrane transporters, namely the dopamine transporter (DAT) (Kilty, Lorang, and Amara 1991; Shimada et al. 1991) and the serotonin transporter (SERT) (Blakely et al. 1991; Hoffman, Mezey, and Brownstein 1991). As such, these transporters play a major role in regulating the amplitude and duration of monoamine signalling. Elucidation of the structure of the homologous bacterial transporter LeuT has greatly facilitated our understanding of the substrate binding sites, and structure-function properties of these SLC6 monoamine transporters (Yamashita et al. 2005). Monoamine transport across the plasma membrane is controlled by the concentration gradient of Na^+ and Cl^- (Gu, Wall, and Rudnick 1994), which is regulated by the membrane Na^+K^+ ATPase pump (Dunham and Glynn 1961; Tissari et al. 1969). Recycled monoamine in the presynaptic neuron is then re-packaged into the synaptic vesicles for re-release.

1.3 The AADC Enzyme in Health and Disease

1.3.1 Structure-Function Properties of AADC Enzyme

The AADC enzyme derives its name from its substrate specificity and ability to decarboxylate specific amines. The enzyme's main catalytic activity consists of the conversion of L-dopa and 5-HTP to the monoamine neurotransmitters, dopamine and serotonin respectively. These monoamines are also the precursors of adrenaline, noradrenaline and melatonin. In addition, although much less efficiently, AADC is able to convert other aromatic amino acids such as p-tyrosine, tryptophan and phenylalanine to the corresponding amines (i.e. trace amines p-tyramine, tryptamine, 2-phenylethylamine), which are postulated to play a role in neuromodulation (Miller 2011). AADC enzyme is therefore not only widely expressed in mammalian neuronal tissue including pre-synaptic dopaminergic and serotonergic neurons (where its presence reflects its activity in neurotransmitter biosynthesis), but also in other tissues of non-neuronal origin. Outside the central nervous system, dopamine and serotonin have a number of non-neuronal roles, acting as exocrine or paracrine factors exerting their function in a limited area within specialised tissues, including the kidney (Hussain and Lokhandwala 2003), liver, gastrointestinal tract (Berger, Gray, and Roth 2009; Rubí and Maechler 2010) and immune cells (Buttarelli et al. 2011).

The native AADC enzyme is a tightly associated homo-dimeric protein, as shown in **Figure 1-6**, which represents the postulated structure derived from *sus scrofa* , solved in complex with PLP and substrate analog carbiDOPA (Burkhard et al. 2001).

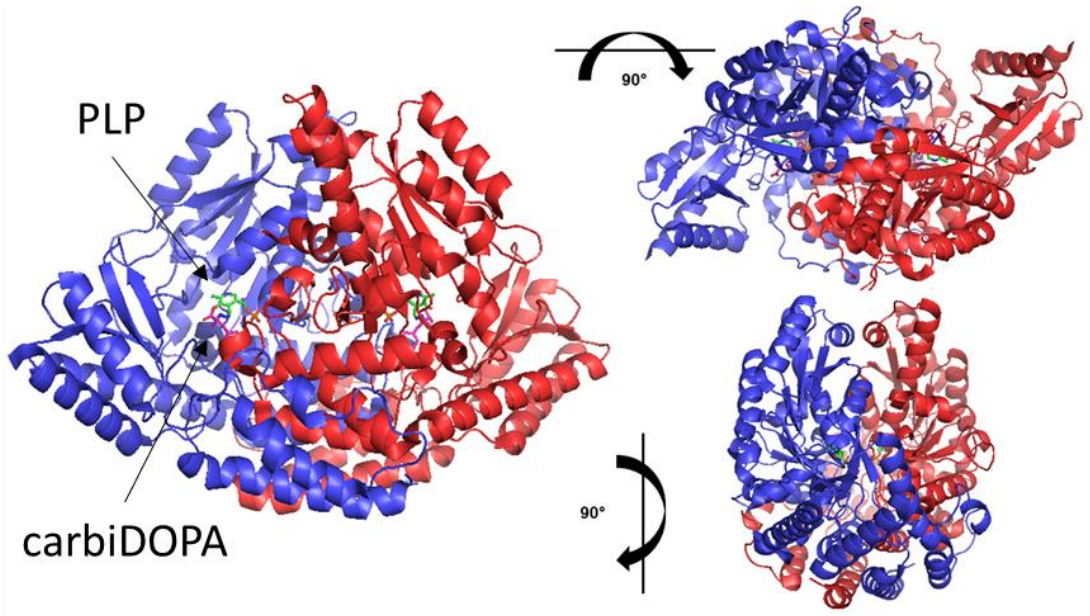

Figure 1-6: Representation of AADC enzyme in the holo-form.
The AADC enzyme structure corresponds to the *sus scrofa* holoenzyme (PDB code: 1JS3), solved in complex with PLP and carbiDOPA, and rendered using PyMol™ software (1.7.4.5. Edu version). AADC is shown with the two monomers composing the native rearrangement of the enzyme coloured in red and blue. PLP and carbiDOPA are represented as sticks (and indicated by black arrows) and coloured by element, based on green and magenta, respectively. Image courtesy of Giada Rossignoli (University of Verona, Department of Neuroscience, Bio-medicine and Movement).

Each monomer of the homo-dimeric rearrangement consists of three distinct domains: a N-terminal domain (residues 1-85), a Large Domain (residues 86-372), and a C-terminal or Small Domain (residues 373-486) (Giardina et al. 2011). The dimeric structure is stabilised by the wide contact surface between the Large Domains of the two monomers, and also by interactions between the two N-terminal domains.

The wide AADC dimeric interface hosts the two active sites, one for each monomer. The active site of the enzyme stably binds PLP cofactor, the active form of vitamin B6. It is covalently bound to the side-chain amino group of Lys303 in absence of substrate, and its linkage is further stabilised through an extended bond network, as visible in **Figure 1-7**, which represents the PLP-carbiDOPA complex in the available structure (Burkhard et al. 2001).

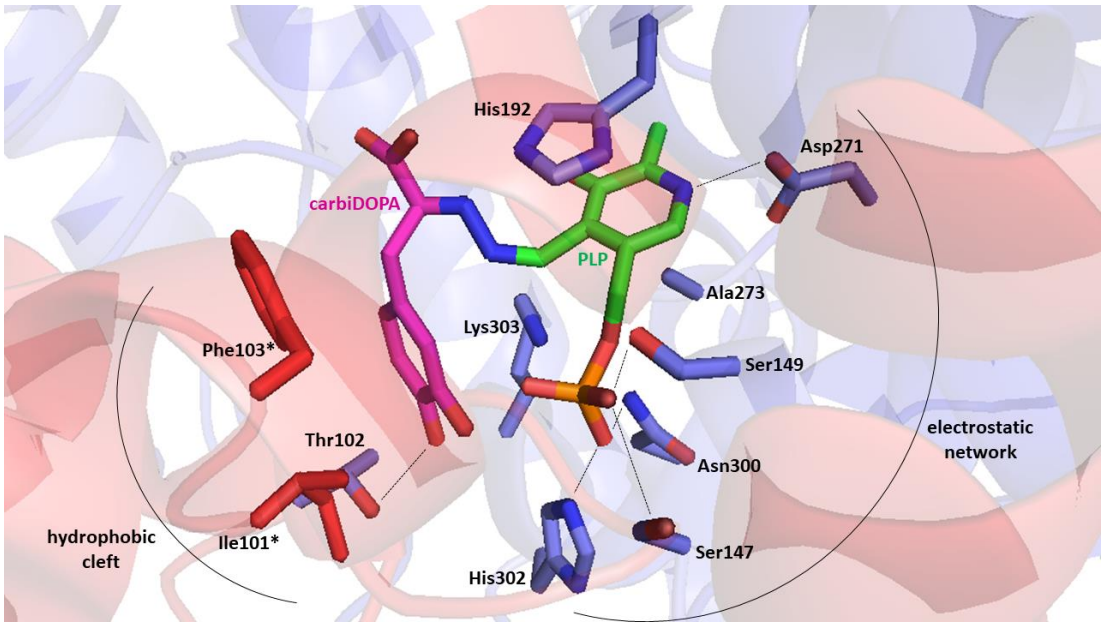

Figure 1-7: Representation of AADC active site.
The structure corresponds to *sus scrofa* holoenzyme (PDB code: 1JS3), solved in complex with PLP and carbiDOPA, and rendered using PyMol™ software (1.7.4.5. Edu version). AADC is shown as transparent cartoon, with the two monomers composing the native rearrangement of the enzyme coloured in red and blue. Active sites residues important for the cofactor or substrate-analog binding are represented as sticks, labelled and coloured by element, based on the corresponding subunit. PLP and carbiDOPA are represented as sticks and coloured by element, based on green and magenta, respectively. Dotted lines highlight the most important interactions between protein residues and PLP or carbiDOPA, while solid lines highlight local protein features relevant to PLP or carbiDOPA binding and positioning. Image courtesy of Giada Rossignoli (University of Verona, Department of Neuroscience, Bio-medicine and Movement).

The most important interactions that stabilise AADC-PLP contact mainly involve:

- Asp271, which makes a salt bridge with PLP pyridine nitrogen
- His192, which is the pyridine stacking residue positioning the PLP ring
- A large number of residues (such as Ser147, Ser149, and Asn300) contributing to stabilisation through hydrogen binding interaction with PLP phosphate group

The solved structure in complex with AADC inhibitor carbiDOPA (Burkhard et al. 2001) allows the identification of important residues involved in substrate binding, shown in **Figure 1-7**. The inhibitor covalently binds to PLP replacing Lys303, and it is stabilised in the active site by other interactions, such as a hydrogen bond with Thr79 and hydrophobic interactions with Ile101* and Phe103* (* symbol indicates residues belonging to the other monomer in relation to the main monomer composing the considered active site).

Even if the active and stable form of AADC is in complex with PLP (holo-form, or closed conformation), the enzyme can also present an open conformation known as apo-form, that does not bind PLP in its active sites. The addition of cofactor drives the conversion from apo to holo-form. AADC apo-form was solved from the human enzyme (Giardina et al. 2011), and is represented in **Figure 1-8**.

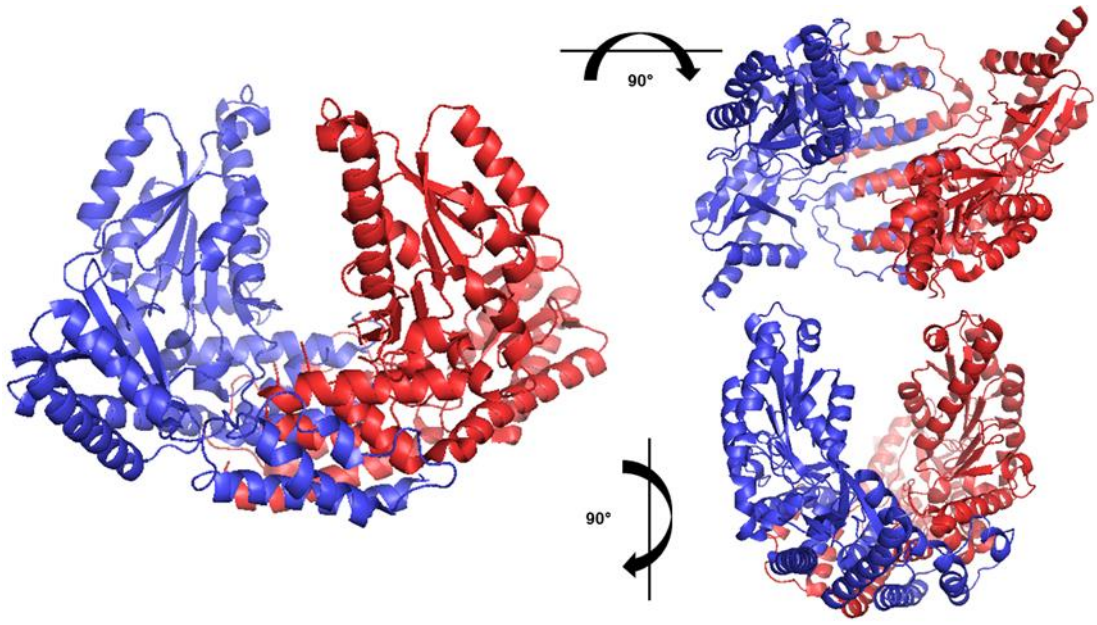

Figure 1-8: Representation of AADC in its apo-form.
The structure corresponds to human apoenzyme (PDB code: 3RBL), solved without PLP, and rendered using PyMol™ software (1.7.4.5. Edu version). AADC is shown as cartoon, with the two monomers composing the native rearrangement of the enzyme coloured in red and blue. Image courtesy of Giada Rossignoli (University of Verona, Department of Neuroscience, Bio-medicine and Movement).

In contrast to AADC holo-form, the apo-form shows a decreased dimer interface that just comprises the N-terminal domains of the two monomers, while the central part of the protein is completely exposed to the solvent. Since the active sites do not bind the cofactor, and they are not properly structured due to the lack of the monomer-monomer interface, AADC apo-form does not present any enzymatic activity.

Interestingly, in both AADC forms, a stretch of amino acids (residues 326-346) is invisible in solved structures, highlighting the presence of a mobile loop, also known as the catalytic loop. This loop contains the important residue Tyr332, which was shown to take part in the catalytic mechanism in enzyme catalysis (Bertoldi et al. 2002). Thus, it has been suggested that the catalytic loop together with neighbouring residues, could cover and occlude the active site cleft after substrate binding.

1.3.2 Mutations in the *DDC* Gene

To date, more than 76 different mutations in *DDC* have been reported in association with AADC deficiency (**Figure 1-9**) (Arnoux et al. 2013; Atwal et al. 2015; Barth et al. 2012; Brun et al. 2010; Dai, Ding, and Fang 2019; Gücüyener et al. 2014; Helman, Pappa, and Pearl 2014; Lee et al. 2009; Leuzzi et al. 2015; Montioli et al. 2014; Pons et al. 2004; Tay et al. 2007; Verbeek et al. 2007).

The *DDC* gene has 15 exons (GRCh37/hg19: NM_000790.3). There are no obvious mutation hotspots and a wide variety of disease variants have been reported, including missense, frameshift, nonsense and splice site variants (**Figure 1-9**). A recurrent mutation (c.714+4A>T) is commonly reported in the Taiwanese population and likely to represent a founder effect (Lee et al. 2009).

Interestingly, different types of mutations are predicted to have different effects on the AADC enzyme, although all are postulated to impair AADC function. Nonsense and frameshift mutations cause a premature stop codon, which are likely to lead to nonsense-mediated decay. In contrast , most missense mutations are predicted to lead to an altered (mutant) gene product (Montioli et al. 2013), which may show altered affinity for the AADC cofactor and/or substrate when compared to wild-type enzyme (Montioli et al. 2014). Sometimes, the genotype may have treatment implications for patients. For mutations affecting the binding of L-dopa to AADC for example, it has been shown that patients clinically respond to L-dopa medication as increasing substrate availability is thought to promote substrate binding to AADC and consequently dopamine production (Chang et al. 2004).

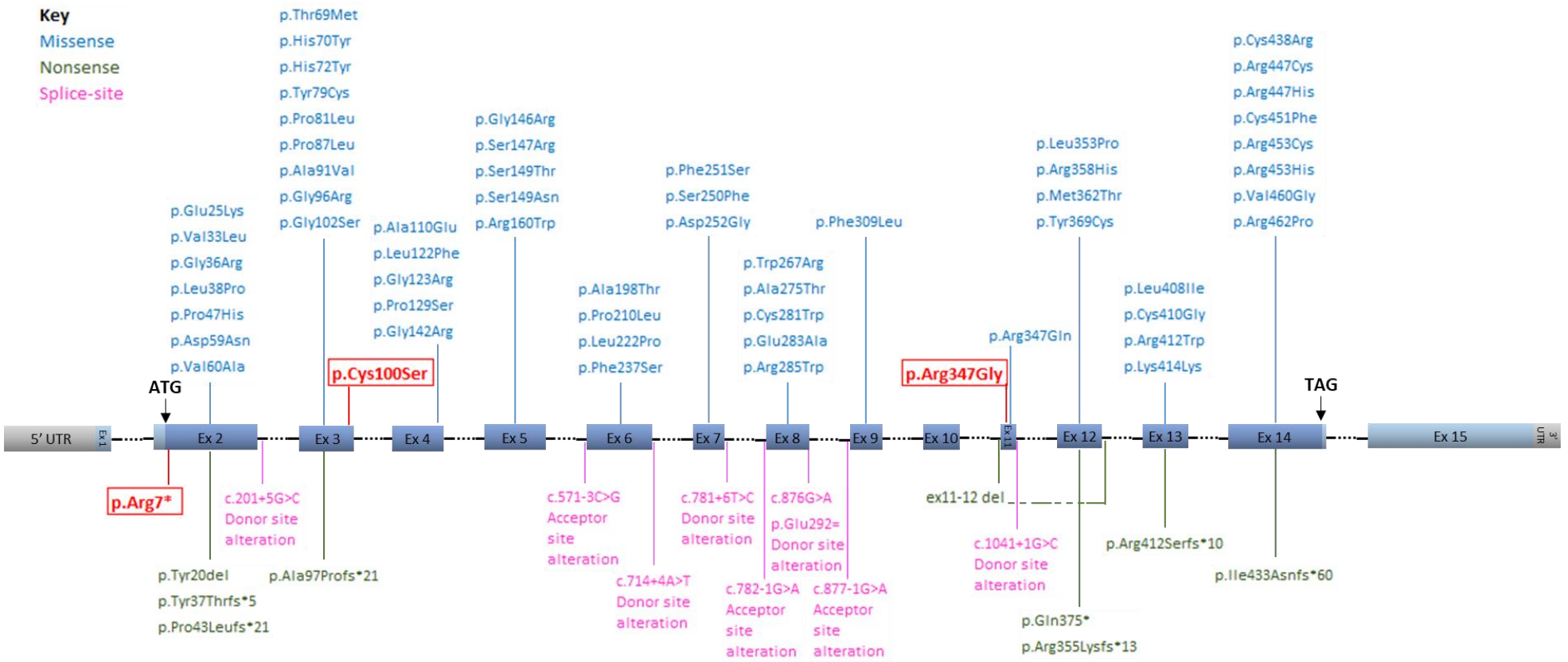

Figure 1-9: Distribution of AADC associated *DDC* (NM_00790.3) mutations relative to the genomic organisation of the gene.
The *DDC* transcript is displayed as blocks and intronic regions as black dotted lines. The coding region (cDNA) is shaded in dark blue. Missense mutations are displayed above the gene in blue, while nonsense and splice-site mutations are displayed below the gene in green and pick, respectively. The mutations investigated in this project are shown in bold red boxes.

1.3.3 Effects of *DDC* Mutations in Patient lines on AADC Enzyme Structure-Function Properties

In this thesis, I have specifically worked on patients with the following genotype:
Patient 1: p.Arg347Gly in exon 11.
Patient 2: p.Arg7*, and p.Cys100Ser in exon 2 and 3 respectively.

The predicted effect of these patient genotypes on protein structure-functions will now be discussed.

Some missense mutations have been shown to specifically affect the catalytic activity of the AADC enzyme, without consistent alteration of substrate or cofactor binding, for example, the missense substitution of Arg347 (Montioli et al. 2016) (**Figure 1-10**), which is homozygously mutated in Patient 1.

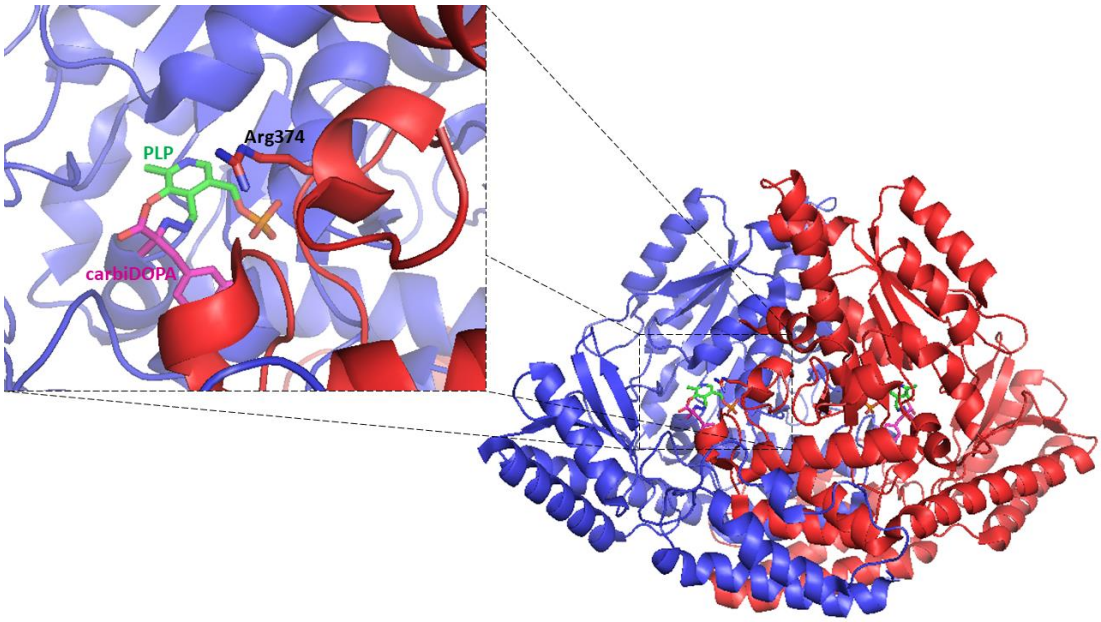

Figure 1-10: Localisation of Arg347 in the AADC protein structure.
The structure corresponds to *sus scrofa* holoenzyme (PDB code: 1JS3), solved in complex with PLP and carbiDOPA, and rendered using PyMol™ software (1.7.4.5. Edu version). AADC is shown as a schematic, with the two monomers composing the native rearrangement of the enzyme coloured in red and blue. Side chain of Arg347 is represented as stick, labelled and coloured by element, based on the corresponding subunit. PLP and carbiDOPA are represented as sticks and coloured by element, based on green and magenta, respectively. Image courtesy of Giada Rossignoli (University of Verona, Department of Neuroscience, Bio-medicine and Movement).

Residue Arg347 is located downstream from the mobile loop fundamental for enzyme catalysis after substrate binding. In particular, Arg347 was shown to participate in a hydrogen bond network comprising also Leu333 and Asp345 that seems to be essential for proper positioning of the mobile loop (Montioli et al. 2016). Thus, it was suggested that the huge decrease in catalytic efficiency for R347G mutant could be directly linked to an incorrect and or/incomplete conformation acquisition of the mobile loop, and subsequent impossibility to participate in the decarboxylation reaction.

In contrast, Patient 2 presents with a compound heterozygous genotype. The frameshift variant occurs early in the gene sequence and leads to a premature stop codon at Arg7 in one allele. This is likely to result in nonsense mediated decay. The second variant is a missense mutation, p.Cys100Ser. Both residues altered in Patient 2 genotype are shown in **Figure 1-11**.

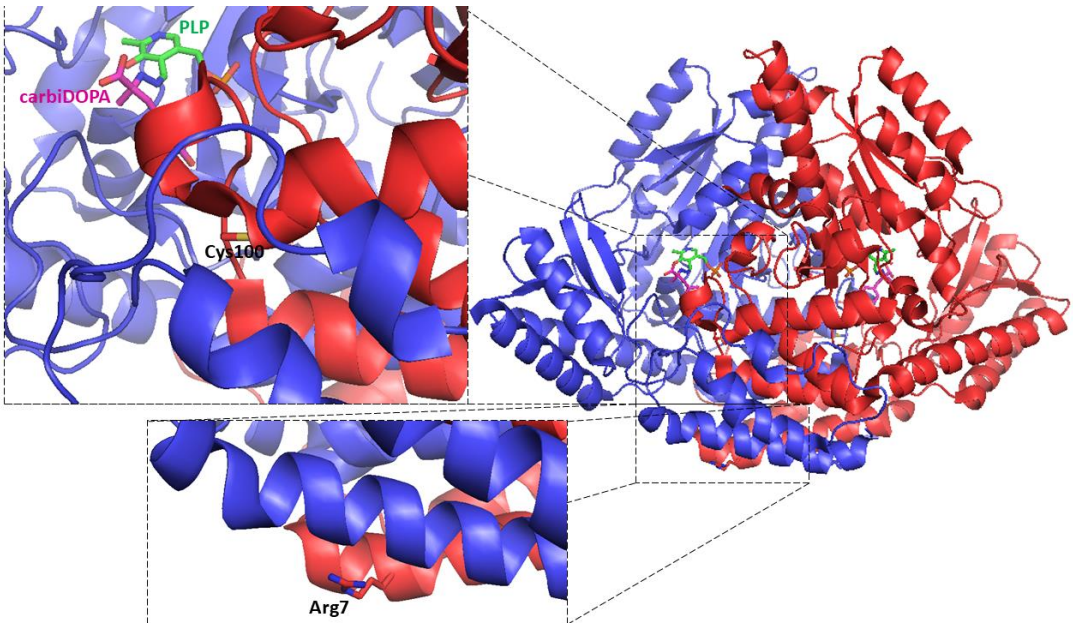

Figure 1-11: Localisation of Arg7 and Cys100 in the AADC protein structure.
The structure corresponds to *sus scrofa* holoenzyme (PDB code: 1JS3), solved in complex with PLP and carbiDOPA, and rendered using PyMol™ software (1.7.4.5. Edu version). AADC is shown as a schematic, with the two monomers composing the native rearrangement of the enzyme coloured in red and blue. Side chains of Arg7 and Cys100 are represented as stick, labelled and coloured by element, based on the corresponding subunit. PLP and carbiDOPA are represented as sticks and coloured by element, based on green and magenta, respectively. Image courtesy of Giada Rossignoli (University of Verona, Department of Neuroscience, Bio-medicine and Movement).

Cys100 is located in close proximity to some important active site residues involved in substrate binding, in particular right upstream to the Isoleucine101-Threonine102-Phenylalanine103 stretch (**Figure 1-11**). Since these amino acids are fundamental for normal substrate binding and positioning (Burkhard et al. 2001; Daidone et al. 2012), the mutation C100S could potentially alter the substrate-binding cleft conformation and consequently decrease the affinity of AADC enzyme for its substrate.

1.3.4 Disease Features of AADC deficiency

1.3.4.1 Symptoms

Patients with AADC deficiency show many of the typical features seen in recessively inherited, severe early-onset neurotransmitter disorders (Kurian et al. 2011; Ng et al. 2015). Common features at presentation include severe neurodevelopmental delay and hypotonia (often misattributed to a neuromuscular cause) as well as oculogyric crises (often misdiagnosed as seizures). Oculogyric crises are paroxysmal, characterised by fixed (often upward) deviation of the eyes, often associated with dystonic posturing and/or dyskinetic movements. Although often the cause for these paroxysmal episodes is not clear, they may be triggered by sleep deprivation, illness, anxiety and emotion. Many families report that inducing sleep, either naturally or with the aid of melatonin or sedatives, can help abate the crises.

Over time, patients with AADC deficiency develop a multisystemic condition (**Figure 1-12**). The majority develop a complex, mixed movement disorder with early generalised hypotonia, dystonia, dyskinesia, myoclonus, chorea and ballismus. Infantile parkinsonism-dystonia is also reported. Most patients have generalised neurodevelopmental delay with delay in achieving cognitive and motor milestones. Autonomic symptoms are frequently reported, including ptosis, excessive sweating, temperature dysregulation and nasal congestion. Additional neurological symptoms include epileptic seizures (rarely reported), behavioural problems (irritability, excessive crying, dysphoria, autistic features), and sleep disturbance (insomnia and hypersomnia). The gastrointestinal issues reported in AADC deficiency are a major source of morbidity for patients; symptoms of diarrhoea, constipation, gastroesophageal reflux, and feeding difficulties can cause discomfort and pain. Hypoglycaemia (particularly in infancy and during times of stress/illness) and cardiovascular issues are also reported and clinicians will often screen for these with 24 hour continuous glucose monitoring and a routine echocardiogram respectively (Wassenberg et al. 2017).

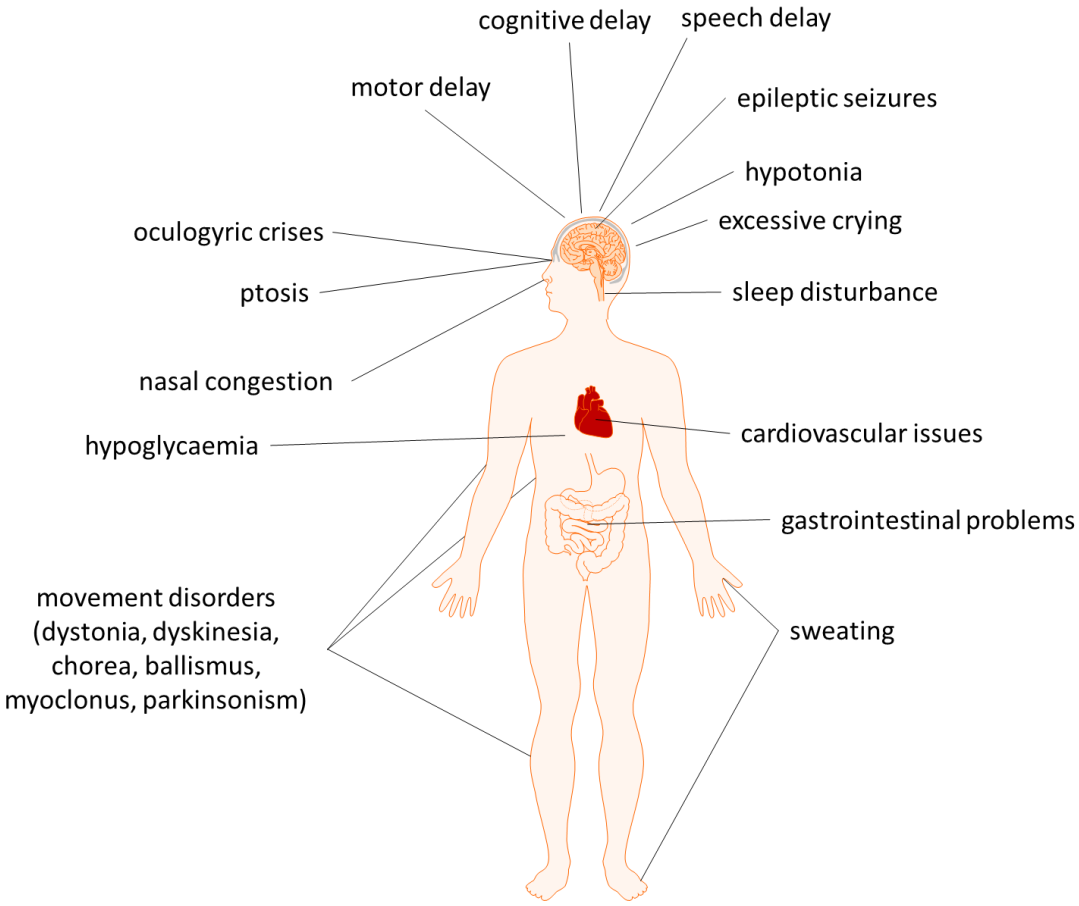

Figure 1-12: Schematic representation of the symptoms of AADC deficiency.

1.3.4.2 Diagnosis of AADC Deficiency

To diagnose AADC deficiency, further laboratory tests need to be undertaken where the diagnosis is clinically suspected. Key diagnostic tests include:

- **Cerebrospinal fluid (CSF) analysis of neurotransmitters**: This is undertaken in a specialist laboratory. Characteristically a typical CSF pattern is evident in AADC deficiency, with evidence of normal pterins, reduced HVA, MHPG, increased L-dopa, increased 3-OMD, elevated 5-HTP, and reduced 5-HIAA (**Figure 1-13**). The finding of normal pterin levels (neopterin, dihydrobiopterin and tetrahydrobiopterin) and raised 3-OMD levels is important to help differentiate AADC deficiency from primary disorders of tetrahydrobiopterin synthesis (Ng et al. 2015). Normal PLP levels help

differentiate AADC deficiency from B6-related disease (Bräutigam et al. 2002; Mills et al. 2005).

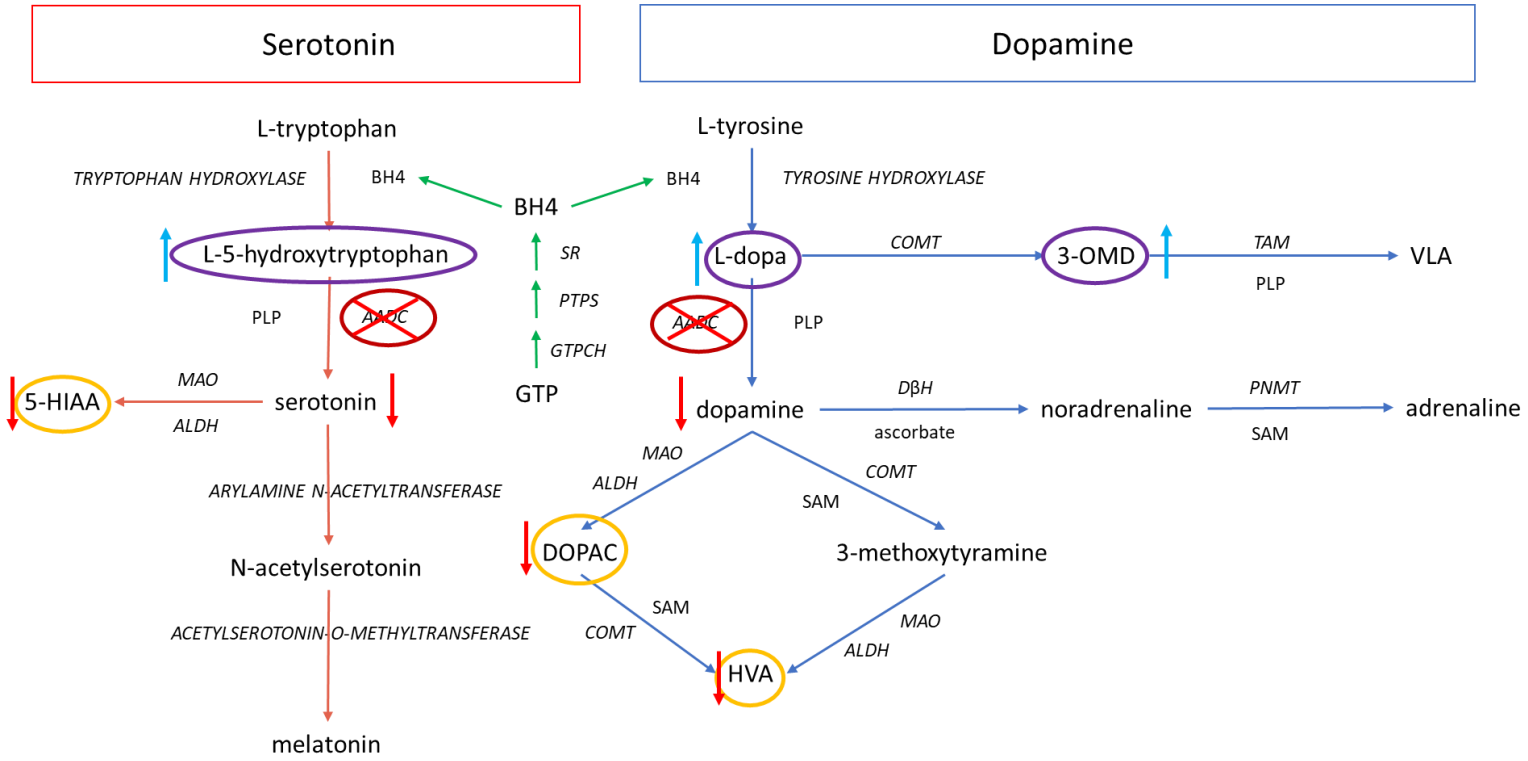

Figure 1-13: Dysregulation in serotonin and dopamine metabolism in AADC deficiency.
BH4 (green arrows), serotonin (red arrows) and dopamine (blue arrows) in neurons. BH_4= tetrahydrobiopterin, GTP= guanosine triphosphate, GTPCH= GTP cyclohydrolase, PTPS= 6-pyruvoyltetrahydropterin synthase, SR= sepiapterin reductase, PLP= pyridoxal 5'phosphate, AADC= aromatic L-amino acid decarboxylase, ALDH= aldehyde dehydrogenase, MAO= monoamine oxidase, 5-HIAA= 5-hydroxyindoleacetic acid, L-dopa= L-3,4-dihydroxyphenylalanine, 3-OMD= 3-orthomethyldopa, VLA= vanillylactic acid, DβH= dopamine β-hydroxylase, PNMT= phenolethanolamine N-methyltransferase, SAM= S-adenosylmethionine, DOPAC= 3,4-dihydroxyphenylacetic acid, COMT= Catechol O-methyltransferase, HVA= Homovanillic acid.

- **Measurement of AADC enzyme activity**: AADC enzyme activity can be measured in plasma. Both L-dopa and 5-HTP can be used as potential substrates for this assay, although L-dopa is usually utilised in diagnostic practice, as it provides a higher analytical yield of measurable neurotransmitter levels. A significant decrease or absence of enzyme activity (usually <10% of control AADC enzyme activity) is detected in AADC deficiency patients. Interestingly, in heterozygous carriers the AADC activity is reported to be moderately reduced (35-40% of normal activity) (Arnoux et al. 2013; Fiumara et al. 2002; Tay et al. 2007; Verbeek et al. 2007) but not as low as that observed in patients.
- **Genetic confirmation:** The *DDC* gene is sequenced to identify bi-allelic pathogenic mutations which occur in trans as either homozygous or compound heterozygous variants. Familial studies are usually undertaken to confirm appropriate disease segregation.

In clinical practice, for most patients AADC deficiency is suspected clinically (which usually prompts CSF testing) and then confirmed genetically. Additional diagnostic tests that may be undertaken include:

- **Blood prolactin levels**: As for other dopamine biosynthesis disorders, the prolactin levels in blood may be elevated although in many AADC deficiency patients, it may be normal. Prolactin levels are neither 100% specific nor sensitive for dopamine deficiency and should thus not be interpreted in isolation.
- **Whole blood serotonin** levels: may be decreased in patients.
- **Urine organic acids:** Detection of increased urine vanillylactic acid (VLA) levels may also be helpful towards making a diagnosis (Wassenberg et al. 2017).

1.3.4.3 Current Therapeutic Approaches

The management of AADC deficiency is complex and requires specialist clinical expertise and knowledge. Recently, a consensus guideline for the treatment of AADC deficiency has been published to aid clinicians in disease management [(Wassenberg et al. 2017), **Figure 1-14**]. Augmentation of PLP, the active form of pyridoxine (cofactor of the AADC enzyme) is usually considered as a first line strategy. Either PLP or pyridoxine can be given. Although pyridoxine is often preferred over PLP due to tolerability. Subsequent to this, patients are usually started on dopaminergic therapy. This may either be as a dopamine agonist that will directly activate the postsynaptic dopamine receptors or monoamine oxidase (MAO) inhibitors which prevent the breakdown of dopamine and serotonin. Both types of drugs are aimed at promoting dopaminergic neurotransmission. Additional medications are often needed as adjunct therapies (**Figure 1-15**) including anticholinergic drugs for the treatment of some AADC-related movement disorders. The precise mechanisms of agents like Trihexyphenidyl is unknown, though it is postulated that they influence the imbalance of dopaminergic and cholinergic pathways. Melatonin supplementation is commonly utilised for the treatment of sleep disturbance. Benzodiazepines are also sometimes used for the treatment of dystonia and/or oculogyric crises. There is limited evidence in the literature for the efficacy of both melatonin and benzodiazepines in AADC deficiency. Alpha-adrenoreceptor nasal drops (such as Xylometazoline) are often used to treat nasal congestion. Folinic acid may be given for potential cerebral folate deficiency; the accumulation of L-dopa and subsequent methylation to 3-OMD requires cleavage of a methyl group from 5-methyltetrahydrofolate which may potentially lead to cerebral folate depletion (Wassenberg et al. 2017).

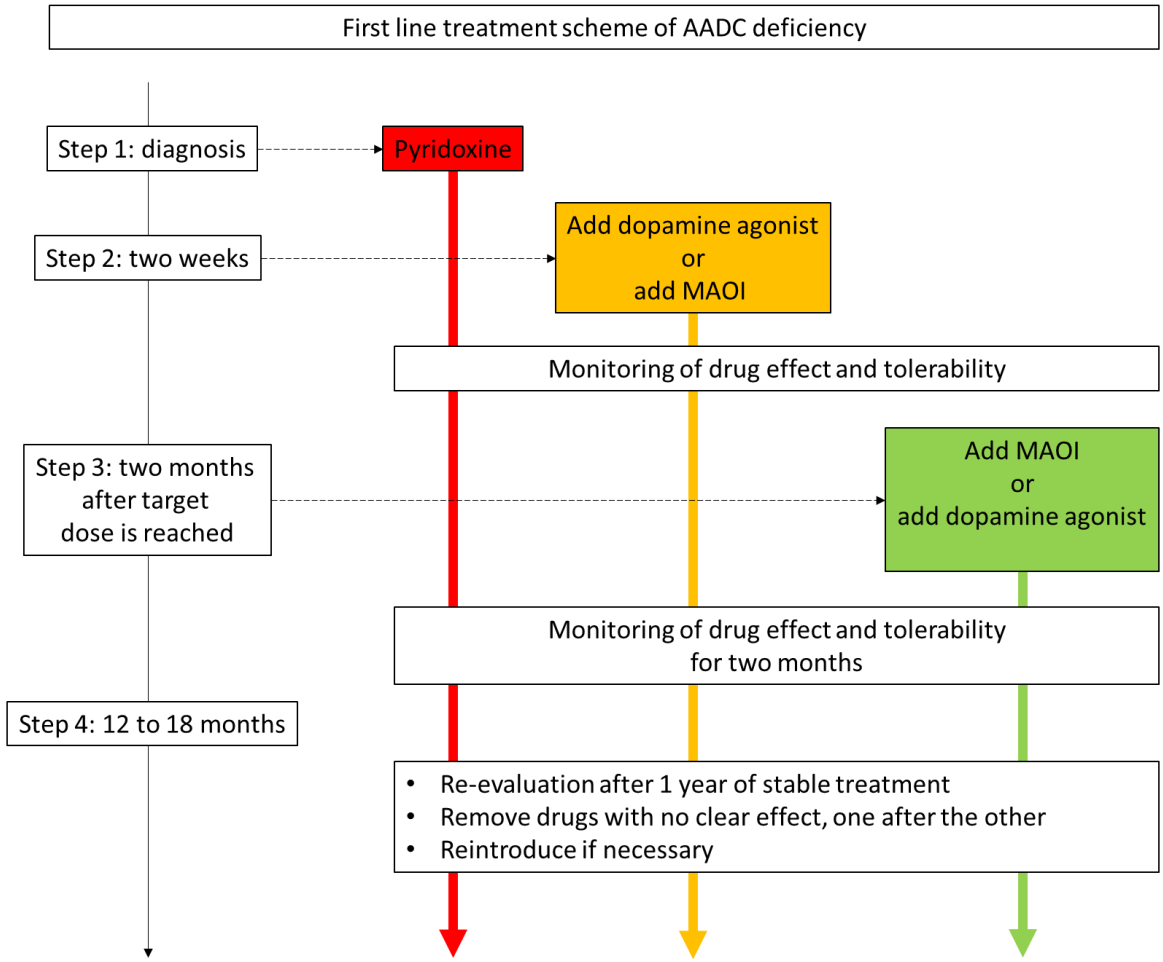

Figure 1-14: Potential treatment flow chart for a newly diagnosed patient with AADC deficiency. Step 1: after the diagnosis pyridoxine is usually given first. Step 2 (after around two weeks) either a dopamine agonist or MAOI are added (in a dose-escalating manner). Step 3: after approximately two months of treatment at the target dose, MAOI or dopamine agonist is added. After approximately one year re-evaluation takes place. Where drugs have no clear effect, these are removed one after the other, and reintroduced if necessary at a later stage. (Figure adapted from Wassenberg et al. 2017).

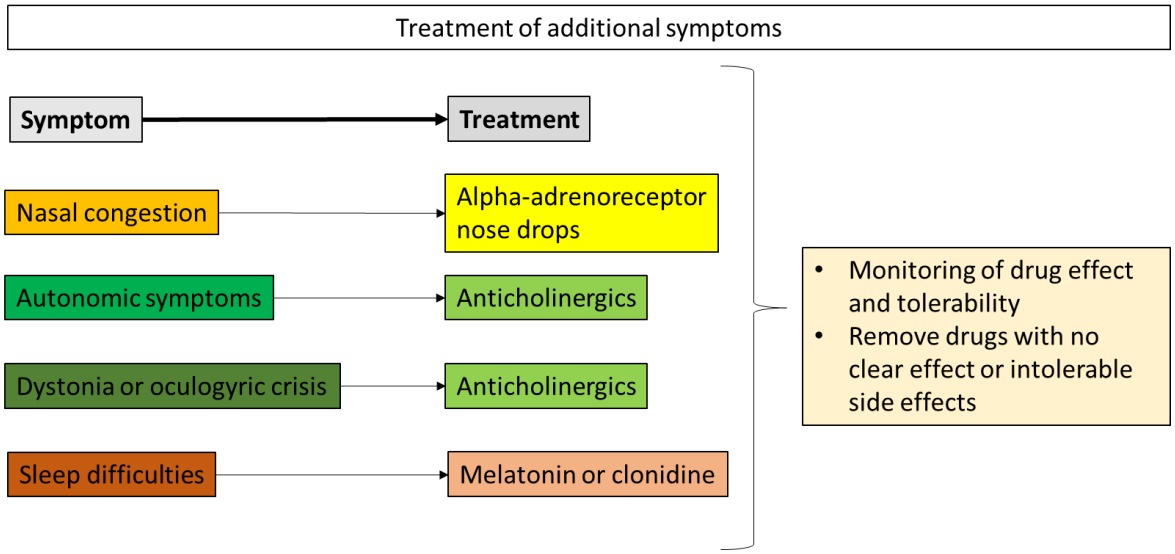

Figure 1-15: Treatment scheme for additional symptoms.
(Figure adapted from Wassenberg et al. 2017).

1.3.5 A Gene Therapy Approach for AADC Deficiency

Although many of the drugs discussed above can lead to improvement of symptoms in AADC deficiency, there are currently no licensed therapies that either cure or significantly modify the disease course of this primary neurotransmitter disorder. In this era of precision medicine, personalised strategies are increasingly recognised as the future of rare disease therapeutics. Indeed, a number of international research groups and pharmaceutical companies have been recently evaluating the potential role of gene therapy in reducing morbidity and mortality in AADC deficiency.

1.3.5.1 Proof-of-Concept Gene Therapy/ Gene Editing in the AADC Mouse Model

In 2013, the AADC knock in (KI) mouse model was published, harbouring the common ('Taiwanese') variant, c.714+4A>T. This is the first reported surviving murine model, as previous attempts to develop a knock out model were not successful, with fetal mice dying in utero (Lee et al. 2013).

The AADC KI mouse model recapitulates many of the key features observed in human disease, including low AADC activity of >0.3% compared to wild-type, mice showed severe dyskinesia, as well as hindlimb clasping. Later on, surviving mice were presented with cardiovascular dysfunction and behavioural problems. Moreover, this phenotype was fully rescued using an AAV9-CMV-hAADC vector [which had previously been used in a Parkinson's disease gene therapy trial (Christine et al. 2009)] by intracerebroventicular injection (Hwu et al. 2013). In 2015, Lee and colleagues subsequently rescued the AADC-deficient KI mice with a fAAV9/3-Syn-I-mAADC vector via intraperitoneal injection. The mice showed even better neuronal transduction, possibly related to the choice of neuronal-specific promoter (synapsin) (Lee et al. 2015).

In 2016, the AADC KI mouse model was used to investigate splicing repair of the AADC splice site variants. A modified U1 snRNA (IVS-AAA) in an adeno-associated serotype 9 (AAV9) vector was used to correct the splicing error and the virus was injected into the cerebral ventricles of the KI mice. A high dose of $2x10^{10}$ vector genomes/µl of AAV9-IVS-AAA was used. The mice showed improved survival, with

an increase in brain levels of dopamine and serotonin. The U1 snRNA-based gene editing proved to be efficient and safe in the murine model, heralding a potentially useful future tool for correcting splice variant mutations in genetic diseases (Lee et al. 2016).

1.3.5.2 Gene Therapy Trials in AADC Patients

The first AADC gene therapy trial was undertaken by Hwu and colleagues in a group of Taiwanese AADC deficiency patients (Hwu et al. 2012). Researchers and clinicians clearly recognised the urgent unmet clinical need for effective treatments for patients with AADC deficiency – which was particularly severe, and associated with significant mortality in the Taiwanese population (Christine *et al.*, 2009; Muramatsu *et al.*, 2010). As an adeno-associated virus type 2 (AAV-2) delivery system with *DDC* was already established for gene therapy in Parkinson's disease, this readily available vector was then trialled in patients with AADC deficiency.

In the first AADC gene therapy trial, 4 Taiwanese patients, aged between 4 and 6 years, all with the common splice variant c.714+4A>T, were treated. Three patients were homozygous for this mutation, and one was heterozygous, harbouring another *DDC* variant (c.1297_1298insA). The AAV2-hAADC vector with CMV promoter was infused bilaterally through a stereotactic approach into the putamen of these patients. The dosage of the AAV2-hAADC viral vector was $1.8x10^{11}$ vector genomes. After one month, dyskinesias were observed in all patients, which settled over time. Motor improvements were observed as soon as the dyskinesia disappeared. Six months post-gene therapy, putaminal AADC activity was evident on 6-[^{18}F] fluorodopa (FDOPA) imaging. Furthermore, patient CSF analysis showed increased levels of both dopamine and serotonin metabolites, suggestive of increased endogenous monoamine production. One year after treatment, the treated patients showed increased bodyweight and motor developmental gains, as well as fewer oculogyric crises, improvement of emotional stability and better sleep patterns. Gene therapy was deemed to be safe and efficacious for patients with AADC deficiency (Hwu et al. 2012).

In 2017, an open-label phase 1/2 AADC gene therapy trial was performed in 10 further Taiwanese patients (M=F, age range 1.7 to 8.4 years). The AAV2-hAADC vector was

bilateral injected intraputaminally, each patient received a dose of $1.81x\ 10^{11}$ vector genomes in total. All patients tolerated the stereotactic neurosurgery. Clinical assessments were undertaken just prior to surgery, and again at 3, 6, 9, 12, 18, and 24 months after treatment. Several patients showed an increase in CSF HVA levels. However, there was no changes in 5-HIAA and 3-OMD levels. Evaluation with the Peabody Developmental Motor Scales-2 (PDMS-2) revealed that all patients showed clinical improvement 12 months after gene therapy. All patients also showed improvements in the abnormal involuntary movement scale (AIMS), as well as further cognitive and language development. Similar to the 2012 study, dyskinesias appeared in all patients after gene therapy, but these settled over time. This study further confirms that intraputaminal delivery of AAV2-hAADC appears to be safe, and well tolerated, with some clinical efficacy for children with AADC deficiency (Chien et al. 2017).

Another open-label phase 1/2 AADC gene therapy trial was performed in AADC deficiency patients with variable phenotypic severity. Six patients were treated, including 4 boys (age 4, 10, 15 and 19 years old), one 12-year old girl with a severe phenotype, and one 5-year old girl with a moderate phenotype. The AAV2-hAADC vector was infused into the same target as previously, with bilateral intraputaminal stereotactic injections. Two years after therapy, all patients were reported to show improvements in motor function. The authors reported that three severely affected patients were able to stand with support, one patient was able to walk with a walker, and one patient with a moderate phenotype was able to run and ride a bicycle. In this study, the authors suggest that although patients > 8 years showed improvement, it was the younger patients who showed the greatest benefits from treatment (Kojima et al. 2019).

A trial is also underway in the USA, evaluating the safety and efficacy of AAV2-hAADC delivered to the substantia nigra pars compacta and ventral tegmental area in children with AADC deficiency (https://clinicaltrials.gov/ct2/show/NCT02852213). In contrast to the previous studies, this trial aims to evaluate the potential benefit of targeting the ventral midbrain, with anterograde axonal transport of vector.

In summary, gene therapy is emerging as an important therapeutic option for patients with AADC deficiency. As more patients are treated, the effect of patient genotype, age at surgery, pre-treatment motor function and target delivery site on overall therapeutic efficacy will become more apparent, allowing further refinement of this new and exciting form of precision medicine.

1.4 Induced Pluripotent Stem Cells

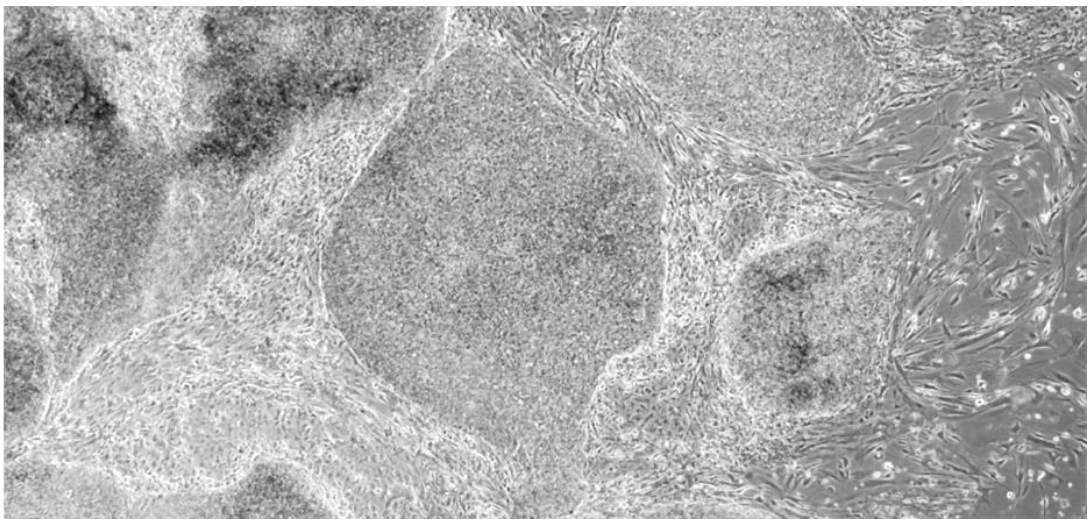

Figure 1-16: Induced pluripotent stem cell colonies on a MEF feeder layer.

In 1998, when the first human embryonic stem cells (hESC) were isolated (Thomson et al. 1998) a new revolutionary tool to model human-related disorders became available. Pre-implantation genetic diagnosis (PDG), used to screen transmission of genetic mutations, allowed isolation of hESC harbouring specific mutations that could be used to model diseases (Eiges et al. 2007; Niclis et al. 2013). Despite these advances, the use of ESC lines has raised a number of ethical concerns, mainly because their generation involves the destruction or manipulation of pre-implantation stage embryos (Klimanskaya et al. 2006). The use of ESCs is therefore strictly governed by law in many countries. It is with the discovery of cellular reprogramming that a fundamental step forward in the *in vitro* modelling of human disease was achieved. In 2007, Yamanaka and his colleagues were able to elegantly reprogram adult human dermal fibroblasts to a pluripotent state by ectopic expression of 4 factors: Oct4, Sox2,

Klf4, and cMyc (Takahashi et al. 2007; Takahashi and Yamanaka 2016). The generated induced pluripotent stem cells (iPSCs) shared most of the characteristics seen in hESCs (including the ability to indefinitely proliferate and differentiate in cells of all three germs layers), thereby providing a new source of patient-derived cells. Yamanaka was awarded the Nobel Prize (Physiology) for his advances in the stem cell field. Even though a decade has passed from generation of the first iPSC lines, the mechanisms by which somatic cells are reprogrammed remain yet to be fully elucidated (Takahashi and Yamanaka 2016). Several studies have provided some mechanistic insight into the reprogramming process. Indeed, the mesoderm to ectoderm transition that occurs in reprogrammed fibroblasts may be viewed as a reversal of the physiological differentiation process that normally occurs in embryos (Takahashi and Yamanaka 2016).

1.4.1 Reprogramming Strategies

Since the originally published methods, many new strategies have been developed to effectively refine the reprogramming of somatic cells into pluripotency. The initial use of integrating retrovirus or lentivirus delivery has been side-stepped by several other technologies aimed at generating transgene-free iPSCs with improved reprogramming efficiency.

1.4.1.1 Non-integrating Vector Strategies

In 2009, Zhou et al. generated human iPSCs from embryonic fibroblasts using adenoviral vectors expressing c-Myc, Klf4, Oct4, and Sox2 cells. The adenovirus, in contrast to other vectors like lentivirus and retroviruses, does not integrate into the targeted host genome, therefore reducing the risk of insertional mutagenesis (Zhou and Freed 2009). Another method for delivering reprogramming-transcription factors was developed by Okita et al. in 2008. This reprogramming strategy was based on two plasmid constructs: the first expressing c-Myc, and the second expressing the other three factors (Okita et al. 2008). This DNA-based method for delivery of the reprogramming transcription factors should ensure episomal existence, but there is still a risk of integration into the host genome. In order to circumvent this, a Sendai Virus-based methodology has been developed. This single strand RNA virus, responsible for respiratory tract infection in rodents, has been developed as delivery vector to

efficiently reprogram human pluripotent cells in a transgene-free way (Fusaki et al. 2009). I have used Sendai Virus technology to reprogram AADC-patient derived human dermal fibroblasts lines into iPSCs (**Figure 1-17**) (**Section 2.2.3**). The commercially available kit (CytoTune™-iPS 2.0 Sendai Reprogramming Kit) is based on a modified non-transmissible form of Sendai Virus used for the delivery of the Yamanaka reprogramming transcription factors. Efficiency of reprograming is among the highest reported, ranging from ~0.01% to 1% depending on the cell type used for reprogramming.

1.4.1.2 Vector -free Strategies

In order to avoid use of any type of vector, genome integration, and to increase the efficiency of the reprograming process, several new strategies involving the use of small molecules or microRNA have emerged. Specific chemicals that can mimic the transcriptional effect of the original Yamanaka transcription factors have been developed, including cellular reprograming through the action of the histone deacetylase (HDAC) inhibitor, valproic acid (Huangfu et al. 2008) and histone methyl transferase (HMT) inhibitor, BIX-0129 (Shi et al. 2008). In 2013, Deng at al. derived iPSCs from mouse somatic cells using a cocktail of 7 small molecules (Hou et al. 2013). The so-called CiPSCs were generated with an efficiency comparable to other reprograming strategies and were proven to be fully pluripotent. Strategies for reprogramming somatic cells into iPSCs have also been developed using ESC-specific microRNAs, which enhance the efficiency of inducing pluripotency, by acting upstream of Oct4, Sox2 and Klf4, but downstream of c-Myc (Bao et al. 2013; Judson et al. 2009).

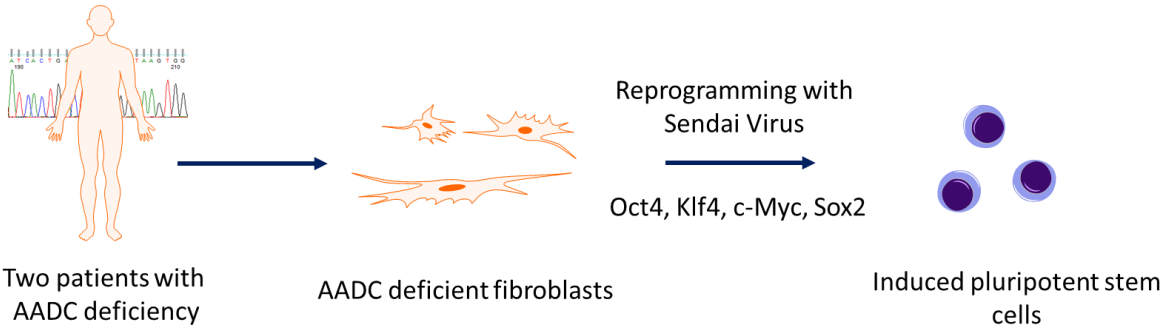

Figure 1-17: Sendai Virus reprogramming from AADC patient fibroblasts.

1.5 Deriving neuronal Cell Types from iPSCs: established Protocols for Differentiation

One of the cell types that have been most successfully derived from iPSCs is the neural stem cell (NSC). Patient-derived neural cells retain the genetic background of the donor offering a unique *in vitro* model. In the literature, there are several available protocols for differentiation of a broad variety of mature neurons as well as glial cellular subtypes (**Table 1-1**).

Human iPSCs have been differentiated into mature cortical neurons, capable of generating action potentials, synaptogenesis and complex neuronal circuits (Shi, Kirwan, and Livesey 2012). GABAergic neurons can be generated from human iPSCs to model disorders such as epilepsy, in which inhibitory synaptic transmission is affected. Differentiation protocols are based on neurodevelopmental principles, with initial specification of developing neural stem cells into medial ganglionic eminence-like progenitors, and further maturation into forebrain-type interneurons. Derived interneuron progenitors develop into a subtype of GABAergic interneuron showing mature physiological properties (Nicholas et al. 2013; Tu et al. 2018; Yang et al. 2017). GABAergic medium-sized spiny neurons have been generated from iPSCs, a model useful for studying Huntington's disease. When generated striatal precursors are grafted into a quinolinic acid-lesioned rat model, they showed survival, further maturation and rescued motor deficits (Delli Carri et al. 2013). Moreover, protocols for the derivation of ventral forebrain cholinergic neurons from hiPSCs have been generated in order to study Alzheimer's disease, Down's syndrome and dementia (Hu et al. 2016).

Several protocols have been published for the generation of midbrain dopaminergic neurons from hESCs (Kirkeby, Grealish, et al. 2012; Kriks et al. 2011). Derived midbrain dopaminergic neurons have been shown to integrate into Parkinson's disease animal models and restore motor function deficits (Kikuchi et al. 2017).

Chemical defined conditions have been utilised to differentiate iPSCs into a number of cell types, including (1) motor neurons to model amyotrophic lateral sclerosis (ALS) (Burkhardt et al. 2013), (2) serotonergic neurons to model neuropsychiatric disorders

(Lu et al. 2016) and (3) cerebellar neurons to model ataxia-telangiectasia (Erceg et al. 2012; Nayler et al. 2017).

Several protocols are also now readily available for the differentiation of iPSCs into glial cells. Astrocytes generated from iPSCs show functional glutamate uptake and calcium activation, similar to that seen in primary human astrocytes (Santos et al. 2017). Moreover, oligodendrocytes have been generated from iPSCs to study myelin-related disorders (Ehrlich et al. 2017).

More recently, differentiation protocols have capitalised on the ability of iPSCs to self-organise and differentiate *in vitro* into three-dimensional (3D) aggregates, leading to the generation of regional-specific 3D brain cultures (Lancaster and Knoblich 2014). Recently, a protocol for the derivation of human midbrain-like organoids (hMLO) has been published (Jo et al. 2016). Generated hMLO present with mature midbrain characteristics, including neuromelanin aggregation. Moreover, hMLO show clusters of genes expressed in late gestational fetal human midbrain, indicating a cellular complexity that is more similar to human brain tissue (Jo et al. 2016).

Table 1-1: Neural cell types derived from human iPSCs.

Differentiated cell type	Type of PSCs	Disease/Potential Applications	Reference
Pyramidal neurons (forebrain)	hiPSCs	Cognitive processes, epilepsy, pyramidal disorders	(Espuny-Camacho et al. 2013)
Cerebral neurons	hiPSCs	White matter disorders	(Shi et al. 2012)
Motor neurons	hiPSCs	ALS	(Burkhardt et al. 2013)
Dopaminergic neurons	hESCs	Neurodevelopmental/neurodegenerative diseases	(Kirkeby, Grealish, et al. 2012)
Dopaminergic progenitors	iPSCs	Primate Parkinson's disease model	(Kikuchi et al. 2017)
GABAergic neurons	hiPSCs	Diseases that affect the inhibitory synaptic transmission	(Yang et al. 2017)
Cortical interneurons (GABAergic neurons)	hiPSCs	Neuropsychiatric diseases – autism, schizophrenia	(Tu et al. 2018)
Forebrain interneurons (GABAergic neurons)	hiPSCs	Neurodevelopmental and degenerative disorders	(Nicholas et al. 2013)
Medium-sized spiny neurons (grafted striatal precursors)	hiPSCs	Rat model of Huntington's disease	(Delli Carri et al. 2013)
Basal forebrain cholinergic neurons	hiPSCs	Alzheimer's disease, Down's syndrome and dementia	(Hu et al. 2016).
Serotonergic neurons	hiPSCs	Psychiatric disorders	(Lu et al. 2016)
Caudal neurons	hESCs	Spinal disorders	(Kirkeby, Grealish, et al. 2012)
Caudal neural progenitor cells	hiPSCs	Chronic cervical spinal cord injury	(Nutt et al. 2013)
Cerebellar neurons	hiPSCs	Cerebellar disorders	(Erceg et al. 2012)
Cerebellar neurons	hiPSCs	Ataxia-telangiectasia	(Nayler et al. 2017)
Astrocytes	hiPSCs	Neurodegenerative disease affecting astrocytes	(Santos et al. 2017)
Oligodendrocytes	hiPSCs	Myelin diseases	(Ehrlich et al. 2017)

hiPSC: human induced pluripotent stem cells; hESC: human embryonic stem cells; PSC: pluripotent stem cells.

1.6 Embryological Development of midbrain dopaminergic (mDA) Neurons: The Basis of mDA Differentiation

Normal neurodevelopment is based upon spatio-temporal regulation and sequential progressive restrictions of cellular fate. Derivation of neural cells from pluripotent stem cells is therefore based on protocols that recapitulate the *in vivo* action of morphogens and signalling molecules that are key contributors in the development of the nervous system. In particular, generation of midbrain dopaminergic (mDA) neurons *in vitro* follows physical and chemical conditions that recapitulate the development processes observed in the developing midbrain.

During the gastrulation process, three distinct germ layers form in the developing embryo: the endoderm, from which the internal organs develop; the mesoderm, which gives rise to bone, muscle, and vasculature; and the ectoderm, from which results skin and the nervous system (Zirra, Wiethoff, and Patani 2016).

Neural development starts in the ectoderm as a consequence of an initial process in neural induction, which forms the neural plate. Morphological changes in the cells forming the neural plate trigger the development of the neural tube. During the early developmental phases of the neural tube, two main signalling centres develop: the isthmic organiser (IsO), and the floor plate (FP). The IsO is responsible for the midbrain-hindbrain boundary (MB-HB boundary) (Joyner, Liu, and Millet 2000; Rhinn et al. 1998; Wassarman et al. 1997), while the FP defines ventral identity of the forming brain [reviewed in (Placzek and Briscoe 2005)]. IsO and FP release morphogens that drive specific gene expression profiles responsible for regional identity of the neural tube, specification and proliferation of progenitors, neurogenesis, differentiation and survival of all different neuronal types. In particular, the two signalling centres IsO and the FP play important roles in the regional identity of the VM, as well as in the development, maturation, and survival of mDA neurons.

1.6.1 Patterning of the Neuronal Tube

During the development of the neuronal tube, the signalling centre IsO is generated at the MB-HB boundary. In mouse models, at embryonic age E7.5, the MB-HB boundary is defined by the transcription factor orthodenticle homolog 2 (Otx2), expressed in the midbrain, and the gastrulation brain homeobox 2 (Gbx2), expressed in the hindbrain (Broccoli, Boncinelli, and

Wurst 1999; Millet et al. 1999; Wassarman et al. 1997) (**Figure 1-18**, green box, anterior-posterior patterning). The coordinated expression of Otx2 and Gbx2 has an inhibitory effect on the expression of morphogen wingless-int1 (Wnt1) (**Figure 1-18**, red box, midbrain), and the fibroblast growth factor 8 (Fgf8) (**Figure 1-18**, green box, anterior-posterior patterning) (Joyner et al. 2000; Rhinn et al. 1998). Both Wnt1 and FgF8 play an essential role in the fate specification of the neural stem cells in the midbrain area of the developing neural tube.

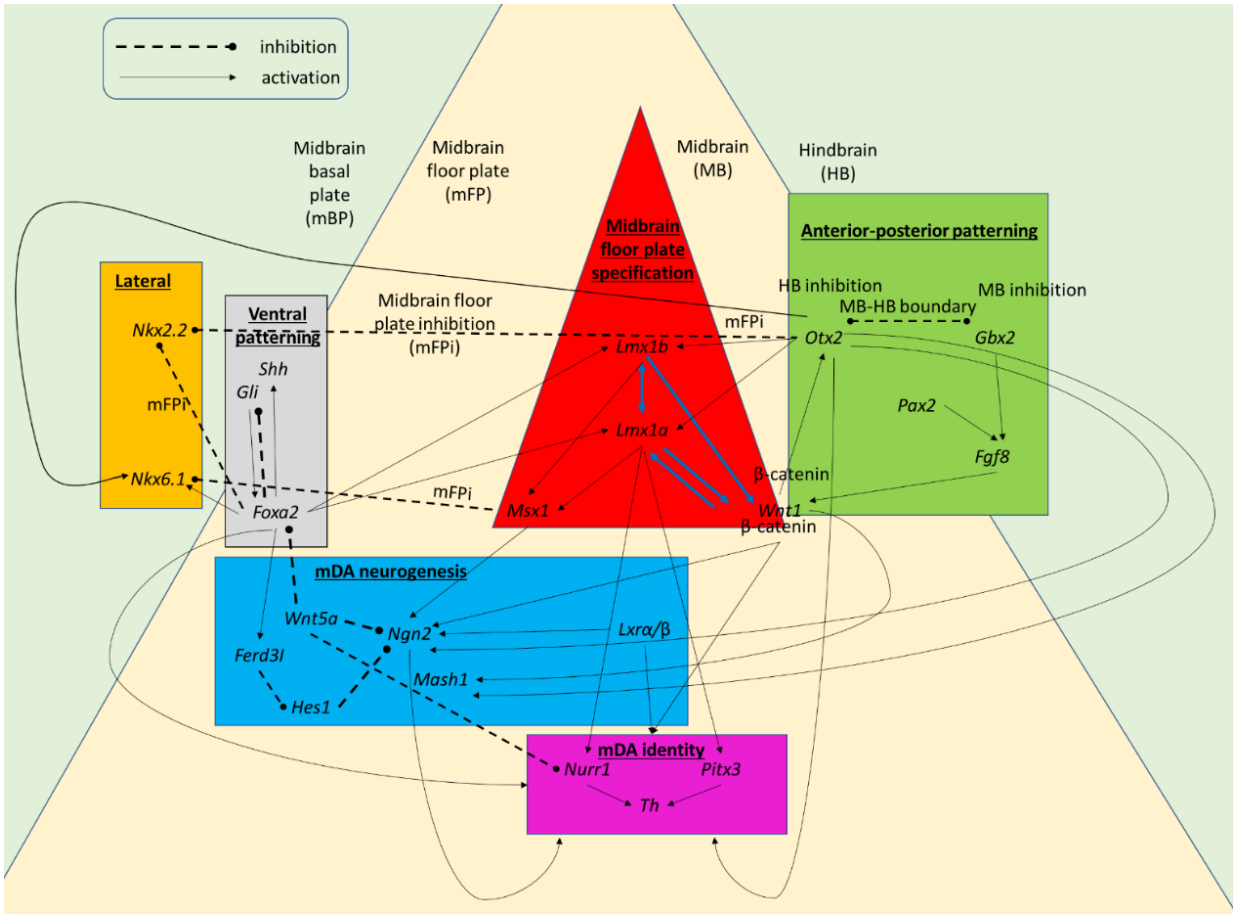

Figure 1-18: Network of genes involved in the development of mDA neurons in the mouse brain.
Image derived from Arenas et al. 2015.

Specification of the signalling centre in the FP is mediated by the transcription factor forkhead box protein A2 (FoxA2). Initially, secretion of the morphogen sonic hedgehog (Shh) from the notochord induces expression of FoxA2 in the ventral area of the neural tube mediating the development of the FP. Subsequently, FoxA2 induces secretion of Shh from the FP itself, which then becomes a secondary organiser, responsible for the ventral patterning (Ang et al. 1993; Sasaki et al. 1997). In mouse, at embryonic age E8.5, the gradient of Shh, expressed

from the FP, controls the ventro-dorsal axis patterning. Shh concentrations are higher in the area of ventral progenitors compared to dorsal cells. High concentrations of Shh in the midbrain FP lead to FoxA2 expression (Sasaki et al. 1997), while lower concentrations in the roof plate lead to expression of NK homeobox protein 6.1 and 2.2 (Nkx6.1 and Nkx2.2) (**Figure 1-18**, orange box, lateral). Consequently different transcription factors are expressed leading to specific and unique ventro-dorsal identities (Briscoe and Ericson 1999; Chiang et al. 1996; Ericson et al. 1996; Marti et al. 1995; Roelink et al. 1995).

Information from both signalling centres, IsO and FP, are essential for the development of mDA progenitors. In particular, FoxA2 and Otx2 regulate the expression of the two LIM homeobox transcription factors Lmx1a and Lmx1b (Lin et al. 2009; Ono et al. 2007) (**Figure 1-18**, red box, midbrain). The combined transcriptional activity of Lmx1a and Lmx1b in the FP, triggers the downstream pathways required for mDA progenitors fate specification and mDA neuron maturation (Andersson, Tryggvason, et al. 2006; Deng et al. 2011; Smidt et al. 2000). Lmx1a activates muscle segment homeobox homolog 1 (Msx1) and inhibits the roof plate fates (Andersson, Jensen, et al. 2006). Moreover, Lmx1a and Lmx1b regulate the activation of Wnt/β-catenin signalling pathway, which triggers the expression of several transcription factors, Wnt1, Msx1, Nurr1, and Pitx3. Nuclear receptor related 1 protein (Nurr1) and pituitary homeobox 3 (Pitx3) are also involved in maturation and survival of mDA neurons. (**Figure 1-18**, pink box, mDA identity) (Chung et al. 2009).

Therefore, the early signalling cascade activated by the combined and coordinated action of the Shh-Foxa2 and Otx2-Wnt1-Lmx1a pathways is essential for the specification of the midbrain progenitors in FP and concomitantly for the suppression of alternative neural fates.

1.6.2 Neurogenesis of mDA Neurons

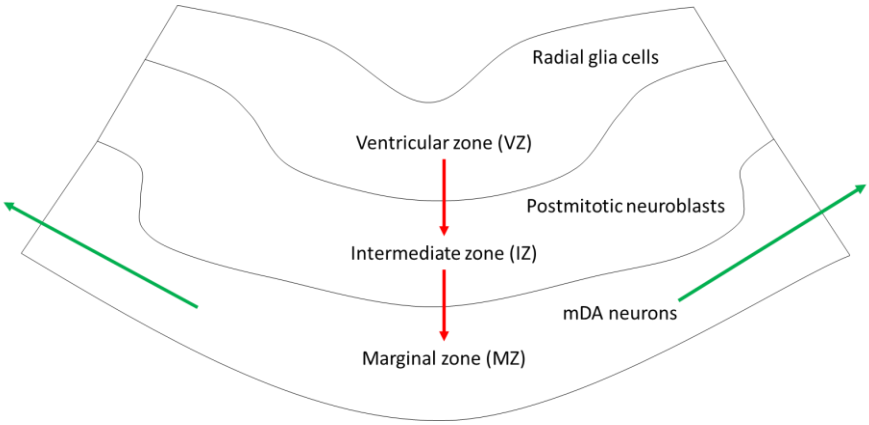

Figure 1-19: Neurogenesis and migration of the mDA neurons.
Image derived from Arenas et al. 2015.

The developmental processes described in the above section take place in the ventricular zone (VZ) of the embryonic midbrain (**Figure 1-19**). In the VZ, neural stem cells from the FP give rise to radial glial mDA progenitors expressing mouse achaete-schute homolog 1 (Mash1) and neurogenin 2 (Ngn2), which then undergo asymmetric mitotic division, generating post-mitotic neural precursors (neuroblasts) (Arenas et al. 2015). Neuroblasts migrate radial through the intermediate zone (IZ) and differentiate in the mantle zone (MZ), where they acquire a dopaminergic phenotype (**Figure 1-19**) (Hanaway, Mcconnell, and Netsky 1971; Kawano et al. 1995). From the MZ, mDA neurons then migrate tangentially forming the substantia nigra SNpc, VTA, and the RrF (Hanaway et al. 1971; Marchand and Poirier 1983).

Expression of Mash1 and Ngn2 is regulated by Shh-Foxa2 and Otx2-Wnt1-Lmx1a pathways. In particular, Foxa2 induces mDA neurogenesis by directly regulating Lmx1a, which in turn upregulates Msx1-mediated Ngn2 expression (Andersson, Jensen, et al. 2006; Kele et al. 2006) (**Figure 1-18**, blue box, mDA neurogenesis). In contrast, FoxA2 is responsible for the expression of Ferd3l (Fer3-like), which in turn represses Hes1 (hairy and enhancer of Split1), a suppressor of pro-neural genes Mash1 and Ngn2 (Ono et al. 2010).

During the process of radial migration through the IZ, neuroblasts progressively acquire a dopaminergic phenotype and express later transcription factors such as Nurr1 and Pitx3. Nurr1 and Pitx3 activation is regulated by several transcription factors responsible for dopaminergic

neuronal differentiation. Indeed, the expression of Pitx3, is indirectly sustained by Wnt1/βcat (Prakash et al. 2006), while Lmx1a/b directly regulates Nurr1 and Pitx3 (Chung et al. 2009).

During migration from IZ to MZ mDA, neuroblasts further mature and start to express dopaminergic related proteins such as TH, an enzyme involved in dopamine synthesis. The neuroblast maturation process is regulated by some early transcriptional factors such as Otx2, Lmx1a/b, Foxa1/2, together with the homeobox genes engrailed 1/2 (En1/2), and late transcription factors such as Nurr1 and Pitx3. Therefore, the two main signalling pathways of the midbrain FP, Wnt1-Lmx1a and Shh-Foxa2, not only regulate the midbrain dopaminergic fate, but are also essential for the differentiation and survival of mDA neurons. Foxa2 regulates the expression of Nurr1, and En1 in mDA neuroblasts and neurons, as well as the expression of TH in mDA mature neurons (Ferri et al. 2007; Stott et al. 2013). Nurr1 regulates the expression of several genes expressed in mature mDA neurons and necessary for their physiology, including TH, solute carrier family-18 member-2/vesicular monoamine transporter-2 (Slc18a2/Vmat2), solute carrier family-6 member-3/dopamine transporter (Slc6a3/DAT), and brain-derived neurotrophic factor (Bdnf) (Jankovic, Chen, and Le 2005; Joseph et al. 2003; Volpicelli et al. 2007). Moreover, Pitx3 upregulates expression of TH, the dopamine receptor 2 (D_2), Vmat and DAT (Jacobs et al. 2011; Veenvliet et al. 2013). En1/2 promotes the survival of adult mDA neurons (Alvarez-Fischer et al. 2011), together with neurotropic factors like BDNF (Hyman et al. 1991) and glial cell-line derived neurotrophic factor (GDNF) (Åkerud et al. 2001; Arenas et al. 1995). Factors and genes which regulate mDA neuronal development have been extensively studied in several animal models, but the exact mechanisms underlying human midbrain development are still poorly elucidated. A few studies report that key regulators of mDA neuronal development are present in the human ventral fetal midbrain. Analysis of the human brain at several embryonic developmental stages, ranging from 5 to 8 weeks post conception, showed that development of the ventral midbrain and mDA neurons is characterised by expression of the same factors described in animal models. The human ventral midbrain at early stages of development is similarly marked by the expression of LMX1A and FOXA2 as well as NGN2 and MASH1. Midbrain neural stem cells and neuroblasts follow spatial localisation in the midbrain neural wall as described in the previous **Sections 1.6.1** and **1.6.2**. Progressive maturation of human mDA neurons occurs in the MZ where TH expressing neurons accumulate around 8 weeks post conception. As described in the animal model, human mDA neurons also express PITX3 and NURR1, which are necessary for mDA neuronal maturation and survival (Nelander, Hebsgaard, and Parmar 2009). Single cell

RNA sequencing studies attempting to compare the mouse and human ventral midbrain, have highlighted the level of complexity in both animal and human developing midbrain. La Manno et al. in 2016 identified 25 molecularly defined human cell types, with different radial glia cells and progenitors. Interestingly, between mouse and human, cell types and gene expression were conserved overall, but several differences were observed for cell proliferation rates, developmental timeframe and mDA neuronal maturation. Moreover, in both the mouse and human, three distinct subtypes of embryonic dopaminergic neurons were identified, highlighting the complexity of the developing midbrain (La Manno et al. 2016).

1.7 Using iPSC-derived neuronal Systems to model Neurological Diseases

Historically, the modelling of neurological diseases has been complex and fraught with difficulties for multiple reasons. The human brain is relatively inaccessible, when for example, compared to skin, liver and muscle tissue. Isolating healthy neural cells from post-mortem brains is challenging, given their susceptibility to oxygen deprivation and external stressors. Furthermore, post-mitotic neurons and oligodendrocytes are difficult to expand in an *in vitro* culture system. To complicate matters, there is a relative paucity of 'perfect' animal models that both harbour disease-causing genetic mutations and fully recapitulate the human neurological phenotype.

It is universally acknowledged that iPSC platforms have the potential to revolutionise how we model disease, particularly for neurological disorders. As previously described, a wide range of neural cells can now be differentiated using embryology-derived developmental principles. Such iPSC-derived model systems are proving to be valuable tools to further understand neurobiology, elucidate disease mechanisms and develop novel precision therapies (**Figure 1-20**). Indeed, such models have already been developed for a number of monogenic defects, chromosomal disorders and complex polygenic diseases.

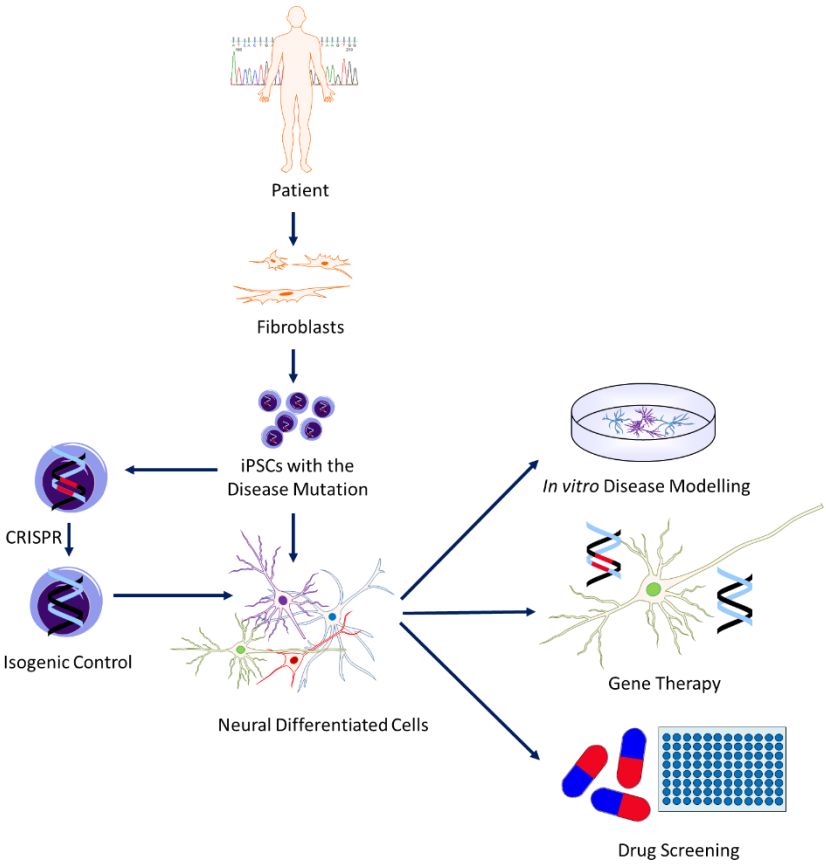

Figure 1-20: Schematic representation of iPSC-based disease modelling for neurological disorders.

1.7.1 Modelling adult-onset Neurodegenerative Diseases

Many monogenic and complex neurodegenerative disorders have been modelled using iPSC systems. For example, *in vitro* modelling of ALS has provided insight into underlying disease mechanisms, with different research groups reporting diverse disease-specific phenotypes, from neurite degeneration to mitochondrial dysfunction. iPSC models have also been utilised to investigate both sporadic and early-onset familial (*LRRK2, PARK2, PINK1)* Parkinson's disease, revealing involvement of alpha-synuclein, dopamine dysregulation, autophagy, mitochondrial dysfunction, abnormal neurite outgrowth/ arborisation, and aberrant network activity as putative pathogenic disease mechanisms. One major challenge when modelling such later-onset diseases is the relatively 'fetal' stage of iPSC neurons at derived maturation. This may be overcome by age-inducing compounds, including progerin, MG132 and concanamycin (Cooper et al. 2013; Miller et al. 2013; Nguyen et al. 2011), which may facilitate appropriate ageing of cells, thereby benefitting iPSC disease modelling for these adult-onset diseases.

1.7.2 Modelling childhood Neurodevelopmental Disorders

iPSC derived neuronal model systems are increasingly recognised as an ideal tool for elucidating disease mechanisms in childhood neurological diseases. Many are fully penetrant, single gene disorders, where disease manifestation usually occurs in infancy or early childhood. Some diseases may even be of prenatal onset thereby rendering the 'fetal' stage of derived neuronal maturation as highly relevant and clinically applicable when studying disease.

Many childhood-onset genetic disorders have now been studied, which has facilitated further elucidation of the underlying disease pathophysiology for a wide variety of different diseases (**Table 1-2**). Despite these advances, there is very little published data regarding disease modelling in the primary neurotransmitter disorders - which is somewhat surprising, given the high suitability of mDA model for studying such infantile-onset disorders. To date, Jung-Klawitter and colleagues (2016) reported successful generation of an iPSC line from a patient with tyrosine hydroxylase deficiency. Further information on the neuronal phenotype is not available (Jung-Klawitter et al. 2016). Patient iPSC-derived mDA lines have also been generated for two pterin defects, namely dihydropteridine reductase (DHPR) deficiency and 6-pyruvoyltetrahyropterin synthase (PTPS) deficiency. For both diseases, disease-specific alterations in dopamine metabolites, pterin species and tyrosine hydroxylase levels were reported (**Table 1-2**).

Table 1-2: Selected examples of iPSC-based modelling studies for childhood neurological disorders.

Disease	Causative gene	Key findings in iPSC derived cell model	Reference(s)
Neurodevelopmental disorders			
Rett Syndrome	*MECP2*	Disease-related genetic mutations can increase the frequency of neuronal L1 transposition.	(Muotri et al. 2010)
		Disease-related defects in action potential firing and inward currents.	(Farra et al. 2012)
		Disease-related alterations in dysbindin interactome.	(Larimore et al. 2013)
		Glial contribution to disease pathology.	(Williams et al. 2014)
		Disease-related alterations in soma size, information encoding properties and synaptic connectivity.	(Djuric et al. 2015)
		Disease-related altered regulation of GRID1.	(Livide et al. 2015)
		Key role of KCC2 in disease.	(Tang et al. 2016)
		Disease-specific neuronal migration and maturation (neurite outgrowth and synapses).	(Zhang et al. 2016)
Fragile X Syndrome	*FMR1*	FMR1 gene inactive. DNA methylation and histone modifications were seen indicating inactive heterochromatin.	(Urbach et al. 2010)
		Aberrant differentiation into post-mitotic neurons and glia cells. Epigenetic modifications of the FMR1 gene.	(Sheridan et al. 2011)
		Generated forebrain neurons showed defective neurite initiation and extension.	(Doers et al. 2014)
		Aberrant upregulation of genes involved in axonal guidance and neural differentiation. RE-1 silencing transcription factor (REST) elevation.	(Halevy, Czech, and Benvenisty 2015)
		Aberrant neurogenic phenotype affecting developmental signalling, cell migration and neuronal maturation.	(Boland et al. 2017)
Movement Disorders			
DYT28 Dystonia	*KMT2B*	KMT2B is essential for epigenetic and transcriptomic resetting for transdifferentiation of fibroblasts into induced neuronal cells (iNs) (suppressing alternative fates and promotion of iNs).	(Barbagiovanni et al. 2018)

Ataxia-telangiectasia	*ATM*	Model showed defective radiation-induced signalling, radio sensitivity, as well as cell cycle checkpoint defects.	(Nayler et al. 2012)
		Impairment of neuronal maturation, suppression of the response and repair of DNA double-strand breaks (DSBs), accumulation of topoisomerase 1-DNA covalent complexes (Top1-ccs).	(Carlessi et al. 2014)
		Disruption of gene networks connected with oxidative stress and synaptic vesicle dynamics.	(Nayler et al. 2017)
Neurometabolic Disorders			
Pterin defects	*PTPS/DHPR*	Using the BH4 precursor sepiapterin improved the PTPS deficient phenotype.	(Ishikawa et al. 2016)
Niemann Pick Type C	*NPC1*	Accumulation of cholesterol in hiPSCs, and neural progenitor cells of NPC1 patients.	(Trilck et al. 2013)
		Protocol to differentiate neurons and glial cells. Immunocytochemistry, patch clamp recordings as well as calcium imaging showed functional maturation.	(Trilck, Hübner, and Frech 2016)
		Cholesterol may influence GM2 degradation pathway which leads to accumulation of GM2.	(Trilck et al. 2017)
Neurodegenerative Diseases			
Beta-propeller associated neurodegeneration (BPAN)	*WDR45*	Increased cellular iron levels and oxidative stress. Also, mitochondrial abnormalities, autophagic defects, as well as diminished lysosomal function.	(Seibler et al. 2018)

1.7.3 iPSC Systems to evaluate novel Therapies

As well as providing insight into disease mechanisms, iPSC-derived neuronal models are increasingly being utilised as platforms for therapeutic evaluation. Indeed, such models have already been used to test approved compounds and novel molecules, as well as gene therapy and other gene editing technologies.

1.7.3.1 Targeted Candidate Drug Approaches

A candidate drug approach is often adopted when a druggable target is identified. For example, in spinal muscular atrophy, patient iPSCs-derived motor neurons manifest a disease-specific mitochondriocytopathy. When treated with N-acetylcysteine (NAC), patient-derived lines showed improved mitochondrial function, with subsequent rescue of motor neuron degeneration *in vitro*. Rescue of the mouse model of Rett syndrome with insulin-like growth factor (IGF1) prompted testing in the MECP2-deficient iPSC model. Disease-specific phenotypes were ameliorated by IGF1, with an observed increase in glutaminergic synapse number. Following on from these pre-clinical studies, a phase 2 trial with the compound Trofinetide (a IGF1 analogue) has been recently undertaken in patients with Rett syndrome; participants showed amelioration of a number of clinical outcome measures, which translated into meaningful disease improvement. For Alzheimer's disease, iPSC-based testing has focused on agents with putative effects on β-amyloid secretion (Yagi et al. 2011). With the aim of reducing β-amyloid secretion, a γ-secretase inhibitor and amyloid precursor protein cleavage modulator were tested and found to suppress β-amyloid secretion in a dose-dependent manner. Finally, the use of kinetin in a patient-derived neuronal model of familial dysautonomia showed improvement of the splicing defect, with higher percentages of neurons during the differentiation process. Kinetin has already been tested in patients and in a pilot clinical trial, where it has been shown to increase wild-type IKBKAP mRNA production. A phase 2 trial of kinetin is underway (ClinicalTrials.gov identifier: NCT02274051). The iPSC-derived neuronal platform therefore appears to be a useful platform for targeted drug screening, which has the potential to accelerate promising therapies to the clinic.

1.7.3.2 Library Drug Screening Approaches

iPSC-derived neuronal platforms can be utilised to screen small (<10,000 compounds) or medium to large (>10,000 compounds) libraries. Such testing is particularly useful if clear target pathways are not identified, allowing evaluation of an unbiased hypothesis, as well as

the potential to identify new structural scaffolds and chemical functions. Library screening usually requires either 96- or 384- well plates, with seeding of cells at one point of the neuronal differentiation process. A number of different readouts can be used to assess drug effects, including high content imaging with immunofluorescence, expression of reporter gene and cell viability. High throughput screening has been applied to a number of different diseases and will hopefully evolve in the future as a standard approach for new drug evaluation (**Table 1-3**).

Table 1-3: Selected examples of large screens using iPSC disease models [adapted from (Little et al. 2019)**].**

Disease/Target	Cell type for screening	Compounds (number and type)	Outcome (hits/potential drugs)	References
Spinal muscular atrophy	Motor neurons derived from hiPSCs	200,000	Not published	Reviewed in (Grskovic et al. 2011)
Parkinson's Disease	Motor neurons derived from hESCs	2000	6 hits, Isoxazole was tested further	(Ryan et al. 2013)
ALS	Motor neurons derived from hiPSCs	1757	38 hits reduced percentage of cells with aggregates. Compounds were cyclin-dependent kinase inhibitors, c-Jun N-terminal kinase inhibitors, Tripotolide and cardiac glycosides	(Burkhardt et al. 2013)
Alzheimer's Disease	Commercially available neurons (iCell) derived from hiPSCs	Several hundred compounds from the compound library of GSK	19 hits, one was a Cdk2 inhibitor	(Xu et al. 2013)
Alzheimer's Disease	Cortical neurons with trisomy of chromosome 21 derived from hiPSCs	1,200 from the Prestwick Chemical library	55 compounds were identified, validated hits included ®-flurbiprofen and ivermectin	(Brownjohn et al. 2017)
Alzheimer's Disease	Cortical neurons derived from hiPSCs	1258 pharmaceutical compounds	27 hits after secondary testing; 6 lead compounds were chosen: bromocriptine, cilostazol, cromolyn, fluvastatin, probucol, topiramate	(Kondo et al. 2017)

1.8 Hypothesis and Main Aims

1.8.1 Background

AADC deficiency is a severe, early onset neurological disorder, for which there are no established disease-modifying or curative treatments. Although there are mouse and zebrafish models of AADC deficiency (Caine et al. 2017; Hwu et al. 2013; Shih et al. 2013), neither fully recapitulate the human phenotype and disease mechanisms remain yet to be fully elucidated. This, combined with the relative inaccessibility of the human brain, necessitates a novel research approach.

1.8.2 Hypothesis

Development of a patient-derived, midbrain dopaminergic neuronal model will provide a new research tool for both unravelling disease mechanisms and testing novel therapies for AADC deficiency (**Figure 1-21**).

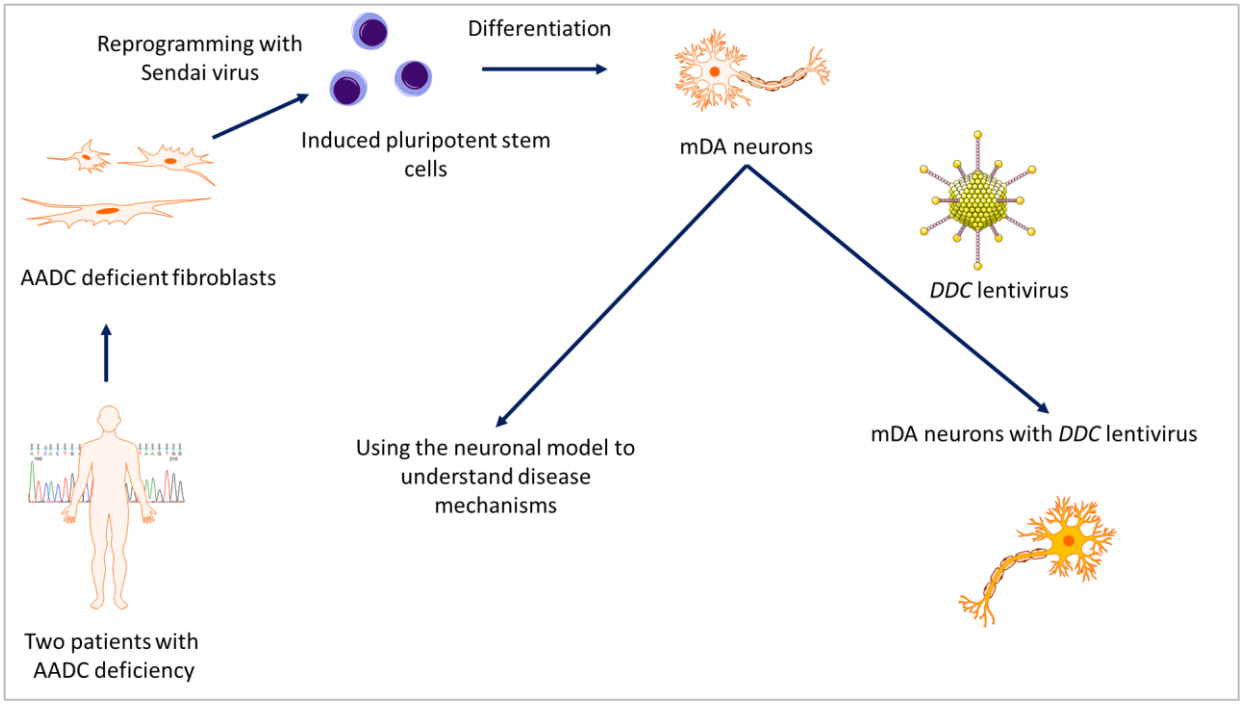

Figure 1-21: Work plan for my PhD project.

1.8.3 Aims

1. To reprogram fibroblasts from patients with AADC deficiency into induced pluripotent stem cells (iPSC)
2. To generate a midbrain dopaminergic (mDA) cell model of AADC deficiency from patient iPSCs
3. To determine whether patient-derived mDA neurons recapitulate key features of AADC deficiency
4. To investigate the downstream effects of AADC deficiency on a mDA model of disease
5. To evaluate the utility of this model as a therapeutic platform by investigating the effect of lentiviral gene transfer on the cellular phenotype of AADC deficiency

Chapter 2
Material and Methods

2.1 Material

2.1.1 Technical Equipment and Buffers

Table 2-1: High-Performance Liquid Chromatography (HPLC) instrumentation for the AADC enzyme activity assay.

Equipment	Equipment name
Pump	PU-2080 Plus (JASCO)
Autosampler	AS-2057 (JASCO)
Degasser	DP-Series (Degasys)
Column Heater	Plus Column Thermostat (Jetstream)
Column	HiQSil C18 column (Kya technologies) Dimensions - 4.6 mM pore size by 250 mm length
Detector	Coulochem III (ESA)
Analytical cell	5010 (ESA)
Data capture	Azur software package

Table 2-2: HPLC instrumentation for the detection of dopamine and metabolites.

Equipment	Equipment name
Pump	PU-1580 intelligent HPLC (JASCO)
Autosampler	AS-1555 intelligent cooled (JASCO)
Degasser	DG-980-50 3-line (JASCO)
Column Heater	Co-1560 intelligent column thermostat (JASCO)
Column	C:18HS column 250 mm × 4.5 mm (Kromatek)
Detector	Coulochem II electrochemical detector (ESA)
Analytical cell	5010A analytical cell (Thermo Fisher Scientific)
Data capture	Computer with EZChrom Elite chromatography system v 3.1.7 (JASCO)

Buffers provided with specific kits were used as described by the manufacturer. All other solutions were prepared as described in the following paragraphs.

2.1.1.1 0.1% Gelatin

0.5 g of gelatin (Sigma-Aldrich) were added to 500 ml 18.2 Ω HPLC grade water. The solution was autoclaved in a glass bottle for further use.

2.1.1.2 Blocking Solution and Antibody Dilution Buffer for Immunocytochemistry

Detection of surface-epitopes in iPSCs (TRA-1-60, TRA-1-81) was performed in 1x PBS (Invitrogen) and 10% Fetal Calf Serum (FCS) (Sigma-Aldrich). Detection of intracellular epitopes, in iPSCs, spontaneous *in vitro* differentiation of iPSCs, and day 11 mDA progenitors, was performed in 1x PBS, 10% FCS, and 0.1% Triton from Triton x-100 (Sigma-Aldrich) for the antibodies OCT4, NANOG, SOX17, SMA, TUJ1, LMX1A and FOXA2. Detection of intracellular epitopes in day 65 mDA neurons was performed in 1x PBS, 10% FCS, and 0.3% Triton for the antibodies MAP2, TH, AADC, TPH2, GIRK2, NeuN, and PanNav.

2.1.1.3 Buffers for Immunoblotting

TBS-T (Tris Buffered Saline-Tween) Solution

The solution was made of 500 ml 18.2 Ω HPLC grade water, one Tris Buffered Saline tablet (Sigma-Aldrich), and 0.5 ml TWEEN® 20 (Sigma-Aldrich).

TGS 1x Running Buffer

The buffer consisted of 900 ml 18.2 Ω HPLC grade water and 100 ml TGS (Tris/Glycine/SDS) Buffer 10x (Bio-Rad).

Blocking Solution

The solution was prepared by adding 5% or 1% Skim Milk Powder (Sigma-Aldrich) to TBS-T buffer.

2.1.1.4 Buffers for AADC Enzyme Assay

Homogenation Buffer

The buffer was prepared with 10 mM Tris base (pH 7.4) (Sigma-Aldrich), 1 mM EDTA (Ethylenediaminetetraacetic acid dipotassium salt dihydrate) (Sigma-Aldrich), 320 mM sucrose (Sigma-Aldrich). Protease Inhibitor Cocktail (1:10; Roche) was added before use.

Sodium Phosphate Buffer

The buffer was prepared with: A) 500 mM Disodium hydrogen phosphate (VWR Chemicals), 0.167 mM EDTA (Sigma-Aldrich); B) 500 mM Sodium dihydrogen orthophosphate (VWR Chemicals), 0.167 mM EDTA. For both solutions A and B, pH was adjusted to the value 7.00.

Assay Buffer for L-dopa Decarboxylation

The buffer was prepared with 39 mM 1,4-Dithioerythritol (Sigma-Aldrich) dissolved in 500 mM Sodium phosphate buffer.

2.1.1.5 Medium for iPSC Generation and Cultivation

MEF Medium

The MEF (mouse embryonic fibroblasts) medium was made with 445 ml DMEM (Gibco®), 50 ml FCS (10%), and 5 ml Penicillin-Streptomycin (1%; Invitrogen).

KOSR Complete Medium for iPSCs

Medium composition: 390 ml Knockout- DMEM (Invitrogen), 100 ml Knockout-Serum Replacement (20%; Invitrogen), 5 ml L-glutamine (2 mM; Invitrogen), 500 µl 2-Mercaptoethanol (50 mM; Invitrogen), and 5 ml Non-Essential Amino Acids 100x (1%, Invitrogen). Human Fibroblast Growth Factor (Human FGF-2) was added fresh on the day of use (10 ng/ml; Miltenyi Biotec).

mTeSR Complete Medium for iPSCs

mTeSR complete medium was prepared following manufacturer's instructions: 5x mTeSR supplements were added to 450 ml of mTeSR medium (STEMCELL™ Technologies). Medium was supplemented with 1% Penicillin-Streptomycin.

Coating with Matrigel for iPSCs in Culture

In 25 ml KOSR medium 10 mg/ml of Matrigel (Corning) was resuspended. 1 ml was plated in a 6-well plate and incubated for 1 h at 37°C.

2.1.1.6 Medium for spontaneous Differentiation *in vitro*

DMEM with 20% FBS

The medium was prepared with 395 ml of DMEM, with 20% FCS, and 1% Penicillin-Streptomycin.

KOSR Complete Medium

See **Section 2.1.1.5**.

2.1.1.7 Medium for Differentiation

EB medium (Embryoid Body Medium)

DMEM⁄F-12 (Invitrogen) and Neurobasal medium (Invitrogen) were used 1:1, with the addition of the following components: N2 Supplement (1:100; Invitrogen), B-27® Supplement 50x (1:50; Invitrogen), L-glutamine (2 mM), Penicillin-Streptomycin (1:100), Thiazovivin (only first day) (0.5 µM; Cambridge Bioscience), SB431542 (10 µM; Cambridge Bioscience), LDN193189 (100 nM; Sigma-Aldrich), CHIR99021 (0.8 µM; Tocris Bioscience), Recombinant modified human Sonic Hedgehog C24II (SHH) (200 ng/ml; R&D Systems), and Purmorphamine (from day 2) (0.5 µM; Cambridge Bioscience).

ND Medium (Neuronal Induction Medium)

DMEM⁄F-12 and Neurobasal medium were used 1:1. With the addition of the following components: N2 Supplement (1:200), B-27® Supplement 50X (1:100), L-glutamine (2 mM), Penicillin-Streptomycin (1:100), SB431542 (until day 6) (10 µM), LDN193189 (until day 9) (100 nM), CHIR99021 (until day 9) (0.8 µM), SHH (until day 9) (200 ng/ml), and Purmorphamine (until day 9) (0.5 µM).

FD medium (Final Differentiation Medium)

Neurobasal medium was used with the addition of the following components: B-27® Supplement 50X (1:50), L-glutamine (2 mM), Penicillin-Streptomycin (1:100), L-Ascorbic acid (0.2 mM; Sigma-Aldrich), and Human BDNF (Brain-derived neurotrophic factor) (20 ng/ml; Miltenyi Biotec).

FDf medium

Neurobasal medium was used with the addition of the following components: B-27® Supplement 50X (1:50), L-glutamine (2 mM), Penicillin-Streptomycin (1:100), L-Ascorbic acid (0.2 mM), Human BDNF (20 ng/ml), Human GDNF (Glial cell line-derived neurotrophic factor) (20 ng/ml; Miltenyi Biotec), db-cAMP (N6,2′-O-Dibutyryladenosine 3′,5′-cyclic monophosphate sodium salt) (0.5 mM; Sigma-

Aldrich), and DAPT ((2S)-N-[(3,5-Difluorophenyl)acetyl]-L-alanyl-2-phenyl]glycine 1,1-dimethylethyl ester) (from day 30) (2.5 µM; Tocris Bioscience).

2.1.1.8 Medium for Plasmid Cultivation

LB Medium

12.5 g LB Broth Base powder (Thermo Fisher Scientific) was dissolved in 500 ml of 18.2 Ω HPLC grade water and autoclaved. Kanamycin (Gibco™) was then added to a final concentration of 50 µg/ml.

Agar Plate Preparation

1 l of 18.2 Ω HPLC grade water and 35.6 g LB Broth with agar powder (Sigma-Aldrich) were autoclaved and 50 µg/ml Kanamycin was added. The liquid medium was added to petri dishes (VWR). The plates were left to solidify and were stored in the fridge for further use.

2.1.2 Antibodies

Table 2-3: Primary antibodies for immunofluorescence.

Primary antibody	Company	Dilution
TRA-1-60 (pluripotency) Mouse monoclonal antibody	Santa Cruz	1:200
TRA-1-81 (pluripotency) Mouse monoclonal antibody	Millipore	1:200
OCT4 (pluripotency) Mouse monoclonal antibody	Santa Cruz	1:50
NANOG (pluripotency) Mouse monoclonal antibody	Millipore	1:500
Tyrosine Hydroxylase (TH) Chicken polyclonal antibody	Aves	1:400
Microtubule-Associated Protein 2 (MAP2) Mouse monoclonal antibody	Sigma-Aldrich	1:400
Homeobox Transcription Factor 1 Alpha (LMX1A) Mouse monoclonal antibody	Millipore	1:2000
Forkhead Box Protein A2 (FOXA2) Rabbit polyclonal antibody	BD Pharmigen™	1:500
Dopa Decarboxylase (DDC) Rabbit polyclonal antibody	Millipore	1:500
Alpha Smooth Muscle Actin (SMA) Rabbit monoclonal antibody	Abcam	1:100
Neuronal Class III β-Tubulin (TUJ1) Mouse monoclonal antibody	BioLegend	1:400
SOX17 (member of the SOX family of transcription factors) Goat polyclonal antibody	R&D Systems	1:20
Neuronal Nuclei (NeuN) Mouse monoclonal antibody	Millipore	1:100
Tryptophan Hydroxylase 2 (TPH2) Rabbit polyclonal antibody	Novusbio	1:100

G-protein Regulated Inward-Rectifier Potassium 2 Channel (GIRK2) ($K_{ir}3.2$) Rabbit polyclonal antibody	Alomone Labs	1:400
Voltage-gated Sodium Channel Nav1.1 (PanNav) Mouse monoclonal antibody	Sigma-Aldrich	1:50

Table 2-4: Secondary antibodies for immunofluorescence.

Secondary antibody	Company	Dilution
Alexa Fluor® 594 Goat Anti-Mouse IgG (H L) Antibody	Invitrogen	1:400
Alexa Fluor® 488 Goat Anti-Mouse IgG (H L) Antibody	Invitrogen	1:400
Alexa Fluor® 488 Goat Anti-Rabbit IgG (H L) Antibody	Invitrogen	1:400
Alexa Fluor® 594 Goat Anti-Chicken IgG (H L) Antibody	Invitrogen	1:400
Alexa Fluor® 488 Donkey Anti-Goat IgG (H L) Antibody	Invitrogen	1:400
Alexa Fluor® 647 Goat Anti-Mouse IgG (H L) Antibody	Invitrogen	1:400

Table 2-5: Nuclei staining with DAPI.

Name	Company	Dilution
DAPI Solution (1 mg/ml) for nuclear counterstain	Thermo Fisher Scientific	1:1000

Table 2-6: Primary antibodies for immunoblotting.

Primary antibody	Company	Dilution
L-DOPA decarboxylase (DDC) Rabbit monoclonal antibody	Cell Signaling	1:1000
Tyrosine Hydroxylase (TH) Rabbit polyclonal antibody	TH Millipore	1:3000
Monoamine Oxidase A (MAOA) Rabbit monoclonal antibody	Abcam	1:5000
Glyceraldehyde-3-phosphate dehydrogenase (GAPDH) HRP conjugated	Cell Signaling Technology	1:1000

Table 2-7: Secondary antibodies for immunoblotting.

Secondary antibody	Company	Dilution
Anti-rabbit HRP-linked	Cell Signaling Technology	1:3000

2.1.2.1 Cell Lines

Table 2-8: Cell lines used in the project.

Cell line	Source
Human dermal fibroblasts AADC Patient 1 AADC Patient 2	Patients kindly provided skin fibroblasts for this study.
Human iPSC lines Control-03 Control-05	Aged-matched controls from a healthy donor. Fibroblasts from the ICH Dubowitz Biobank. Previously reprogrammed into iPSCs in the Kurian laboratory.
Mouse embryonic fibroblasts	CF-1 Mouse Embryonic Fibroblasts (MEF) feeder cells, irradiated, Ultra Low Density 0.5E6 (Life Technologies)
HEK 293T cells	Dr John Counsell (UCL GOS-ICH)
One Shot™ TOP10 Chemically Competent *E. coli*	Thermo Fisher Scientific

2.1.3 Kits

Table 2-9: Kits used in this project.

Kit	Company
CytoTune®-iPS Sendai 2.0 Reprogramming Kit	Invitrogen
MycoAlert mycoplasm detection Kit	Lonza
RNeasy Mini Kit	Qiagen
DNeasy Blood & Tissue Kit	Qiagen
SuperScript™ III Reverse Transcriptase Kit	Thermo Fisher Scientific
DNase I Kit	Invitrogen
Miniprep Kit (250)	Qiagen

QIAquick Gel Extraction Kit	Qiagen
PureLink™ HiPure Plasmid Filter Maxiprep Kit	Thermo Fisher Scientific
PureLink™ HiPure Precipitator Module	Thermo Fisher Scientific

2.1.4 Plasmids and Viruses

Table 2-10: Plasmids.

Plasmid name	Source
Lentiviral packaging plasmid pCMVR8.74	Addgene
Envelope expressing plasmid pMD2.G	Addgene
DDC plasmid (pCCL-hSYN-DDC-IRES-EGFP)	Generated by me
Mock plasmid (pCCL-hSYN-EGFPv2 JN 240517)	Kindly provided by Dr. Joanne Ng, UCL, Institute of Women's Health
DAT plasmid (pCCL-hSYN-DAT-IRES-EGFP)	Kindly provided by the Prof. Kurian research group, UCL GOS-ICH
Standard plasmid for LV titration (pMKRQ BTW2R)	Kindly gifted by Dr. Conrad Vink, UCL

Table 2-11: Viruses.

Virus name	Source
CytoTune™-iPS 2.0 Sendai Virus	Invitrogen
DDC lentivirus	Generated by myself
Mock lentivirus	Generated by myself

2.1.5 Primers

Table 2-12: *DDC* primers for Sanger sequencing.

Exon/primer name	Sequence (5'-3')	PCR product size (bp)	Annealing temperature (˚C)
***DDC*_5'UTR_F**	CAGAATGTGCTCTCAGGATTCC	840	TD58
***DDC*_5'UTR_R**	CATGGCAAGTTGGTGGGAAA		
***DDC*_X1_F**	TTACTTGGGATCCAAGTGGCC	598	TD55
***DDC*_X1_R**	TCAGTTGTAAAATAGAAATGAC		
***DDC*_X2_F**	TGACATTTGGGGAACTGCAC	697	TD59
***DDC*_X2_R**	GGACACATCTGATAGGCTGGT		
***DDC*_X3_F**	CCCTTCTGTGAGTGAACAAA	760	TD55
***DDC*_X3_R**	TGCCTGGAAAATGCTTAGG		
***DDC*_X4_F**	CTGAAGTGGTGGTCTCAGGT	492	TD59
***DDC*_X4_R**	TCCAGTTCCCACCCAAGAAT		
***DDC*_X5_F**	CAATGTTGGCTGCTCTCTG	321	TD62
***DDC*_X5_R**	ACCATGCCCGGCTAATTT		
***DDC*_X6_F**	TCCATGGGCTTACGTTTCCA	393	TD64
***DDC*_X6_R**	TCTGAGTTTGTGGAGTTCAAGC		
***DDC*_X7_F**	GCTTTAGACCCTTTGAATGAGG	903	TD64
***DDC*_X7_R**	GTCTGAAATAACACACCACAGT		
***DDC*_X8_F**	CACTCCAGAAGACTCCCCTAC	449	TD61
***DDC*_X8_R**	GCCAGTATGTTGCAATGATATTCC		
***DDC*_X9_F**	TCACTAGGAGATCTCAAGGGTTTT	700	TD59
***DDC*_X9_R**	TGGAAGGTGATGCAAAGCCT		
***DDC*_X10_F**	TTTGTGTTTTGGGCATCCTGTT	357	TD60
***DDC*_X10_R**	CCCAGTTAGAAGGTGCCCAC		
***DDC*_X11_F**	CCCAGTTAGAAGGTGCCCAC	626	TD64
***DDC*_X11_R**	ACCCAAACTACAGTCTGGTTCTC		
***DDC*_X12_F**	ATGAGTTTCTTAGCCTGCCT	396	TD56
***DDC*_X12_R**	CTTTGCTCTGCCATCTCTG		
***DDC*_X13_F**	GATGCATGCAGTCTTTTAGG	647	TD55
***DDC*_X13_R**	CAGGATGGTCTCAATCTCTT		
***DDC*_3'UTR_F**	AGATGGCAGCAGTACAGTCC	821	TD61
***DDC*_3'UTR_R**	TTCCACAGAAGTTGAAGTCATCT		

Table 2-13: Sendai Virus clearance primers.

Primer name	Sequence (5'-3')	PCR product size (bp)
SeV F	GGATCACTAGGTGATATCGAGC	181
SeV R	ACCAGACAAGAGTTTAAGAGATATGTATC	
SeV *SOX2* F	ATGCACCGCTACGACGTGAGCGC	451
SeV *SOX2* R	AATGTATCGAAGGTGCTCAA	
SeV *KLF4* F	TTCCTGCATGCCAGAGGAGCCC	410
SeV *KLF4* R	AATGTATCGAAGGTGCTCAA	
SeV *c-MYC* F	TAACTGACTAGCAGGCTTGTCG	532
SeV *c-MYC* R	TCCACATACAGTCCTGGATGATGATG	
SeV *OCT4* F	CCCGAAAGAGAAAGCGAACCAG	483
SeV *OCT4* R	AATGTATCGAAGGTGCTCAA	
***GAPDH* F**	ATCCCATCACCATCTTCCAG	382
***GAPDH* R**	CCATCACGCCACAGTTTCC	

Table 2-14: Pluripotency primers.

Primer name	Sequence (5'-3')	PCR product size (bp)
***OCT4* F**	CGAAACCCACACTGCAGCAG	402
***OCT4* R**	CCTGGCACAAACTCCAGGTTT	
***SOX2* F**	GGGAAATGGGAGGGGTGCAAAAGAGG	151
***SOX2* R**	TTGCGTGAGTGTGGATGGGATTGGTG	
***NANOG* F**	CAGCCCCGATTCTTCCAGTCCC	343
***NANOG* R**	CGGAAGATTCCCAGTCGGGTTCACC	
***c-MYC* F**	GCGTCCTGGGAAGGGAGATCCGGAGC	328
***c-MYC* R**	TTGAGGGGCATCGTCGCGGGAGGCTG	
***ESG1* F**	ATATCCCGCCGTGGGTGAAAGTTC	243
***ESG1* R**	ACTCAGCCATGGACTGGAGCATCC	

Table 2-15: qRT-PCR primers.

Primer name	Sequence (5'-3')
***GAPDH* F**	TTGAGGTCAATGAAGGGGTC
***GAPDH* R**	GAAGGTGAAGGTCGGAGTCA
***FOXA2* F**	CCGTTCTCCATCAACAACCT
***FOXA2* R**	GGGGTAGTGCATCACCTGTT
***EN1* F**	CGTGGCTTACTCCCCATTTA
***EN1* R**	TCTCGCTGTCTCTCCCTCTC
***EN2* F**	CCTCCTGCTCCTCCTTTCTT
***EN2* R**	GACGCAGACGATGTATGCAC
***LMX1A* F**	CGCATCGTTTCTTCTCCTCT
***LMX1A* R**	CAGACAGACTTGGGGCTCAC
***LMX1B* F**	CTTAACCAGCCTCAGCGACT
***LMX1B* R**	TCAGGAGGCGAAGTAGGAAC
***OCT4* F**	TCTCCAGGTTGCCTCTCACT
***OCT4* R**	GTGGAGGAAGCTGACAACAA
***NANOG* F**	TTGGGACTGGTGGAAGAATC
***NANOG* R**	GATTTGTGGGCCTGAAGAAA
***TH* F**	CGGGCTTCTCGGACCAGGTGTA
***TH* R**	CTCCTCGGCGGTGTACTCCACA
***AADC* F**	TGCGAGCAGAGAGGGAGTAG
***AADC* R**	TGAGTTCCATGAAGGCAGGATC
***MAOA* F**	CTGATCGACTTGCTAAGCTAC
***MAOA* R**	ATGCACTGGATGTAAAGCTTC

Table 2-16: Primers for plasmid confirmation.

Primer name	Sequence (5'-3')
Plasmid_1F	GGACGCGTCAATTGACTACAA
Plasmid_1R	GCCACCAGCTTCTCCATGAT
Plasmid_2F	ACTGTGATGATGGACTGGCT
Plasmid_2R	CCACATGGCAGAACAGTCAA
Plasmid_3F	ACCACAACATGCTGCTCCTT
Plasmid_3R	GCCTTATTCCAAGCGGCTTC
Plasmid_4F	TTCTCGCACGGTGGAATCTG
Plasmid_4R	CTTGCTCACCATGGTTGTGG
Plasmid_5F	CAGTGCCACGTTGTGAGTTG
Plasmid_5R	CTTGTAGTTGCCGTCGTCCT
Plasmid_1F	GGACGCGTCAATTGACTACAA
Plasmid_1R	GCCACCAGCTTCTCCATGAT
Plasmid_2F	ACTGTGATGATGGACTGGCT
Plasmid_2R	CCACATGGCAGAACAGTCAA

Table 2-17: Primers for the lentiviral vector titration by qRT-PCR.

Primer name	Sequence (5'-3')
Late-RT probe	CAGTGGCGCCCGAACAGGGA
Late-RT F	TGTGTGCCCGTCTGTTGTGT
Late-RT R	GAGTCCTGCGTCGAGAGC
Beta-actin probe	TAATGTCACGCACGATTT
Beta-actin F	GCCATCTCTTGCTCGAAGT
Beta-actin R	GACTGACTACCTCATGAAGATCC

2.1.6 Computer Software

Table 2-18: Computer software.

Software	Source
ImageJ	www.imagej.net
GraphPad Prism V. 6.01	www.graphpad.com
Image Lab™	Bio-Rad
Bluefuse Multi	Illumina

2.2 Methods

2.2.1 Ascertainment of Patient and Control Fibroblasts

For this study I used two fibroblast lines collected from two patients harbouring mutations in the *DDC* gene (Patient 1 and Patient 02). A clinical and genetic summary is provided in **Table 2-19**. Written informed consent was obtained from all patients (REC reference 13/LO/0171).

Table 2-19: Clinical and genetic data of the two AADC patients.

Patient number	Patient line	Clinical phenotype	Location of mutation	Type of mutation	Predicted amino acid change
1	Patient 1	Hypotonia Neurodevelopmental delay Oculogyric crises Complex movement disorder with autonomic features	Exon 11		p.R347G
2	Patient 2	Hypotonia Neurodevelopmental delay Oculogyric crises Complex movement disorder with autonomic features	Exon 2 Exon 3	Non-sense mutation Missense Mutation (compound heterozygous)	Premature stop codon p.Arg7* p.C100S

An age-matched control fibroblast sample from a healthy donor was collected from ICH Dubowitz Biobank. Control lines are essential in order to identify any disease-relative phenotype observed in patient-derived cells.

2.2.2 Isolation of Skin Fibroblasts

Maintenance of skin biopsies, isolation of dermal fibroblasts and further cultivation was performed by the Enzyme Unit, Chemical Pathology, Botnar's Laboratories, Great Ormond Street Hospital, London.

Isolation of fibroblasts from skin biopsy was performed as following: skin biopsies were placed in a 5 cm petri dish, kept moist with a few drops of medium made of Hams F10 with 12% FCS, and reduced to small fragments. Tissue fragments were then transferred to a 25 cm^2 culture flasks, with the use of a scalpel blade, and further incubated in 5 ml of medium in 5% CO_2 at 37°C for 7 days. Fibroblast arising from skin fragments were normally collected after 3 to 5 weeks.

2.2.3 Reprogramming human dermal Fibroblasts using CytoTune™

The described protocol was adapted from the CytoTune™-iPS 2.0 Sendai Reprogramming Kit (Invitrogen) with the reprogramming vectors hOCT4, hSOX2, hKLF4, and hc-MYC. Human dermal fibroblasts (HDF) were collected from patients and controls (as described above) and frozen at -80°C. After thawing out, HDF were seeded in T25 flasks, and expanded for 5 days with every other day medium change. HDF were then harvested and plated for further reprogramming as described below. HDF cells were rinsed with 1x PBS and incubated for 5 min with 2 ml TrypLE™ (Invitrogen) at 37°C. TrypLE™ enzymatic reaction was stopped by adding 4 ml of MEF medium. Cells were then counted and seeded out to a 12-well plate with densities of 0.75 x 10^5, 1 x 10^5, 1.25 x 10^5, 1.5 x 10^5 and 2.0 x 10^5 cells per well. At the day of infection, cells with 90% confluence were infected with the Sendai Virus containing the 4 transcription factors (hOCT4, hSOX2, hKLF4, hc-MYC) from the CytoTune™-iPS 2.0 Sendai Reprogramming Kit following the ration of 1.0 x 10^5 cells at MOI of 3. Cells were then incubated overnight, Sendai Virus was withdrawn after 24 hours, and medium was changed every other day. After 6 days, infected HDF cells were transferred to previously seeded MEF cells (5x $10^4/cm^2$) on 0,1% gelatin in MEF medium: HDF cells were rinsed two times with 2 ml 1x PBS, incubated with TrypLE™ for 5 min at 37°C counted and seeded out on the MEF cell plates in a density of 8.000 cells/ml. Cells were distributed in order to have 2x 6well plates with 8.000

cells per well, and 1x 6well plate with 16.000 cells per well. After one day of cultivation, reprogramming fibroblast were switched to a KOSR-MEF conditioning media +10 ng/ml Human FGF-2, in order to support the emerging iPSCs. KOSR-MEF conditioned medium was prepared as follow: MEF cells were thawed and plated in three T75 flask with a density of 6.6 x 10^5 cells/flask in MEF medium; media was then replaced by KOSR medium, 15 ml for each T75 flask, and daily collected. At day 7 media for the reprogramming cells was changed to KOSR with Human FGF-2 (10 ng/ml). From day 17, daily media change was performed.

After 30-40 days from the day of infection, 10 iPSC clones were picked for each patient, and further maintained on MEF cells with daily media change (KOSR complete medium). iPSCs passaging was performed when colonies where at appropriated confluency with a non-enzymatic solution in order to select only pluripotent colonies (ReLeSR™; Stem Cell Technologies). When clones were stable, they were transferred into feeder free conditions using Matrigel and mTeSR™ 1 complete medium (**Section 2.1.1.5**) with daily media change. The best three lines were expanded to 18 wells and frozen down at passage 25. Pellets were collected, and cells were fixed with 4% paraformaldehyde (Alfa Aesar) for further analysis.

2.2.4 Characterisation of AADC iPSCs Lines

2.2.4.1 Genomic DNA Extraction

The genomic DNA (gDNA) was extracted using DNeasy Blood & Tissue Kit (Qiagen), according to the manufacturer's instructions. Briefly, cell pellet was re-suspended in 200 µl 1x PBS supplemented with 1:10 proteinase K. 200 µl of buffer AL for lysation was added to the cells in suspension and mixed thoroughly by vortexing. The sample was then incubated at 56°C for 10 min. In order to perform DNA precipitation, 200 µl of 100% ethanol was added to the sample and mixed thoroughly by vortexing. The mix was then pipetted into the DNeasy Mini spin column supplemented with collection tube and centrifuged at 8000 rpm for 1 min, the flow through and collection tube were discarded. Column was first washed with 500 µl of AW1 buffer (stringent washing buffer containing low concentrations of quinidine), centrifuged for 1 min at 8000 rpm, and tube and flow through were discarded. Sequently, the column was washed with 500 µl of AW2 buffer (tris-based ethanol

solution to remove salts) and centrifuged for 3 min at 14000 rpm. Tube and flow through were discarded. DNA elution was performed in 100 µl of buffer after 1 min incubation at room temperature (RT) and centrifuged for 1 min at 8000 rpm.

The purity and concentration of the extracted DNA was measured with the UV-Vis spectrophotometer NanoDrop™ 1000 from Thermo Fisher Scientific. The A_{260}/A_{280} ratio of around 1.8 is defined as pure DNA.

2.2.4.2 Direct Sanger Sequencing of *DDC* Mutation in patient derived iPSCs

Sanger sequencing and primer design was kindly performed by Dr Katy Barwick (Genetics Research Associate from Kurian group, UCL GOS-ICH).

Direct Sanger sequencing was performed to confirm patient mutation of *DDC* locus for all iPSC lines. The gDNA sequences were obtained from the Alamut® Visual 2.11 software. Genome Reference Consortium Human Build 37 (GRCh37), chromosome 7: 50,458,436-50,565,457; NM_000790.3). The primers (**Section 2.1.5**) were designed with Primer3Plus software (http://www.bioinformatics.nl/cgi-bin/primer3plus/primer3plus.cgi). For each set of primer pairs, reaction solution was prepared as shown in **Table 2-20**.

Table 2-20: PCR constituents and their volumes.

Component	Volume (µl)
ddH_2O	4
BioMix™ Red 2x reaction mix (Bioline)	10
Forward Primer (5 ρM/µl; Sigma-Aldrich)	2
Reverse Primer (5 ρM/µl; Sigma-Aldrich)	2
DNA	2
Total Volume	20

The polymerase chain reaction (PCR) is used to exponentially amplify specific DNA sequences of interest. With a PCR, DNA fragments can be amplified *in vitro* by up to 10^9 times.

A touch-down PCR protocol was used (**Table 2-21**) to improve the specificity of the primer binding. Initially starting from a temperature that is 4°C greater than that of the annealing temperature (Tm) The temperature was then lowered by 2°C every two cycles until the desired Tm is reached. The elongation time was set according to the PCR product size.

Table 2-21: Touchdown PCR thermal cycling program.

Number of cycles	Temperature (°C)	Time (s)
1	95 (denaturation)	240
2	95 (denaturation) Tm + 4°C 72 (elongation)	30 30 30 (per Kb)
2	95 (denaturation) Tm + 2°C 72 (elongation)	30 30 30 (per Kb)
35	95 (denaturation) Tm 72 (elongation)	30 30 30 (per Kb)
1	72 (elongation)	300

Purity of the amplified PCR product was checked with a 1,5% agarose gel before proceeding with the sequencing. Amplified DNA was then purified with MicroCLEAN Kit (Clent Life Science) and further processed with the BigDye® Terminator v1.1 Cycle Sequencing Kit (Thermo Fisher Scientific). Sequencing was performed with the ABI PRISM 3730 DNA Analyzer (Applied Biosystems). The results were then analysed using Sequencher (https://www.genecodes.com) and Chromas software (http://technelysium.com.au/wp/chromas).

2.2.4.3 Karyotyping with Single-Nucleotide Polymorphism Array (SNP)

gDNA from iPSC lines was prepared in a concentration of 75 ng/µl in a total volume of 10 µl. The cytoSNP array was performed by UCL genomics and the raw IDAT files were analysed with the software Bluefuse Multi from Illumina.

2.2.4.4 Extraction of total RNA

Total RNA was extracted using RNeasy Mini Kit (Qiagen) and according to the manufacturer's instructions. In brief, collected cells were lysed in RLT buffer (containing guanidinium isothiocyanate to break the cell walls and denature RNases) and 500 µM β-mercaptoethanol (which allows breaking down of disulfide bonds from RNases and prevents degradation of the RNA). Samples were homogenated by vortexing for 1 min. Addition of the equivalent volume of 70% ethanol precipitated the RNA. After binding to a silica membrane through centrifugation (15 s, 8000 rpm), the RNA was washed with 700 µl RW1 buffer containing guanidine salt and ethanol which removes carbohydrates, proteins and fatty acids, and centrifuged for 15 s, 8000 rpm. Column was then washed with 500 µl of buffer RPE containing ethanol, which removes traces of salt. The sample was then centrifuged for 15 s, 8000 rpm. A second washing step with RPE was performed and column was centrifuged for 2 min, 8000 rpm. The RNA was then eluted with RNA free water with centrifugation for 1 min, 8000 rpm.

The purity and concentration of the extracted RNA was measured with the UV-Vis spectrophotometer NanoDrop™ 1000. The A_{260}/A_{280} ratio of around 2.0 is defined as pure RNA. The product was then stored at -80°C for further use.

2.2.4.5 RNA Purification

RNA was purified with DNase I Kit (Invitrogen). DNase I digests single- and double-stranded DNA to oligodeoxyribonuleotides. In brief 1 µg of RNA sample was mixed with 1 µl 10x DNase I Reaction Buffer, 1 µl DNase I and Nuclease-Free Water (Thermo Fisher Scientific) to 10 µl. The mix was incubated for 15 min at RT. To inactivate the DNAse I 1 µl of EDTA solution was added and incubated for 10 min at 65°C.

2.2.4.6 Reverse Transcription

cDNA was generated with Superscript III Reverse Transcriptase (Invitrogen). In brief, 10 µl of RNA sample were added with 1 µl of oligo (dT) primers (Thermo Fisher Scientific), 1 µl of dNTP Mix (Thermo Fisher Scientific), 1 µl of Nuclease-Free Water. The mix was loaded into a PCR plate and run for 5 min at 65°C in the PCR machine. The plate was then incubated on ice for 1 min. Samples were then added with: 4 µl 5x first-strand buffer, 1 µl 0.1 M (DTT), 1 µl Nuclease-Free Water, and 1 µl SuperScript™ III RT. Samples were processed for 60 min at 50°C and 15 min at 70°C. Generated cDNA was then diluted 1:25 with Nuclease-Free Water. The product was then stored at -20°C for further use.

2.2.4.7 Sendai Virus Clearance

In order to confirm the generation of viral free iPSCs, SeV clearance analysis was performed, following instructions provided by the CytoTune™-iPS 2.0 Sendai Reprogramming Kit. The SeV genome and pluripotent genes were detected in reprogrammed iPSCs using a specific set of primers (**Section 2.1.5**).

Total RNA was extracted from 1 x 10^6 iPSCs with the RNeasy Mini Kit, and purified with the DNase I Kit (**Sections 2.2.4.4** and **2.2.4.5**). For the generation of cDNA 1 µg of total RNA was used and the reverse transcription was performed with the Superscript III Reverse Transcriptase Kit (**Section 2.2.4.6**).

The PCR mix consisted of 10 µl cDNA and 10 µl AccuPrime™ SuperMix I (Thermo Fisher Scientific). PCR protocol: denaturation 95°C for 5 min; 35x (cycles denaturation 95°C for 30 s, annealing 55°C for 30 s, elongation 72°C for 30 s); 72°C for 5 min. Products were separated in 2% agarose gel (**Section 2.2.4.9**). As a positive control SeV genome was used, while the samples H9 embryonic stem cell and the human fibroblast line were used as negative controls.

2.2.4.8 PCR Detection of expressed pluripotent-related Genes

The PCR was performed with the following buffer: deoxynucleotides (dNTPs: dGTP, dCTP, dATP, dTTP), magnesium chloride ($MgCl_2$), and Taq DNA polymerase BioMix™ Red (Bioline). 2 µl of cDNA from each samples and primers specific to each gene of interest (**Section 2.1.5**) were added.

The master mix consisted of: 0.4 µl F primer (1:10 diluted in water), 0.4 µl R primer (1:10 diluted in water), 7.2 µl water, 10 µl BioMix™ Red, and 2 µl cDNA. BioMix™ Red contains a stable *Taq* DNA polymerase and a red dye. Each set of oligonucleotides required a specific PCR protocol. In particular, for *GAPDH*, *SOX2*, *cMYC*, *NANOG*, *ESG* the PCR conditions were: 1x 95°C for 5 min, 35x (denaturation 95°C for 30 s, annealing 60°C for 45 s, elongation: 72°C for 1 min) and 1x 72°C for 5 min. For *OCT4* PCR conditions were: 1x 95°C for 5 min, 35x (denaturation 95°C for 30 s, annealing 58°C for 45 s, elongation: 72°C for 1 min) 1x 72°C for 5 min. Amplified cDNA was separated with a 1.5% agarose gel (**Section 2.2.4.9**) in 1xTBE buffer (Merck) at 120 V for 50 min. PCR products were loaded alongside the GeneRuler 100 bp DNA Ladder (Thermo Fisher Scientific). Detection was performed with the Bio-RAD® Gel Doc Imager and the Image Lab™ software (Bio-Rad) (**Section 2.2.4.9**).

2.2.4.9 Agarose Gel Electrophoresis for PCR Products

Agarose gel electrophoresis is used to separate charged molecules (such as DNA) due to their size through a porous gel under an electric current. Separation trough electrophoresis was applied on PCR products to confirm the correct size.

Instructions on how to prepare an agarose gel is provided as follows with the example of a 1.5% agarose gel: 1.5 g of agarose powder (Bioline) was dissolved in 100 ml 1xTBE and the solution was heated in a microwave for about 3 min until clearance of the solution. 5 µl of SYBR™ Safe DNA Gel Stain (Thermo Fisher Scientific) was added and swirled until evenly distributed. SYBR™ Safe intercalates into the DNA and is fluorescent under ultraviolet (UV) light. The mix was casted into a gel mould that already had the 25-toothed combs inserted. The gel was left to solidify for 30 min.

2.2.4.10 General Immunocytochemistry

Immunocytochemistry was performed as described in the following paragraphs. The cells were washed three times with 1x PBS, incubated for 10 min with 4% paraformaldehyde and washed again in 1x PBS. Fixed cells were blocked for 30 min in blocking buffer (**Section 2.1.1.2**) and incubated with primary antibody overnight at 4°C (**Section 2.1.2**). Cells were then rinsed three times with 1x PBS and incubated with secondary antibody (**Section 2.1.2**) for 45 min at RT in the dark. After secondary antibody binding, samples were washed two times with 1x PBS and

incubated in the dark with DAPI (1 µg/ml) for 5 min. After washing with 1x PBS, samples were stored at 4°C until further analysis. For the day 65 mDA neurons that where seeded on LabTeck slides the LabTek case was removed after immunostaining and the coverslip was mounted with ProLong Gold Antifade Mountant (Invitrogen).

Images were acquired with the Olympus IX71 inverted TC scope for the cell samples of iPSCs, spontaneous *in vitro* differentiation of iPSCs, and day 11 mDA progenitors. Images for the day 65 mDA neurons were taken with the multiphoton confocal microscope (Zeiss LSM880). The quantification for the day 11 mDA progenitors and the day 65 mDA neurons was performed for three independent experiments. For each experiment three random fields were imaged and 1200 (progenitors) or 1800 (neurons) randomly selected nuclei were counted.

2.2.4.11 Immunocytochemistry for Pluripotency Markers TRA-1-60, TRA-1-81, NANOG and OCT4

Staining was performed for TRA-1-60, TRA-1-81, NANOG, and OCT4 as described in **Section 2.2.4.10**.

2.2.4.12 Spontaneous Differentiation *in vitro*

iPSCs were harvested with TrypLE™, centrifuged for 5 min at 300 rpm and resuspended in KOSR full medium (**Section 2.1.1.5**) without bFGF-2. Thiazovivin (0.5 µM) was added. To form embryoid bodies (EBs), 2 x 10^6 cells were plated on a 2 cm no-adherent bacterial dish. Medium was changed on day two. On day 4 the EBs were seeded into a 24-well plate for further differentiation. For mesodermal differentiation, EBs were seeded onto 0.1% gelatin coated plates (**Section 2.1.1.1**), in DMEM with 20% FBS (**Section 2.1.1.6**). Neuroectoderm and endoderm were derived after plating EBs on Matrigel coated plates (**Section 2.1.1.5**) with KOSR full medium (**Section 2.1.1.5**) without bFGF-2. Medium change was undertaken every second day. On day 16 cells were fixed and stained for further analysis (**Section 2.2.4.10**). Samples were stained for the detection of the endoderm related protein SOX17, the mesoderm smooth muscle protein SMA, and the neuronal microtubule protein TUJ1.

2.2.4.13 Epi-Pluri-Score

The Epi-Pluri-Score analysis was provided by the company Cygenia. gDNA was extracted (**Section 2.2.4.1**). The Epi-Pluri-Score compares pluripotent with non-pluripotent cells and is based on the combination of DNA methylation levels at the two CpG sites of *ANKRD46* and *C14orf115*. 5 µl of gDNA with the concentration of 200 ng/µl were sent to the company Cygenia (Lenz et al. 2015).

2.2.5 Differentiation of AADC iPSCs into dopaminergic midbrain Neurons

2.2.5.1 Differentiation Protocol

iPSCs were differentiated into midbrain dopaminergic neurons following a modified version of a previously published protocol (Kirkeby, Nelander, and Parmar 2012) (**Figure 2-1**).

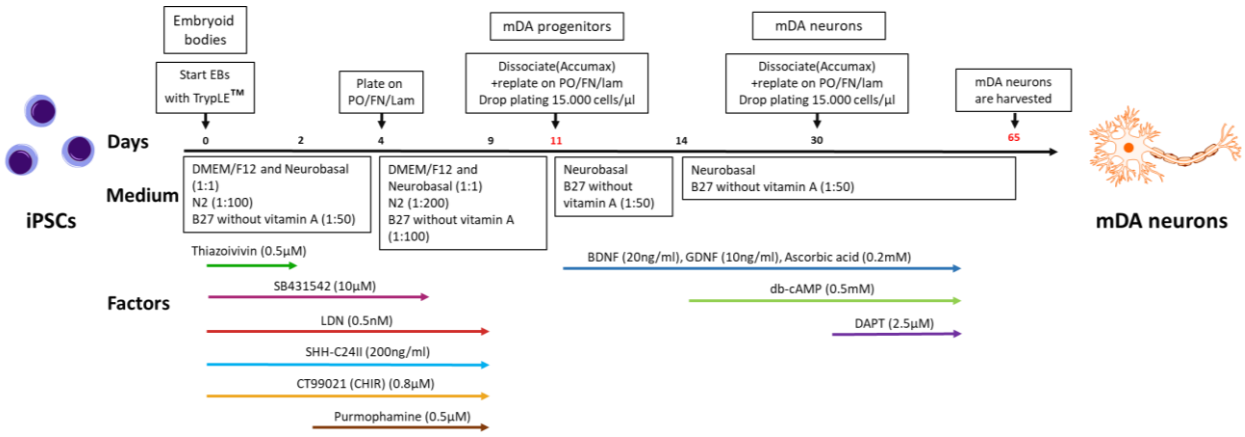

Figure 2-1: Differentiation protocol for dopaminergic midbrain neurons.

On day 0 of differentiation, iPSCs were harvested with TrypLE™ as previously described (**Section 2.2.4.12**), and resuspended onto non-adherent bacterial dishes, with a concentration of 5 x10^5/cm^2 in EB medium (**Section 2.1.1.7**). At day 2, the EB medium was changed: EBs were collected and spun down for 1 min at 300 rpm, the supernatant was aspirated, EBs resuspended in freshly prepared medium and re-seeded on the same non-adherent bacterial dish. On day 4, EBs were spun down for 1 min at 300 rpm, resuspended in freshly prepared Neural Induction (ND) medium (**Section 2.1.1.7**) and plated on a Poly-L-ornithine, Fn/Lam coated plate (three wells of a 12-well plate for a 6 cm dish and 6 wells of a 12-well plate for a 10 cm dish) (**Section 2.2.5.2**). Media was changed every other day. At day 6 SB431542 was withdrawn from the ND medium. On day 9 cells were switched to the ND medium without LDN193189, CHIR99021, SHH and Purmorphamine. On day 11 dopaminergic progenitors were harvested and re-plated via drop plating (**Section 2.2.5.3**) for final differentiation in FD medium (**Section 2.1.1.7**). At day 14 the medium was switched to the Final Differentiation medium *f* (FD*f*) (**Section 2.1.1.7**). Cells were then re-plated

after 30 days of differentiation onto dishes or Lab-Tek™ slides so the cells then further matured into dopaminergic neurons.

2.2.5.2 Coating with Poly-L-ornithine and Fibronectin/ Laminin

Coating was performed as followed. Poly-L-ornithine (PO) (Sigma-Aldrich) was diluted in 1x PBS to yield a final concentration of 15 µg/ml. The solution was then added to wells and incubated at 37ºC for 48-72 hours (i.e. 0.2 ml/cm^2= 350 µl in a 24-well plate and 700µl in a 12-well plate). After 48-72 hours, PO solution was aspirated, and wells were washed three times in 1x PBS. Fibronectin/ Laminin (FN/Lam) solution was prepared by diluting Fibronectin (Invitrogen) and Laminin (Sigma-Aldrich) in 1x PBS to a final concentration of 5 µg/ml. FN/Lam solution was added to coated PO wells and incubate at 37ºC for 48-72 hours.

2.2.5.3 Drop Plating for final Differentiation

FN/Lam coating was aspirated, and the plate left to dry open in a cell culture safety cabinet. Cells were washed once with 1x PBS and incubated with 500 µl of Accumax (Sigma-Aldrich) for 20 min at 37°C. The enzymatic reaction was stopped with KOSR complete medium (**Section 2.1.1.5**) and cells were spun down at 300 rpm for 5 min. The dopaminergic progenitors were plated with Final Differentiation medium (FD) (**Section 2.1.1.7**) via drop plating (5-10 µl of cell suspension) of 15.000 cells per µl. The cell drops were incubated for 1 h at 37°C and 1 ml of medium was added when the cells attached to the plate. (Plated were 25 µl/well for a Lab-Tek™ slide and 100 µl/well for a 12-well plate).

2.2.6 Characterisation of dopaminergic Neurons

2.2.6.1 Immunocytochemistry for the Expression of midbrain related Markers in dopaminergic Progenitors

Immunocytochemistry for midbrain progenitor specific transcription factors Forkhead Box Protein A2 (FOXA2) and Homeobox Transcription Factor 1 Alpha (LMX1A) was performed as described in **Section 2.2.4.10**.

2.2.6.2 Expression of midbrain-related Genes in dopaminergic Progenitors with Real-Time Quantitative Reverse Transcription Polymerase Chain Reaction (qRT-PCR)

RNA was extracted (**Section 2.2.4.4**) and purified (**Section 2.2.4.5**), and cDNA was generated (**Section 2.2.4.6**). The qRT-PCR primers for detection of midbrain-related genes (*FOXA2*, *EN1*, *EN2*, *LMX1A*, and *LMX1B*) and pluripotency-related genes (*NANOG* and *OCT4*) are listed in **Section 2.1.5**. cDNA was diluted 1:1 with Nuclease-Free Water. Master mix was prepared with 10 µl of MESA BLUE qPCR 2X MasterMix Plus for SYBR® Assay (Eurogentec) and 1 µl of primer mix (forward and reverse). 9 µl of diluted cDNA and 11 µl of master mix were added to each well and plates were centrifuged at 2000 rpm for 2 min. Targets were plotted in triplicates for each sample. Glyceraldehyde-3-phosphate dehydrogenase (*GAPDH*) was used as housekeeping gene in order to normalise cDNA sample levels. qRT-PCR was performed with the StepOnePlus™ Real-Time PCR System (Applied Biosystems) with the following protocol: denaturation at 95°C for 5 min, 40 x (denaturation at 95°C for 15 s and annealing/extension at 60°C for 1 min). Gene expression was analysed using the $\Delta\Delta C_T$ method:

$$\Delta C_T = M_T \text{ target} - M_T \text{ GADPH}$$

$$\Delta\Delta C_T = \Delta C_T \text{ sample} - \Delta C_T \text{ control}$$

$$\text{Fold change (FC)} = 2\text{^} - (\Delta\Delta C_T)$$

The control for normalisation was either an iPSC line or an age-matched control mDA neuronal line depending on the experiment.

2.2.6.3 Immunocytochemistry for mature dopaminergic Neurons

Day 65 mDA neurons were stained for the neuronal marker microtubule-associated protein 2 (MAP2), the dopaminergic marker tyrosine hydroxylase (TH), the dopaminergic marker and affected protein in AADC deficiency Aromatic Amino Acid Decarboxylase (AADC), the serotonergic marker Tryptophan Hydroxylase 2 (TPH2), the G Protein-Activated Inward Rectifier Potassium Channel 2 (GIRK2), the neuronal nuclei marker (NeuN) for mature neuronal cells, and the voltage-gated sodium channel Nav1.1 (PanNav) for electrochemical properties (**Section 2.2.4.10**).

2.2.6.4 Immunoblotting

Protein Lysation followed by Protein Determination with the Bicinchoninic Acid (BCA) assay

Cells were lysed and the total protein amount was measured of every sample. For the protein extraction, 200 µl RIPA buffer (Sigma-Aldrich) containing Protease Inhibitor Cocktail (1:10) was added. The pellet was resuspended, vortexed for 1 min, incubated on ice for 30 min and centrifuged at 13.000 rpm for 15 min. The supernatant was collected and used for the Pierce™ BCA Protein Assay Kit (Thermo Fisher Scientific). In a 96-well plate 10 µl of sample and 7 separated prediluted protein standards and the blank (H_2O) were incubated for 30 min at 37°C with 200 µl of reagent mix A + B (B is 1:50). The samples were measured with a multiplate reader at 555 nm.

Data analysis to determine the protein concentration **x** was undertaken with the linear equation:

$$y = m * x + t$$

$$x = \frac{y - t}{m}$$

Western Blotting

10 µg of protein was loaded per well of a 4-20% Mini-PROTEAN® TGX™ Stain free Protein Gel (Bio-Rad) together with 2.5 µl Laemmli Sample Buffer (Bio-Rad) and 2 µl of 0.1 M Dithiothreitol (DTT) (Sigma-Aldrich).

Each sample mix consisted of 10 µg of protein together with 2.5 µl Laemmli Sample Buffer (Bio-Rad) and 2 µl of 0.1 M Dithiothreitol (DTT) (Sigma-Aldrich). Samples were vortexed, spun down and incubated for 5 min at 100°C. The protein mix was loaded on a 4-20% Mini-PROTEAN® TGX™ Stain free Protein Gel (Bio-Rad). Protein separation was obtained at 300 V and 400 mA for 15 min with the TGS1x Running buffer (**Section 2.1.1.3**). The proteins from the gel were then blotted to the Trans-Blot® Turbo™ Mini PVDF Transfer membrane with the Trans-Blot® Turbo™ Transfer System (Bio-Rad) at 25 V, 2.5 A for 3 min. The membrane was blocked in 5% milk (**Section 2.1.1.3**) for 1 h. Primary antibody (**2.1.2**) was incubated in 1% milk (**Section 2.1.1.3**) overnight. The membrane was then washed 3 x for 10 min with TBS-T (**Section 2.1.1.3**), incubated with the secondary antibody (**2.1.2**) in 1% milk for 1 h, and washed 3 times again. The membrane was visualised with SuperSignal™ West Pico Chemiluminescent Substrate (Bio-Rad) and the Bio-RAD® Gel Doc Imager.

In order to detect more epitopes on the same membrane, stripping of previous antibodies was performed with Restore™ Western Blot Stripping Buffer (Thermo Fisher Scientific) followed by blocking in 5% milk (**Section 2.1.1.3**) for 1 h. The house-keeping gene (GAPDH) was detected after incubation in 1% milk (**Section 2.1.1.3**) for 1 h, and washing 3 x for 10 min with TBS-T (**Section 2.1.1.3**). The blot was visualised with SuperSignal™ West Pico Chemiluminescent Substrate (Bio-Rad) and the Bio-RAD® Gel Doc Imager. Protein quantification was performed with the software ImageJ.

2.2.7 Electrophysiology

Whole cell patch clamp recordings and preliminary analysis were performed by Eleonora Lugarà (UCL, Institute of Neurology, Department of Clinical and Experimental Epilepsy). I generated and analysed the presented graphs. Representative images of electrophysiological recordings have been kindly gifted by Eleonora Lugarà. Figures were prepared by me.

Whole patch clamp with intracellular recordings was performed to record the action potential waveform in mDA neurons. For the experiment the coverslips were transferred into the chamber of an upright Olympus BX50WI microscope. Recordings were performed at RT (23-25°C) in extracellular recoding solution. The coverslips were visualised with a 40x objectives with infrared filters (Olympus) through a CCD camera which was connected to a monitor. The mDA neurons were patched in voltage clamp mode whereas cells were not used for experiments with a higher access resistance than 25 MΩ. Liquid junction potentials were not corrected. The DIC (differential interference contrast) system helped with the three-dimensional view of the cells on the screen. The micropipettes used for the experiment were made of borosilicate thin glass (4-6 MΩ, vertical puller Narishige PC-10, capillaries were GC150T-4). The pipettes were filled with filtered cold K-gluconate solution for the recordings. For the experiment the pipette was installed over an Axon Multiclamp 700B amplifier (Molecular Devices). The headstage (Axon-Instrument CV-7B) was installed over a Luigs & Neumann micromanipulators (Mini25). The data were generated at 10 kHz. Data were filtered at 2 kHz (Bessel filter) with WinEDR (John Dempster, University of Strathclyde).

The whole patch clamp internal solution consisted of potassium gluconate (K-Glu). The solution was prepared with 135 mM of potassium-gluconate, 4 mM of KCl, 10 mM of Hepes, 4 mM of Mg-ATP, 0.3 mM of Na-GTP, and 10 mM of Na_2-phosphocreatine. With a pH of 7.3 and mOsm of 291-295. The whole patch clamp external solution consisted of a HEPES-aCSF solution. The solution was prepared with 125 mM of NaCl, 2.5 mM of KCl, 2 mM of MgCl2, 1.25 mM of KH2PO4, 2 mM of CaCl2, 30 mM of glucose, and 25 mM of HEPES. With a pH of 7.4, adjusted with the base NaOH.

2.2.8 AADC Enzyme Activity Assay

The AADC enzyme assay was performed using the refined method of George F. G. Allen from his PhD thesis "The neurochemical consequences of aromatic L-amino acid decarboxylase deficiency" (Allen 2010) based on the previously published method (Hyland and Clayton 1992). Each differentiation counted as one independent experiment. From each differentiation one well of a 12-well plate was used for the assay. The cells were washed with 1x PBS and harvested after incubation with 0.5 ml Accumax for 20 min at 37°C. The enzymatic reaction was stopped with 1 ml of KOSR complete medium (**Section 2.1.1.5**). Samples were then centrifuged at 500 rpm for 5 min at 4°C, washed with 1x PBS and centrifuged again. The pellet was resuspended in 120 µl homogenation buffer (**Section 2.1.1.4**) and stored at – 80°C. Directly before the assay, the cells were lysed by snap freezing them twice in liquid nitrogen, and thawing out at RT. The BCA assay was performed to determine the total protein amount per sample. Subsequently, samples were incubated with PLP (Sigma-Aldrich) and L-dopa (Sigma-Aldrich). For every measurement, controls were provided: a blank control consisting of no incubation condition, and a plasma blank consisting of buffer but no biological sample. 50 µl of cell lysate were incubated with 25 µl of 70 µM PLP in assay buffer (500 mM sodium phosphate pH 7.0, 0.167 mM EDTA, 39 mM dithioerythritol) for 120 min at 37°C. 25 µl of 20 mM L-dopa (in 6 mM HCl) was added and incubated for 20 min at 37°C. To stop the reaction 250 µl of 0.8 M perchloric acid was added to the reaction mixture, incubated for 10 min at RT and centrifuged at 12.000 rpm for 5 min at 4°C. The supernatant was transferred to a new tube and stored at – 80°C until dopamine was measurement by HPLC (work flow summary in **Figure 2-2**).

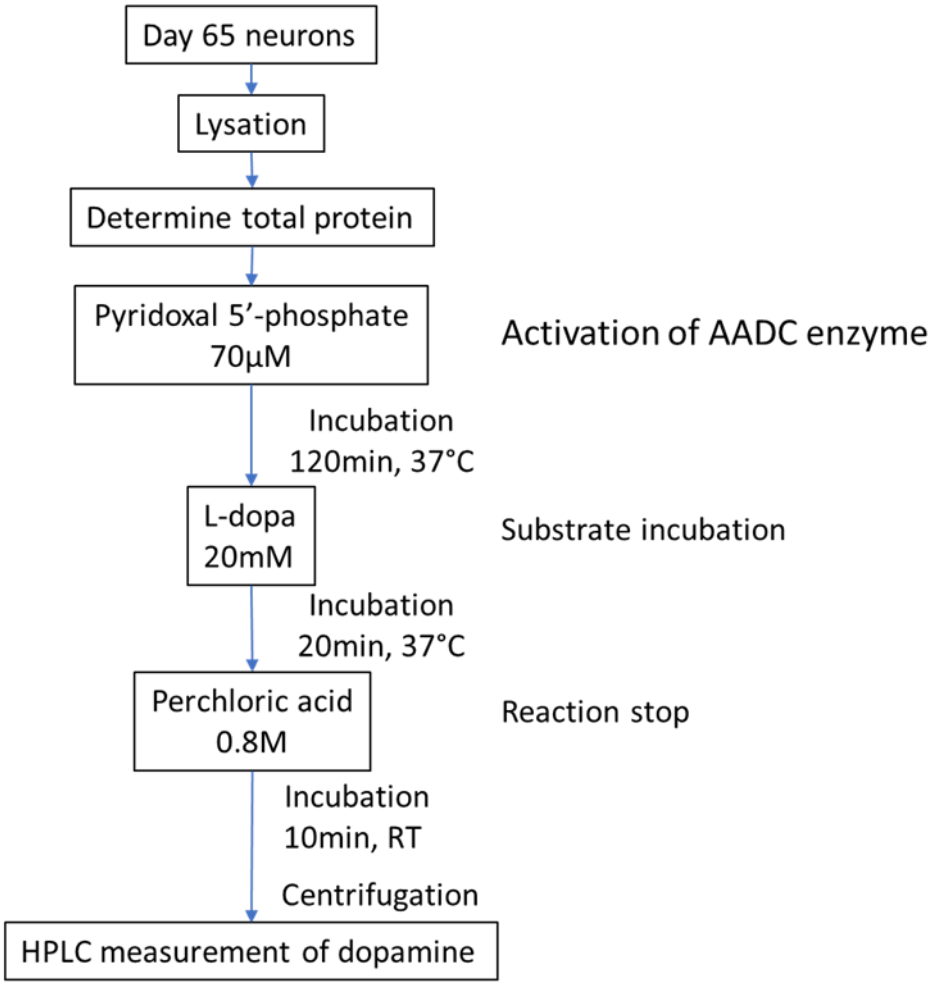

Figure 2-2: Work flow for the AADC enzyme activity assay incubation.

Measurement and quantification of the dopamine concentration was kindly performed by Dr Simon Pope (UCL Hospitals, National Hospital for Neurology and Neurosurgery, Neurometabolic Unit). The mobile phase consisted of 50 mM sodium phosphate with pH 3.6, 5 mM of octaensulfonic acid, 67 µM EDTA, 43 mM orthophosphoric acid, and 230 ml/l methanol diluted in 18.2 Ω HPLC grade water. 200 µl of the sample, that was thawed at RT, was added to the autosampler and kept at 4°C. At a flow rate of 1.2 ml/min and a column temperature of 25°C, 50 µl of sample was injected. The sample was separated on a HiQSil C18W column of 250 x 4.6 mm (KYA Tech. Corp. Tokyo, Japan). Coulometric electrochemical detection was used for the measurement of dopamine. The electrodes E1 and E2 were set up the following way: E1 as the screening electrode with 20 mV for oxidation. E2 as the detector electrode with potentials of 350 mV. Dopamine quantification was performed with a

dopamine standard of 1000 nM. Data was analysed with the AZUR Version 4.6 software. Dopamine was measured with the equation:

$$Dopamine\ conc\ (nmol/L) = \frac{sample\ peak\ area}{external\ standard\ peak\ area} * calibration\ standard\ conc\ (nmol/L)$$

The AADC enzyme activity was calculated for the L-dopa decarboxylation as follows:

$$AADC\ activity = \frac{\frac{final\ sample\ conc\ (pmol)}{incubation\ time\ (\mathrm{min})}}{total\ protein\ (\mathrm{m}g)}$$

The AADC activity in cell homogenates is expressed as pmol/min/mg of protein.

2.2.9 HPLC Measurements for Dopamine and Metabolites

HPLC analysis for dopamine and metabolites was performed in phenol free media collected from iPSCs-derived mDA neurons after 65 days of differentiation. FDF+D medium without the indicator phenol red was collected from seeded cells after 48 hours incubation: 400 µl of medium was added to 400 µl of ice-cold perchloric acid (0.8 M) and the samples were incubated on ice for 10 min. Samples were then centrifuged at 4°C for 5 min at 12.000 rpm, supernatant was collected and stored at -80°C until further analysis. Compound separation using HPLC was performed following a previously published method (De la Fuente et al. 2017).

Quantification of the metabolites was kindly performed by Haya Alrashidi (UCL GOS-ICH). Briefly, mobile phase was prepared in 18.2 Ω HPLC grade water to the composition listed in **Table 2-22**.

Table 2-22: Composition of the mobile phase.

Components	Concentrations
Sodium acetate trihydrate	20 mM
Citric acid monohydrate	12.5 mM
EDTA disodium	0.1 mM
1-octanosulfonic acid	3.35 mM
Methanol	16%
pH (adjusted using concentrated HCl)	3.45

Flow rate was set at 1.5 ml/min and column temperature was maintained at 27°C. Screening electrode (E1) was maintained at 50 mV while detector electrode (E2) at 400 mV. Volume of injection was kept at 50 µl. 500 nM external standard mixture containing DOPAC, 3-OMD, and dopamine was prepared in 18.2 Ω HPLC grade water and a few drops of concentrated HCl prior to experimental run.

The following equation was used to calculate the unknown metabolites.

$$unknown\ concentration\ (pmol) = \frac{Peak\ area\ (sample)}{Peak\ area\ (external\ standard)} \times External\ standard\ concentration\ (pmol)$$

The concentration was then multiplied by the dilution factor 2 and divided by the total protein (mg) to give a final concentration of pmol/mg protein.

2.2.10 Gene Therapy Approach with the *DDC* Lentivirus

2.2.10.1 Generation of the DDC Expression Plasmid

All buffers, cells and restriction enzymes were kindly provided by Dr John Counsell (UCL GOS-ICH) if not stated otherwise. All plasmids and viruses are listed in **Section 2.1.4**.

The *DDC* lentiviral expression plasmid (pCCL-hSYN-DDC-IRES-EGFP) was developed by inserting the *DDC* human gene coding sequence into a previously developed DAT plasmid (pCCL-hSYN-DAT-IRES-EGFP), in place of the human DAT coding sequence. The DAT plasmid was initially propagated in competent bacterial cells and the correct structure confirmed by restriction digest. The DAT plasmid (pCCL-hSYN-DAT-IRES-EGFP) was kindly provided by Dr Joanne Ng (UCL, Institute of Women's Health, UCL), who also gifted the mock plasmid construct expressing only GFP (pCCL-hSyn-EGFPv2).

DAT Plasmid Verification

Transformation, amplification, and purification of all plasmid constructs was performed as described here. 50 ng of plasmid DNA was added to one vial of One Shot™ TOP10 Chemically Competent *E. coli* bacteria (Thermo Fisher Scientific) and incubated for 30 min on ice. After that, bacteria cells were heat shocked at 42°C for 30 s to allow uptake of plasmid DNA, before returning to ice for a further 5 min. Then, 500 µl of SOC Medium (Takara) was added to cells, which were then cultured at 37°C for 1 h with agitation (200-225 rpm). After 1 h of incubation, 500 µl of the culture was plated on a dry agar plate (**Section 2.1.1.8**), containing 50 µg/ml Kanamycin. The plate was incubated at 37°C for 20 hours. Single bacterial colonies were picked and seeded into 3 ml mini cultures of LB medium (**Section 2.1.1.8**) and incubated at 37°C while shaking at 200-225 rpm over-night.

Plasmid DNA was extracted from the overnight miniprep cultures using a commercial plasmid purification kit [Miniprep Kit (QIAGEN)]. Briefly, the method involves alkaline lysis of bacterial cells, followed by clearance of the bacterial lysate, adsorption of DNA onto the silica membrane, and washing and elution of plasmid DNA.

1 ml of overnight culture was transferred to a 1.5 ml tube and centrifuged for 5 min at 6000 rpm. The supernatant was removed and 250 µl of the P1 resuspension buffer was added to the pellet and lysed with 250 µl of P2 lysis buffer for 5 min at room RT before neutralisation with 350 µl of N3 for a further 5 min at RT. The mix was finally centrifuged for 10 min at 14000 rpm. Supernatant was then transferred into the supplied spin column. The column was centrifuged for 1 min at 14000 rpm and the flow-through was discarded. Columns were then washed with 750 µl of PE buffer (which contains ethanol (EtOH), and removes salts), centrifuged again for 1 min at 14000 rpm, and the flow-through was discarded. After a second step of centrifugation for 1 min at 14000 rpm (to remove any residual ethanol) to dry the column, DNA was eluted with 50 µl of EB elution buffer, after centrifugation for 1 min at 14000 rpm. The DNA concentration was measured with the UV-Vis spectrophotometer NanoDrop™ 1000 in ng/µl.

Amplification of the correct construct was analysed after restriction enzyme digestion of 1 µg of DNA.

The DAT plasmid (pCCL-hSYN-DAT-IRES-EGFP) was detected with 5 BamHI (Thermo Fisher Scientific), which generates a 600 bp fragment of the DAT plasmid.

Table 2-23: Master mix for the digest of the DAT plasmid with the restriction enzyme 5 BamHI.

Constituent	Per sample (µl)	4x (µl)
Buffer (Anza red 10x) use 1:10	5	20
Enzyme 5 BamHI	2	8
H_2O	33	132

40 µl of master mix was added for each sample to a new tube. Then 10 µl of DNA was added and the mix was digested at 37°C for 45 min.

The gel was loaded with 10 µl of Quick-Load® 1 kb DNA Ladder, 30 µl of sample and was run for 45 min at 110 V in 1xTBE buffer.

Preparation of the DAT Plasmid for the *DDC* Gene Insertion

Digestion was performed to cut the *DAT* gene from the DAT plasmid. Therefore, two restriction enzymes were used: SgrDI (Thermo Fisher Scientific) and 6 NheI (Thermo Fisher Scientific).

Table 2-24: First digest master mix with the restriction enzyme SgrDI.

Constituent	Per sample (µl)
Buffer (Tango 10x) use 1:5 to get Tango 2x	5
Restriction enzyme SgrDI	2
H_2O	3

For the first digest (**Table 2-24**) 20 µl of master mix was added for each sample to a new tube. Then 10 µl of DNA (2 µg) was added (two samples) and digested at 37°C for 45 min.

Table 2-25: Second digest master mix with the restriction enzyme 6 Nhel.

Constituent	Per sample (µl)
Buffer (Anza red 10x) use 1:10	5
Restriction enzyme 6 Nhel	2
H_2O	13

For the second digest (**Table 2-25**) 20 µl of master mix was added to each sample from the first digest (volume was now 50 µl in total). The second digest was performed at 37°C for 45 min.

A 0.7% agarose gel (**Section 2.2.4.9**) was casted with 50 ml 1xTBE and SYBR™ Safe. The gel was run at 110 V for 45 min with the Quick-Load® 1 kb DNA Ladder. The gel band was cut at 8.5 kb, which was the size of backbone plasmid. DNA was then purified using the QIAquick Gel Extraction Kit (Qiagen). QG buffer was added to solubilise the DNA in accordance to the gel weight in a radio 1:3. The gel was then incubated for 10 min at 50°C. The sample was vortexed and then incubated for another

3 min at 50°C. 110 µl of isopropanol was added for precipitation of the DNA. The mix was then transferred to a spin column and centrifuged for 1 min at 13.000 rpm, the flow through was discarded. 500 µl of QG buffer was added and centrifuged for 1 min at 13.000 rpm to remove all traces of agarose, the flow through was discarded. Afterwards, the sample was washed with 750 µl of PE buffer and centrifuged again for 1 min at 13.000 rpm, flow through was discarded. The column was then transferred into a new 1.5 ml tube, and 30 µl of pre-warmed elution Buffer EB was added. The mix was incubated for 4 min at 50°C and centrifuged for 1 min at 13.000 rpm. The DNA concentration was measured with the UV-Vis spectrophotometer NanoDrop™ 1000.

Cloning of the *DDC* Gene and Transformation of the *DDC* Plasmid

The *DDC* sequence was designed by Dr John Counsell (UCL GOS-ICH). The *DDC* synthetised DNA was resuspended in 20 µl H_2O for a concentration of 50 µg/µl and incubated for 5 min at RT. Then 4 µl of *DDC* DNA was mixed in a PCR tube with 4 µl of the empty plasmid and 2 µl of the 5x In-Fusion ® HD Enzyme (Takara). The PCR was performed for 15 min at 50°C and incubated on ice for 2 min afterwards.

The *DDC* plasmid was transformed, purified and analysed as described above. Amplification of the construct was obtained after dilution 1:10 of the bacterial culture in LB medium with Kanamycin (50 µg/ml). A stock of the *DDC* plasmid bacterial culture was frozen down in 20% glycerol and stored at -80°C.

DNA was then extracted with the PureLink™ HiPure Plasmid Filter Maxiprep Kit and the PureLink™ HiPure Precipitator Module (Thermo Fisher Scientific) according to the manufacturer's instructions. Previous, the following buffers were warmed up in the water bath: E4, L7, and TE. The Filtration Cartridge was inserted into the PureLink® HiPure Maxi Column. The column was then equilibrated with 30 ml of Equilibration Buffer EQ1. The LB culture was centrifuged for 10 min at 4000 rpm and the medium was removed. The cell pellet was resuspended in 10 ml Resuspension Buffer R3. Afterwards the cells were lysed with 10 ml of Lysis Buffer L7 and incubated for 5 min at RT. Precipitation was performed with 10 ml of Precipitation Buffer N3. The DNA was washed with 50 ml of Wash Buffer W8 and the flow through

was discarded. A sterile 50 ml centrifuge tube was placed under the HiPure Filter Column and the plasmid DNA was eluted with 15 ml of Elution Buffer E4. The precipitation of DNA was performed with the PureLink™ HiPure Precipitator Module according to the manufacturer's instructions. 10.5 ml of isopropanol was added to the eluate and incubated for 2 min at RT. The DNA mix was added to the syringe, pressed through, and the flow-through was discarded. The DNA was washed with 5 ml of 70% ethanol, eluted with 750 µl of TE buffer, and stored at -20°C.

2.2.10.2 Plasmid Sequencing

The plasmid's sequences were verified by Dr Katy Barwick (Genetics Research Associate from Kurian group, UCL GOS-ICH). Dideoxy sequencing (**Section 2.2.4.2**) was undertaken to confirm the presence of the human synapsin (*hSYN*) gene promoter and the *EGFP* reporter gene in both vectors, as well as the presence of *DDC* gene in the *DDC* plasmid (pCCL-hSYN-DDC-IRES-EGFP), and its absence in the mock plasmid (pCCL-hSYN-EGFPv2JN).

Figure 2-3 and **Figure 2-4** show schematic representations of the *DDC* and mock plasmid, which were utilised for the lentivirus generation for *in vitro* gene transfer. Both vectors contain the *hSYN* promoter, however only the *DDC* plasmid contains the desired human *DDC* gene (*hDDC*) and the Internal Ribosome Entry Site sequence (IRES). Both vectors express the reporter gene *EGFP*. The constructs are not drawn to scale.

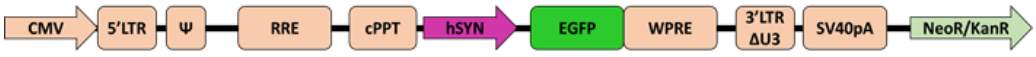

Figure 2-3: Mock plasmid map (pCCL-hSYN-EGFPv2JN).
CMV= human cytomegalovirus immediate early promoter, 5'LTR= truncated 5' long terminal repeat, ψ= packaging signal, RRE= Rev response element, cPPT= central polypurine tract, hSYN= human synapsin promoter, EGFP= enhanced green fluorescent protein, WPRE= woodchuck hepatitis virus posttranscriptional regulatory element, 3'LTR ΔU3= self-inactivating 3'long terminal repeat, SV40pA= simian virus 40 polyadenylation signal, NeoR/KanR= neomycin and kanamycin antibiotic resistance.

Figure 2-4: *DDC* plasmid map (pCCL-hSYN-DDC-IRES-EGFP).
Same as the mock plasmid (**Figure 2-3**) with the addition of *hDDC*= human *DDC* gene, and IRES= Internal Ribosome Entry Site sequence.

2.2.10.3 Lentivirus Production

The DNA mix was prepared with 40 µg transgene plasmid, 30 µg of the lentiviral packaging plasmid pCMVR8.74 (1 µg/µl; Addgene) and 10 µg of envelope expressing plasmid pMD2.G (1 µg/µl; Addgene). 5 ml Opti-MEM I medium (Gibco®) was added to the DNA mix and filtered through a 0.22 µm pore size membrane filter with hydrophilic polyethersulfone (PES) (Millipore), mixed with a filtered solution 1:20 of Opti-MEM I medium and 10 mM polyethylenimine (PEI) (Sigma-Aldrich). The mix was incubated for 20 min at RT. 1.8 x 10^7 HEK 293T cells, maintained in DMEM high glucose pyruvate (Gibco®), 10% FBS, and 1:100 Penicillin-Streptomycin, were infected with 10 ml of the DNA-PEI mix and incubated for 4 hours in the incubator at 37°C. After 4 hours medium was collected from the cells and centrifuged at 500 rpm for 5 min to remove dead cells. The supernatant was filtered through a 0.22 µm filter (Millipore) and centrifuged at 4600 rpm and 4°C for 21 hours. Supernatant was then disposed, and the 50 ml tube was dried upside-down on a dry paper towel. 50 µl of Opti-MEM I medium was added to the tube and incubated on ice for 60 min. The pellet was resuspended in the medium and stored in aliquots at -80°C.

Lentiviral Vector Titration by qPCR

In order to dose viral vectors by multiplicity of infection (MOI), vector titres were quantified by transducing HEK 293T cells and quantifying the total number of integrated genomes per cell. HEK 293T cells were seeded into 6-well plates at a density of 1 x 10^5 cells per well, before administering a dose escalation of viral vector.

Table 2-26: Transduction volumes of the 1 x 10^5 HEK 293T cells per well with lentivirus.

50 µl	10 µl	2 µl	0.4 µl	0.08 µl	No virus

The integrated vector copy number (VCN) in the HEK 293T cells was then quantified by a previously validated qPCR assay (Vink et al. 2017). Seven days after transduction, gDNA was extracted from the cells using the commercial kit DNeasy Blood & Tissue Kit (**Section 2.2.4.1**), according to the manufacturer's protocol. gDNA sample concentrations were adjusted to 20 ng/µl and a plasmid standard curve was prepared in a 10-fold dilution series, ranging from 1×10^2 to 1×10^7 copies per 5 µl. The standard plasmid for LV titration (pMKRQ BTW2R) was kindly gifted by Dr. Conrad Vink (UCL). The reaction master mix for the genomic target (virus genome), was prepared as summarised in **Table 2-27** using the TaqMan® Universal PCR Master Mix (Applied Biosystems).

Table 2-27: The reaction master mix for the genomic target (virus genome).

Constituent	Volume (µl) per 25 µl reaction
H_2O	6.99
TaqMan® Universal PCR Master Mix	12.5
Forward oligo	0.23
Reverse oligo	0.23
Probe	0.06

20 µl of the reaction master mix was added to each well, before adding 5 µl of the relevant samples/standards and mixing by pipetting.

The calculation was performed as followed:

1. Titre calculation with the standard curve and the equation from Ct

$$y = m * x + t$$

Assuming 15200 human genome copies per 100 ng DNA

2. Viral copy number per cell $(\mathrm{VCN}) = \frac{x}{15200}$

3. Titer $\left(\frac{\mathrm{iu}}{\mathrm{ml}}\right) = \frac{VCN * number\ of\ transduced\ cells}{\frac{number\ of\ \mu l\ used\ in\ titration}{1000\ (conversion\ from\ \mu l\ to\ ml)}} = \frac{VCN * 100000}{\frac{10}{1000}}$

(iu= infectious unit)

4. Calculation MOI

$$\frac{amount\ of\ cells}{virus\ titre\ [\frac{iu}{ml}]} * 1000 * \mathrm{MOI} = amount\ of\ virus\ for\ infection\ [\mu l]$$

Assuming: 15.000/µl while drop plating, drop 100 µl ->1.5x10^6 cells

$$\frac{1.5 * 10\hat{}6}{titer\ [\frac{iu}{ml}]} * 1000 * \mathrm{MOI} = x\ [\mu l]$$

Validation of Lentivirus Infection via Immunoblotting for AADC Protein

In order to assure the *DDC* plasmid was successfully built into the viral particle immunoblotting was performed to show AADC protein expression. Therefore, HEK 293T cells were seeded into 6-well plates at a density of 1 x 10^5 cells per well, before administering a dose escalation of viral vector.

Table 2-28: Transduction volumes of the 1 x 10^5 HEK 293T cells per well with lentivirus.

50 µl	10 µl	2 µl	0.4 µl	0.08 µl	No virus

Seven days after transduction, protein was extracted from the cells, quantified and immunoblotting for the AADC protein was performed (**Section 2.2.6.4**). The presence of the AADC band confirmed the presence of the *DDC* gene in the virus.

Lentivirus Infection of mDA Neurons to determine the right Multiplicity of Infection (MOI)

mDA neurons on day 28 of differentiation of a 12-well plate were infected with a MOI of 10, 5 and 1 for both viruses pCCL-hSYN-DDC-IRES-EGFP, and the pCCL-hSYN-EGFPv2 virus. The appropriate amount of virus was added for each MOI (**Table 2-29**) to 500 µl of FDF medium (**Section 2.1.1.7**). After 2 hours of incubation at 37°C medium was removed and fresh FDF medium was added to the cells.

Table 2-29: Set up of a 12-well plate with both viruses and three different MOIs (10, 5, and 1).

	MOI 10	**MOI 5**	**MOI 1**
***DDC* lentivirus**	16.31 µl	8.16 µl	4.08 µl
Mock lentivirus	13.84 µl	6.92 µl	3.46 µl

Three days after infection the cells were analysed with a bright field microscope to determine level of toxicity at different MOIs. To confirm GFP expression cells were analysed with the fluorescent microscope. A MOI of 5 was considered as the best condition for further experiments.

Treatment of AADC mDA Neurons with Lentivirus

AADC patient-derived mDA neurons were infected at day 28 of differentiation. Lentivirus was resuspended in 500 µl of FDF medium at a MOI of 5. After two hours of incubation in the 37°C incubator the virus medium was discarded, and the cells were fed with 1 ml of fresh FDF medium. mDA neurons were matured following the differentiation protocol (**Section 2.2.5.1**) and harvested at day 65 for further analysis.

2.2.11 Statistical Analysis

Statistical analysis was performed using the GraphPad Prism V. 6.01 software. The samples were compared using the Student's unpaired two tailed t-test or using the ordinary one-way ANOVA test. Means are represented by the longer horizontal bars and error bars represent SEM.

Significance levels are determined through p-values. On graphs the p-values are shown with asterisks. One asterisk (*) represents p-values between 0.05 and 0.01. Two asterisks (**) represent p-values between 0.01 and 0.001. Three asterisks (***) represent p-values less than 0.001. Non-significance (ns) indicates a p-value greater than 0.05.

Chapter 3
Generation and Characterisation of AADC patient-derived Induced Pluripotent Stem Cells

3.3 Introduction

The first step towards creating a neuronal model of AADC deficiency involves the generation of induced pluripotent stem cells (iPSC) for subsequent midbrain dopaminergic differentiation. In the following chapter, I will describe how patient human dermal fibroblasts (HDF) were reprogrammed into iPSCs.

3.4 Hypothesis

iPSCs can be generated from HDFs isolated from patients with AADC deficiency.

3.5 Aims

1 To reprogram HDFs from patients into iPSCs
2. To confirm genomic integrity of patient and control iPSC lines after the reprogramming process
3. To confirm the presence of the original *DDC* mutations in patient iPSC lines
4. To prove clearance of the reprogramming virus in all iPSC lines
5. To prove true pluripotency in all iPSC lines

3.6 Results

3.6.1 Generation of iPSCs from Patient HDFs

3.6.1.1 Sendai Virus Reprogramming of Patient HDFs into iPSCs

As discussed in Chapter 1, there are now a variety of different reprogramming techniques for generating human induced pluripotent stem cells (hiPSCs) from somatic cells (**1.4.1)**. In this project, I utilised the CytoTune™-iPS 2.0 Sendai Reprogramming Kit to generate iPSCs from human fibroblasts, as this was the method that had been already established in my host laboratory (**2.2.3**).

The reprogramming process was undertaken with HDFs derived from two AADC patients (Patient 1 and Patient 2). After 30 days post Sendai Virus infection, the infected fibroblasts developed into iPSC colonies. At day 34 post-infection (**Figure 3-1**), the iPSC colonies were manually picked. Overall, 14 colonies were picked for each patient line. The age-matched control lines used in this project were previously

reprogrammed and fully characterised by my secondary supervisor, Dr Serena Barral, UCL Great Ormond Street Institute of Child Health (UCL GOS-ICH). Control lines (Control-03 and Control-05) were thawed, cleaned, and expanded. Ten vials were frozen for the further use.

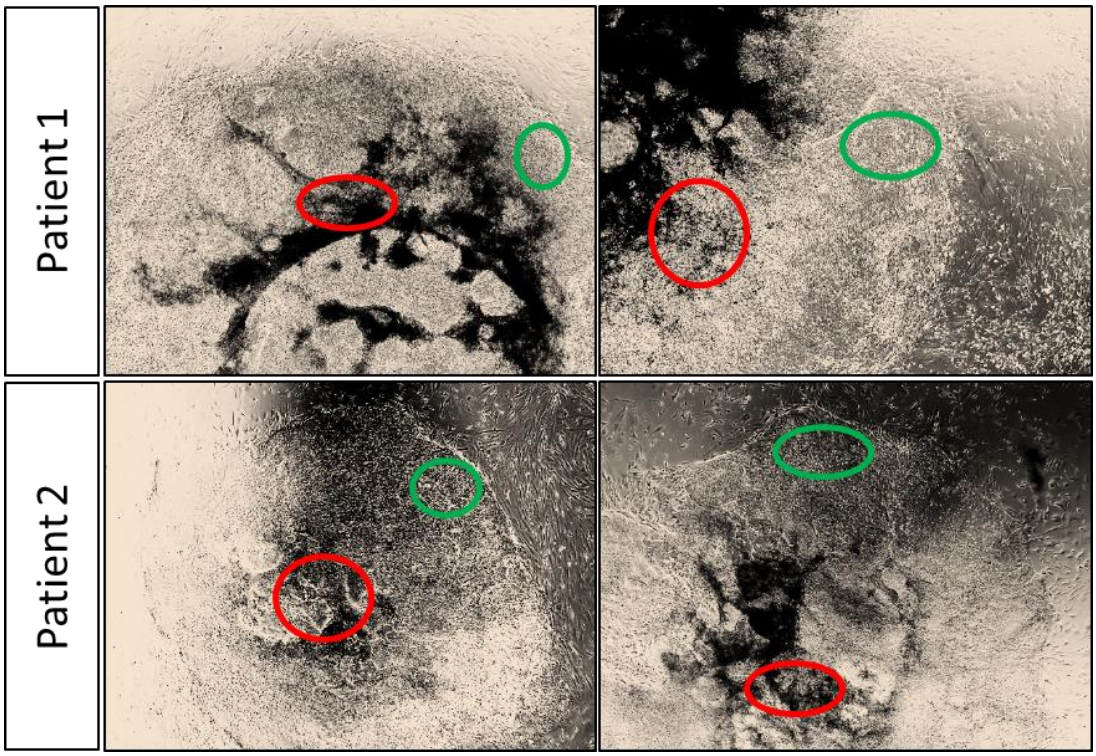

Figure 3-1: iPSC colonies at day 34 after infection with Sendai Virus.
Representative images from Patient 1 and Patient 2, with iPSC colonies on mouse embryonic fibroblasts. Examples of iPSC colonies are marked in green, and differentiated cells are marked in red circles.

As seen in **Figure 3-1,** colonies consist of areas with both differentiated cells and iPSCs. iPSCs are commonly found at distinct borders of the colonies, and present with characteristic epithelial morphology: round shape, little cytoplasm and densely packed. In contrast to iPSCs, differentiated cells show morphology that is more complex, are bigger in size, and present a more uneven pattern within the colony.

3.6.1.2 iPSCs in Cell Culture: iPSCs on a Mouse Embryonic Fibroblast (MEF) Feeder Layer

A MEF feeder layer is commonly utilised to maintain the iPSCs in an undifferentiated pluripotent state as they secrete bFGF that is essential for the pluripotent state. Therefore, the newly generated iPSCs were initially expanded on MEF layer to promote strengthening of pluripotency. After successful manual picking of iPSC colonies, the cells were cultured on a MEF feeder layer (**Figure 3-2**).

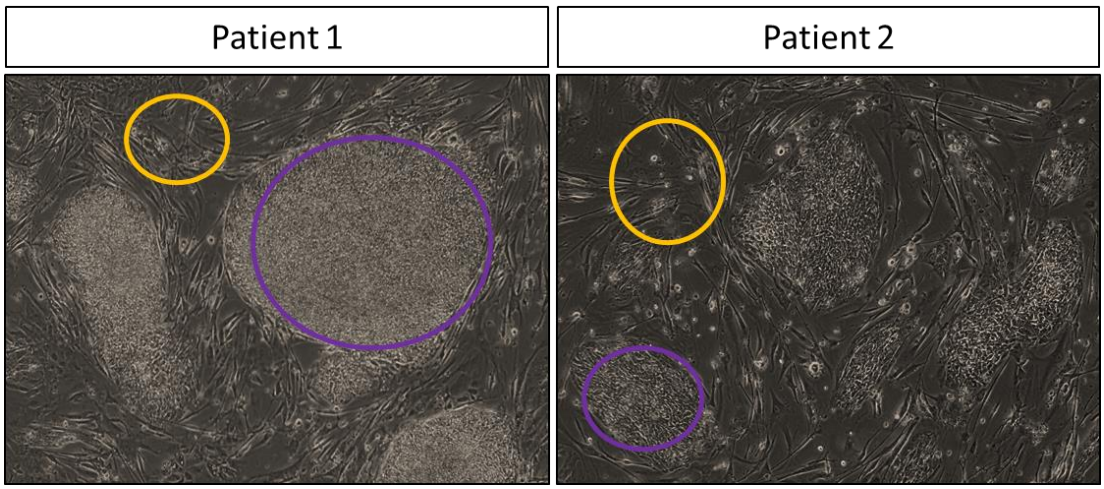

Figure 3-2: iPSC lines on MEF cells.
Representative iPSC lines from Patient 1 at passage 7 and Patient 2 at passage 4. Characteristically, the iPSCs on MEF grow in colonies. Examples of iPSC colonies are marked in purple and MEF cells in yellow circles.

iPSCs were then cultured for around 13 to 17 passages on the MEF feeder layer. From the 14 clones initially picked for each patient, 5 lines for Patient 1 and 6 lines for Patient 2 (4 vials each) were frozen and stored in liquid nitrogen. In tandem, 3 out of the 5 iPSCs lines per patient were transferred for further culture on Matrigel without a feeder layer.

3.6.1.3 iPSCs in Cell Culture: iPSCs on a Matrigel feeder-free System

I utilised Matrigel as a feeder-free culture system for further maintenance of my iPSC lines. Three lines per patient were converted to Matrigel. Patient 1 (lines Patient 1-04, Patient 1-07, Patient 1-10) and Patient 2 (lines Patient 2-01, Patient 2-02, Patient 2-06). These three lines from each patient line were expanded into 18 wells, and 14 vials were frozen for further use at passage 19-30. Pellets for each line were collected for mRNA and DNA extraction.

3.6.2 Characterisation of the AADC iPSCs

Once the iPSCs were successfully cultured on Matrigel and were approximately passage 25, they are expected to be fully reprogrammed. I therefore undertook iPSC characterisation experiments to demonstrate maintenance of the *DDC* mutations, clearance of Sendai Virus, conservation of genome integrity, and to confirm true pluripotency.

3.6.2.1 Sanger Sequencing for *DDC* Mutations

Genomic DNA (gDNA) was extracted from the control and both patient iPSC lines as described in **Section 2.2.4.1**. Sanger sequencing of gDNA (**Section 2.2.4.2**) was undertaken to show maintenance of the *DDC* mutations from the HDFs to the reprogrammed iPSC stage in patient lines, and to confirm that the control iPSC lines did not have any pathogenic *DDC* variants. Primer design and sequence analysis was kindly performed by Dr Katy Barwick (Genetics Research Associate from Prof Kurian's group, UCL GOS-ICH).

Bi-allelic recessive mutations in *DDC* were confirmed in all patient iPSC lines. Patient 1 was previously reported to carry a homozygous missense mutation NM_001082971: c.1039C>G; NP_001076440: p.Arg347Gly (GRCh37) in exon 11, as called by Alamut® Visual (v2.11) software (**Figure 3-3**) (Montioli et al. 2016).

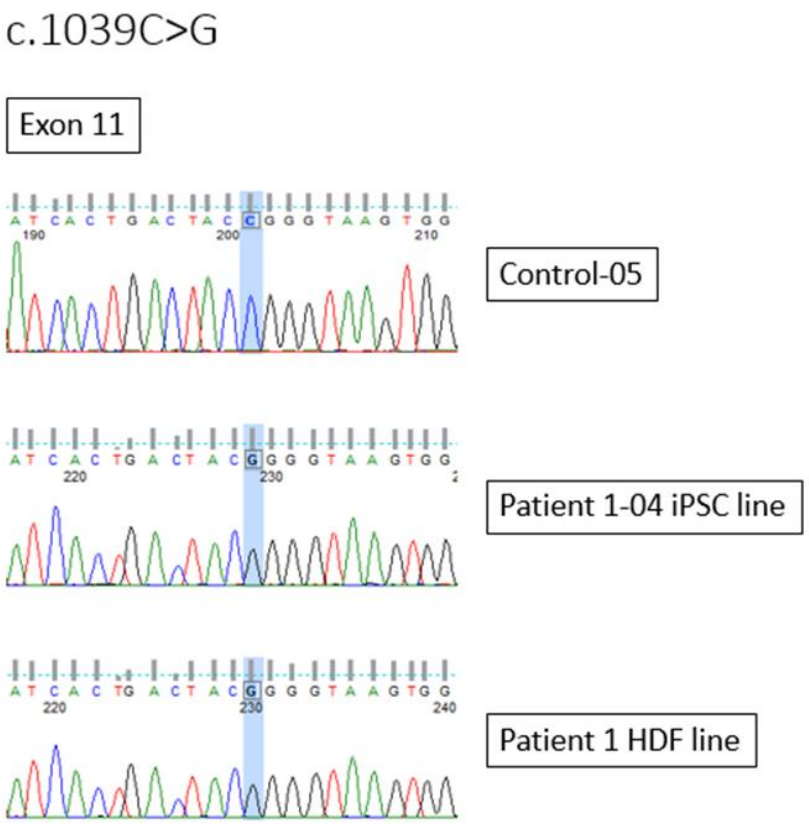

Figure 3-3: Sequencing chromatogram for Patient 1 mutation c.1039C>G; p.Arg347Gly in exon 11.
Sequencing chromatogram for Patient 1. Sequencing chromatograms from the Control-05 iPSC line (top), Patient 1-04 iPSC line (middle), and Patient 1 HDF line (bottom) are illustrated. The *DDC* mutation is highlighted in the blue rectangle. The base change from C (wild type) to G (mutant) is highlighted by the blue box.

As expected, the previously reported homozygous *DDC* mutation was evident in Patient 1's HDF cells, and clearly conserved after reprogramming in the Patient 1-04 iPSC line.

For Patient 2, the previously reported compound heterozygous *DDC* mutations in the literature were a non-sense mutation in exon 2 causing a premature stop codon and a missense mutation p.Leu408Isoleu in exon 11 (Pons et al. 2004). The variant c.19C>T; p.Arg7* in exon 2 (non-sense mutation causing a premature stop codon) was detected in the HDF lines from Patient 2 (**Figure 3-5**). However, the second reported mutation, which is a missense mutation p.Leu408Isoleu, was not detected on repeated sequencing. Complete sequencing of the *DDC* gene was therefore undertaken to try and identify the true second pathogenic change. A missense variant was detected,

NM_001082971: c.299G>C; NP_001076440: p.Cys100Ser (GRCh37) in exon 3, as called by Alamut® Visual (v2.11) software (**Figure 3-5**). *In silico* analysis of this variant using Alamut software revealed that this missense substitution was classified as a variant of uncertain significance, which has not been previously reported in AADC deficiency, was rarely reported in the heterozygous state in gnomAD (frequency 0.00041%) and was never reported in the homozygous state. The missense substitution occurs in an amino acid that is highly conserved across species (**Figure 3-4**; Alamut® Visual 2.11 software).

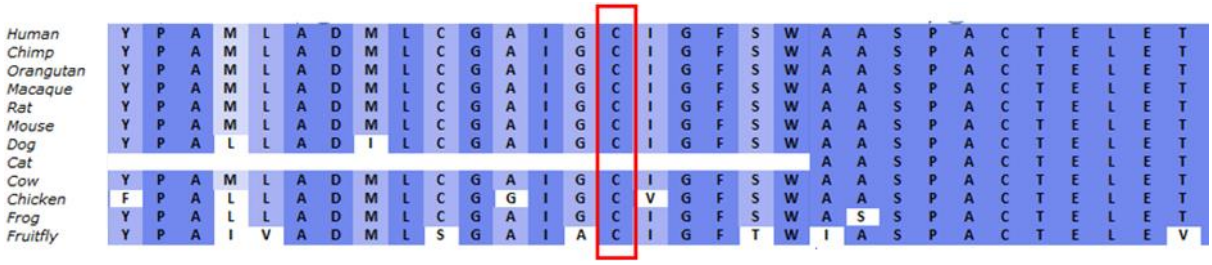

Figure 3-4: The amino acid Cys100 in the AADC protein is highly conserved across species (marked in the red box).

The missense substitution is located close to a key domain of the *DDC* protein. Giada Rossignoli used the PyMol software to investigate the Cys100 position in the AADC protein structure (**Section 1.3.3**, **Figure 1-11**). The missense substitution Cys100 is located in a residue in close proximity to the substrate-binding domain of the AADC protein. The mutation p.Cys100Ser could alter the substrate-binding cleft conformation and could consequently decrease the affinity of the AADC enzyme for its substrates. A number of prediction programs including Polyphen (score 0.958) and Mutation Taster (p value 1.0) support pathogenicity of this variant. Subsequently, lymphocytic DNA was taken from Patient 2 and their family for confirmatory testing and segregation analysis. This revealed that the variant segregated appropriately with disease status. Patient 2's lymphocytic-derived DNA showed both c.19C>T and c.299G>C. The father was an obligate heterozygous carrier of c.299G>C and it was not detected in the mother. No other *DDC* variants were detected on whole gene screening. Overall, it was felt that c.299G>C was likely to be the second disease-causing variant for Patient 2.

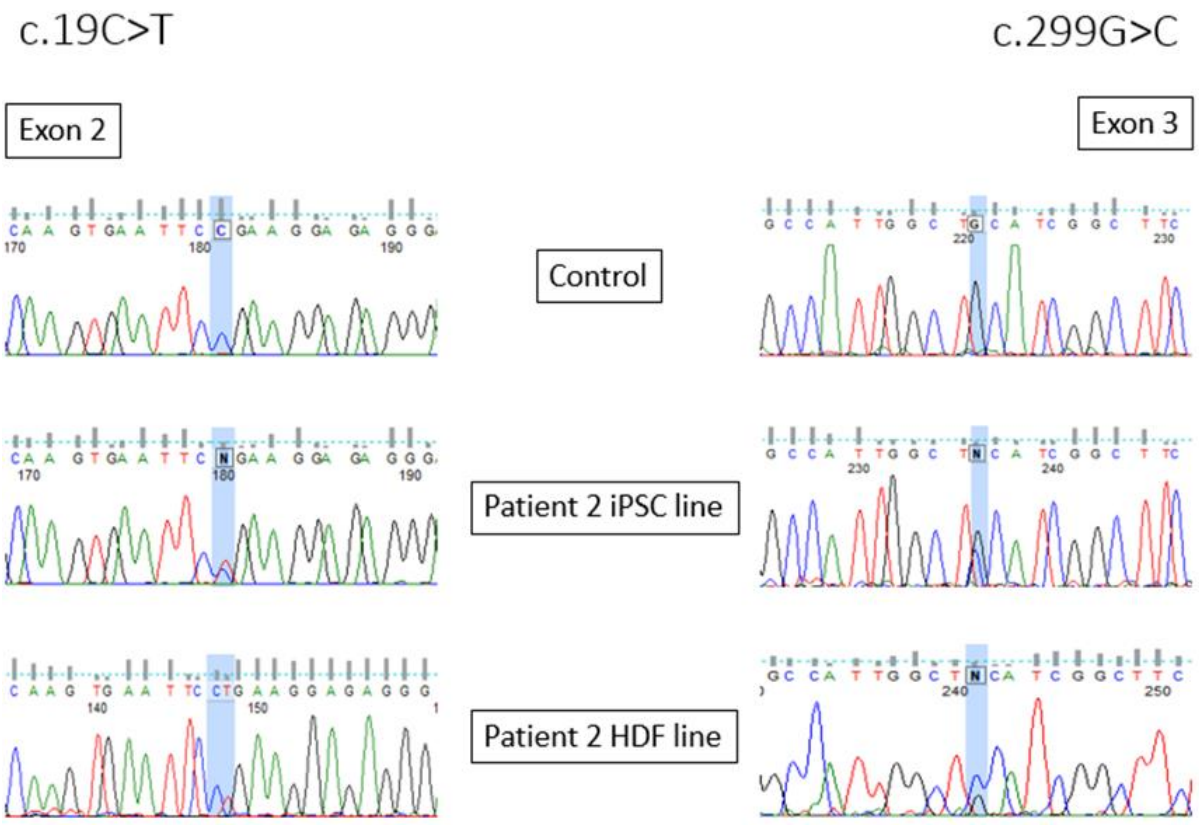

Figure 3-5: Sequence chromatograms for Patient 2 mutations: point mutation c.19C>T, p.Arg7* in exon 2 and missense mutation c.299G>C, p.Cys100Ser in exon 3.
Sequencing chromatogram from the Control-05 iPSC line (top), Patient 2 iPSC line (middle), and the Patient 2 HDF line (bottom) are presented. *DDC* mutations are highlighted in the blue rectangle. On the left, both HDF and iPSC lines show the heterozygous change C (blue peak) to T (red peak). On the right, both HDF and iPSC lines manifest the heterozygous change G (black peak) to C (blue peak).

Again, the mutations from Patient 2 HDF line were conserved after reprogramming into iPSCs.

3.6.2.2 Analysis for Genomic Integrity using Single-Nucleotide Polymorphism (SNP) array

Confirmation of genomic integrity is essential to allow utilisation of iPSC lines for downstream experiments. In 2010, it was reported that human induced hiPSCs are at high risk of chromosomal aberrations. Such acquired deletions and duplications may have significant effects on gene expression, protein expression and differentiation potential, rendering them unusable for subsequent differentiation and disease modelling (Mayshar et al. 2010). In this project, I used a genome-wide SNP array to determine genome stability, specifically to look for structural variations in the human genome that may have occurred during the re-programming process. The Infinium™ HumanCytoSNP-12 v2.1 BeadChip array from Illumina was performed by UCL genomics. I analysed the raw data provided in IDAT files using Bluefuse Multi software (Illumina).

Three iPSC lines from each patient that were previously transferred to Matrigel were tested for genomic integrity (Patient 1-04, Patient 1-07, Patient 1-10, Patient 2-01, Patient 2-02, Patient 2-06). iPSC control lines Control-03 and Control-05 were also included with their respective HDF Control line.

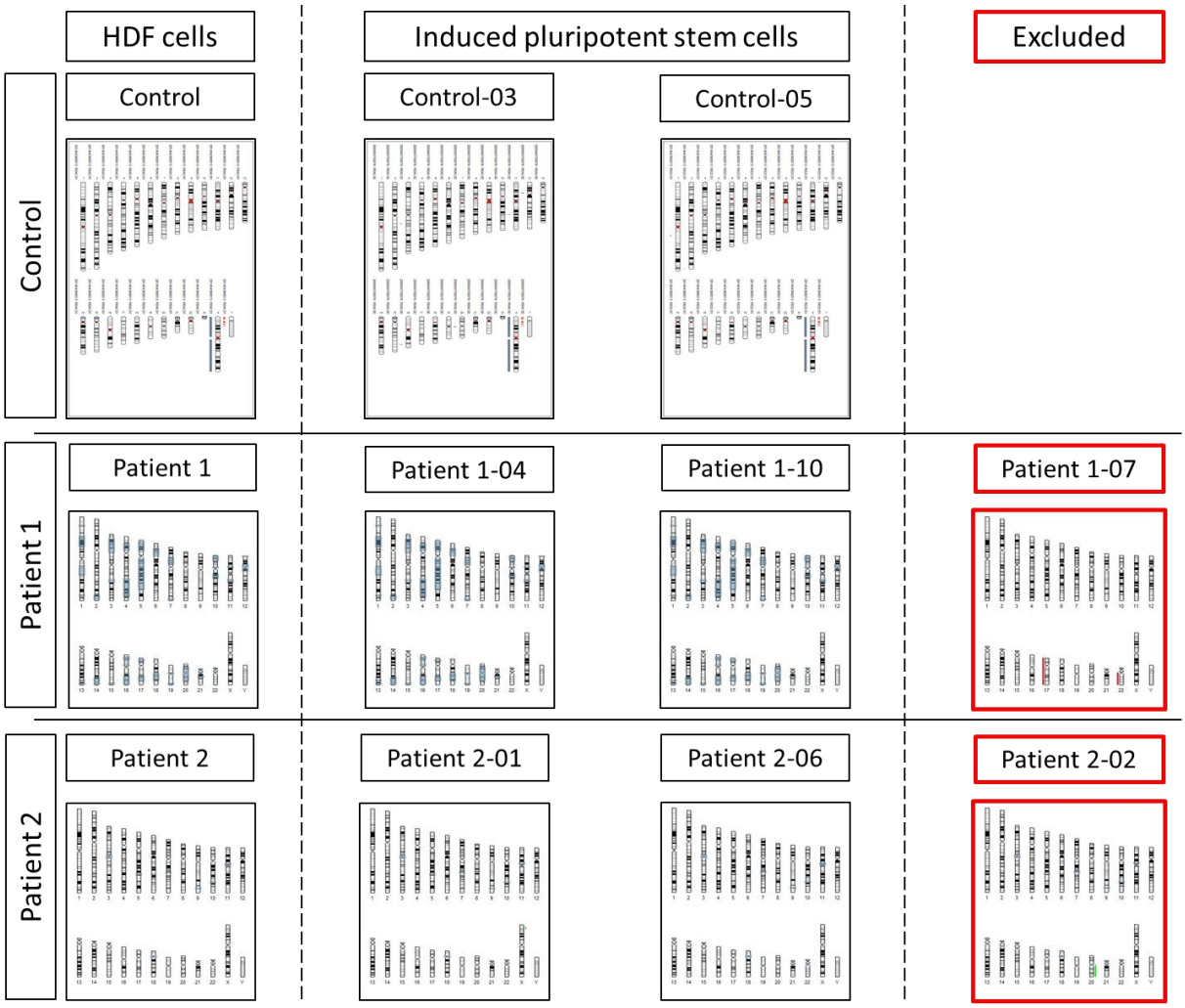

Figure 3-6: Results of SNP array analysis in iPSC lines. Karyograms from previously characterised control lines and newly characterised AADC deficiency patient lines.
Results from both dermal fibroblasts and their respective derived iPSC lines are shown. Control: Control-03 and Control-05 iPSCs from the Control HDF line. Patient 1: Patient 1-04, Patient 1-10, and Patient 1-07 iPSCs from the Patient 1 HDF line. Patient 2: Patient 2-01, Patient 2-06, and Patient 2-02 iPSCs from the Patient 2 HDF line. Excluded iPSC lines due to chromosomal aberrations are marked in red (Patient 1-07 and Patient 2-02 lines). Regions of blue shading on chromosomes represent regions of SNP homozygosity.

SNP array studies therefore confirmed that for the control line, the derived iPSC lines (Control-03 and Control-05) show genome integrity when compared to their HDF Control line. iPSC lines Patient 1-4 and Patient 1-10 had no chromosomal abnormalities when compared to their respective HDF line. However, Patient 1-07 showed a 81 Mb deletion on chromosome 17 and a 35.1 Mb deletion on chromosome 22 (both pathogenic). This iPSC line was therefore excluded from downstream experiments. Patient 2 iPSC lines, Patient 2-01 and Patient 2-06 showed genome

integrity when compared to their respective HDF line. In contrast, the iPSC line Patient 2-02 had acquired a gain of 32.7 Mb on chromosome 20 and was also therefore excluded from further experiments.

All lines that showed genomic integrity after the re-programming process (Patient 1-04, Patient 1-10, Patient 2-01, Patient 2-06, Control-03, Control-05) were then further characterised for markers of pluripotency.

3.6.2.3 Sendai Virus Clearance

In order to confirm that Sendai Virus (SeV) was cleared from host cells after reprogramming, reverse transcription polymerase chain reaction (RT-PCR) was undertaken to detect SeV genome and transgenes (SeV, Klf4, OCT4, c-MYC, SOX2). RT-PCR primers were those provided with the Sendai Virus kit. Results are presented in **Figure 3-7** below.

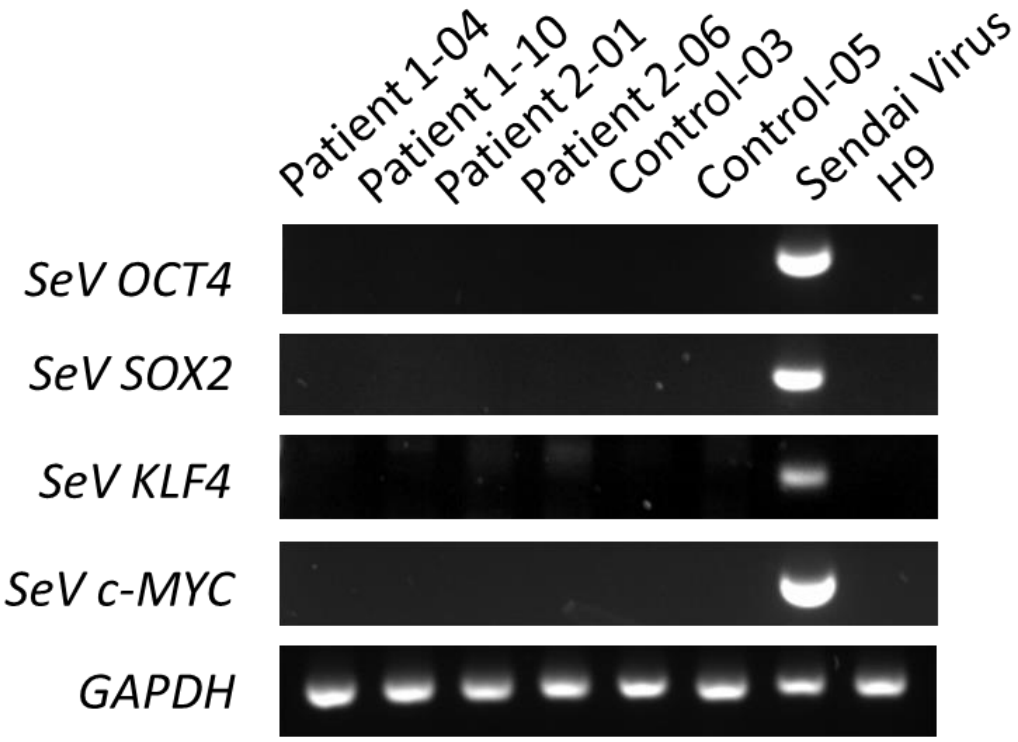

Figure 3-7: Silencing of transgenic Sendai Virus genes.
RT-PCR for detection of SeV-specific transcription factors (*OCT4, SOX2, KLF4, c-MYC*) and the generically expressed housekeeping gene (*GAPDH*) in patient lines, control lines, Sendai Virus (positive control) and human embryonic stem cells H9 (negative control).

Figure 3-7 shows results of RT-PCR analysis for detection of transgenes delivered using SeV vector *SeV OCT4, SeV SOX2, SeV KLF4, SeV c-MYC,* and the housekeeping gene *GAPDH*. The following cell lines were tested: Patient 1-04, Patient 1-10, Patient 2-01, Patient 2-06, Control-03, and Control-05. A positive control (Sendai Virus DNA) and human embryonic cell line H9 (negative control) were also included in the analysis. A PCR product for *GAPDH* was seen in all cell lines. Transgenes expressed in SeV vector were present in the control Sendai Virus DNA sample, but not detected in any of the iPSC or embryonic stem cell lines.

3.6.2.4 Expression of pluripotency markers

RT-PCR was utilised to determine expression of the endogenous pluripotency-related transcription factors *OCT4*, *SOX2*, *c-MYC*, *NANOG*, and *ESG1*. DNA samples analysed included HDF (negative control), human embryonic stem cells H9 (positive control), Patient 1-04, Patient 1-10, Patient 2-01, Patient 2-06, and two control iPSC lines (Control-03 and Control-05). All patient and control iPSC lines, and the human embryonic stem cell H9 line showed expression of all 5 pluripotency-related transcription factors tested, which were not detected in the HDF line. All tested lines showed PCR product for *GAPDH*.

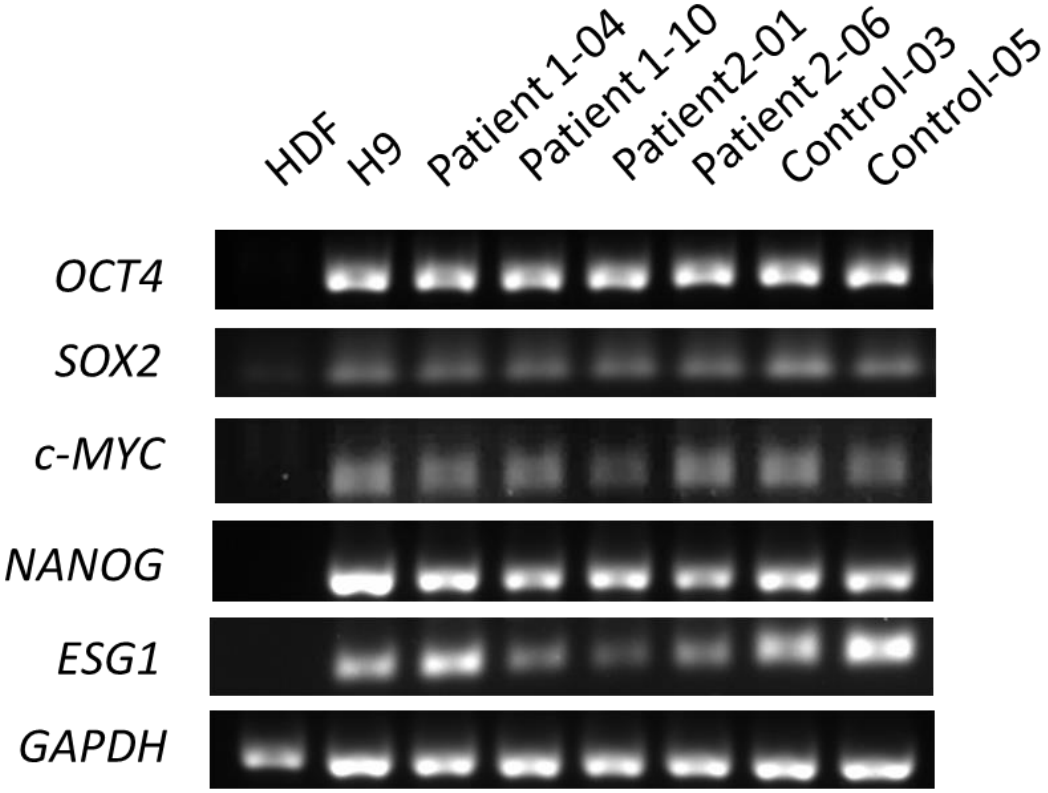

Figure 3-8: RT-PCR for detection of 5 pluripotency markers and the housekeeping gene *GAPDH* in HDF, H9 and the generated patient and control iPSCs.
RT-PCR for detection of pluripotency genes (*OCT4*, *c-MYC*, *NANOG*, *ESG1*) and the generically expressed housekeeping gene (*GAPDH*) in human dermal fibroblasts HDF (negative control), human embryonic stem cells H9 (positive control), in patient lines, and control lines.

3.6.2.5 Expression of pluripotency markers with immunocytochemistry

I also utilised immunofluorescence to assess pluripotency in the iPSC lines. Staining for 4 pluripotency-associated makers (TRA-1-60, TRA-1-81, NANOG, and OCT4) was undertaken.

As seen in **Figure 3-9**, all iPSC lines expressed the 4 pluripotency-associated markers.

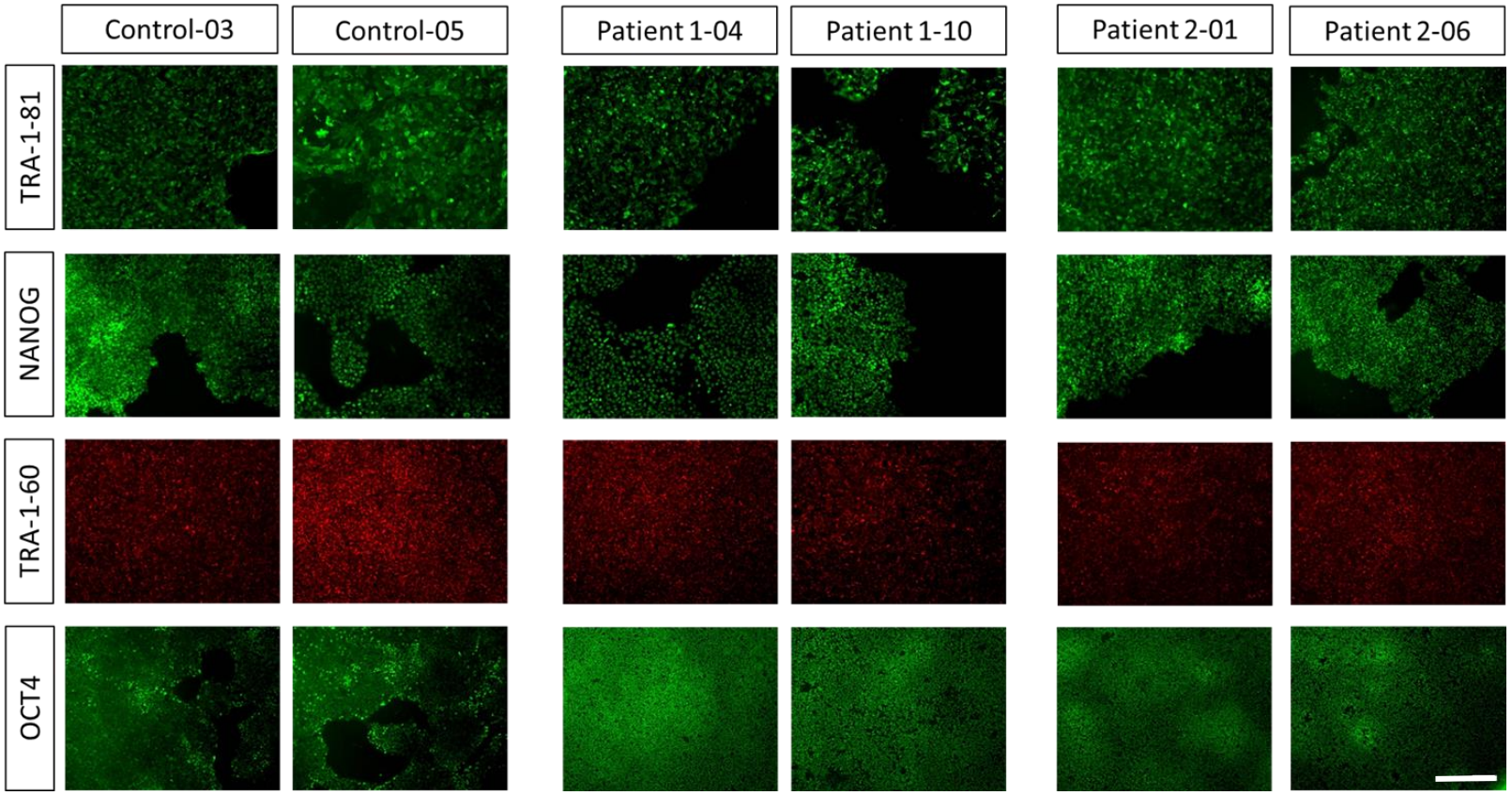

Figure 3-9: Immunofluorescence staining for pluripotency markers TRA1-81, NANOG, TRA-1-60, and OCT4 in derived iPSC control lines (Control-03 and Control-05), Patient 1 lines (Patient 1-04 and Patient 1-10) and Patient 2 lines (Patient 2-01 and Patient 2-06).
The markers TRA 1-81, NANOG and OCT4 are shown in green, TRA 1-60 is shown in red. Expression of all 4 markers is seen in all iPSC lines. Scale bar=200 µm.

3.6.2.6 Spontaneous differentiation *in vitro*

Spontaneous *in vitro* differentiation was undertaken to determine whether the generated iPSC lines had the ability differentiate derivate of the three germ layers (endoderm, mesoderm, and ectoderm) that give rise to specific tissue lineages. For all iPSC lines, embryoid bodies based spontaneous differentiation was performed, with 16 days of culture and subsequent immunofluorescent staining. All derived patient and control iPSC lines were stained for the endodermal marker, SOX17 (transcription factor of the SOX family), mesodermal marker alpha smooth muscle actin (SMA), and ectodermal marker neuronal class III β-tubulin (TUJ1). As seen in **Figure 3-10**, all 6 iPSC lines expressed markers from all three germ layers.

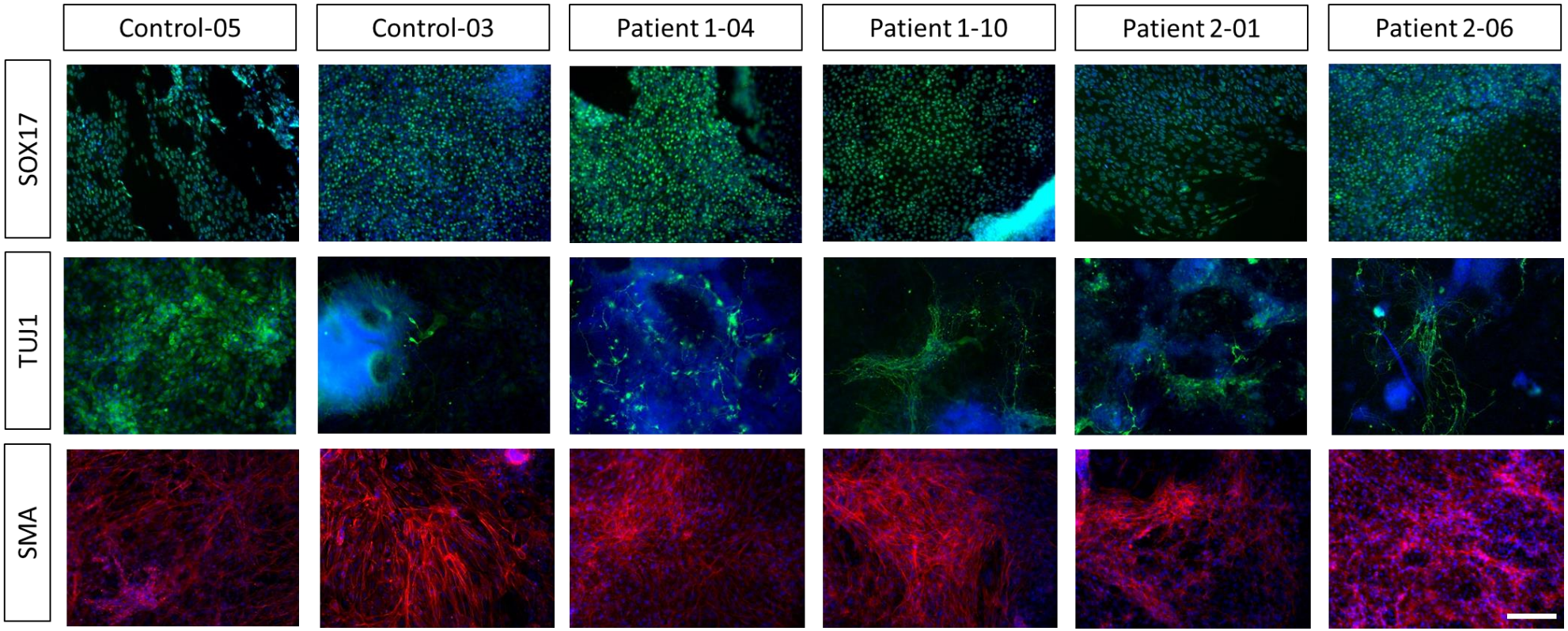

Figure 3-10: Immunofluorescence staining for SOX17 (endoderm, green), TUJ1 (ectoderm, green), and SMA (mesoderm, red) in derived iPSC control lines (Control-03 and Control-05), Patient 1 lines (Patient 1-04 and Patient 1-10), and Patient 2 derived lines (Patient 2-01 and Patient 2-06).
Nuclei were stained for DAPI (blue). Scale bar= 100 µm.

3.6.2.7 Epi-Pluri-Score Test

Epi-Pluri-Score analysis was undertaken for all iPSC lines. This commercially available test (Cygenia) distinguishes between pluripotent and non-pluripotent cell lines, based on differential DNA methylation of CpG sites (CpGs). DNA methylation (DNAm) levels (β-values) at three CpGs are measured by pyrosequencing assays. Two CpGs within the genes *ANKRD46* (methylated in pluripotent cells) and *C14orf115* (non-methylated in pluripotent cells). The Epi-Pluri-Score is a measure of the difference between these two β-values. A positive Epi-Pluri-Score indicates a trend towards pluripotency. The third CpG site checked for DNA methylation is within the pluripotency gene *POU5F1* (*OCT4*), with graded β-values increasing from 0 to 1.0 with reduced pluripotency. Methylation within *POU5F1* may demarcate early differentiation events (Lenz et al. 2015).

The Epi-Pluri-Score test was undertaken for all control and patient iPSC lines.

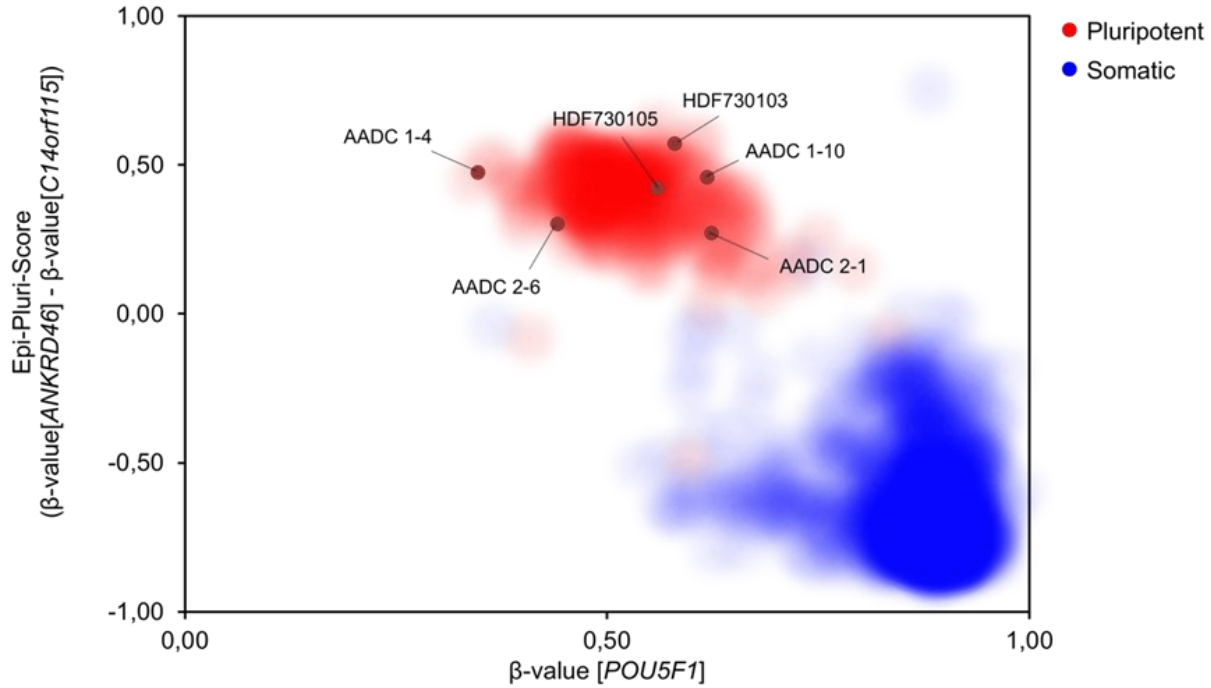

Figure 3-11: Epi-Pluri-Score analysis.
Epi-Pluri-Score analysis was performed for control lines (Control-03=HDF730103 and Control-05=HDF730105), Patient 1 lines (Patient 1-04=AADC 1-4 and Patient 1-10=AADC 1-10), and Patient 2 derived lines (Patient 2-01=AADC 2-1 and Patient 2-06=AADC 2-6).

As illustrated in **Figure 3-11**, the red cloud shows DNA methylation profiles of 264 pluripotent samples. The blue cloud demonstrates DNA methylation profiles of 1,951 non-pluripotent somatic samples. The methylation profile of all 6 iPSC lines were located in the red cloud, providing further evidence for pluripotency of the control and patient lines.

3.7 Summary

In this chapter, I have described the generation of iPSC lines from patients with AADC deficiency using Sendai Virus methodology. Detailed characterisation of these patient-derived iPSCs and previously generated control iPSCs was also undertaken. As a result, I was able to confirm genomic integrity after the re-programming process, demonstrate Sendai Virus clearance, and true pluripotency. This work has thus confirmed that these iPSC lines are suitable for differentiation into midbrain dopaminergic neurons.

Chapter 4
Differentiation and Characterisation of midbrain dopaminergic Neurons

4.1 Introduction

This chapter will focus on differentiation of iPSC lines into midbrain dopaminergic neurons (mDA) and subsequent characterisation of the mDA phenotype in control and AADC patient derived neurons. Overall, 6 iPSC lines were utilised for neuronal differentiation: two control iPSC lines (Control-03 and Control-05), two iPSC lines from Patient 1 (Patient 1-04 and Patient 1-10), and two iPSC lines from Patient 2 (Patient 2-01 and Patient 2-06). iPSC lines were differentiated into midbrain dopaminergic neurons and characterised at both midbrain progenitor stage (day 11 of differentiation) and at mature dopaminergic (day 65) stage (**Figure 4-1**). All lines were differentiated following a modified version of the Kirkeby protocol (Kirkeby, Nelander, et al. 2012). In order to further characterise maturation of the derived mDA neurons, one iPSC line for Control (Control-05), Patient 1 (Patient 1-04) and Patient 2 (Patient 2-01) were selected.

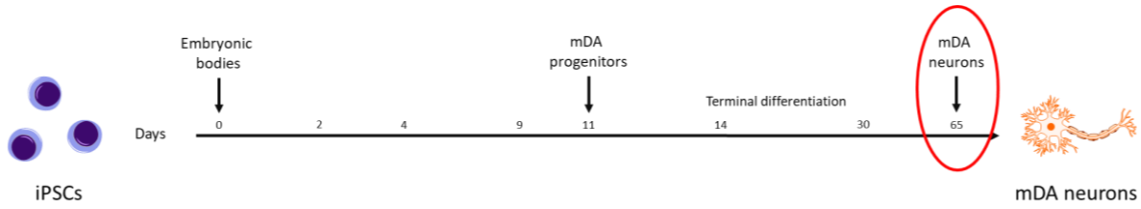

Figure 4-1: Timeline for generation of mDA neurons.
Graphical representation illustrating the time course for neuronal differentiation and points of analysis as follows: day 0 embryonic bodies; day 11 mDA progenitor characterisation; day 65 derived mature mDA characterisation.

4.2 Hypothesis

mDA neurons differentiated from AADC deficiency patient-derived iPSCs can be differentiated into mDA dopaminergic neurons.

4.3 Aims

1. To differentiate and characterise midbrain progenitors (day 11 of differentiation) derived from control iPSC lines (Control-03, Control-05) and patient iPSC lines (Patient 1-04, Patient 1-10, and Patient 2-01, Patient 2-06)

2. To differentiate and characterise mature midbrain dopaminergic neurons (day 65 of differentiation) from the three selected iPSC lines (Control-05, Patient 1-04, and Patient 2-01)

4.4 Results

4.4.1 Characterisation of neuronal Progenitors

4.4.1.1 *In vitro* derived Control and Patient midbrain Progenitors show Up-Regulation of midbrain-related Genes and Down-Regulation of pluripotency related Genes

Midbrain progenitors from control (Control-03 and Control-05) and patient (Patient 1-04 and Patient 1-10; Patient 2-01 and Patient 2-06) lines were analysed after 11 days of differentiation via Real-Time Quantitative Reverse Transcription Polymerase Chain Reaction (qRT-PCR) as described (**Section 2.2.6.2**). In order to ensure desired differentiation through midbrain lineage, I analysed the expression of pluripotency-associated genes (*OCT4* and *NANOG*) as well as transcription factors associated with midbrain progenitor identity (*FOXA2*, *LMX1A*, *LMX1B*, *EN1*, and *EN2*). Both control and patient-derived midbrain progenitors show down-regulation of pluripotency-related genes and upregulation of midbrain related genes (**Figure 4-2**).

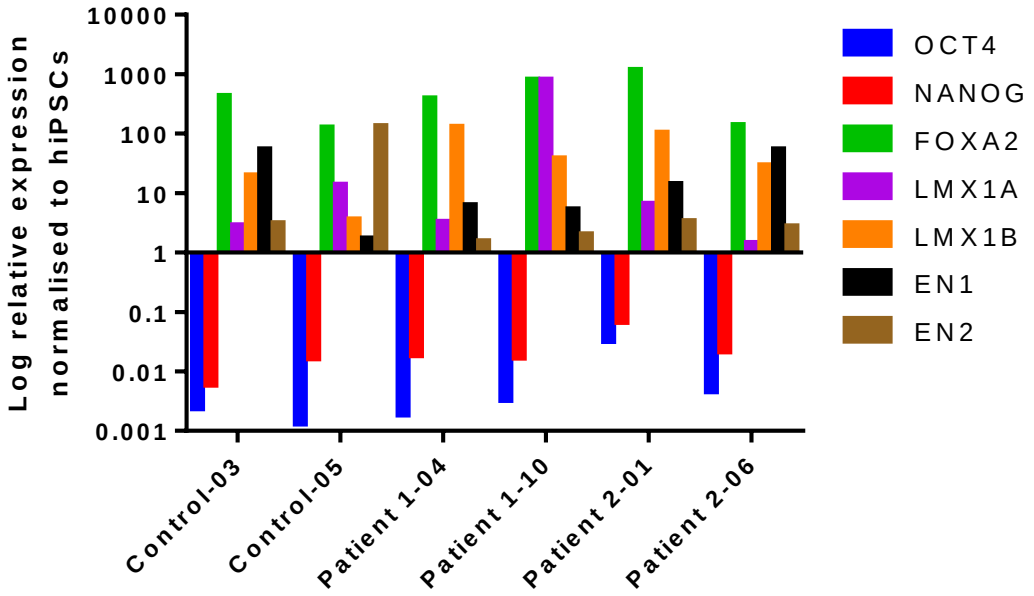

Figure 4-2: qRT-PCR analysis at day 11 of differentiation.
qRT-PCR results for control (Control-03 and Control-05) and patient-derived (Patient 1-04 and Patient 1-10; Patient 2-01 and Patient 2-06) midbrain precursors. Gene expression is relative to the housekeeping gene (GAPDH) and normalised to the respective iPSCs line.

4.4.1.2 Both control and patient-derived mDA Progenitors show early Midbrain Identity with co-localisation of FOXA2 and LMX1A

It is well established that Forkhead Box A2 (FOXA2) expression indicates floor plate identity and LIM Homeobox Transcription Factor 1 Alpha (LMX1A) expression indicates ventral midbrain identity. The co-localisation of FOXA2 and LMX1A is therefore suggestive of midbrain floor plate identity (Arenas et al. 2015). Immunocytochemistry was undertaken to detect co-expression of these two transcription factors at day 11 of differentiation for both control (Control-03 and Control-05) and patient-derived lines (Patient 1-04 and Patient 1-10; Patient 2-01 and Patient 2-06) (**Figure 4-3**). Samples were fixed and stained for FOXA2 and LMX1A as described in **Section 2.2.6.1**. Nuclei were contra-stained with DAPI.

Immunofluorescence analysis showed the expected levels of mDA progenitors expressing FOXA2 and, in particular, co-localising with LMX1A in all 6 cell lines (**Figure 4-4**), in keeping with published data (Kirkeby, Grealish, et al. 2012). Patient and control lines were compared to each using the one-way ANOVA multiple comparison Tukey's test. No statistically significant differences were observed when comparing percentages of FOXA2 positive cells (mean ± SEM; p-value) [Standard Error of Mean (SEM)] of Control-03 line (87.72 ± 2.85); Control-05 line (90.73 ± 3.793); Patient 1-04 line (94.44 ± 1.41); Patient 1-10 line (87.82 ± 3.57); Patient 2-01 line (89.83 ± 2.99); and Patient 2-06 line (79.92± 5.28) (**Figure 4-4 A** and **Table 4-1)**. No statistically significant differences were observed when comparing percentages of FOXA2/LMX1A double positive cells of Control-03 line (77.82 ± 5.15); Control-05 line (81.6 ± 6.33); Patient 1-04 (87.85 ± 2.12); Patient 1-10 line (82.72 ± 3.51); Patient 2-01 line (79.03 ± 4.65); and Patient 2-06 line (84.97 ± 3.80) (**Figure 4-4 B** and **Table 4-1**).

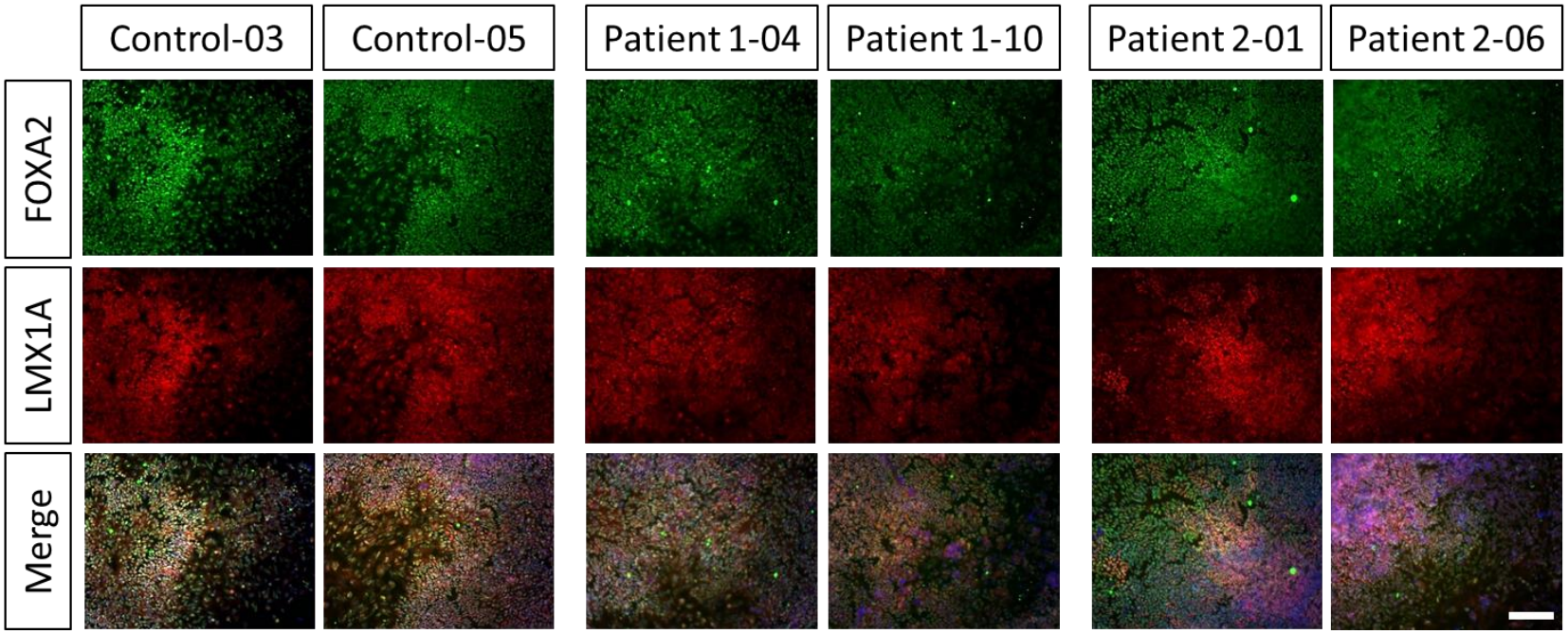

Figure 4-3: Immunofluorescence analysis of control and patient-derived mDA progenitors at day 11 of differentiation.
Immunofluorescence analysis at d11 of differentiation shows co-localisation of midbrain progenitor markers FOXA2 (green) and LMX1A (red). Nuclei are contra-stained with DAPI (blue). Scale bar= 100 µm.

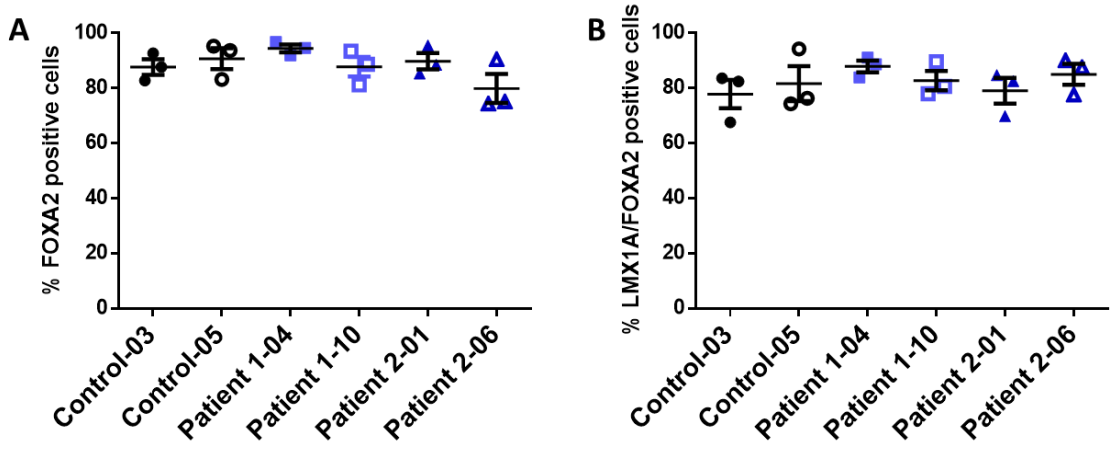

Figure 4-4: FOXA2 and LMX1A immunofluorescence quantification at mDA progenitor stage. **A**: Quantification of FOXA2 positive cells among DAPI positive cells (n= 3). **B** Quantification of LMX1A positive cells among FOXA2 positive cells (n= 3). Error bars represent ± SEM. One-way ANOVA test with the Tukey's multiple comparisons test.

Table 4-1: One-way ANOVA Tukey's multiple comparisons test for FOXA2 and LMX1A/FOXA2 positive cells.

Tukey's multiple comparisons test	Adjusted p-value	Adjusted p-value
Cell lines	**FOXA2**	**LMX1A/FOXA2**
Control-05 vs. Control-03	0.9885	0.9891
Patient 1-04 vs. Control-03	0.7517	0.6187
Patient 1-10 vs. Control-03	> 0.9999	0.9664
Patient 2-01 vs. Control-03	0.9978	> 0.9999
Patient 2-06 vs. Control-03	0.6301	0.8579
Patient 1-04 vs. Control-05	0.9715	0.912
Patient 1-10 vs. Control-05	0.99	> 0.9999
Patient 2-01 vs. Control-05	> 0.9999	0.9982
Patient 2-06 vs. Control-05	0.3141	0.9934
Patient 1-10 vs. Patient 1-04	0.7619	0.9593
Patient 2-01 vs. Patient 1-04	0.9313	0.7274
Patient 2-06 vs. Patient 1-04	0.1023	0.9969
Patient 2-01 vs. Patient 1-10	0.9982	0.9902
Patient 2-06 vs. Patient 1-10	0.6191	0.999
Patient 2-06 vs. Patient 2-01	0.3975	0.9273

4.4.2 Characterisation of mature derived mDA Neurons

4.4.2.1 Both Control and Patient Lines differentiate into derived mDA Neurons

In order to assess the neuronal dopaminergic population derived from AADC patient lines, immunofluorescence analysis for neuronal microtubule associated protein 2 (MAP2) and the enzyme tyrosine hydroxylase (TH) was performed in derived neurons at day 65 of differentiation. MAP2 belongs to the family of proteins that can assemble and stabilise microtubules in dendrites. MAP2 are especially expressed in neurons (Cassimeris and Spittle 2001) and are localised to the dendrites in postmitotic neurons that are terminally differentiated (Harada et al. 2001). TH is involved in dopamine synthesis.

The Control-03, Patient 1-10, and Patient 2-06 lines were differentiated, stained and analysed by Giada Rossignoli (University of Verona, Italy, Department of Neuroscience, Biomedicine and Movement). Both control (Control-03 and Control-05), Patient 1 (Patient 1-04 and Patient 1-10) and Patient 2 lines (Patient 2-01 and Patient 2-06) showed similar levels of co-localisation of TH and MAP2 (**Figure 4-5**). Quantification with the ordinary one-way ANOVA multiple comparisons Tukey's test of single MAP2-positive cells in the Control-03 line (49.07 ± 2.26); Control-05 line (49.72 ± 0.66); Patient 1-04 line (52.04 ± 1.49); Patient 1-10 line (50.27 ± 0.87); Patient 2-01 line (52.6 ± 3.47); and Patient 2-06 line (50.60 ± 3.47) (mean ± SEM), showed no significant difference between control and patient lines (**Figure 4-6 A** and **Table 4-2**).

Analysis of single TH positive cells in the Control-03 line (20.49 ± 1.33); Control-05 line (22.12 ± 0.48); Patient 1-04 line (23.14 ± 0.47); Patient 1-10 line (21.98 ± 0.27); Patient 2-01 line (23.62 ± 1.85); and Patient 2-06 line (22.27 ± 1.01), showed no significate difference between control and patient lines (**Figure 4-6 B** and **Table 4-2**).

Quantification of double TH/MAP2 positive cells in Control-03 line (41.75 ± 1.30); Control-05 line (44.62 ± 1.24); Patient 1-04 line (44.47 ± 0.80); Patient 1-10 line (43.89 ± 0.79); Patient 2-01 line (44.75 ± 1.52); and Patient 2-06 line (44.04 ± 0.99), showed no statistically significant differences when comparing patient lines to control lines (**Figure 4-6 C** and **Table 4-2**). These results showed that all derived patient and

control iPSC lines led to successful generation of mDA neurons. Further downstream experiments thus focused on analysing one line for each control and patient-derived iPSC line.

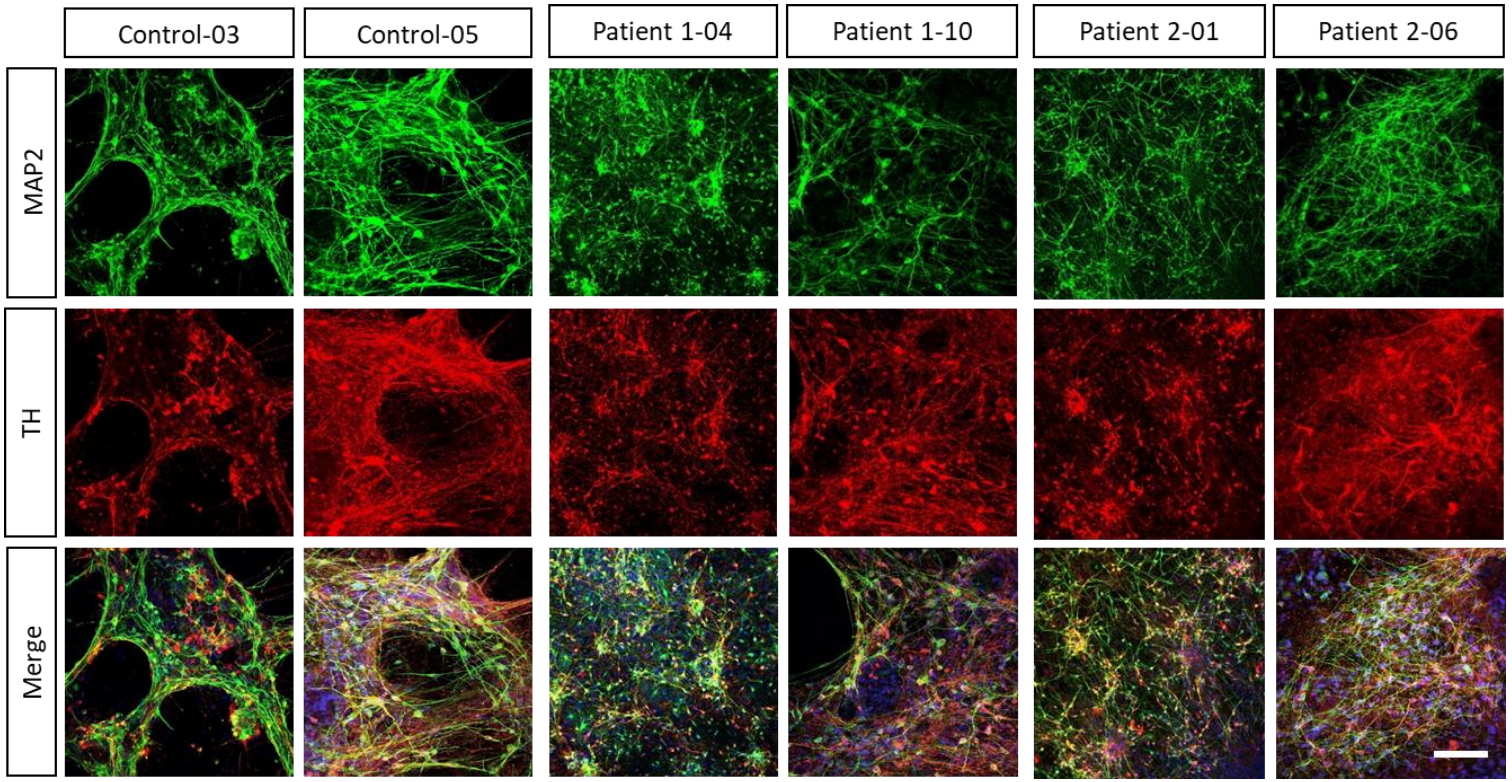

Figure 4-5: Control and patient derived mDA neurons at day 65 of differentiation.
Representative images of mDA immunostaining at day 65 of differentiation. Control (Control-03 and Control-05) and Patient lines (Patient 1-04 and Patient 1-10; Patient 2-01 and Patient 2-06) were stained for MAP2 (green) and TH (red). DAPI (blue) was used to stain the nuclei. Scale bar= 100 µm.

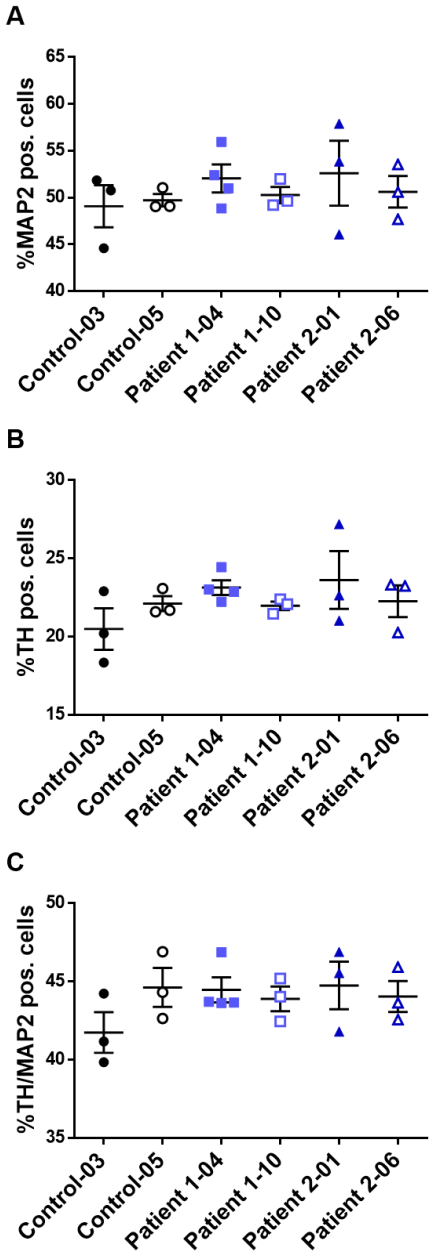

Figure 4-6: Quantification of mature derived dopaminergic neurons for control and patient lines. Quantification of immunofluorescence analysis for the neuronal and mDA markers MAP2 and TH in derived neurons at day 65 of differentiation. **A** Analysis of MAP2 positive cells among DAPI stained cells. **B** Analysis of TH-positive cells among DAPI stained cells. **C** Analysis of TH positive cells among MAP2 positive cells. Images were analysed with ImageJ software. A total of 1200 nuclei were counted from two images. n= 3, 3, 4, 3, 3, 3 for Control-03, Control-05, Patient 1-04, Patient 1-10, Patient 2-01, and Patient 2-06 respectively. Error bars represent ± SEM. Statistical analysis was performed for all patient and control lines using one-way ANOVA Tukey's multiple comparisons test.

Table 4-2: One-way ANOVA Tukey's multiple comparisons test for MAP2 positive cells.

Tukey's multiple comparisons test	Adjusted p-value	Adjusted p-value	Adjusted p-value
Cell lines	**MAP2**	**TH**	**TH/MAP2**
Control-03 vs. Control-05	0.9999	0.8656	0.5056
Control-03 vs. Patient 1-04	0.8593	0.4205	0.4939
Control-03 vs. Patient 1-10	0.9977	0.9025	0.7633
Control-03 vs. Patient 2-01	0.8017	0.323	0.4617
Control-03 vs. Patient 2-06	0.9929	0.8192	0.7127
Control-05 vs. Patient 1-04	0.944	0.9716	> 0.9999
Control-05 vs. Patient 1-10	> 0.9999	> 0.9999	0.997
Control-05 vs. Patient 2-01	0.9015	0.8997	> 0.9999
Control-05 vs. Patient 2-06	0.9995	> 0.9999	0.999
Patient 1-04 vs. Patient 1-10	0.9818	0.9516	0.9987
Patient 1-04 vs. Patient 2-01	> 0.9999	0.9991	> 0.9999
Patient 1-04 vs. Patient 2-06	0.9928	0.9858	0.9997
Patient 1-10 vs. Patient 2-01	0.9566	0.8623	0.9936
Patient 1-10 vs. Patient 2-06	> 0.9999	> 0.9999	> 0.9999
Patient 2-01 vs. Patient 2-06	0.9772	0.9328	0.9974

4.4.2.2 Derived neuronal Cultures express Proteins characteristic of mature Neurons and contain substantia nigra-like and ventral tegmental-like mDA Neurons and serotonergic Neurons

In order to assess the degree of maturation and subcellular composition of control and patient-derived neuronal cultures, immunofluorescence analysis was performed at day 65 of differentiation. The staining was performed as previously described (**Section 2.2.6.3**). Images were taken with the Multiphoton LSM880 Confocal microscope.

Co-staining for NeuN and TH in Patient and Control mDA neuronal Lines

Immunocytochemistry staining at day 65 was performed on Control-05, Patient 1-04 and Patient 2-01-derived mDA neurons for TH and neuron-specific nuclear protein named neuronal nuclei (NeuN), which is expressed in post-mitotic mature neurons [reviewed in (Gusel and Korzhevskiy 2015)] (**Figure 4-7**). All lines showed high level of NeuN positive cells and co-localisation with TH.

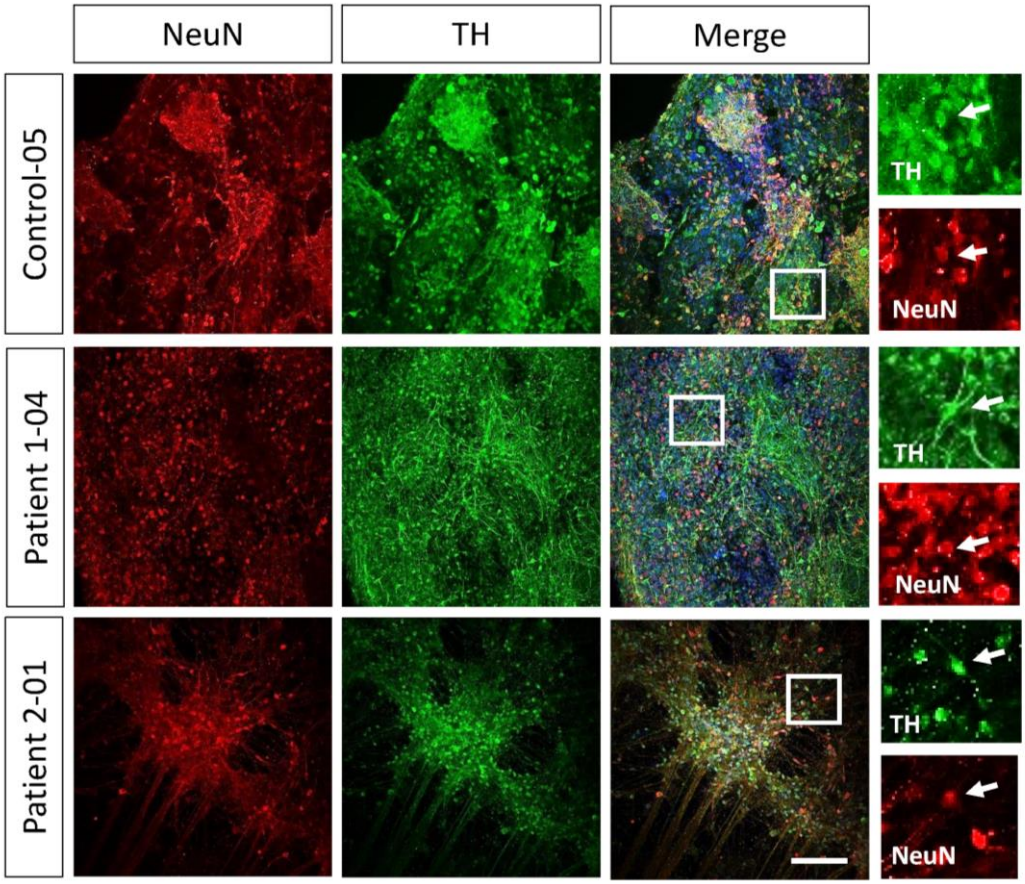

Figure 4-7: Control and patient lines express NeuN co-localising with TH.
Representative images of immunocytochemistry analysis for NeuN (red) and TH (green) on Control-05, Patient 1-04, and Patient 2-01 lines at 65 days of differentiation. Nuclei were contra-stained with DAPI (blue) (arrows indicate co-localisation). Scale bar= 100 µm.

Co-staining for PanNaV and TH in Patient and Control mDA neuronal Lines

To further assess the maturity of the derived mDA neurons, neuronal cultures at day 65 of differentiation were stained with an antibody targeting a common epitope of the voltage-gated sodium channel Nav1.1 (PanNaV). PanNaV is expressed in the mammalian brain and is localised in the axon initial segment and the nodes of Ranvier of neurons. PanNaV aggregates in the axon initial segment and the nodes of Ranvier. With their high density they can support spike initiation. PanNaV is therefore involved in neuronal excitability with control of the generation and propagation of action potentials and indicative of electrical maturity (Duflocq et al. 2008). For all patient

and control lines, co-staining with TH showed expression of sodium voltage gated channels in mDA cultures (**Figure 4-8**).

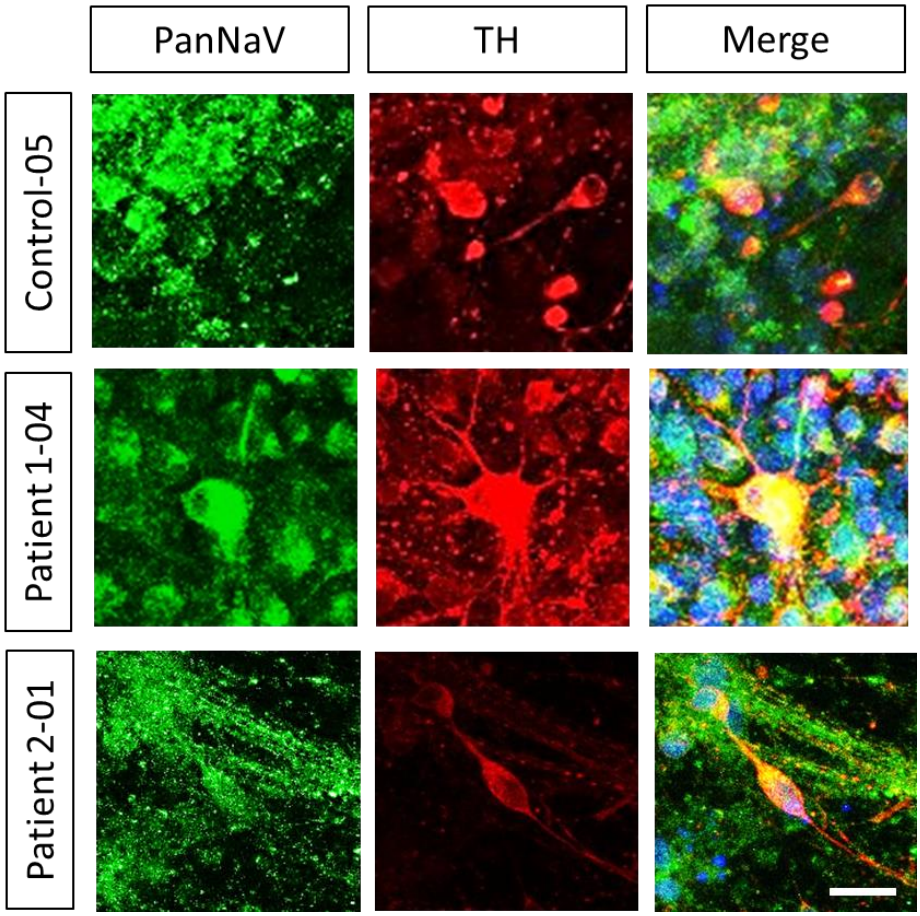

Figure 4-8: Co-staining for PanNaV and TH in control and patient-derived mDA cultures. Representative images of immunocytochemistry analysis for PanNaV (green) and TH (red) in Control-05, Patient 1-04, and Patient 2-01 lines at day 65 of differentiation. Nuclei were contra-stained with DAPI (blue). Scale bar= 10 µm.

Co-staining for GIRK2 and TH for Patient and Control mDA neuronal Lines

The G-protein regulated inward-rectifier potassium 2 (GIRK2) channel is an ion channel influencing the neuronal excitability. GIRK2 is a neuronal marker for the substantia nigra region and the ventral tegmental area (Reyes et al. 2012). Immunocytochemistry analysis for GIRK2 was therefore performed at day 65 in mDA differentiated neurons from Control-05, Patient 1-04, and Patient 2-01 lines. Double immunostaining with TH showed the presence of TH-positive mDA neurons expressing GIRK2 in all three lines (**Figure 4-9**).

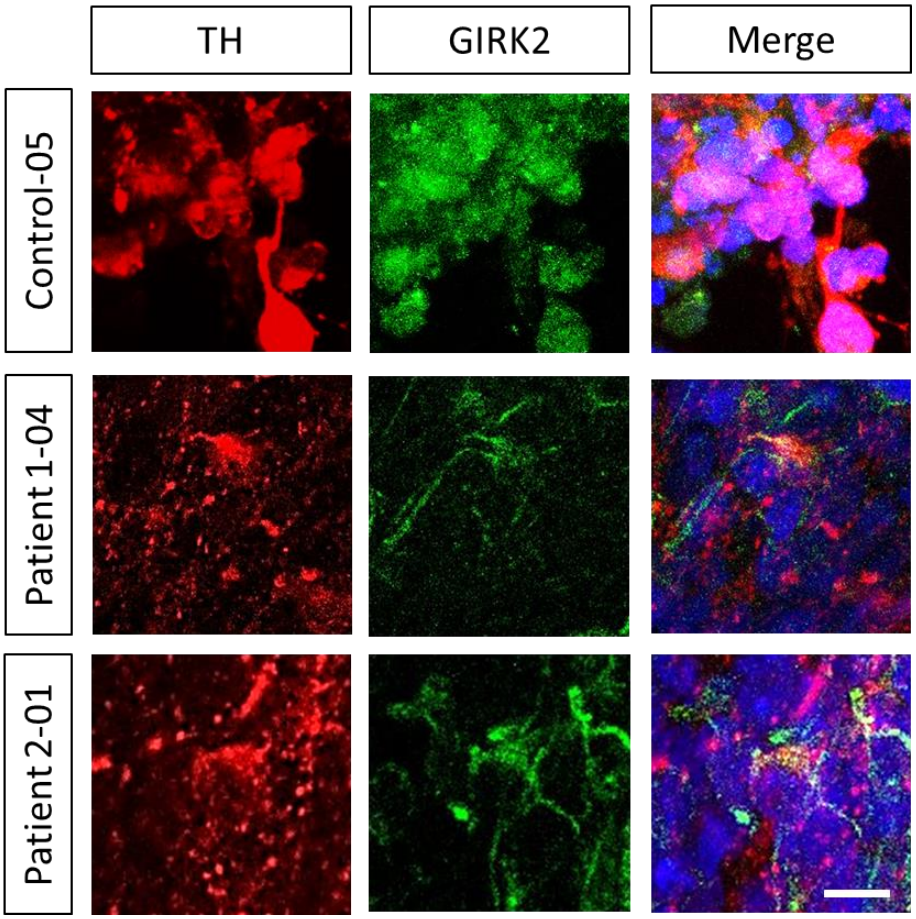

Figure 4-9: Co-staining for TH and GIRK2 in control and patient-derived mDA neurons. Representative images of immunocytochemistry analysis for TH (red) and GIRK2 (green) in Control-05, Patient 1-04 and Patient 2-01 lines. DAPI was used to stain the nuclei (blue). Scale bar= 10 µm.

Co-staining for MAP2 and TPH2 in Patient and Control mDA neuronal Lines

It is well recognised that directed differentiation of iPSCs using the dual SMAD inhibition protocol does not achieve a purely mDA neuronal culture, and indeed, such neuronal culture systems will often harbour other neuronal subtypes, including serotonergic neurons. I undertook immunofluorescence analysis to investigate the presence of a serotonergic neuronal population in control and patient derived cultures. Day 65 mDA derived neurons were stained for tryptophan hydroxylase 2 (TPH2) and MAP2. TPH2 is a brain-expressed enzyme for the conversion of tryptophan to 5-hydroxytryptophan, the precursor of serotonin (Zhang et al. 2004). Immunocytochemistry analysis for TPH2 and MAP2 in control and patient derived neuronal cultures showed co-localisation of the two markers, indicating the presence of serotonergic neurons (**Figure 4-10**).

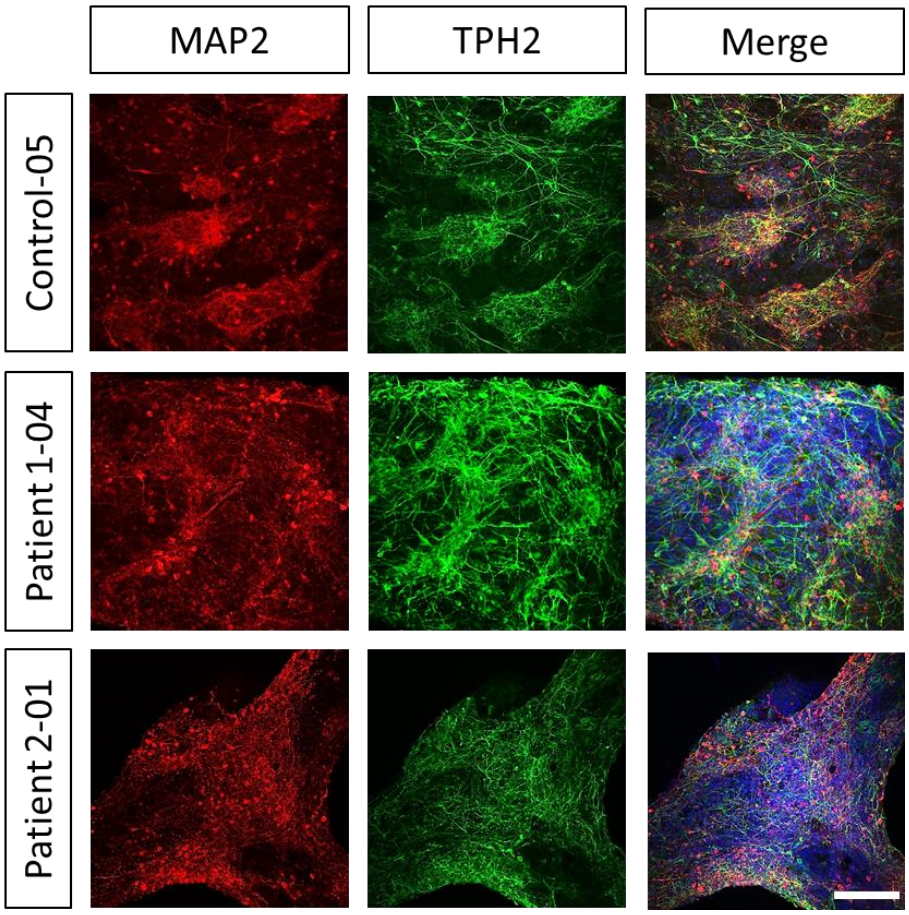

Figure 4-10: Co-staining for MAP2 and TPH2 in control and patient-derived mDA.
Representative images of immunocytochemistry analysis for MAP2 (red) and TPH2 (green) in Control-05, Patient 1-04 and Patient 2-01 lines. DAPI was used to stain the nuclei (blue). Scale bar= 100 µm.

4.4.2.3 Electrophysiology

To further assess the maturity of the derived mDA neurons, electrophysiological analysis was undertaken on control and patient-derived neuronal cultures at day 65 of differentiation. Neuronal maturation and signalling occur through both chemical and electrical transmission. Electrical signals manifest through neuronal membranes in measurable action potentials. An action potential is generated through the rapid change in membrane potential due to the opening of voltage-gated Sodium (Na^+) and Potassium (K^+) channels (Barnett and Larkman 2007), which can be recorded using current clamp recordings.

Whole cell patch clamping was undertaken in order to determine whether control and patient mature derived mDA neurons were able to (1) generate action potentials, (2) drive pacemaker activity characteristic of dopaminergic neurons, and (3) achieve synaptic transmission with spontaneous excitatory post synaptic currents (sEPSC). Whole cell patch clamp recordings were performed by Eleonora Lugarà from the Department of Clinical and Experimental Epilepsy, Queen Square Institute of Neurology, University College London, UK. Images of electrophysiological recordings have been provided by Eleonora Lugarà. I undertook analysis of the electrophysiology data.

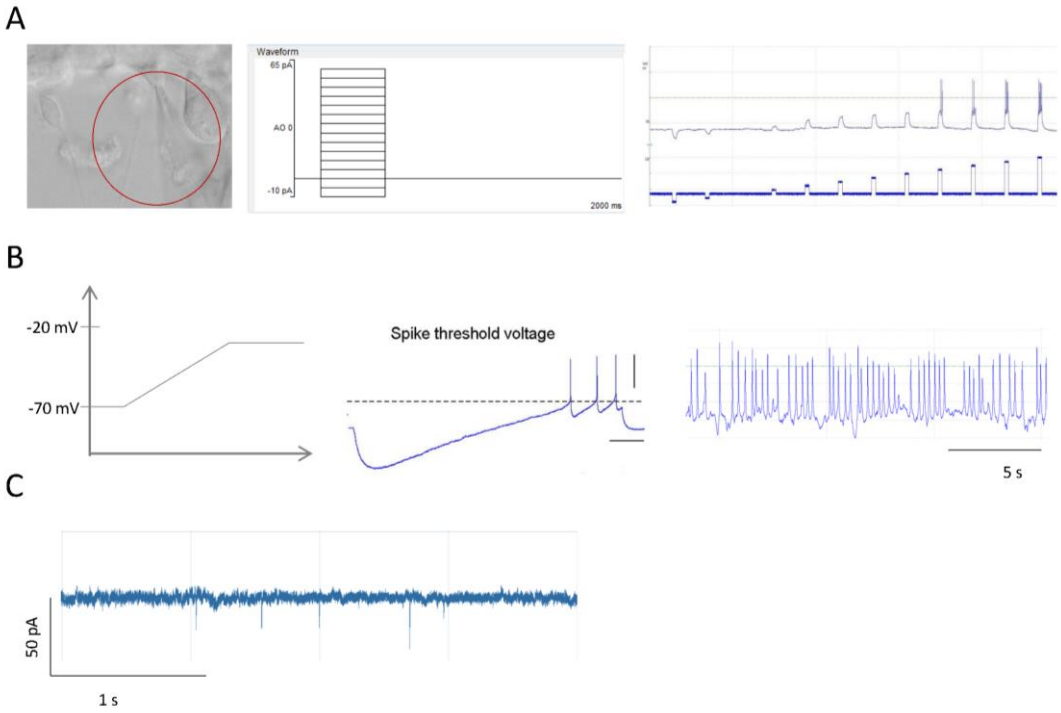

Figure 4-11: Electrophysiology experiments for day 65 derived mDA neurons.
A pA-current clamp, 250 ms current injection, 2 sec/ sweep (from -10pA up to 60pA; step 5pA). **B** Ramp from -70mV up to threshold (range from -50 mV up to -20mV). **C** Voltage clamp mode (cell at -70 mV) in presence of PTX (picrotoxin 30 µM, Gaba-A blocker) in external solution.

The patch clamp recordings were undertaken in 4 stages. Derived neurons were initially patched in voltage clamp mode and the giga seal was checked. After that, three set of analyses were performed (**Figure 4-11**):

1. Injection of current (pA-current clamp) and the recording of voltage change (mV) to test the possible spiking pattern (**Section: Action Potential and Spiking Pattern**) (**Figure 4-11 A**).

2. Injection of a continuous ramp of current to test the pacemaker activity. Manually injection of current from -70 mV up to the spike threshold (**Section: Voltage Ramp reveals significantly fewer Pacemaker Activity Events in Patient 2-01 (but not Patient 1-04) lines when compared to Control-05 derived Neurons**) (**Figure 4-11 B**).

3. Detection of synaptic transmission with sEPSC events in voltage clamp mode (**Section: Spontaneous Excitatory Post Synaptic Current (sEPSC)** (**Figure 4-11 C**).

Action Potential and Spiking Pattern

After injection of currents from - 10 pA to 60 pA (with incremental steps of 5 pA), the voltage change (mV) was recorded in both control and patient lines to determine action potential generation and spiking pattern. This analysis allows investigation of several key factors essential for neuronal electrical activity as follows:

1. Excitability threshold for the generation of an action potential
2. Maximum number of spikes in a single neuron during execution of an action potential
3. Proportion of cells spiking in relation to the total number of patched cells, as an indication of the validity of the experiment
4. Input resistance as an indication of neuronal health and maturity

Excitability Threshold for Control and Patient Neurons is equal

The threshold current (pA) to induce an action potential was similar for both patient lines when compared to the Control-05 line (**Figure 4-12**). The current (pA) (mean ± SEM; p-value) that was necessary to elicit a spike was similar for the Control-05 (45.37 ± 4.90), for Patient 1-04 (40.45 ± 4.76; p=0.481), and for Patient 2-01 (35.00 ± 6.00; p=0.2062).

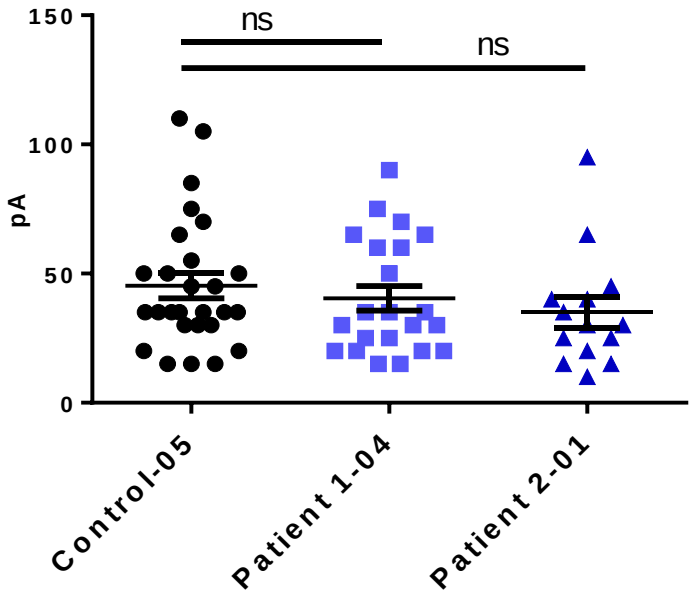

Figure 4-12: Excitability threshold for control and patient lines.
The data points represent the minimal current (pA) injected into the cell to elicit a spike. Three batches of cells were measured for Control-05 (n= 27 cells), Patient 1-04 (n= 22 cells) and Patient 2-01 (n= 14 cells). Error bars represent ± SEM. The patient lines were independently compared to the control using the Student's unpaired, two tailed t-test. ns= non-significant.

Control and Patient-derived Neurons show no difference in Percentage of spiking Cells

Having established the current required to trigger an action potential in the mDA neurons, the number of spiking cells was compared to the total number of patched cells able to generate a spike of action potential (**Figure 4-13**). Analysis revealed that the percentage of spiking cells in AADC deficient Patient 1-04 (96.30 ± 3.70; p=0.2687) and Patient 2-01 (63.97 ± 18.85; p=0.3460) mDA neurons was similar to that in Control-05 (85.61 ± 7.46) derived neurons.

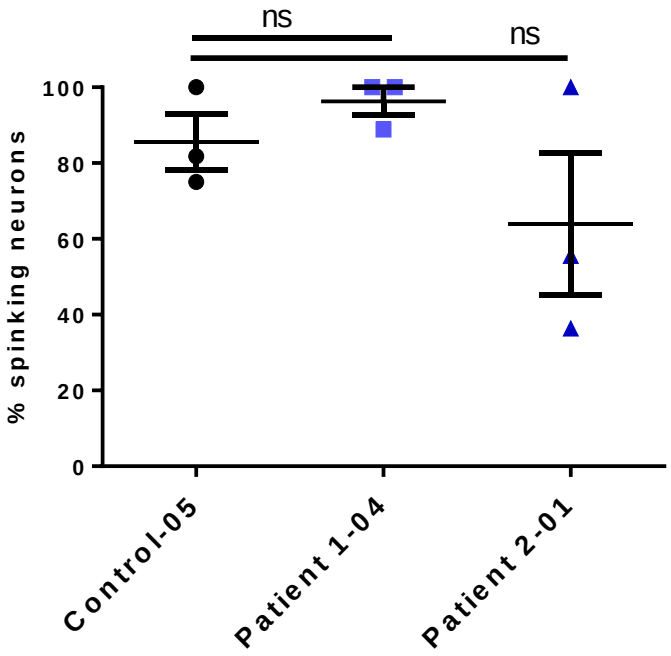

Figure 4-13: Percentage of spiking cells in control and patient mDA neurons.
Control-05 had 27 spiking cells from a total of 32 patched cells, Patient 1-04 had 22 spiking cells of a total of 23 patched cells and Patient 2-01 had 15 spiking cells of a total of 26 patched cells. Error bars represent ± SEM. Patient lines were independently compared to the control using the Student's unpaired, two tailed t-test. ns= non-significant.

The Number of Spikes is significantly higher in Patient 1-04 (but not Patient 2-01) when compared to Control-05 Neurons

Analysis of the maximum number of spikes per neuron was undertaken (**Figure 4-14**). Patient 1-04 derived neurons showed a significantly higher number of spikes (2.77 ± 0.25; p=0.0049) during an action potential when compared to Control-05 neurons (1.85 ± 0.20). In contrast, Patient 2-01 derived neurons (1.80 ± 0.28; p=0.8785) showed no significant difference when compared to Control-05.

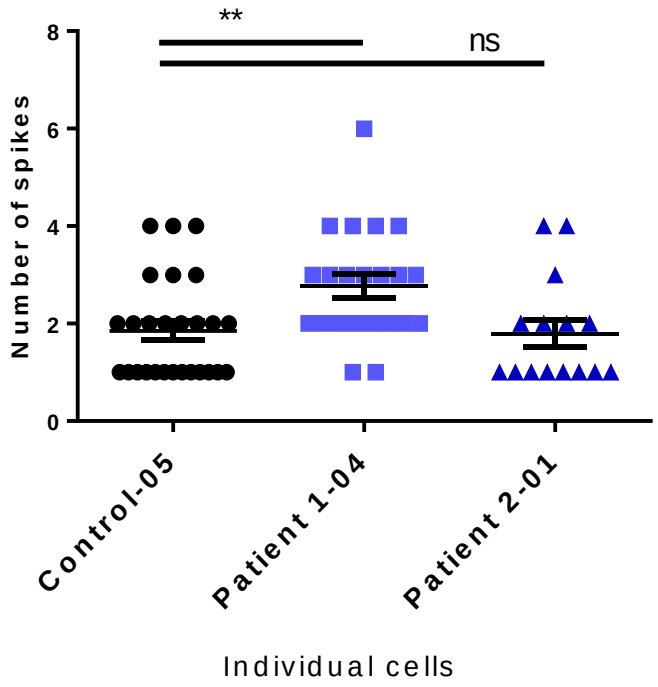

Figure 4-14: Number of spikes per stimulated neuron in patient and control neurons.
The maximum number of spikes during an action potential was measured for Control-05, Patient 1-04 and Patient 2-01 derived neurons (n= 27, 22, 15 respectively). Three batches of cells were measured for each cell line. Error bars represent ± SEM. The patient lines were independently compared to the control using the Student's unpaired, two tailed t-test. *indicates statistically significant differences: ** p<0.01; ns= non-significant.

Input Resistance is similar in all Patient and Control Neurons

The input resistance provides information about the open or closed state of voltage-gated channels. With Ohm's law ($R = \frac{V}{I}$) the input resistance (R) shows how much current (I) is needed to change the membrane voltage (V). Several cellular characteristics can determine membrane resistance, as follows (Ohm 1827; Squire et al. 2008):

- Cell size: as cell surface area increases, resistance decreases.
- Open ion channels: conductance $g = \frac{1}{R}$ is greater when ion channels are open, therefore with an increase in the number of open ion channels, resistance decreases.
- Synaptic input: reduced synaptic input results in less current injection, leading to higher input resistance.

Input resistance (MOhm) was similar for both control and patient mDA neurons (**Figure 4-15**). No significant differences were observed between Patient 1-04 (1,089 ± 166.1; p=0.2250), Patient 2-01 (1,518 ± 273.1; p=0.5891) and Control-05 derived neurons (1,363 ± 148.2) (mean ± SEM; p-value).

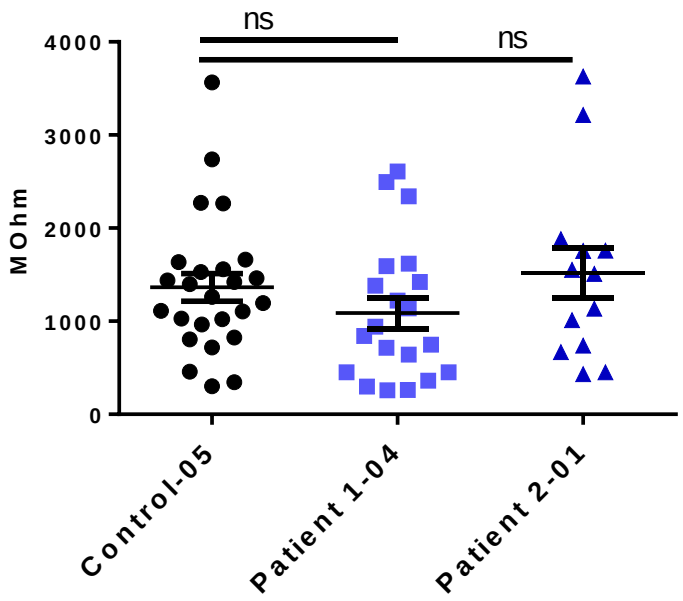

Figure 4-15: Input resistance in control and patient lines.
Input resistance (MOhm) recorded in Control-05 (n= 25), Patient 01-04 (n= 20) and Patient 2-01 (n= 13) derived neurons. Error bars represent ± SEM. Patient lines were independently compared to the control using Student's unpaired, two tailed t-test. ns= non-significant.

Voltage Ramp reveals significantly fewer Pacemaker Activity Events in Patient 2-01 (but not Patient 1-04) lines when compared to Control-05 derived Neurons

Pacemaker activity is defined as the ability of a neuron to generate rhythmic bursting activity. It has a characteristic pattern in dopaminergic neurons. Continuous ramp of current was injected into the cells and the rhythmic activity measured (**Figure 4-16**). Data analysis showed that Patient 2-01 lines had significantly fewer cells with pacemaker activity (8.59 ± 4.82; p=0.0477) than Control-05 (28.28 ± 5.05). No differences were seen between Patient 1-04 (27.51 ± 14.84; p=0.9632) and Control-05 (mean ± SEM; p-value).

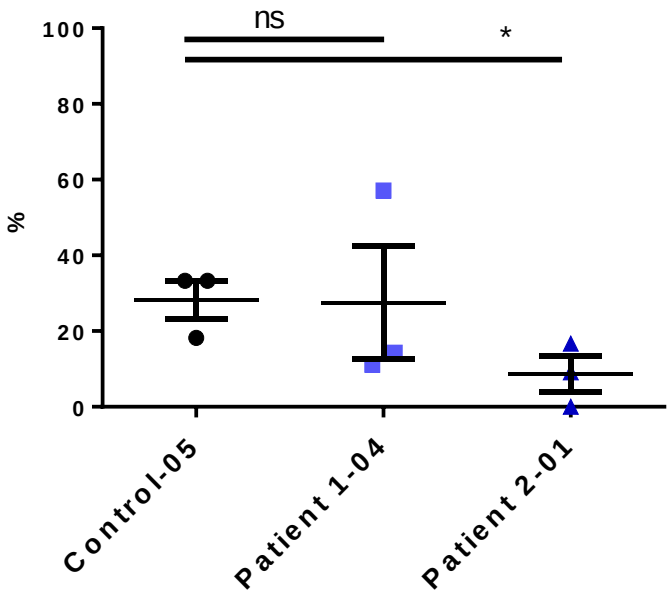

Figure 4-16: Percentage of cells with pacemaker activity in control and patient lines.
The percentage of cells with pacemaker activity following injection of a current ramp was recorded. Three batches of cells were measured for control and patient neurons. For every batch and cell line, the number of cells with pacemaker activity was divided by the total number of patched cells: Control-05 had 9 cells that showed pacemaker activity from a total of 32 patched cells; Patient 1-04 had 6 cells with pacemaker activity from a total of 23 patched cells; Patient 2-01 line had 2 cells with pacemaker activity from a total of 26 patched cells. Error bars represent ± SEM. Samples were compared with Student's unpaired, two tailed t-test. *indicates statistically significant differences: * p<0.05; ns= non-significant.

Spontaneous Excitatory Post Synaptic Current (sEPSC)

In order to investigate synaptic transmission, sEPSC were recorded in voltage clamp mode for both control and patient lines. We then investigated frequency of sEPSC.

The Frequency of sEPSC are similar in both Control and Patient Lines

No differences were observed between Control-05 (0.71 ± 0.15) and Patient 1-04 (1.04 ± 0.21; p=0.2128), and Patient 2-01 (1.22 ± 0.37; p=0.2346) derived neurons (mean ± SEM; p-value) (**Figure 4-17**).

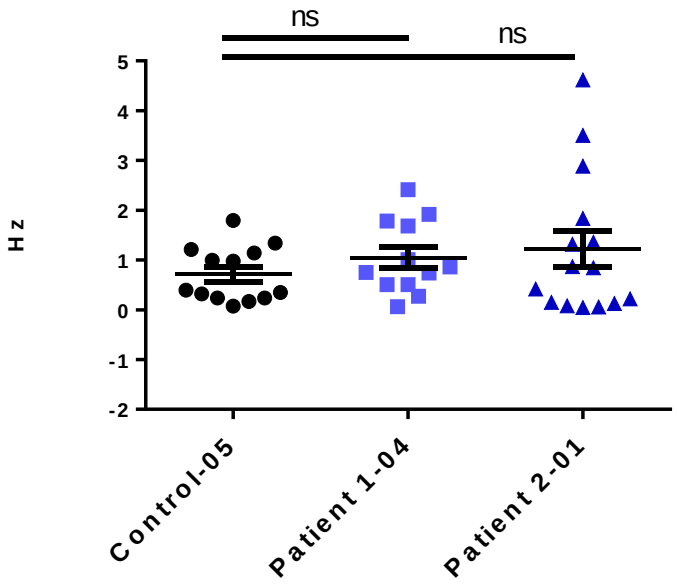

Figure 4-17: Frequency of events of sEPSC in control and patient lines.
sEPSC events recorded in Control-05, Patient 1-04 and Patient 2-01 (n= 13, 12, 15 respectively). Error bars represent ± SEM. Patient lines were independently compared to the control using the Student's unpaired, two tailed t-test. ns= non-significant.

4.4.2.4 Summary of mature mDA neuronal Characterisation

In summary, I have successfully differentiated both control and patient iPSC lines into mature derived mDA neurons. Both control and patient lines have similar levels of TH/MAP2 neurons to that reported in the literature (Kirkeby, Grealish, et al. 2012) confirming that there is no evidence of neurodegeneration in mDA cultures derived from patients with AADC deficiency. All lines also reached neuronal maturity, as detected by the expression of the neuronal nuclei marker NeuN, and Na^+ voltage-gated channel. Moreover, derived cells present with a dopaminergic identity similar to mDA neurons present in the SNpc. As expected, *in vitro* neuronal cultures were characterised by presence of serotonergic neurons expressing TPH2. Electrophysiological analysis confirmed the maturation stage of the derived neurons from iPSC lines.

Chapter 5
Investigation of Disease-Specific Features in the AADC Deficiency Cell Model

5.1 Introduction

This chapter will focus on investigating AADC deficiency specific features in patient-derived mDA neurons. In order to correlate the AADC iPSCs-derived *in vitro* model with findings observed in AADC patients, two main assays were performed: AADC enzymatic activity and High-Performance Liquid Chromatography (HPLC) analysis of dopamine metabolites. Moreover, downstream effects of AADC deficiency on AADC, TH and MAOA, enzymes (involved in dopamine synthesis and degradation), were analysed in Control-05, Patient 1-04 and Patient 2-01 derived mDA culture after 65 days of differentiation.

5.2 Hypothesis

mDA neurons differentiated from AADC deficiency patient-derived iPSCs are a useful *in vitro* tool to elucidate a disease-specific cellular phenotype.

5.3 Aims

1. To investigate whether patient-derived neurons recapitulate key features of the disease phenotype observed in human patients
2. To investigate in patient-derived neurons the mechanisms underlying AADC deficiency

5.4 Results

5.4.1 Identification of the phenotype of AADC deficient neurons

Following completion of basic characterisation of the generated mDA neurons, I then sought to investigate disease-specific phenotypes in the cellular model of AADC deficiency.

5.4.1.1 Marked Reduction in AADC Enzyme Activity is evident in Patient Lines when compared to Control Lines

In order to investigate the effect of *DDC* mutations on AADC enzyme activity, I undertook an AADC enzyme activity assay, as described in **Section 2.2.8**.

A significant reduction in L-dopa-induced AADC enzyme activity (pmol/min/mg protein) (mean ± SEM; p-value) was observed for both patient lines when compared to the control (Patient 1-04 line: 15.61 ± 5.04; p=0.0025; Patient 2-01 line: 77.71 ± 21.61; p=0.0146; Control-05 line: 1,532 ± 294.4) (**Figure 5-1**).

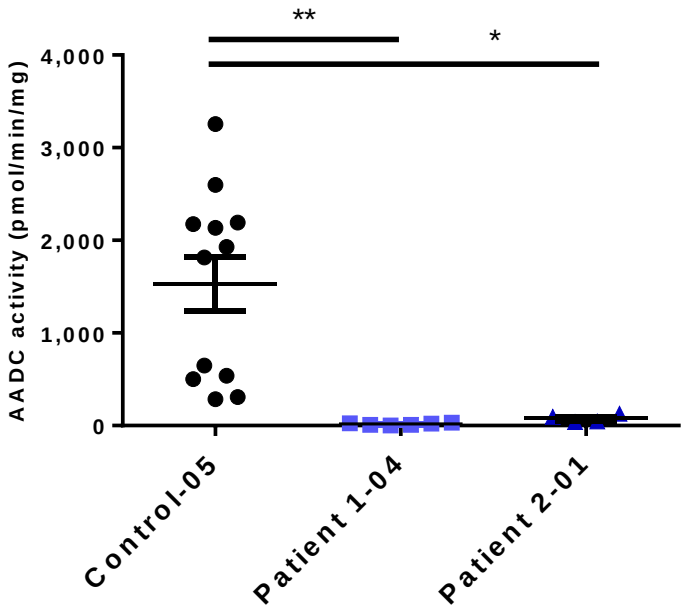

Figure 5-1: AADC enzyme activity for control and patient lines.
AADC enzyme activity (pmol/min/mg) was determined for Control-05, Patient 1-04 and Patient 2-01 lines. Error bars represent ± SEM. Control and patient lines were compared using the Student's unpaired, two tailed t-test. *indicates statistically significant differences when comparing: * $p<0.05$; ** $p<0.01$.

5.4.1.2 Disease-specific Dysregulation of key Monoamine Precursors and Metabolites is evident in patient-derived mDA Neurons

In order to investigate the effects of AADC deficiency on dopamine synthesis, analysis of extracellular levels of dopamine, DOPAC and 3-OMD was undertaken by HPLC (as described in **Section 2.2.9**) in control and patient-derived mDA neurons at day 65 of differentiation. HPLC was undertaken by Haya Alrashidi (UCL GOS-ICH). Analysis of dopamine levels showed complete absence of this neurotransmitter in Patient1-04 and Patient 2-01 neurons, whilst detectable in Control-05 neuronal cell cultures (Patient 1-04 line: 0.00 ± 0.00; p=0.0001; Patient 2-01 line: 0.00 ± 0.00; p=0.0001; Control-05 line: 122.2 ± 7.98). Given the relative instability of dopamine in

physiological pH conditions (Mani and Ryan 2009; Raley-Susman et al. 1991; Schwiening and Boron 1994; Vincent, TenBroeke, and Maiese 1999) (which may have affected the levels recorded on HPLC), I extended my analysis to investigate DOPAC levels in control and patient lines. The monoamine oxidase enzyme catalyses dopamine into DOPAC, which is a stable metabolite, and therefore more reflective of dopamine turnover. When measuring levels of DOPAC in derived mDA neuronal cultures, I observed a significant decrease in DOPAC levels in patient lines when compared to controls (Patient 1-04 line: 109.4 ± 22.08; p=0.001; Patient 2-01 line: 111.5 ± 7.95; p=0.0009; Control-05 line: 480.2 ± 45.48). I also analysed levels of 3-OMD to determine whether accumulation of 3-OMD, as observed in patient CSF analysis, was recapitulated in the patient mDA. Both Patient 1-04 and Patient 2-01 derived neuronal cultures showed significantly increased levels of extracellular 3-OMD when compared to Control-05 (Patient 1-04 line: 632.3 ± 220.4; p=0.0187; Patient 2-01 line: 656.7 ± 281.9; p=0.0387; Control-05 line: 0.00 ± 0.00) (**Figure 5-2**).

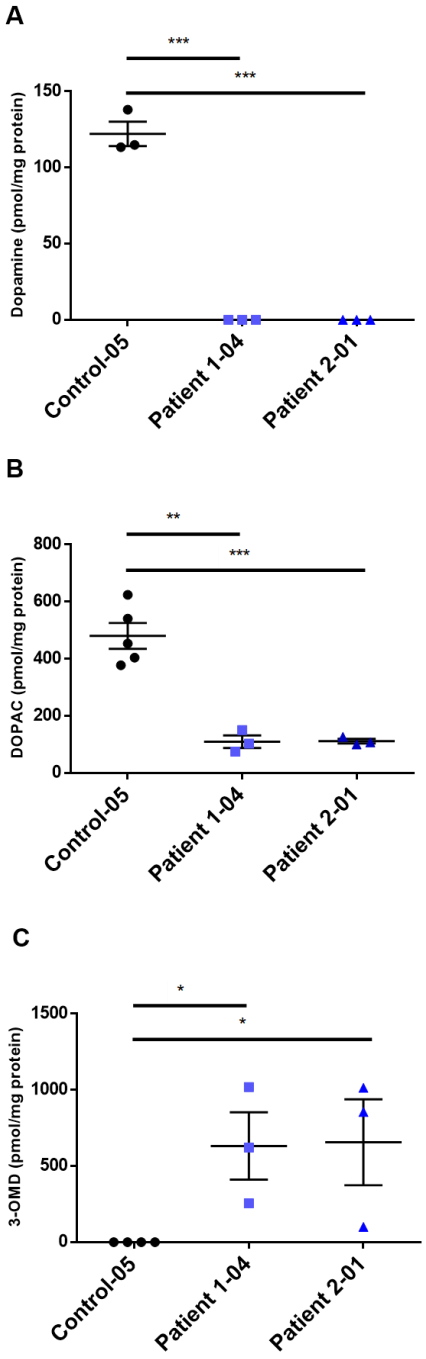

Figure 5-2: HPLC detection of extracellular dopamine, DOPAC and 3-OMD in control and patient lines.

Concentrations of dopamine, DOPAC and 3-OMD (pmol/mg, mean ± SEM; p-value) were measured by HPLC. **A** Dopamine values in Control-05, Patient 1-04 and Patient 2-01 derived neuronal cultures at 65 days of differentiation (n= 3 for each). **B** DOPAC levels in Control-05, Patient 1-04 and Patient 2-01 derived neuronal cultures at 65 days of differentiation (n= 5, 3, 3 respectively). **C** 3-OMD levels in Control-05, Patient 1-04 and Patient 2-01 derived neuronal cultures at 65 days of differentiation (n= 4, 3, 3 respectively). Error bars represent ± SEM. Control-05 and the Patient-01 or Patient 2-01 were compared using the Student's unpaired, two tailed t-test. *indicates statistically significant differences: * $p<0.05$; ** $p<0.01$; *** $p<0.001$.

5.4.1.3 Disease-specific Dysregulation of *DDC*, *TH*, and *MAOA* Gene Expression is evident in patient-derived mDA Neurons

In order to investigate the downstream effects of AADC deficiency on dopamine metabolism, I analysed gene expression levels of key enzymes involved in the dopamine synthesis pathway (*DDC, TH, MAOA)* in both control and patient derived dopaminergic cultures by Real-Time Quantitative Reverse Transcription Polymerase Chain Reaction (qRT-PCR) (**Section 2.2.9**). After 65 days of differentiation Patient 2-01 lines showed significantly lower levels of *DDC* gene expression when compared to the Control-05 line, no difference in AADC expression was observed for Patient 1-04 when compared to the Control-05 (mean ± SEM; p-value) (Patient 1-04 line: 1.51 ± 0.24; p=0.2008; Patient 2-01 line: 0.66 ± 0.19; p=0.0189; Control-05 line: 2.57 ± 0.53) (**Figure 5-3**). The reasons for these observed phenotypic differences are not clear, though may be related to the different patient genotypes. It is possible that the missense variant harboured by Patient 1 may not affect *DDC* gene expression. For Patient 2, a compound heterozygote with a stop mutation and missense variant, it is conceivable that the loss-of-function variant may lead to nonsense mediated decay, thereby lowering *DDC* gene expression levels.

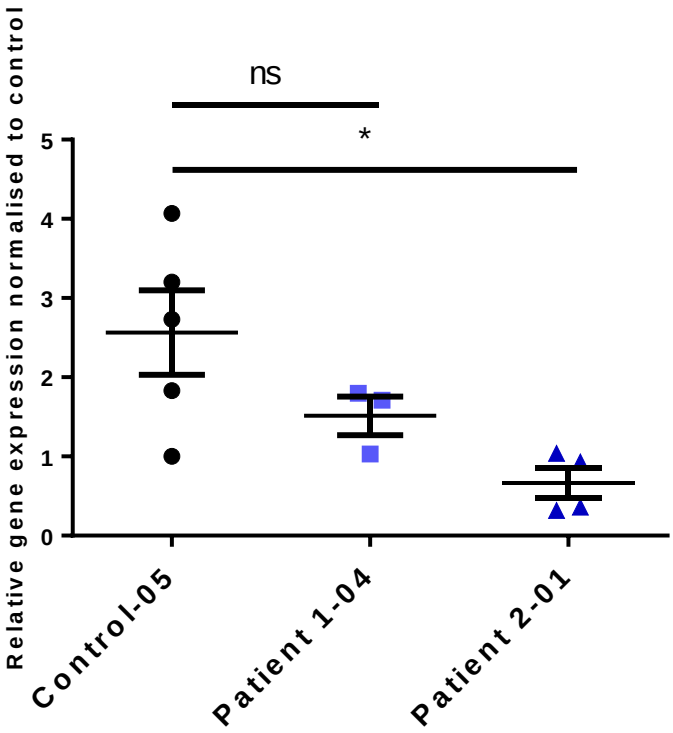

Figure 5-3: *DDC* gene expression for control and patient lines.
qRT-PCR for *DDC* expression was undertaken for Control-05, Patient 1-04 and Patient 2-01 mDA neurons at day 65 of differentiation (n= 5, 3, and 4 respectively). Values are relative to *GAPDH* and normalised to Control-05. Samples were independently compared to the control with the Student's unpaired, two tailed t-test. Error bars represent ± SEM. *indicates statistically significant differences: * $p<0.05$; ns= non-significant.

qRT-PCR analysis of *TH* gene expression in derived mDA neurons showed significantly reduced levels in Patient 1-04, while Patient 2-01 showed upregulation of *TH* (Patient 1-04 line: 0.27 ± 0.15; p=0.0279; Patient 2-01 line: 12.91 ± 2.49; p=0.0075; Control-05 line: 3.07 ± 0.76) when compared to Control-05 (**Figure 5-4**). The differential regulation of *TH* expression between the two patient lines could be downstream effect of *DDC* patient-specific expression.

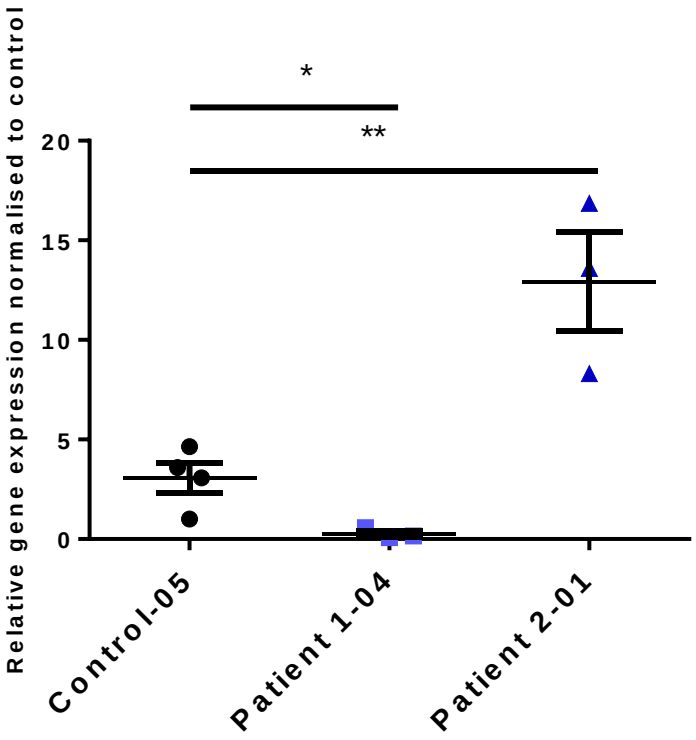

Figure 5-4: *TH* gene expression in control and patient lines.
TH gene expression was analysed with qRT-PCR for Control-05, Patient 1-04 and Patient 2-01 derived mDA at day 65 of differentiation (n= 4, 3, and 3 respectively). Values are relative to *GAPDH* and normalised to Control-05. Patients were independently compared to the control with the Student's unpaired, two tailed t-test. Error bars represent ± SEM. *indicates statistically significant differences: * $p<0.05$; ** $p<0.01$.

Analysis of *MAOA* gene expression in mDA neurons was also undertaken, showing reduced levels in both patient lines when compared to the control (**Figure 5-5**). Both Patient 1-04 and Patient 2-01 had statistically significant lower levels of *MAOA* (Patient 1-04 line: 0.45 ± 0.04; p=0.0275; Patient 2-01 line: 0.37 ± 0.05; p=0.0004; Control-05 line: 1.78 ± 0.39) compared to Control-05.

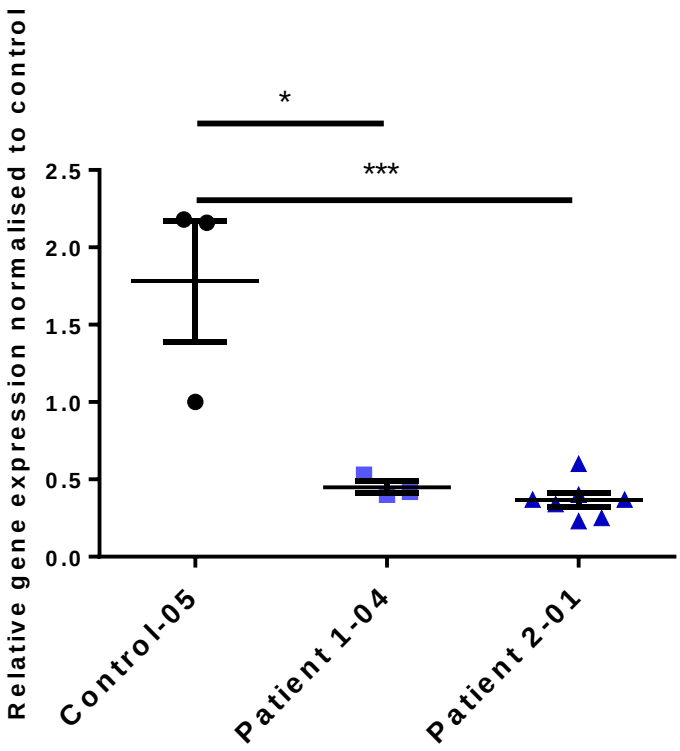

Figure 5-5: *MAOA* gene expression in control and patient lines.
qRT-PCR analysis of relative *MAOA* gene expression in Patient 1-04, Patient 2-01, and Control-05 mDA differentiated neurons (n= 3, 3, and 7 respectively). Patients were independently compared to the control with the Student's unpaired, two tailed t-test. Error bars represent ± SEM. *indicates statistically significant differences: * p<0.05; *** p<0.001.

5.4.1.4 Dysregulation of the Proteins AADC, TH, and MAOA is evident in AADC deficient mDA Neurons

I then extended my analysis of dopaminergic proteins with immunoblotting studies to determine whether there were disease-specific aberrations in protein expression.

Western Blotting for AADC protein was undertaken for Control-05, Patient 1-04, and Patient 2-01 derived neurons at day 65 of differentiation by myself with assistance from Giada Rossignoli (University of Verona, Italy, Department of Neuroscience, Biomedicine and Movement) (**Section 2.2.6.4**). Analysis showed differential expression of AADC protein in patient-derived neurons when compared to the control line. A significant increase in AADC protein was detected in Patient 1-04 cells (Patient 1-04 line: 1.37 ± 0.11; p=0.0132; Control-05 line: 0.95 ± 0.10) when compared to the Control-05 line. In contrast, Patient 2-01 derived neurons show significantly lower AADC protein levels when compared to the Control-05 line (Patient 2-01 line: 0.12 ± 0.03; p<0.0001; Control-05 line: 0.95 ± 0.10) (**Figure 5-6**).

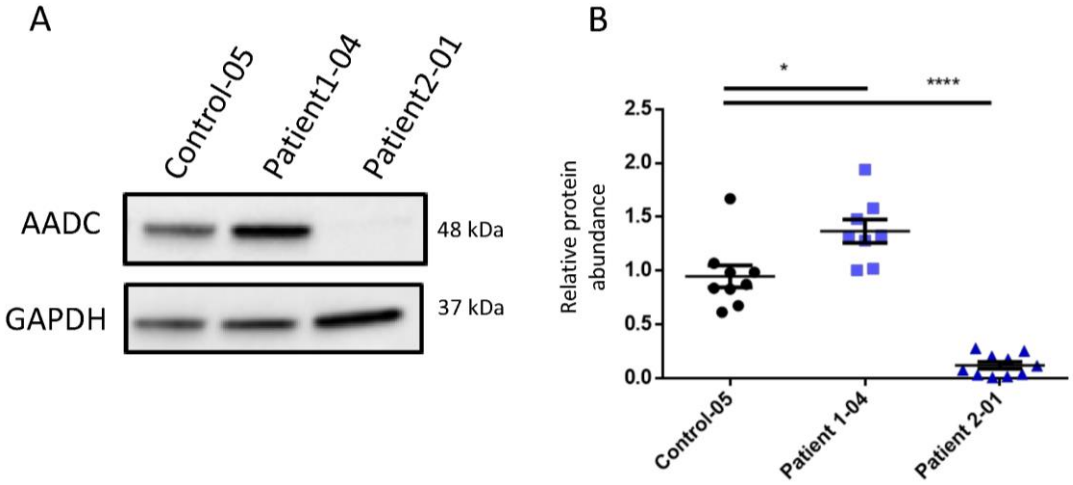

Figure 5-6: Immunoblotting studies and quantification of AADC protein in control and patient lines.
A Representative image of immunoblot for the AADC protein (48 kDa) and loading control, GAPDH (37 kDa) from total cell lysates extracted on day 65 of differentiation from Control-05, Patient 1-04, and Patient 2-01. **B** Densitometry immunoblot analysis for AADC protein in Control-05, Patient 1-04, and Patient 2-01, normalised to loading control GAPDH (n= 9, 8, 10 respectively). Error bars represent ± SEM. Significance was determined using the Student's unpaired, two tailed t-test. *indicates statistically significant differences: * p<0.05; *** p<0.001.

Analysis of TH protein levels in Control-05, Patient 1-04, and Patient 2-01 showed a significant reduction of TH levels in Patient 1-04 derived dopaminergic neurons when compared to Control-05 (Patient 1-04 line: 0.11 ± 0.03; p=0.0001; Control-05 line: 3.45 ± 0.67). A significant decrease in TH protein levels was also observed for Patient 2-01 line (Patient 2-01 line: 1.74 ± 0.27; p=0.0229; Control-05 line: 3.45 ± 0.67) (though to a lesser extent than that observed for Patient 1-04) when compared to the Control-05 line (**Figure 5-7**).

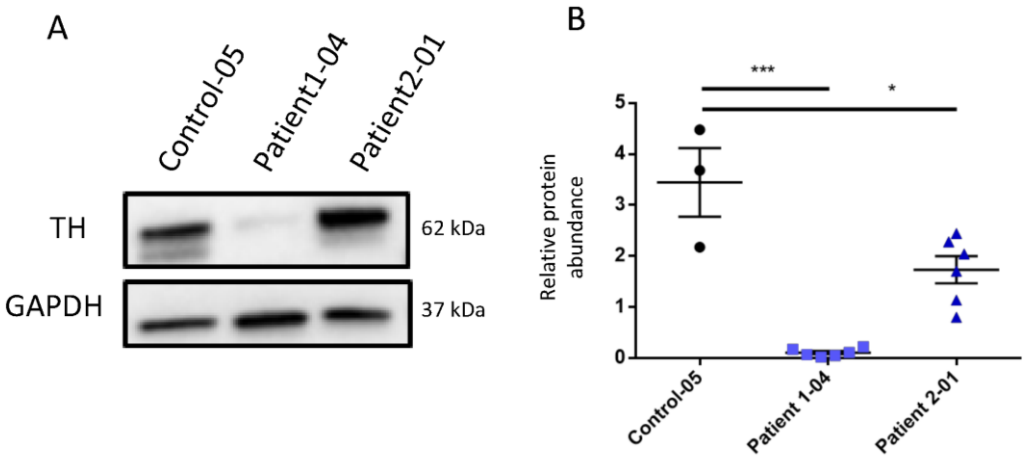

Figure 5-7: Immunoblotting studies and quantification of TH protein in control and patient lines. **A** Representative immunoblot for TH protein (62 kDa) and loading control GAPDH (37 kDa) from total cell lysates extracted on day 65 of differentiation from Control-05, Patient 1-04, and Patient 2-01. **B** Densitometry analysis of immunoblot for Control-05, Patient 1-04, and Patient 2-01 (n= 3, 6, 6 respectively). Error bars represent ± SEM. Significance was determined using the Student's unpaired, two tailed t-test. *indicates statistically significant differences: * $p<0.05$; *** $p<0.001$.

Western Blotting for MAOA also showed significantly decreased levels of MAOA protein in mDA neurons generated from Patient 1-04 (Patient 1-04 line: 0.79 ± 0.16; p=0.0082; Control-05 line: 1.81 ± 0.13) and Patient 2-01 lines (Patient 2-01 line: 0.50 ± 0.13; p=0.0021; Control-05 line: 1.81 ± 0.13) when compared to Control-05 (**Figure 5-8**).

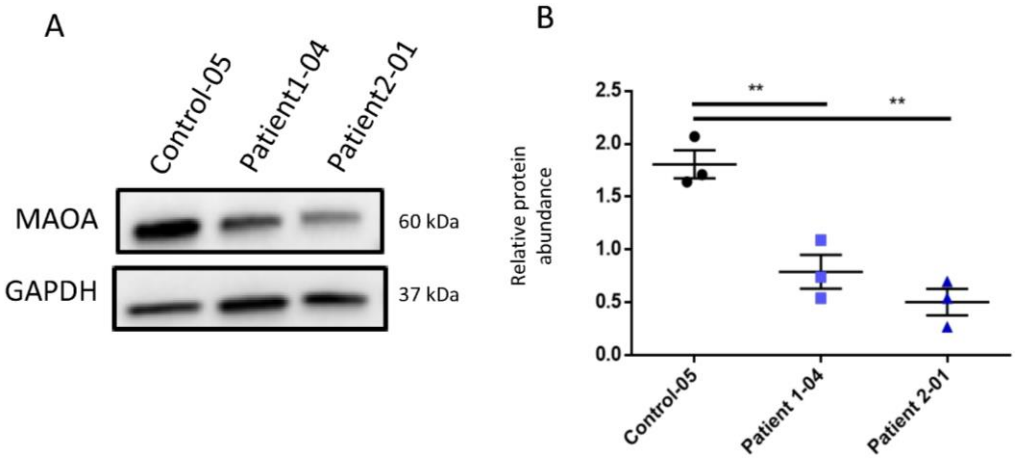

Figure 5-8: Immunoblotting studies and quantification of MAOA protein in control and patient lines.
A Representative immunoblot for TH protein (60 kDa) and loading control GAPDH (37 kDa) from total cell lysates extracted on day 65 of differentiation from Control-05, Patient 1-04, and Patient 2-01 lines. **B** Immunoblot densitometry analysis of TH protein for Control-05, Patient 1-04, and Patient 2-01 (n= 3, 3, 3 respectively). Error bars represent ± SEM. Significance determined using the Student's unpaired, two tailed t-test. *indicates statistically significant differences: ** p<0.01.

5.4.1.5 Summary

In this chapter, I have defined the phenotype of AADC deficiency in day 65 mDA neurons at a gene and protein level, as well as with the AADC enzyme activity assay. I have showed that firstly, at mature stage, patient derived neuronal cultures show a significant decrease in AADC enzymatic activity, exactly as observed in patient plasma samples. Secondly, in line with analysis of dopamine metabolites performed in patients CSF, AADC iPSCs-derived neurons show dysregulation of dopamine, DOPAC and 3-OMD. Thirdly, I have shown gene and protein dysregulation of AADC, TH and MAOA in patient-derived mDA neurons.

Chapter 6
Investigating Therapeutic Approaches for AADC Deficiency

6.1 Introduction

Although gene therapy is increasingly a reality for patients with AADC deficiency [(Chien et al. 2017; Hwu et al. 2012; Kojima et al. 2019); and (https://clinicaltrials.gov/ct2/show/NCT02852213), **Section 1.3.5.2**], the cellular effects of such *DDC* overexpression remain yet to be fully elucidated. I therefore planned to investigate a lentiviral gene-therapy approach in my mDA model of AADC deficiency. This chapter will describe in first instance, the generation and validation of the *DDC*-expressing lentivirus construct. Preliminary data regarding the effects of gene transfer in patient-derived mDA neurons will also be presented.

6.2 Hypothesis

Gene therapy is an emerging treatment for patients with AADC deficiency. I hypothesise that the effects of AADC deficiency in patient-derived mDA neurons can be reversed via ectopic expression of human *DDC* using a lentivirus vector delivery system in the cellular model.

6.3 Aims

1. To generate a neuronal-specific lentivirus construct expressing either EGFP (mock) or DDC-EGFP with human synapsin promoter
2. To transfect and culture patient mDA cell lines with these lentivirus constructs
3. To achieve rescue of AADC enzyme activity in patient-derived mDA neurons using the AADC activity assay and HPLC analysis of key dopaminergic metabolites

6.4 Results

6.4.1 Generation of Lentiviral Constructs for Gene Transfer Experiments

6.4.1.1 Cloning of *DDC* into the DAT Plasmid Backbone

The human *DDC* lentivirus gene construct (**Figure 6-2**) was prepared as described in **Section 2.2.10.1**, starting from the DAT plasmid construct. The mock plasmid (**Figure 6-1**) was kindly provided by Dr Joanne Ng (UCL, Institute of Women's Health). Several components were present in the mock plasmid sequence, including

- The generic human cytomegalovirus (CMV) immediate early promoter which is expressed transiently
- The truncated 5' long terminal repeat (5'LTR) from HIV-1, that acts as the promoter for synthesis of viral RNA
- ψ is the packaging signal of HIV-1
- The Rev response element (RRE) of HIV-1, which allows for Rev-dependent mRNA export from the nucleus to the cytoplasm
- The central polypurine tract (cPPT) of HIV-1, which helps with the transduction into non-dividing cells and gene transfer efficiency
- The human synapsin promoter (hSYN) is a neuronal promoter driving gene expression
- The enhanced green fluorescent protein (EGFP) is the reporter gene for visual detection
- The woodchuck hepatitis virus posttranscriptional regulatory element (WPRE) enhances viral RNA stability for higher titres
- The self-inactivating 3'long terminal repeat (3'LTR ΔU3) from HIV-1 terminates upstream transcript production
- The simian virus 40 polyadenylation signal (SV40pA) supports transcriptional termination
- And NeoR/KanR confers resistance to the antibiotics neomycin and kanamycin

The *DDC* plasmid construct contained in addition

- The human *DDC* gene (*hDDC)*
- And the Internal Ribosome Entry Site (IRES) which uses ribosomes and is involved in cap-independent translation, linking the two coding sequences (*DDC* and *EGFP*) which allows the translation of both proteins

Dr John Counsell (UCL GOS-ICH) provided additional support and advice, as needed for this part of my project. All experiments were performed by me, unless otherwise stated.

After the *hDAT* gene was removed from the DAT plasmid, the human *DDC* gene was cloned between the hSYN promoter and the IRES. Sanger sequencing was performed in order to confirm the presence and correct ordering of the complete human synapsin (hSYN) promoter, and the *EGFP* reporter gene in the mock plasmid (pCCL-hSYN-EGFPv2JN) (**Figure 6-1**), and hSYN promoter, *DDC* gene, Internal Ribosome Entry Site sequence (IRES), and *EGFP* reporter gene in the *DDC* plasmid (pCCL-hSYN-DDC-IRES-EGFP) (**Figure 6-2**).

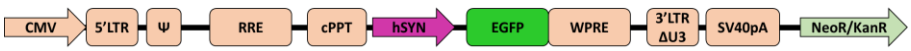

Figure 6-1: Confirmed mock plasmid (pCCL-hSYN-EGFPv2JN).
CMV= human cytomegalovirus immediate early promoter, 5'LTR= truncated 5' long terminal repeat, ψ= packaging signal, RRE= Rev response element, cPPT= central polypurine tract, hSYN= human synapsin promoter, EGFP= enhanced green fluorescent protein, WPRE= woodchuck hepatitis virus posttranscriptional regulatory element, 3'LTR ΔU3= self-inactivating 3'long terminal repeat, SV40pA= simian virus 40 polyadenylation signal, NeoR/KanR= neomycin and kanamycin antibiotic resistance.

Figure 6-2: Confirmed *DDC* plasmid (pCCL-hSYN-DDC-IRES-EGFP).
Same as the mock plasmid (**Figure 6-1**) with the addition of *hDDC*= human *DDC* gene, and IRES= Internal Ribosome Entry Site sequence.

6.4.1.2 Identification of Multiplicity of Infection for HEK-293T cells

In order to establish multiplicity of infection (MOI) values for the generated viral constructs, incremental vector titres were assessed by transducing HEK 293T cells and quantifying the total number of integrated genomes per cell using a qRT-PCR assay (**Section 2.2.10.3, Lentiviral Vector Titration by qPCR**). Results are presented in **Table 6-1**.

Table 6-1: Vector titres (µl) for MOI of 10, 5, and 1 in DDC and mock lentiviral constructs.

	MOI 10	**MOI 5**	**MOI 1**
***DDC* lentivirus**	16.31 µl	8.16 µl	4.08 µl
Mock lentivirus	13.84 µl	6.92 µl	3.46 µl

6.4.1.3 Validation of Gene Transfer Efficacy through AADC Protein Immunoblotting

In order to confirm successful integration of the *DDC*-plasmid into the viral particle, immunoblotting was performed to evaluate AADC protein expression after *DDC* lentivirus infection into an ectopic system not expressing endogenous AADC enzyme. HEK 293T cells were infected with either pCCL-hSYN-DDC-IRES-EGFP or pCCL-hSYN-EGFPv2 with a high (10 µl) and low (2 µl) virus dose. Immunoblotting analysis for AADC protein was undertaken as previously described (**Section 2.2.6.4**). A strong AADC protein band was detected in lysates extracted from HEK 293T cells infected with both 10 µl and 2 µl of *DDC* lentivirus. In contrast no AADC protein was detected in cells infected with mock lentivirus (**Figure 6-3 A and B**).

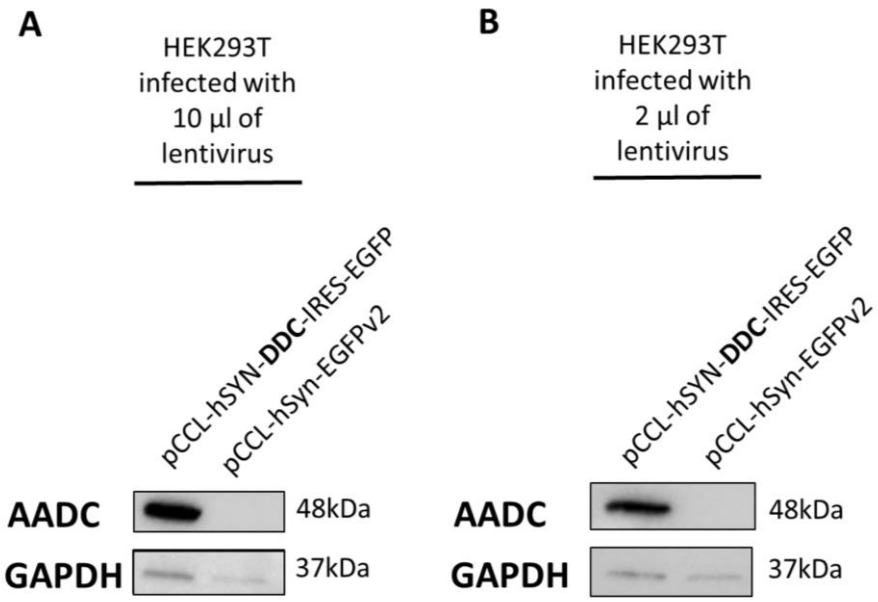

Figure 6-3: AADC protein immunoblotting studies in HEK-293 cells treated with either DDC or mock lentivirus.
Immunoblotting analysis of HEK 293T total lysates after infection with either 10 µl (A)or 2 µl (B) of *DDC* lentivirus (pCCL-hSYN-DDC-IRES-EGFP) and mock lentivirus (pCCL-hSYN-EGFPv2). AADC protein is detected at 48 kDa. GAPDH was utilised as a loading control (37 kDa).

6.4.1.4 Identification of MOI for Infection of mDA Neurons

On day 28 of differentiation, generated control mDA neurons were infected with a MOI of 10, 5 and 1 with either the *DDC* lentivirus (pCCL-hSYN-DDC-IRES-EGFP), or the mock lentivirus (pCCL-hSYN-EGFPv2) as described in **Section 2.2.10.3, Treatment of AADC mDA Neurons with Lentivirus**. The aim of this experiment was to compare the different MOI and to determine the optimum MOI for further work, based on efficiency of gene transfer and toxicity. After infection of *in vitro* derived neurons, immunofluorescence and morphological analysis was performed to detect GFP expression and survival. Three days post-infection, neurons infected with MOI 10, 5 or 1 showed expression of GFP with both lentivirus constructs. Overall, MOI of 1 showed weaker expression and lower number of cells expressing GFP when compared to MOI 10 and 5. For all MOI, cells maintained normal morphology without evidence of cell death (**Figure 6-4**). As GFP expression for MOI of 10 and 5 were deemed to be similar, a MOI of 5 was preferentially chosen for downstream experiments to reduce the risk of longer-term toxicity.

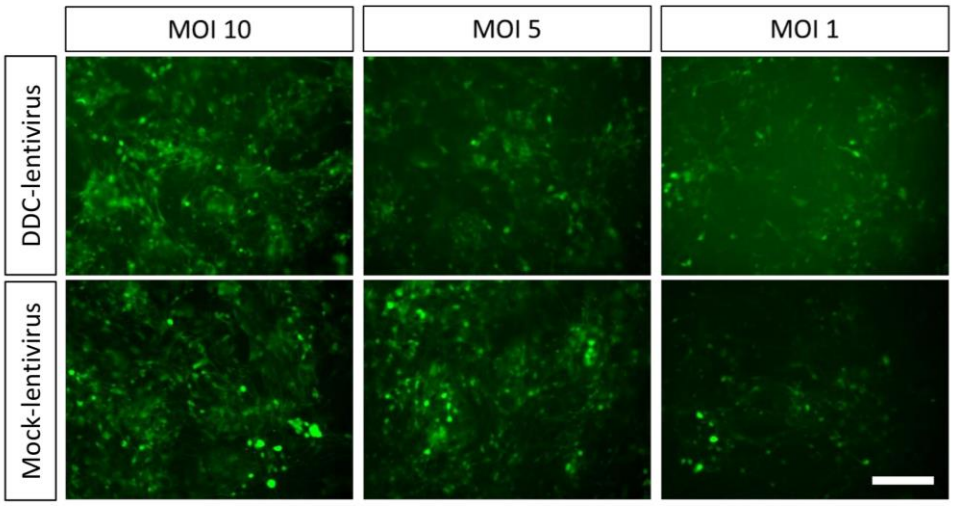

Figure 6-4: Immunofluorescence analysis of GFP in control mDA neurons.
GFP expression (green) three days after control mDA neuronal cultures have been infected with either *DDC* (top) or control (bottom) lentivirus, at MOIs of 10, 5, and 1. Scale bar= 100 µm.

6.4.2 Immunofluorescence for AADC, MAP2, and GFP after AADC Lentivirus Treatment

Patient-derived neurons were treated with either DDC- or GFP-only expressing lentivirus (mock) on day 28 of differentiation. Cultures were matured to day 65 of differentiation and analysed by immunofluorescence for expression of AADC and GFP in MAP2 positive cells. AADC and MAP2 protein expression showed strong correlation with GFP-expressing cells (**Figure 6-5**).

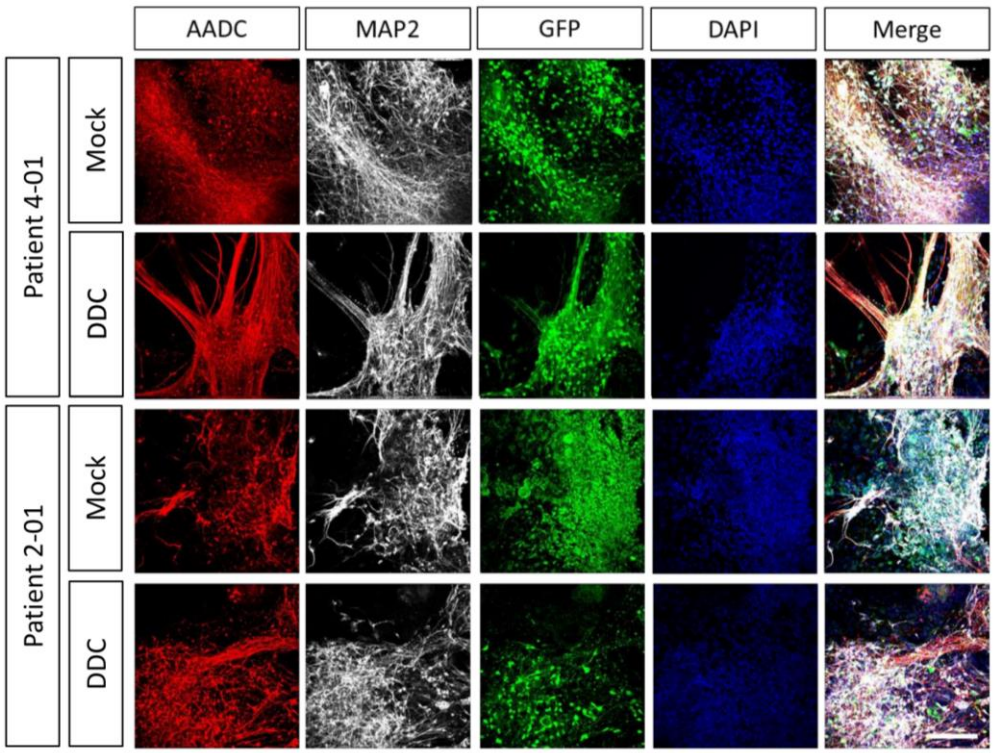

Figure 6-5: Immunofluorescence analysis of patient lines treated with either mock or *DDC* lentivirus.
Immunocytochemistry analysis for AADC (red), MAP2 (white), and GFP (green). The first and second row show Patient 1 mDA neurons treated with DDC and mock lentivirus. The third and fourth row show Patient 2 mDA neurons treated with DDC and mock lentivirus respectively. DAPI was used to contra stain nuclei. Scale bar= 100 µm.

6.4.3 Restoration of AADC Enzyme Activity in *DDC* Lentivirus treated patient derived Neurons

In order to determine whether *DDC* lentivirus treatment restored AADC enzyme activity, the AADC activity assay was perform on treated Patient 1-04 and Patient 2-01 mDA neurons at day 65 of differentiation. Patient-derived neurons treated with mock lentivirus showed lower levels of AADC activity than those observed for Control-05, which is in line with enzyme activity results for untreated patient-derived neurons (**Section 5.4.1.1**) (Patient 1 line: 15.61 ± 5.04; p=0.0025; Patient 2 line: 77.71 ± 21.61; p=0.0146; Control line: 1,532 ± 294.4). In contrast, *DDC* lentivirus treated Patient 1-04 and Patient 2-01 mDA cultures showed increased AADC activity (pmol/min/mg protein) (mean ± SEM; p-value) when compared to both mock lentivirus treated patient mDA neurons (for Patient 1-04 with DDC-GFP LV 1-04: 7,983 ± 6,089; p=0.3135; GFP LV 1-04: 18.25 ± 0.31; For Patient 2-01 with DDC-GFP LV 2-01: 11,322 ± 4,834; p=0.0320; GFP LV 2-01: 153.5 ± 83.16) and Control-05 neurons (for Patient 1-04 with DDC-GFP LV 1-04: 7,983 ± 6,089; p=0.2914; for Patient 2-01 with DDC-GFP LV 2-01: 11,322 ± 4,834; p=0.0192; and Control-05: 1,532 ± 294.4) (**Figure 6-6**). Despite the observed marked increase in AADC activity for treated patient neurons, statistical significance was only obtained for Patient 2-01, due to a limited n number of experiments. Of note, *DDC* lentivirus treatment achieved significant higher enzyme activity in Patient 2-01 lines when compared to Control-05 (**Figure 6-6**).

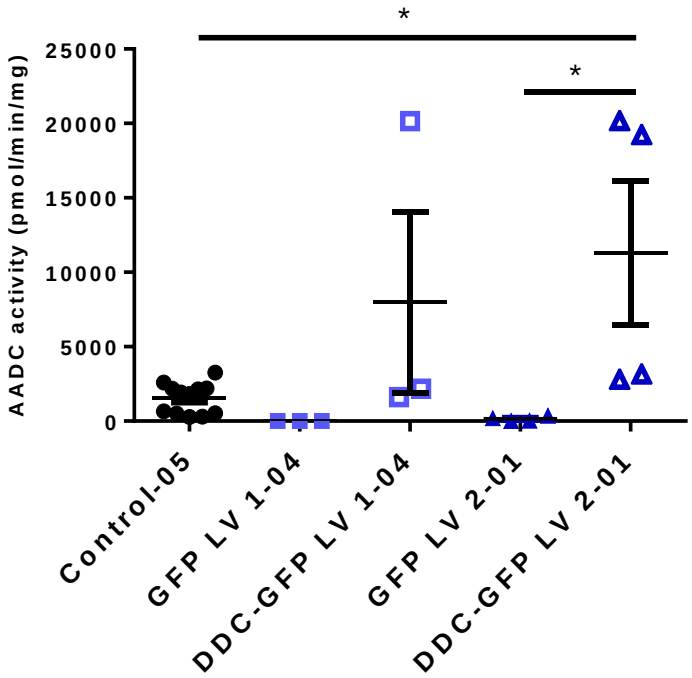

Figure 6-6: AADC activity assay in control and patient lines treated with mock or *DDC* lentivirus
AADC enzyme activity was measured in Control-05, mock lentivirus treated Patient 1 (GFP LV 1-04), *DDC* lentivirus treated Patient 1 (DDC-GFP LV 1-04), mock lentivirus treated Patient 2 (GFP LV 2-01), and *DDC* lentivirus treated Patient 2 (DDC-GFP LV 2-01) (n= 12, n= 3, and n= 4 respectively). Error bars represent ± SEM. Statistical analysis was performed using one-way ANOVA test and the Tukey's multiple comparisons test. Significance levels were determined through p-values. *indicates statistically significant differences when comparing: * $p<0.05$.

6.4.4 Restoration of 3-OMD is evident in *DDC* Lentivirus treated Lines

Analysis of dopamine metabolites in non-treated patient-derived mDA neuronal cultures showed dysregulation of dopamine, DOPAC and 3-OMD when compared to control lines (**Section 5.4.1.2**). In order to determine whether lentiviral gene therapy restored physiological levels of dopamine and its metabolites, I performed HPLC measurements on *DDC* lentivirus treated patient-derived mDA neuronal cultures at day 65 of maturation, as described in **Section 2.2.5.1**. Briefly, mDA precursors, derived from Patient 1-04 and Patient 2-04, were infected with either *DDC* or mock lentivirus at day 28 of differentiation. Extracellular dopamine, DOPAC and 3-OMD was then analysed by HPLC, as previously described (**Section 2.2.9**).

When compared to Control-05 derived neurons, mock lentivirus treated patient mDA neurons showed a significant decrease of dopamine and DOPAC. For dopamine (Patient 1-04 with GFP LV 1-04: 0.00 ± 0.00; p=0.0259; Patient 2-01 with GFP LV 2-01: 0.00 ± 0.00; p=0.0169; Control-05: 122.2 ± 7.98). For DOPAC (Patient 1-04 with GFP LV 1-04: 169.9 ± 6.95; p=0.0015; Patient 2-01 with GFP LV 2-01: 127.0 ± 32.64; p=0.0002; Control-05: 480.2 ± 45.48) (**Figure 6-7 A, B**).Which was also observed in treatment-naïve samples (**Section 5.4.1.2**). This confirmed that the lentivirus construct did not affect this AADC disease-specific phenotype in patient derived mDA neurons. The expected increase in dopamine and DOPAC metabolites after treatment with *DDC* lentivirus was not observed however, for either Patient 01-04 or Patient 2-01 lines. For dopamine (Patient 1-04 with DDC-GFP LV 1-04: 58.66 ± 58.66; GFP LV 1-04: 0.00 ± 0.00; p=0.4603) (Patient 2-01 with DDC-GFP LV 2-01: 0.00 ± 0.00; GFP LV 2-01: 0.00 ± 0.00; p>0.9999). For DOPAC (Patient 1-04 with DDC-GFP LV 1-04: 231.2 ± 10.17; GFP LV 1-04: 169.9 ± 6.95; p=0.8975) (Patient 2-01 with DDC-GFP LV 2-01: 173.0 ± 61.73; GFP LV 2-01: 127.0 ± 32.64; p=0.9362) (**Figure 6-7 A, B**). Further experiments will be necessary to assess the validity of these preliminary results. When analysing 3-OMD, a statistically significant increased level was observed in mock lentivirus treated Patient 1-04 and Patient 2-01 mDA neurons, when compared to Control-05 lines (Patient 1-04 with GFP LV 1-04: 1326 ± 155.3; p<0.0001; Patient 2-01 with GFP LV 2-01: 793.5 ± 163.2; p=0.0014; Control-05: 0.00 ± 0.00) (**Figure 6-7 C**). Similar to the results observed for untreated patient lines

(**Section 5.4.1.2**). Overexpression of *DDC* through lentivirus vector delivery, led to a statistically significant decrease in 3-OMD levels in treated Patient 1-04 mDA neurons (Patient 1-04 with DDC-GFP LV 1-04: 559.2 ± 150.1; GFP LV 1-04: 1,326 ± 155.3; p=0.0062) (**Figure 6-7 C**). A marked reduction (though not significant), was also observed in *DDC* lentivirus treated Patient 2-01 mDA neurons (Patient 2-01 with DDC-GFP LV 2-01: 463.6 ± 36.49; GFP LV 2-01: 793.5 ± 163.2; p=0.2597) (**Figure 6-7 C**). Further analysis is currently ongoing in order to confirm and validate this preliminary data.

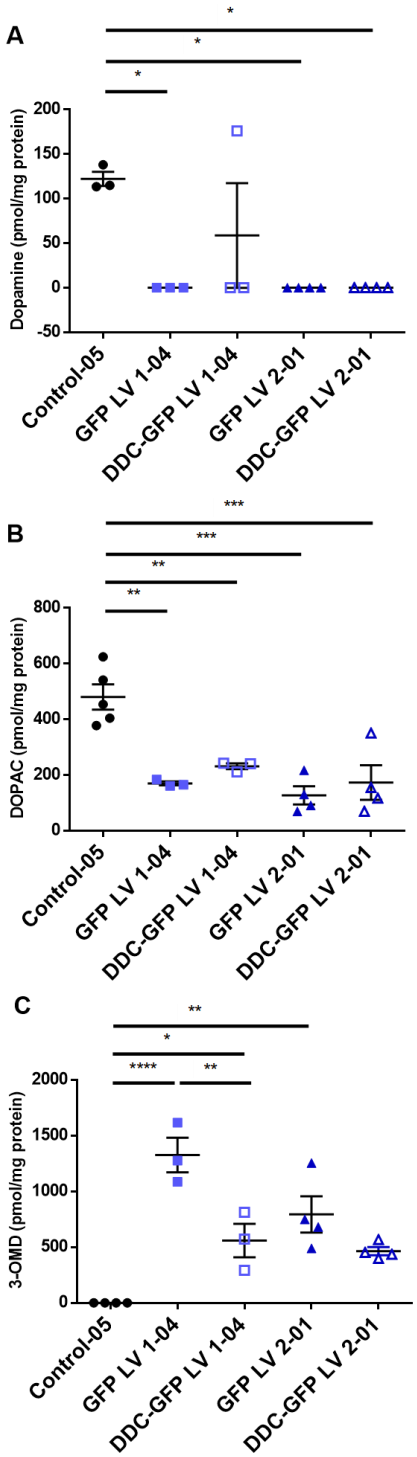

Figure 6-7: HPLC detection of extracellular dopamine, DOPAC and 3-OMD in mock and *DDC* lentivirus treated patient lines.
HPLC analysis of dopamine **A**, DOPAC **B**, and 3-OMD **C**. Error bars represent ± SEM. Statistical analysis was performed using one-way ANOVA test and the Tukey's multiple comparisons test. Significance levels were determined through p-values. *indicates statistically significant differences when comparing: * $p<0.05$; ** $p<0.01$; *** $p<0.001$.

6.5 Summary of the Gene Therapy with *DDC* Lentivirus Delivery

In this chapter, I have described the successful generation of a lentivirus construct for neuronal-specific expression of human *DDC* under control of human synapsin promoter. I utilised this vector for gene transfer into the mDA cell model of AADC deficiency and have shown *in vitro* neuronal expression of AADC enzyme in the patient-derived mDA neurons. Although this work requires further validation, preliminary results of *DDC* lentivirus treated patient-derived mDA neurons shows rescue of AADC activity with associated reduction in 3-OMD levels.

Chapter 7 Discussion

AADC deficiency is an ultra-rare primary neurotransmitter disorder with less than 150 patients reported worldwide (Himmelreich et al. 2019). It is associated with significant morbidity and increased risk of mortality. Although there is a broad phenotypic spectrum of disease, most affected patients are very fragile, manifesting a severe complex hyperkinetic movement disorder with regular oculogyric crises, delayed neurodevelopment and neuropsychiatric or behavioural issues. Systemic features are commonly reported, including life-threatening hypoglycaemia and debilitating gastric dysmotility. Affected patients also often have orthopaedic complications, with joint contractures, spinal deformity and a susceptibility to respiratory infections. Whilst there is some degree of (modest) improvement and/or disease stabilisation with available therapies, truly disease-modifying or curative treatments are not currently available for AADC deficiency. More recently, clinical gene therapy trials have offered new hope to AADC patients (Chien et al. 2017; Hwu et al. 2012; Kojima et al. 2019) and the current ongoing clinical trial (https://clinicaltrials.gov/ct2/show/NCT02852213). Further understanding of the underlying disease mechanisms, with the aim of developing even more efficacious therapies, thus constitutes research priority.

A number of different models have been utilised to study AADC deficiency, which have their advantages and disadvantages. AADC deficiency has been modelled in the mouse (Caine et al. 2017; Lee et al. 2013). In the homozygous knock-in (KI) mouse model (DdcIVS6/IVS6) very low enzymatic activity (0.3% of wild type) was observed, and low levels of dopamine in the brain. Half of the KI mice were born alive, showed poor growth and showed severe dyskinesia and hindlimb clasping. Later on, improvement of growth and motor functions was achieved. Serotonergic deficiency led to cardiovascular dysfunction and behavioural problems. Dopamine levels increased over time from 9.39% to 37.86% of wild type from 2 to 8 weeks of age (Lee et al. 2013). The homozygous KI mouse model ($Aadc^{S250F/S250F}$) showed low enzyme activity levels, the dopamine levels in the basal ganglia were modestly reduced and the substantia nigra neurons were unaffected. Serotonergic levels were markedly reduced leading to altered behavioural and autonomic function. No neurodegeneration was observed (Caine et al. 2017). Research has also been undertaken in a zebrafish model (Shih et al. 2013). In zebrafish inhibition of the *Ddc* gene by an AADC inhibitor

(NSD-1015) or anti-sense morpholino oligonucleotides (MO) resulted in reduced volume of the brain and smaller body length. Embryos injected with the MO showed apoptosis of brain cells and the loss of diencephalic catecholaminergic cluster neurons, as well as seizure-like activity. The MO embryos where less sensitive to touch, showed impaired swimming activity, and impaired eye movement (Shih et al. 2013). To date, research in AADC deficiency has yet to establish a robust disease model derived from affected individuals, harbouring disease-causing mutations on a patient's specific genetic background. As previously discussed, brain tissue from patients is not readily available, and even if it was, there are huge difficulties in the long-term culture of such post-mitotic neurons for laboratory study.

In this PhD, I have aimed to develop a patient-derived stem cell model of AADC deficiency. iPSC modelling of this disease is a new approach that will hopefully complement other available laboratory models. AADC deficiency is an ideal disease to study with iPSC-derived neurons, given the fact that it is a fully penetrant, recessive loss-of-function disease, with early (possibly fetal) age of disease onset. Furthermore, the key role of the AADC enzyme in mDA dopamine synthesis renders the derived mDA model an excellent platform to study disease mechanisms and investigate new therapies.

I have shown successful generation of **iPSC lines from patients with AADC deficiency, using Sendai Virus methodology**. All generated lines were characterised in detail (in tandem with a previously generated control iPSC line), showing true pluripotency. Establishing pluripotency is a key experimental step prior to an extended differentiation protocol, ensuring that lines will easily transform into any of the three germ layers. Furthermore, generated iPSC lines were shown to be Sendai Virus-free, and importantly maintained their genomic integrity. In a study by Mayshar *et al*., 2010, 66 hiPSC lines were analysed for chromosomal integrity. 13 cell lines were reported to have full or partial chromosomal aberrations, attributed to either *in vitro* culture adaption or originating from parent somatic cells. Aneuploidy was present in early passages, postulated to be caused by the reprogramming process. Whilst chromosome 12 duplications resulted in enrichment for cell cycle-related genes, abnormal chromosomal number limited differentiation potential (Mayshar et al. 2010).

Confirmation of genomic integrity is therefore an essential requirement for iPSC modelling.

When confirming *DDC* mutations for all patient iPSC lines (to ensure maintenance of the patients' genomic variants after reprogramming before the differentiation process) some interesting findings came to light. The mutation for Patient 1 was confirmed as previously reported (Montioli et al. 2016). However, for Patient 2, I was surprised to find that one of the two previously reported mutations was not present in either my fibroblast or iPSC lines (Pons et al. 2004). This prompted whole *DDC* gene sequencing, through which we identified a new and different 2nd mutation to that described in the literature for this patient. Our research laboratory then analysed fresh lymphocytic DNA samples from the patient's whole family, which confirmed that the new mutation identified in the fibroblast and iPSC lines showed appropriate disease segregation. The variant, p.Cys100Ser is located in exon 3, and has not been previously reported in AADC deficiency. Given its novelty, Alamut software has classified this officially as a variant of uncertain significance, though CADD and Polyphen *in silico* predictions suggest pathogenicity for this substitution, where the affected amino acid residue (and nucleotide) is highly conserved throughout species. Overall, I predict that it is likely to be causative, given the reasons above, and that no other variants were identified on gene sequencing. This work highlights the crucial importance of clarifying the genetic background of laboratory lines when developing iPSC model systems, given the potential variable effects of genotype of cellular phenotype.

Through this work, **I have also shown that iPSCs can be successfully differentiated into typical mDA neuronal progenitors before maturation into day 65 mDA neurons, showing characteristic derived-mDA identity**. Importantly, my model system showed that when compared to control lines, the generated patient-derived neurons show no evidence of neurodegeneration. This key finding aligns well with both, the Aadc$^{520F/520F}$ mouse model (Caine et al. 2017), where there is also no neurodegeneration, and human patients who have normal brain magnetic resonance imaging (MRI) and normal DAT scan imaging (Professor Krys Banckiewicz, Dr Toni Pearson, personal communication, 2019*).* Despite severe baseline disability, many

patients also show some degree of neurodevelopmental progress and clinical stabilisation over time; clinical regression and loss of previously acquired skills is rarely reported. My work thus provides more evidence that AADC deficiency is likely to be a neurodevelopmental, rather than a neurodegenerative, disease, where the enzymatically-determined dopamine deficiency does not seem to lead to neuronal cell loss over the course of the disease. The absence of neurodegeneration is an important concept, with many implications. An intact mDA system will be important for maximising the chances of success with gene therapy trials and other future developed therapies. As a "neurodevelopmental syndrome" the preliminary electrophysiological findings in my AADC disease model are potentially interesting, though more work is now necessary to see if these observed electrophysiological differences are replicable, reliable and truly disease-specific.

My iPSC-derived neuronal model recapitulated a number of key features observed in AADC deficiency. Despite differing genotypes, I found that AADC enzyme activity was significantly reduced in both patient lines, (1-5% of normal) - similar to findings observed in the diagnostic plasma AADC enzyme assay (Wassenberg et al. 2017). For a third of reported AADC deficiency cases, the AADC activity was not detectable. The highest detected value in a patient was 12 pmol/ml/min (36% of the accepted lower limit of normal). Interestingly, 'apparently' asymptomatic heterozygous carriers have also been reported with reduced AADC activity levels (35-40% of normal) revealing some overlap with ranges reported in disease (Wassenberg et al. 2017) – the reasons for this, and in fact, why AADC activity is below 50% is not clear. Developing an iPSC-derived mDA line from a carrier may help answer some of these questions. From a Mendelian perspective, AADC deficiency has always been classified as a bi-allelic recessive disorder, but these observations question whether harbouring a single allele may further reduce enzyme activity putatively by subtle dominant negative effects or the effect of genetic background environment on gene and protein function. It also raises the question as to whether obligate carriers of AADC deficiency should be more extensively investigated, through detailed clinical, neurological and neuropsychiatric testing. Anecdotally, a number of obligate carriers have reported anxiety, depression and

obsessive-compulsive symptoms, though formal research is now warranted to investigate this further.

As well as reduced AADC enzyme activity, the iPSC derived mDA neuronal model of disease also showed similar derangement of dopaminergic metabolites to that seen in human patients on CSF neurotransmitter analysis. In my project, I investigated extracellular concentrations of the precursor metabolite 3-OMD, dopamine, and the dopamine degradation metabolite, DOPAC. As seen in human patients, the extracellular 3-OMD concentrations were elevated and DOPAC concentrations were lower in the patient lines when compared to controls. Dopamine was not present in both patient lines, though detectable in the control line. It is well recognised that dopamine is not stable in physiological pH conditions and within synaptic vesicles, is stored stably in an acidic environment (pH ~5.6) (Mani and Ryan 2009; Raley-Susman et al. 1991; Schwiening and Boron 1994; Vincent et al. 1999). Given the possibility of dopamine instability and possible degradation, it is likely that measuring dopamine levels will not be an accurate representation of dopamine turnover. Ideally, I would have liked to have included analysis of the stable dopamine metabolite, HVA levels in my study. Unfortunately, I consistently observed that HPLC analysis was not able to detect extracellular levels of HVA in both my control and patient lines. We observed this phenomenon in another concurrent project in the lab, where HVA was not detectable in control samples, and only detected at higher levels in Dopamine Transporter Deficiency Syndrome patient lines, where raised HVA levels are a hallmark of disease (personal communication, Prof. Kurian, ICH-GOSH, UCL). The HPLC experiments for this thesis was performed in accordance with previous published work (De la Fuente et al. 2017) and the reasons for the difficulties in detecting HVA in the iPSC-derived neuronal model are not clear. De la Fuente and colleagues report that dopamine and its metabolites were only detected from their SH-SY5Y cells in cell culture medium after the addition of L-dopa. Whether this is due to the fact that SH-SY5Y cells do not synthesise or store significant amounts of intracellular dopamine (Balasooriya and Wimalasena 2007), or due to technical difficulties in detecting HVA from cell lines, is currently unclear. Future optimisation of HVA assay for use in iPSC-derived lines will no doubt benefit similar future projects of iPSC-based modelling for neurotransmitter disorders.

Both patient lines showed low levels of AADC enzyme activity and abnormalities of dopaminergic metabolites on HPLC analysis. As a result, I wanted to investigate whether this could be attributed to differences in AADC protein expression. For Patient 2, I observed reduced levels of both gene and protein expression when compared to control lines; this may be contributory to the observed enzyme deficiency. In contrast, for Patient 1, gene expression was comparable to control lines, whilst AADC protein levels were increased. The reasons for this remain yet to be fully elucidated; it is possible that this particular missense variant does not directly impact upon gene expression. With regard to the increased protein expression observed for mutant R347 lines, one could postulate that there may be an intrinsic cellular mechanism that detects dysfunctional AADC enzyme with compensatory reduction in enzyme degradation. Given that gene and protein levels are not reduced, the impact of R347G may thus reside in how this mutation affects the *function* of mutant protein. Indeed, work by Montioli et al. (2016) has shown that p. R347G affects catalytic activity, which may be an important mechanisms underpinning enzyme dysfunction for this particular variant (Montioli et al. 2016).

Having established an iPSC stem cell derived neuronal model of AADC deficiency, I wanted to determine whether AADC enzyme deficiency and deranged dopamine homeostasis had further downstream effects on the dopaminergic system. The results of my study are summarised, including data on AADC gene and protein expression, in **Table 7-1**.

Table 7-1: Summary of gene and protein expression for dopaminergic proteins.

Gene/protein expression compared to controls	Patient 1	Patient 2
AADC gene expression	Non-significant	↓
AADC protein expression	↑	↓↓↓↓
TH gene expression	↓	↑ ↑
TH protein expression	↓↓↓	↓
MAOA gene expression	↓	↓ ↓ ↓
MAOA protein expression	↓↓	↓ ↓

For Patient 1 there was evidence of both reduced gene and protein expression of TH. The reasons for this are not completely clear, but it may be hypothesised that it could be linked to a cellular negative feedback loop detecting increased AADC protein and responding by reducing TH levels. For Patient 2, *TH* gene expression level was increased but protein levels were decreased. Further experiments will be needed to clarify this data, but again this work provides preliminary indications that TH may be dysregulated in AADC deficiency. *MAOA* relative gene and protein expression was statistically significantly lower for both patient lines when compared to controls. Although the mechanisms governing this are not yet clear, it may be postulated that cellular homeostatic mechanisms may downregulate this enzyme as a feedback response to either low AADC enzymes levels or reduced dopamine/dopamine metabolites in the cell. Interestingly MAO inhibitors are often used in the first line treatment of new AADC deficiency patients (Wassenberg et al. 2017). Given that my work suggests that MAOA levels are low in the AADC cell model, it would be important to see if this could be determined *in vivo* – indeed the question arises if the MAO protein levels are similarly low in patients, whether MAO inhibitors are truly a useful therapeutic intervention for AADC deficiency.

During my PhD I was also able to **preliminarily investigate the effects of a lentiviral-mediated *DDC* gene transfer in patient-derived mDA neurons**. Both *DDC* lentivirus treated patient cell lines showed higher enzyme activity and a reduction in 3-OMD levels than their respective mock control. More experiments will help validate these initial findings to statistical significance, work that will hopefully contribute to understanding the cellular consequences of a gene therapy approach.

Overall, during the course of my PhD, I have recognised a number of strengths in using an iPSC-based modelling system to study AADC deficiency. To my knowledge, it is the first laboratory model for this condition generated from patient-derived cells with patient mutations. For the first time, we have been able to study this disease in a directly patient-centric mDA neuronal model. AADC deficiency is a highly suitable disease for studying in this way, given that it is monogenic disorder with complete penetrance, and early neonatal or infantile disease onset. As a result, even though derived mDA neurons likely equate to a human fetal stage of neuronal maturity, I was still able to recapitulate key disease features, including significant impairment of AADC enzyme activity and abnormal neurotransmitter metabolites. This was achievable without using cellular ageing techniques, such as progerin or chemical induction (Cooper et al. 2013; Miller et al. 2013; Nguyen et al. 2011). This suggests not only that the mDA model is a robust system for future research in this condition, but also that AADC deficiency may have important effects in prenatal neurodevelopment, which could be further studied in this model. Another major advantage of this model is that I was able to study the mDA system to evaluate a therapeutic strategy (gene therapy); by establishing clear phenotypic readouts (enzyme activity and measurement of monoamine metabolites). I have identified specific parameters that can be used for measurement of efficacy in future drug screening projects.

I am also aware that there are a number of limitations to my AADC deficiency iPSC-derived model. For this study, I utilised only one control line and two different patient lines. The conclusions drawn from the study would be significantly strengthened by overall increasing the experimental number (n) as well as using more age-matched control lines and multiple different patient lines (i.e. from patients with different levels of disease severity) with corresponding CRISPR-corrected lines. Such work would help overcome the unavoidable issues of clonal variability and also facilitate better understanding of the influence of specific genotypes on cellular phenotypes. In this project, I have developed a mDA model of disease, but it is well recognised that AADC deficiency also has significant impact on the serotonergic system with a number of key disease features attributed to central (and possibly peripheral) serotonin deficiency (Wassenberg et al. 2017). Future development of a

serotonergic iPSC derived model of disease may therefore provide important insight into the effects of AADC deficiency on the serotonergic system. Furthermore, development of midbrain-like (Jo et al. 2016) and cortical organoid models (Lancaster et al. 2017) may confer significant advantages over the two-dimensional system that I have developed with regard to neuronal maturity, connectivity, and cell type. Such three-dimensional model systems are likely to provide deeper understanding of the neuronal consequences of AADC deficiency. The lentiviral approach is useful to show the potential therapeutic utility of a gene therapy approach (and the optimum vector for delivery into a cellular model). However, it is not the vector type that is being developed for human trial, where AAV-based vectors are currently used [(Chien et al. 2017; Hwu et al. 2012; Kojima et al. 2019) and (https://clinicaltrials.gov/ct2/show/NCT02852213)]. This highlights the emerging concept that although iPSC models may be a good tool for drug screening, it is possible that promising agents in a cell model may not translate to animal models and human patients. Potential therapies identified through iPSC-based screening would therefore need much more rigorous testing in different models to be assured of clinical utility with regard to safety and efficacy.

The work undertaken in this PhD thus has a number of wider implications to both the field of AADC deficiency and stem cell-based modelling of disease. To my knowledge, it is the first reported patient-derived laboratory model of AADC deficiency, providing an important proof-of-concept basis for future work in this field. Importantly, generation of the mDA system has allowed me to study this disease in a highly appropriate neuronal model, harbouring patient-relevant genetic mutations. It is hoped that this work will pave the way for further mechanistic studies and novel drug discovery in AADC deficiency. Such work is likely to provide new insight into the disease, in addition to the already established mouse (Caine et al. 2017; Lee et al. 2013) and zebrafish models (Shih et al. 2013). The use of emerging technologies such as single cell RNA sequencing (to define cell types by gene expression patterns) (La Manno et al. 2016), CRISPR-cas9 techniques (to generate mutation-corrected patient lines to both study disease and also potentially treat patients) (Ding et al. 2013), robust organoid models (for three-dimensional disease modelling) (Lancaster and Knoblich 2014), and high content imaging/high throughput screening (for therapeutic

investigation) (Little et al. 2019) in iPSC-based model systems will no doubt lead to the development of better models, facilitating deeper elucidation of disease mechanisms and identification of new treatments, not only for AADC deficiency, but also for many other genetic diseases. My preliminary study of two patient lines (with different bi-allelic *DDC* mutations) suggests that although disease is likely to result from significant impairment of AADC enzyme activity, the effects of different gene variants on gene and protein expression, protein localisation, enzyme function, and downstream sequelae may indeed be mutation-specific. This is an emerging concept in the field of stem cell modelling (Trilck et al. 2017). Generation of mDA lines from a broader range of patients (with CRISPR-corrected lines) will not only allow us to delineate these differences (providing further insight into protein structure-function properties), but also to develop even more precise personalised medicine strategies for individual patients. Another important finding from my study is the observation of no neurodegeneration in patient lines. Other neurotransmitter disorders, such as Dopamine Transporter Deficiency Syndrome (DTDS) manifest clinically with a progressive disease course, and there is evidence of significant neurodegeneration in the patient-derived mDA cell model (*Barral et al,* manuscript under review, 2019). This is in contrast to my findings in the AADC deficiency cell model, which correlates well to both patient phenotype (some patients may show a degree of plateauing of their disease symptoms, with ongoing acquisition of neurodevelopmental skills through childhood and adolescence), and neuroimaging findings (no evidence of basal ganglia degeneration on MRI or DATscan). Overall, these observations suggest that AADC deficiency is likely to be a neurodevelopmental, rather than a neurodegenerative disease, which may be important for both disease prognostication and future therapeutic considerations. Indeed, certain approaches (such as the current efforts into AADC gene therapy) are potentially more likely to succeed in a non-neurodegenerative milieu. In the future, work such as that undertaken in this PhD will need to increasingly bear clinical relevance to facilitate 'bench-to-beside translation'. Finally, with increasing scientific focus on NC3R principles, it is likely that iPSC-based disease modelling may in the future contribute to reducing, refining and perhaps even replacing (to some extent) the use of animals for scientific purposes.

In summary, my PhD encompasses generation of a humanised iPSC-derived mDA model of AADC deficiency, which has recapitulated some of the key features of AADC deficiency and provided insight into the downstream effects of this primary neurotransmitter disorder. Preliminary work investigating a lentiviral gene therapy approach will provide a good future basis to understand the cellular consequences of viral vector-mediated gene therapy. This newly generated model may also be a good platform for future high-throughput drug screening and other personalised medicine approaches.

Ultimately I sincerely hope that this work will help one day to cure AADC deficiency.

References

Åkerud, Peter, Josep M. Canals, Evan Y. Snyder, and Ernest Arenas. 2001. "Neuroprotection through Delivery of Glial Cell Line-Derived Neurotrophic Factor by Neural Stem Cells in a Mouse Model of Parkinson's Disease." *The Journal of Neuroscience* 21(20):8108–18.

Albin, RL, AB Young, and JB Penney. 1989. "The Functional Anatomy of Basal Ganglia Disorders." *Trends Neurosci.* 12(10):366–75.

Allen, George Francis Gray. 2010. "The Neurochemical Consequences of Aromatic L-Amino Acid Decarboxylase Deficiency." UCL Institute of Neurology, London, UK.

Alvarez-Fischer, Daniel, Julia Fuchs, Fraṇois Castagner, Olivier Stettler, Olivia Massiani-Beaudoin, Kenneth L. Moya, Colette Bouillot, Wolfgang H. Oertel, Anne Lombès, Wolfgang Faigle, Rajiv L. Joshi, Andreas Hartmann, and Alain Prochiantz. 2011. "Engrailed Protects Mouse Midbrain Dopaminergic Neurons against Mitochondrial Complex I Insults." *Nature Neuroscience* 14(10):1260–66.

Andersson, E., J. B. Jensen, M. Parmar, F. Guillemot, and A. Björklund. 2006. "Development of the Mesencephalic Dopaminergic Neuron System Is Compromised in the Absence of Neurogenin 2." *Development* 133:507–16.

Andersson, E., Ulrika Tryggvason, Qiaolin Deng, Stina Friling, Zhanna Alekseenko, Benoit Robert, Thomas Perlmann, and Johan Ericson. 2006. "Identification of Intrinsic Determinants of Midbrain Dopamine Neurons." *Cell* 124:393–405.

Ang, S. L., A. Wierda, D. Wong, K. A. Stevens, S. Cascio, J. Rossant, and K. Zaret, S. 1993. "The Formation and Maintenance of the Definitive Endoderm Lineage in the Mouse: Involvement of HNF3/Forkhead Proteins." *Development* 119, 1301-.

Arenas, E., M. Denham, and J. C. Villaescusa. 2015. "How to Make a Midbrain

Dopaminergic Neuron." *Development* 142:1918–36.

Arenas, Ernest, Miles Trupp, Peter Åkerud, and Carlos F. Ibáñez. 1995. "GDNF Prevents Degeneration and Promotes the Phenotype of Brain Noradrenergic Neurons in Vivo." *Neuron* 15(6):1465–73.

Arnoux, J. B., L. Damaj, S. Napuri, V. Serre, L. Hubert, M. Cadoudal, G. Simard, I. Ceballos, L. Christa, and P. de Lonlay. 2013. "Aromatic L-Amino Acid Decarboxylase Deficiency Is a Cause of Long-Fasting Hypoglycemia." *J Clin Endocrinol Metab* 98:4279–84.

Atwal, P. S., T. R. Donti, A. L. Cardon, C. A. Bacino, Q. Sun, L. Emrick, V. Reid Sutton, and S. H. Elsea. 2015. "Aromatic L-Amino Acid Decarboxylase Deficiency Diagnosed by Clinical Metabolomic Profiling of Plasma." *Mol Genet Metab* 115:91–94.

Balasooriya, Is and Kandatage Wimalasena. 2007. "Are SH-SY5Y and MN9D Cell Lines Truly Dopaminergic?" *FASEB Journal* 21:25–26.

Bao, Xichen, Xihua Zhu, Baojian Liao, Christina Benda, Qiang Zhuang, Duanqing Pei, Baoming Qin, and Miguel A. Esteban. 2013. "MicroRNAs in Somatic Cell Reprogramming." *Current Opinion in Cell Biology* 25(2):208–14.

Barbagiovanni, Giulia, Pierre Luc Germain, Michael Zech, Sina Atashpaz, Pietro Lo Riso, Agnieszka D'Antonio-Chronowska, Erika Tenderini, Massimiliano Caiazzo, Sylvia Boesch, Robert Jech, Bernhard Haslinger, Vania Broccoli, Adrian Francis Stewart, Juliane Winkelmann, and Giuseppe Testa. 2018. "KMT2B Is Selectively Required for Neuronal Transdifferentiation, and Its Loss Exposes Dystonia Candidate Genes." *Cell Reports* 25(4):988–1001.

Barnett, Mark W. and Philip M. Larkman. 2007. "The Action Potential." *Pract Neurol* 7:192–97.

Barth, M., V. Serre, L. Hubert, Y. Chaabouni, N. Bahi-Buisson, M. Cadoudal, D.

Rabier, S. N. Tich, M. Ribeiro, D. Ricquier, A. Munnich, D. Bonneau, P. de Lonlay, and L. Christa. 2012. “Kinetic Analyses Guide the Therapeutic Decision in a Novel Form of Moderate Aromatic Acid Decarboxylase Deficiency.” *JIMD Rep* 3:25–32.

Berger, Miles, John A. Gray, and Bryan L. Roth. 2009. “The Expanded Biology of Serotonin.” *Annu Rev Med.* 60:355–66.

Bertoldi, M., M. Gonsalvi, R. Contestabile, and C. B. Voltattorni. 2002. “Mutation of Tyrosine 332 to Phenylalanine Converts Dopa Decarboxylase into a Decarboxylation-Dependent Oxidative Deaminase.” *J Biol Chem* 277:36357–62.

Blakely, Randy D., Haley E. Bersont, Robert T. Fremeau Jr, Marc G. Caron, Margaret M. Peek, Heather K. Princet, and Chris C. Bradleyt. 1991. “Cloning and Expression of a Functional SERT from Rat Brain.” *Nature* 354:66–70.

Boland, Michael J., Kristopher L. Nazor, Ha T. Tran, Attila Szücs, Candace L. Lynch, Ryder Paredes, Flora Tassone, Pietro Paolo Sanna, Randi J. Hagerman, and Jeanne F. Loring. 2017. “Molecular Analyses of Neurogenic Defects in a Human Pluripotent Stem Cell Model of Fragile X Syndrome.” *Brain* 140(3):582–98.

Bouyer, J. J., D. H. Park, T. H. Joh, and V. M. Pickel. 1984. “Chemical and Structural Analysis of the Relation between Cortical Inputs and Tyrosine Hydroxylase-Containing Terminals in Rat Neostriatum.” *Brain Research* 302(2):267–75.

Bräutigam, C., K. Hyland, R. Wevers, R. Sharma, L. Wagner, GJ Stock, F. Heitmann, and GF Hoffmann. 2002. “Clinical and Laboratory Findings in Twins with Neonatal Epileptic Encephalopathy Mimicking Aromatic L-Amino Acid Decarboxylase Deficiency.” *Neuropediatrics* 33(3):113–17.

Briscoe, James and Johan Ericson. 1999. “The Specification of Neuronal Identity by Graded Sonic Hedgehog Signalling.” *Semin. Cell Dev. Biol.* 10:353–62.

Broccoli, V., E. Boncinelli, and W. Wurst. 1999. “The Caudal Limit of Otx2

Expression Positions the Isthmic Organizer." *Nature* 401:164–68.

Brownjohn, Philip W., James Smith, Erik Portelius, Lutgarde Serneels, Hlin Kvartsberg, Bart De Strooper, Kaj Blennow, Henrik Zetterberg, and Frederick J. Livesey. 2017. "Phenotypic Screening Identifies Modulators of Amyloid Precursor Protein Processing in Human Stem Cell Models of Alzheimer's Disease." *Stem Cell Reports* 8(4):870–82.

Brun, L., L. H. Ngu, W. T. Keng, G. S. Ch'ng, Y. S. Choy, W. L. Hwu, W. T. Lee, M. A. Willemsen, M. M. Verbeek, T. Wassenberg, L. Regal, S. Orcesi, D. Tonduti, P. Accorsi, H. Testard, J. E. Abdenur, S. Tay, G. F. Allen, S. Heales, I. Kern, M. Kato, A. Burlina, C. Manegold, G. F. Hoffmann, and N. Blau. 2010. "Clinical and Biochemical Features of Aromatic L-Amino Acid Decarboxylase Deficiency." *Neurology* 75:64–71.

Burkhard, P., P. Dominici, C. Borri-Voltattorni, J. N. Jansonius, and V. N. Malashkevich. 2001. "Structural Insight into Parkinson's Disease Treatment from Drug-Inhibited DOPA Decarboxylase." *Nat Struct Biol* 8:963–67.

Burkhardt, Matthew F., Fernando J. Martinez, Sarah Wright, Carla Ramos, Dmitri Volfson, Michael Mason, Jeff Garnes, Vu Dang, Jeffery Lievers, Uzma Shoukat-Mumtaz, Rita Martinez, Hui Gai, Robert Blake, Eugeni Vaisberg, Marica Grskovic, Charles Johnson, Stefan Irion, Jessica Bright, Bonnie Cooper, Leane Nguyen, Irene Griswold-Prenner, and Ashkan Javaherian. 2013. "A Cellular Model for Sporadic ALS Using Patient-Derived Induced Pluripotent Stem Cells." *Molecular and Cellular Neuroscience* 56:355–64.

Buttarelli, Francesca R., Alessandra Fanciulli, Clelia Pellicano, and Francesco E. Pontieri. 2011. "The Dopaminergic System in Peripheral Blood Lymphocytes: From Physiology to Pharmacology and Potential Applications to Neuropsychiatric Disorders." *Curr Neuropharmacol.* 9(2):278–88.

Caine, C., M. Shohat, J. K. Kim, K. Nakanishi, S. Homma, E. V Mosharov, and U. R.

Monani. 2017. “A Pathogenic S250F Missense Mutation Results in a Mouse Model of Mild Aromatic L-Amino Acid Decarboxylase (AADC) Deficiency.” *Hum Mol Genet* 26(22):4406–15.

Calabresi, Paolo, Barbara Picconi, Alessandro Tozzi, Veronica Ghiglieri, and Massimiliano Di Filippo. 2014. “Direct and Indirect Pathways of Basal Ganglia: A Critical Reappraisal.” *Nature Neuroscience* 17(8):1022–30.

Carlessi, L., E. Fusar Poli, G. Bechi, M. Mantegazza, B. Pascucci, L. Narciso, E. Dogliotti, C. Sala, C. Verpelli, D. Lecis, and D. Delia. 2014. “Functional and Molecular Defects of HiPSC-Derived Neurons from Patients with ATM Deficiency.” *Cell Death and Disease* 5(7):e1342-14.

Cassimeris, Lynne and Cynthia Spittle. 2001. “Regulation of Microtubule-Associated Proteins.” *Int Rev Cytol* 210:163–226.

Ceccarelli, B., W. P. Hurlbut, and A. Mauro. 1973. “Turnover of Transmitter and Synaptic Vesicles at the Frog Neuromuscular Junction.” *J Cell Biol.* 57(2):499–524.

Chang, Y. T., R. Sharma, J. L. Marsh, J. D. McPherson, J. A. Bedell, A. Knust, C. Brautigam, G. F. Hoffmann, and K. Hyland. 2004. “Levodopa-Responsive Aromatic L-Amino Acid Decarboxylase Deficiency.” *Ann Neurol* 55:435–38.

Chiang, Chin, Ying Litingtung, Eric Lee, Keith E. Youngt, Jeffrey L. Cordent, Heiner Westphal, and Philip A. Beachyt. 1996. “Cyclopia and Defective Axial Patterning in Mice Lacking Sonic Hedgehog Gene Function.” *Nature* 383:407–13.

Chien, Yin-hsiu, Ni-chung Lee, Sheng-hong Tseng, Chun-hwei Tai, Shin-ichi Muramatsu, Barry J. Byrne, and Wuh-liang Hwu. 2017. “Efficacy and Safety of AAV2 Gene Therapy in Children with Aromatic L-Amino Acid Decarboxylase Deficiency : An Open-Label, Phase 1/2 Trial.” *The Lancet Child and Adolescent Health* 1(4):265–73.

Chojnacki, C., E. Walecka-Kapica, A. Blonska, K. Winczyk, A. Stepien, and J. Chojnacki. 2016. “Serotonin and Melatonin Secretion in Postmenopausal Women with Eating Disorders.” *Endokrynol Pol* 67:299–304.

Christine, C. W., P. A. Starr, P. S. Larson, J. L. Eberling, W. J. Jagust, R. A. Hawkins, H. F. VanBrocklin, J. F. Wright, K. S. Bankiewicz, and M. J. Aminoff. 2009. “Safety and Tolerability of Putaminal AADC Gene Therapy for Parkinson Disease.” *Neurology* 73:1662–69.

Chung, Sangmi, Amanda Leung, Baek-soo Han, Mi-yoon Chang, Jung-il Moon, Chun-hyung Kim, Sunghoi Hong, Jan Pruszak, Ole Isacson, and Kwang-soo Kim. 2009. “Wnt1-Lmx1a Forms a Novel Autoregulatory Loop and Controls Midbrain Dopaminergic Differentiation Synergistically with the SHH-FoxA2 Pathway.” *Cell Stem Cell* 5:646–58.

Cidons, Shulamit and Talvinder S. Sihrao. 1989. “Characterization of a H + -ATPase in Rat Brain Synaptic Vesicles.” *J Biol Chem.* 264(14):8281–88.

Cooper, Oliver, Hyemyung Seo, Shaida Andrabi, Cristina Guardia-laguarta, Maria Sundberg, Jesse R. Mclean, Luis Carrillo-reid, Zhong Xie, Gunnar Hargus, Michela Deleidi, Tristan Lawson, Helle Bogetofte, Lorraine Clark, Carol Moskowitz, Joseph Mazzulli, Li Chen, Norma Romero, Houbo Jiang, Ryan J. Uitti, Zhigao Huang, Leslie A. Scarffe, Valina L. Dawson, Christine Klein, Jian Feng, Owen A. Ross, John Q. Trojanowski, Virginia M. Lee, Karen Marder, D. James Surmeier, K. Wszolek, Serge Przedborski, Dimitri Krainc, Ted M. Dawson, and Ole Isacson. 2013. “Familial Parkinson’s Disease IPSCs Show Cellular Deficits in Mitochondrial Responses That Can Be Pharmacologically Rescued.” *Science Translational Medicine* 4(141):1–25.

Dahlstroem, A. and K. Fuxe. 1964. “Evidence for the Existence of Monoamine Containing Neurons in the Central Nervous System.” *Acta Physiol Scand Suppl* Suppl 232:1-55.

Dai, Lifang, Changhong Ding, and Fang Fang. 2019. “A Novel DDC Gene Deletion Mutation in Two Chinese Mainland Siblings with Aromatic L-Amino Acid Decarboxylase Deficiency.” *Brain and Development* 41(2):205–9.

Daidone, F., R. Montioli, A. Paiardini, B. Cellini, A. Macchiarulo, G. Giardina, F. Bossa, and C. Borri Voltattorni. 2012. “Identification by Virtual Screening and in Vitro Testing of Human DOPA Decarboxylase Inhibitors.” *PLoS One* 7:e31610.

Daniels, AJ and JF Jr. Reinhard. 1988. “Energy-Driven Uptake of the Neurotoxin 1-Methyl-4-Phenylpyridinium into Chromaffin Granules via the Catecholamine Transporter.” *J Biol Chem.* 263:5034–36.

Darchen, François, Daniel Scherman, Claire Desnos, and Jean Pierre Henry. 1988. “Characteristics of the Transport of the Quaternary Ammonium 1-Methyl-4-Phenylpyridinium by Chromaffin Granules.” *Biochemical Pharmacology* 37(22):4381–87.

Delli Carri, A., M. Onorati, M. J. Lelos, V. Castiglioni, A. Faedo, R. Menon, S. Camnasio, R. Vuono, P. Spaiardi, F. Talpo, M. Toselli, G. Martino, R. A. Barker, S. B. Dunnett, G. Biella, E. Cattaneo, A. D. Carri, M. Onorati, M. J. Lelos, V. Castiglioni, A. Faedo, R. Menon, S. Camnasio, R. Vuono, P. Spaiardi, F. Talpo, M. Toselli, G. Martino, R. A. Barker, S. B. Dunnett, G. Biella, and E. Cattaneo. 2013. “Developmentally Coordinated Extrinsic Signals Drive Human Pluripotent Stem Cell Differentiation toward Authentic DARPP-32+ Medium-Sized Spiny Neurons.” *Development* 140(2):301–12.

DeLong, Mahlon R. 1990. “Primate Models of Movement Disorders of Basal Ganglia Origin.” *Trends in Neurosciences* 13(7):281–85.

Deng, Qiaolin, Elisabet Andersson, Eva Hedlund, Zhanna Alekseenko, Eva Coppola, Lia Panman, James H. Millonig, Jean-francois Brunet, Johan Ericson, and Thomas Perlmann. 2011. “Specific and Integrated Roles of Lmx1a , Lmx1b and

Phox2a in Ventral Midbrain Development." *Development* 138:3399–3408.

Denoyer, M., M. Sallanon, K. Kitahama, C. Aubert, and M. Jouvet. 1989. "Reversibility of Para-Chlorophenylalanine-Induced Insomnia by Intrahypothalamic Microinjection of L-5-Hydroxytryptophan." *Neuroscience* 28:83–94.

Derkach, V., A. Surprenant, and RA North. 1989. "5-HT3 Receptors Are Membrane Ion Channels." *Nature* 339:706–9.

Ding, Qiurong, Stephanie N. Regan, Yulei Xia, Leoníe A. Oostrom, Chad A. Cowan, and Kiran Musunuru. 2013. "Enhanced Efficiency of Human Pluripotent Stem Cell Genome Editing through Replacing TALENs with CRISPRs." *Cell Stem Cell* 12(4):393–94.

Djuric, Ugljesa, Aaron Y. L. Cheung, Wenbo Zhang, Rebecca S. Mok, Wesley Lai, Alina Piekna, Jason A. Hendry, P. Joel Ross, Peter Pasceri, Dae Sung Kim, Michael W. Salter, and James Ellis. 2015. "MECP2e1 Isoform Mutation Affects the Form and Function of Neurons Derived from Rett Syndrome Patient IPS Cells." *Neurobiology of Disease* 76:37–45.

Doers, Matthew E., Michael T. Musser, Robert Nichol, Erich R. Berndt, Mei Baker, Timothy M. Gomez, Su-Chun Zhang, Leonard Abbeduto, and Anita Bhattacharyya. 2014. "IPSC-Derived Forebrain Neurons from FXS Individuals Show Defects in Initial Neurite Outgrowth." *Stem Cells and Development* 23(15):1777–87.

Dubé, L., AD Smith, and JP Bolam. 1988. "Identification of Synaptic Terminals of Thalamic or Cortical Origin in Contact with Distinct Medium-Size Spiny Neurons in the Rat Neostriatum." *Journal of Comparative Neurology* 267(4):455–71.

Duflocq, Amandine, Barbara Le Bras, Erika Bullier, François Couraud, and Marc Davenne. 2008. "Nav1.1 Is Predominantly Expressed in Nodes of Ranvier and

Axon Initial Segments." *Mol Cell Neurosci.* 39:180–92.

Dunham, E. T. and I. M. Glynn. 1961. "Adenosinetriphosphatase Activity and the Active Movements of Alkali Metal Ions." *The Journal of Physiology* 156(2):274–93.

Ehrlich, Marc, Sabah Mozafari, Michael Glatza, Laura Starost, Sergiy Velychko, Anna-Lena Hallmann, Qiao-Ling Cui, Axel Schambach, Kee-Pyo Kim, Corinne Bachelin, Antoine Marteyn, Gunnar Hargus, Radia Marie Johnson, Jack Antel, Jared Sterneckert, Holm Zaehres, Hans R. Schöler, Anne Baron-Van Evercooren, and Tanja Kuhlmann. 2017. "Rapid and Efficient Generation of Oligodendrocytes from Human Induced Pluripotent Stem Cells Using Transcription Factors." *Proceedings of the National Academy of Sciences* 114(11):E2243–52.

Eiges, Rachel, Achia Urbach, Mira Malcov, Tsvia Frumkin, Tamar Schwartz, Ami Amit, Yuval Yaron, Amir Eden, Ofra Yanuka, Nissim Benvenisty, and Dalit Ben-Yosef. 2007. "Developmental Study of Fragile X Syndrome Using Human Embryonic Stem Cells Derived from Preimplantation Genetically Diagnosed Embryos." *Cell Stem Cell* 1(5):568–77.

Erceg, Slaven, Dunja Lukovic, Victoria Moreno-Manzano, Miodrag Stojkovic, and Shomi S. Bhattacharya. 2012. "Derivation of Cerebellar Neurons from Human Pluripotent Stem Cells." *Current Protocols in Stem Cell Biology* 1(SUPPL.20):1–10.

Ericson, Johan, Susan Morton, Atsushi Kawakami, Henk Roelink, and Thomas M. Jessell. 1996. "Two Critical Periods of Sonic Hedgehog Signaling Required for the Specification of Motor Neuron Identity." *Cell* 87:661–73.

Espuny-Camacho, Ira, Kimmo A. Michelsen, David Gall, Daniele Linaro, Anja Hasche, Jérôme Bonnefont, Camilia Bali, David Orduz, Angéline Bilheu, Adèle Herpoel, Nelle Lambert, Nicolas Gaspard, Sophie Péron, Serge N. Schiffmann,

Michele Giugliano, Afsaneh Gaillard, and Pierre Vanderhaeghen. 2013. “Pyramidal Neurons Derived from Human Pluripotent Stem Cells Integrate Efficiently into Mouse Brain Circuits In Vivo.” *Neuron* 77(3):440–56.

Farra, N., W. B. Zhang, P. Pasceri, J. H. Eubanks, M. W. Salter, and J. Ellis. 2012. “Rett Syndrome Induced Pluripotent Stem Cell-Derived Neurons Reveal Novel Neurophysiological Alterations.” *Molecular Psychiatry* 17(12):1261–71.

Ferri, Anna L. M., Wei Lin, Yannis E. Mavromatakis, Julie C. Wang, Hiroshi Sasaki, Jeffrey A. Whitsett, and Siew-lan S. L. Ang. 2007. “Foxa1 and Foxa2 Regulate Multiple Phases of Midbrain Dopaminergic Neuron Development in a Dosage-Dependent Manner.” *Development* 134(15):2761–69.

Fiumara, A., C. Brautigam, K. Hyland, R. Sharma, L. Lagae, B. Stoltenborg, G. F. Hoffmann, J. Jaeken, and R. A. Wevers. 2002. “Aromatic L-Amino Acid Decarboxylase Deficiency with Hyperdopaminuria. Clinical and Laboratory Findings in Response to Different Therapies.” *Neuropediatrics* 33:203–8.

Frazer A, Hensler JG. 1999. “Serotonin Receptors.” in *Basic Neurochemistry: Molecular, Cellular and Medical Aspects*, edited by E. Siegel GJ, Agranoff BW, Albers RW, et al. Philadelphia: Lippincott-Raven.

Fusaki, N., H. Ban, A. Nishiyama, K. Saeki, and M. Hasegawa. 2009. “Efficient Induction of Transgene-Free Human Pluripotent Stem Cells Using a Vector Based on Sendai Virus, an RNA Virus That Does Not Integrate into the Host Genome.” *Proc Jpn Acad Ser B Phys Biol Sci* 85:348–62.

Geppert, M., Y. Goda, RE Hammer, C. Li, TW Rosahl, CF Stevens, and TC Südhof. 1994. “Synaptotagmin I: A Major Ca2+ Sensor for Transmitter Release at a Central Synapse.” *Cell* 79(4):717–27.

Gerfen, C. R., T. M. Engber, L. C. Mahan, Z. Susel, T. N. Chase, F. J. Monsma Jr., and D. R. Sibley. 1994. “D1 and D2 Dopamine Receptor-Regulated Gene Expression of Striatonigral and Striatopallidal Neurons.” *Science* 250:1429–32.

Gerfen, Charles R. and D. James Surmeier. 2011. “Modulation of Striatal Projection Systems by Dopamine.” *Annual Review of Neuroscience* 34(1):441–66.

Giardina, G., R. Montioli, S. Gianni, B. Cellini, A. Paiardini, C. B. Voltattorni, and F. Cutruzzola. 2011. “Open Conformation of Human DOPA Decarboxylase Reveals the Mechanism of PLP Addition to Group II Decarboxylases.” *Proc Natl Acad Sci U S A* 108(51):20514–19.

Gilman, Alfred G. 1987. “G Proteins: Transducers of Receptor-Generated Signals.” *Annu Rev Biochem.* 56:615–49.

Grskovic, M., A. Javaherian, B. Strulovici, and G. Q. L. B. Grskovic2011 Daley. 2011. “Induced Pluripotent Stem Cells - Opportunities for Disease Modelling and Drug Discovery.” *Nat Rev Drug Discov* 10.

Gu, Howard, Stephen C. Wall, and Gary Rudnick. 1994. “Stable Expression of Biogenic Amine Transporters Reveals Differences in Inhibitor Sensitivity, Kinetics, and Ion Dependence.” *Journal of Biological Chemistry* 269(10):7124–30.

Gücüyener, K., C. S. Kasapkara, L. Tumer, and M. M. Verbeek. 2014. “Aromatic L-Amino Acid Decarboxylase Deficiency: A New Case from Turkey with a Novel Mutation.” *Ann Indian Acad Neurol* 17:234–36.

Gusel, V. V and D. E. Korzhevskiy. 2015. “NeuN As a Neuronal Nuclear Antigen and Neuron Differentiation Marker.” *Acta Naturae* 7(2):42–47.

Halevy, Tomer, Christian Czech, and Nissim Benvenisty. 2015. “Molecular Mechanisms Regulating the Defects in Fragile x Syndrome Neurons Derived from Human Pluripotent Stem Cells.” *Stem Cell Reports* 4(1):37–46.

Hanaway, Joseph, J. O. A. N. N. Mcconnell, and Martin G. Netsky. 1971. “Histogenesis of the Substantia Nigra , Ventral Tegmental Area of Tsai and Interpeduncular Nucleus : An Autoradiographic Study of the Mesencephalon in

the Rat.” 142:59–73.

Harada, Akihiro, Junlin Teng, Yosuke Takei, Keiko Oguchi, and Nobutaka Hirokawa. 2001. “MAP2 Is Required for Dendrite Elongation , PKA Anchoring in Dendrites , and Proper PKA Signal Transduction.” *J Cell Biol* 158:541–49.

Hegarty, Shane V., Aideen M. Sullivan, and Gerard W. O’Keeffe. 2013. “Midbrain Dopaminergic Neurons: A Review of the Molecular Circuitry That Regulates Their Development.” *Dev Biol* 379(2):123–38.

Helman, G., M. B. Pappa, and P. L. Pearl. 2014. “Widening Phenotypic Spectrum of AADC Deficiency, a Disorder of Dopamine and Serotonin Synthesis.” *JIMD Rep* 17:97.

Heuser, J. E. and TS. Reese. 1973. “Evidence for Recycling of Synaptic Vesicle Membrane During Transmitter Release At the Frog Neuromuscular Junction.” *The Journal of Cell Biology* 57(2):315–44.

Himmelreich, Nastassja, Riccardo Montioli, Mariarita Bertoldi, Carla Carducci, Vincenzo Leuzzi, Corinne Gemperle, Todd Berner, Keith Hyland, Beat Thöny, Georg F. Ho, Carla B. Voltattorni, and Nenad Blau. 2019. “Aromatic Amino Acid Decarboxylase Deficiency : Molecular and Metabolic Basis and Therapeutic Outlook.” (January).

Hoffman, Beth J., Eva Mezey, and Michael J. Brownstein. 1991. “Cloning of a Serotonin Transporter Affected by Antidepressants.” *Science* 254(5031):579–80.

Hou, P., Y. Li, X. Zhang, C. Liu, J. Guan, H. Li, T. Zhao, J. Ye, W. Yang, K. Liu, J. Ge, J. Xu, Q. Zhang, Y. Zhao, and Deng H. 2013. “Pluripotent Stem Cells Induced from Mouse Somatic Cells by Small-Molecule Compounds.” *Science* 341:651–54.

Hu, Yao, Zhuang yin Qu, Shi ying Cao, Qi Li, Lixiang Ma, Robert Krencik, Min Xu, and Yan Liu. 2016. “Directed Differentiation of Basal Forebrain Cholinergic

Neurons from Human Pluripotent Stem Cells." *Journal of Neuroscience Methods* 266:42–49.

Huangfu, Danwei, René Maehr, Wenjun Guo, Astrid Eijkelenboom, Melinda Snitow, Alice E. Chen, and Douglas A. L. B. Huangfu2008 Melton. 2008. "Induction of Pluripotent Stem Cells by Defined Factors Is Greatly Improved by Small-Molecule Compounds." *Nature Biotechnology* 26(7):795–97.

Hussain, T. and MF Lokhandwala. 2003. "Renal Dopamine Receptors and Hypertension." *Exp Biol Med* 228(134–142).

Hwu, W. L., N. C. Lee, Y. H. Chien, S. Muramatsu, and H. Ichinose. 2013. "AADC Deficiency: Occurring in Humans, Modeled in Rodents." *Adv Pharmacol* 68:273–84.

Hwu, W. L., S. Muramatsu, S. H. Tseng, K. Y. Tzen, N. C. Lee, Y. H. Chien, R. O. Snyder, B. J. Byrne, C. H. Tai, and R. M. Wu. 2012. "Gene Therapy for Aromatic L-Amino Acid Decarboxylase Deficiency." *Sci Transl Med* 4:134ra61.

Hyland, K. and P. T. Clayton. 1990. "Aromatic Amino Acid Decarboxylase Deficiency in Twins." *J Inherit Metab Dis* 13(3):301–4.

Hyland, K. and P. T. Clayton. 1992. "Aromatic L-Amino Acid Decarboxylase Deficiency: Diagnostic Methodology." *Clin Chem* 38:2405–10.

Hyland, K., R. A. Surtees, C. Rodeck, and P. T. Clayton. 1992. "Aromatic L-Amino Acid Decarboxylase Deficiency: Clinical Features, Diagnosis, and Treatment of a New Inborn Error of Neurotransmitter Amine Synthesis." *Neurology* 42:1980–88.

Hyman, Carolyn, Magdalena Hofer, Yves Alain Barde, Melissa Juhasz, George D. Yancopoulos, Stephen P. Squinto, and Ronald M. Lindsay. 1991. "BDNF Is a Neurotrophic Factor for Dopaminergic Neurons of the Substantia Nigra." *Nature* 350(6315):230–32.

Ishikawa, Taizo, Keiko Imamura, Takayuki Kondo, Yasushi Koshiba, Satoshi Hara, Hiroshi Ichinose, Mahoko Furujo, Masako Kinoshita, Tomoko Oeda, Jun Takahashi, Ryosuke Takahashi, and Haruhisa Inoue. 2016. "Genetic and Pharmacological Correction of Aberrant Dopamine Synthesis Using Patient IPSCs with BH4 Metabolism Disorders." *Human Molecular Genetics* 25(23):5188–97.

Jacobs, B. L. and C. A. Fornal. 1997. "Serotonin and Motor Activity." *Curr Opin Neurobiol* 7:820–25.

Jacobs, Frank M. J., Jesse V Veenvliet, Wadia H. Almirza, Elisa J. Hoekstra, Lars Von Oerthel, Annemarie J. A. Van Der Linden, Roel Neijts, Marian Groot Koerkamp, Dik Van Leenen, Frank C. P. Holstege, J. Peter H. Burbach, and Marten P. Smidt. 2011. "Retinoic Acid-Dependent and -Independent Gene-Regulatory Pathways of Pitx3 in Meso-Diencephalic Dopaminergic Neurons." *Development* 138:5213–22.

Jankovic, J., S. Chen, and W. D. Le. 2005. "The Role of Nurr1 in the Development of Dopaminergic Neurons and Parkinson ' s Disease." *Prog. Neurobiol* 77:128–38.

Jo, Junghyun, Yixin Xiao, Alfred Xuyang Sun, Engin Cukuroglu, Hoang-Dai Tran, Jonathan Göke, Zi Ying Tan, Tzuen Yih Saw, Cheng-Peow Tan, Hidayat Lokman, Younghwan Lee, Donghoon Kim, Han Seok Ko, Seong-Oh Kim, Jae Hyeon Park, Nam-Joon Cho, Thomas M. Hyde, Joel E. Kleinman, Joo Heon Shin, Daniel R. Weinberger, Eng King Tan, Hyunsoo Shawn, and Huck Hui Ng. 2016. "Midbrain-like Organoids from Human Pluripotent Stem Cells Contain Functional Dopaminergic and Neuromelanin-Producing Neurons." *Cell Stem Cell* 19(2):248–57.

Joseph, Bertrand, Åsa Wallén-mackenzie, Gérard Benoit, Takashi Murata, Sam Okret, Thomas Perlmann, Bertrand Joseph, Asa Wallen-mackenzie, Gerard Benoit, Takashi Murata, Eliza Joodmardi, and Sam Okrett. 2003. "P57(Kip2) Cooperates with Nurr1 in Developing Dopamine Cells." *Proc. Natl. Acad. Sci.* 100:15619–

24.

Joyner, Alexandra L., Aimin Liu, and Sandrine Millet. 2000. “Otx2 , Gbx2 and Fgf8 Interact to Position and Maintain a Mid – Hindbrain Organizer Alexandra L.” *Curr. Opin. Cell Biol.* (12):736–41.

Judson, Robert L., Joshua E. Babiarz, Monica Venere, and Robert Blelloch. 2009. “Embryonic Stem Cell-Specific MicroRNAs Promote Induced Pluripotency.” *Nature Biotechnology* 27(5):459–61.

Jung-Klawitter, Sabine, Nenad Blau, Attila Sebe, Juliane Ebersold, Gudrun Göhring, and Thomas Opladen. 2016. “Generation of an IPSC Line from a Patient with Tyrosine Hydroxylase (TH) Deficiency : TH-1 IPSC.” *Stem Cell Research* 17(3):580–83.

Kawaguchi, Yasuo, Charles J. Wilson, Sarah J. Augood, and Piers C. Emson. 1995. “Striatal Interneurones: Chemical, Physiological and Morphological Characterization.” *Trends in Neurosciences* 18(12):527–35.

Kawano, H., K. Ohyama, K. Kawamura, and I. Nagatsu. 1995. “Migration of Dopaminergic Neurons in the Embryonic Mesencephalon Of.” *Dev. Brain Res.* 86:101–13.

Kebabian, John W. and Donald B. Caine. 1979. “Multiple Receptors for Dopamine.” *Nature* 277:93–96.

Kele, Julianna, Nicolas Simplicio, Anna L. M. Ferri, Helena Mira, François Guillemot, Ernest Arenas, and Siew-lan Ang. 2006. “Neurogenin 2 Is Required for the Development of Ventral Midbrain Dopaminergic Neurons.” *Development* 133:495–505.

Kema, I. P., E. G. de Vries, and F. A. Muskiet. 2000. “Clinical Chemistry of Serotonin and Metabolites.” *J Chromatogr B Biomed Sci Appl* 747:33–48.

Kikuchi, Tetsuhiro, Asuka Morizane, Daisuke Doi, Hiroaki Magotani, Hirotaka Onoe, Takuya Hayashi, Hiroshi Mizuma, Sayuki Takara, Ryosuke Takahashi, Haruhisa Inoue, Satoshi Morita, Michio Yamamoto, Keisuke Okita, Masato Nakagawa, Malin Parmar, and Jun Takahashi. 2017. "Human IPS Cell-Derived Dopaminergic Neurons Function in a Primate Parkinson's Disease Model." *Nature* 548(7669):592–96.

Kilty, John E., Dominique Lorang, and Susan G. Amara. 1991. "Cloning and Expression of a Cocaine-Sensitive Rat Dopamine Transporter." *Science* 254:578–79.

Kirkeby, A., S. Grealish, D. A. Wolf, J. Nelander, J. Wood, M. Lundblad, O. Lindvall, and M. Parmar. 2012. "Generation of Regionally Specified Neural Progenitors and Functional Neurons from Human Embryonic Stem Cells under Defined Conditions." *Cell Rep* 1(6):703–14.

Kirkeby, A., J. Nelander, and M. Parmar. 2012. "Generating Regionalized Neuronal Cells from Pluripotency, a Step-by-Step Protocol." *Front Cell Neurosci* 6:64.

Klimanskaya, Irina, Young Chung, Sandy Becker, Shi Jiang Lu, and Robert Lanza. 2006. "Human Embryonic Stem Cell Lines Derived from Single Blastomeres." *Nature* 444(7118):481–85.

Kojima, Karin, Takeshi Nakajima, Naoyuki Taga, Akihiko Miyauchi, Mitsuhiro Kato, Ayumi Matsumoto, Takahiro Ikeda, Kazuyuki Nakamura, Tetsuo Kubota, Hiroaki Mizukami, Sayaka Ono, Yoshiyuki Onuki, Toshihiko Sato, and Hitoshi Osaka. 2019. "Gene Therapy Improves Motor and Mental Function of Aromatic L -Amino Acid Decarboxylase Deficiency." 322–33.

Kondo, Takayuki, Keiko Imamura, Misato Funayama, Kayoko Tsukita, Michiyo Miyake, Akira Ohta, Knut Woltjen, Masato Nakagawa, Takashi Asada, Tetsuaki Arai, Shinobu Kawakatsu, Yuishin Izumi, Ryuji Kaji, Nobuhisa Iwata, and Haruhisa Inoue. 2017. "IPSC-Based Compound Screening and In Vitro Trials

Identify a Synergistic Anti-Amyloid β Combination for Alzheimer's Disease." *Cell Reports* 21(8):2304–12.

Kriks, Sonja, Jae-Won W. Shim, Jinghua Piao, Yosif M. Ganat, Dustin R. Wakeman, Zhong Xie, Luis Carrillo-Reid, Gordon Auyeung, Chris Antonacci, Amanda Buch, Lichuan Yang, M. Flint Beal, D. James Surmeier, Jeffrey H. Kordower, Viviane Tabar, and Lorenz Studer. 2011. "Dopamine Neurons Derived from Human ES Cells Efficiently Engraft in Animal Models of Parkinson's Disease." *Nature* 480(7378):547–51.

Kurian, M. A., P. Gissen, M. Smith, S. Heales Jr., and P. T. Clayton. 2011. "The Monoamine Neurotransmitter Disorders: An Expanding Range of Neurological Syndromes." *Lancet Neurol* 10(8):721–33.

De la Fuente, Carmen, Derek G. Burke, Simon Eaton, and Simon J. R. Heales. 2017. "Neurochemistry International Inhibition of Neuronal Mitochondrial Complex I or Lysosomal Glucocerebrosidase Is Associated with Increased Dopamine and Serotonin Turnover." *Neurochemistry International* 109:94–100.

Lancaster, Madeline A., Nina S. Corsini, Simone Wolfinger, E. Hilary Gustafson, Alex W. Phillips, Thomas R. Burkard, Tomoki Otani, Frederick J. Livesey, and Juergen A. Knoblich. 2017. "Guided Self-Organization and Cortical Plate Formation in Human Brain Organoids." *Nature Biotechnology* 35(7):659–66.

Lancaster, Madeline A. and Juergen A. Knoblich. 2014. "Organogenesisin a Dish: Modeling Development and Disease Using Organoid Technologies." *Science* 345(6194):283–93.

Lapper, S. R. and JP Bolam. 1992. "Input From the Frontal Cortex and the Nucleus To Cholinergic Interneurons in the Dorsal of the Rat." *Neuroscience* 51(3):533–45.

Larimore, Jennifer, Pearl V. Ryder, Kun Yong Kim, L. Alex Ambrose, Christopher Chapleau, Gaston Calfa, Christina Gross, Gary J. Bassell, Lucas Pozzo-Miller, Yoland Smith, Konrad Talbot, In Hyun Park, and Victor Faundez. 2013. "MeCP2

Regulates the Synaptic Expression of a Dysbindin-BLOC-1 Network Component in Mouse Brain and Human Induced Pluripotent Stem Cell-Derived Neurons." *PLoS ONE* 8(6).

Lee, H. F. J., C. R. Tsai, C. S. Chi, T. M. Chang, and H. F. J. Lee. 2009. "Aromatic L-Amino Acid Decarboxylase Deficiency in Taiwan." *Eur J Paediatr Neurol* 13(2):135–40.

Lee, N. C., S. I. Muramatsu, Y. H. Chien, W. S. Liu, W. H. Wang, C. H. Cheng, M. K. Hu, P. W. Chen, K. Y. Tzen, B. J. Byrne, and W. L. Hwu. 2015. "Benefits of Neuronal Preferential Systemic Gene Therapy for Neurotransmitter Deficiency." *Mol Ther*.

Lee, N. C., Y. D. Shieh, Y. H. Chien, K. Y. Tzen, I. S. Yu, P. W. Chen, M. H. K. Hu, M. H. K. Hu, S. Muramatsu, H. Ichinose, and W. L. Hwu. 2013. "Regulation of the Dopaminergic System in a Murine Model of Aromatic L-Amino Acid Decarboxylase Deficiency." *Neurobiol Dis* 52:177–90.

Lee, Ni-chung, Yu-may Lee, Pin-wen Chen, Barry J. Byrne, and Wuh-liang Hwu. 2016. "Mutation-Adapted U1 SnRNA Corrects a Splicing Error of the Dopa Decarboxylase Gene." 25(23):5142–47.

Lees, A. J., J. Hardy, and T. Revesz. 2009. "Parkinson's Disease." *Lancet* 373:2055–66.

Lenz, Michael, Roman Goetzke, Arne Schenk, Claudia Schubert, Jürgen Veeck, Hatim Hemeda, Steffen Koschmieder, Martin Zenke, Andreas Schuppert, and Wolfgang Wagner. 2015. "Epigenetic Biomarker to Support Classification into Pluripotent and Non-Pluripotent Cells." *Scientific Reports* 5:1–7.

Leuzzi, V., M. Mastrangelo, A. Polizzi, C. Artiola, A. B. van Kuilenburg, C. Carducci, M. Ruggieri, R. Barone, B. Tavazzi, N. G. Abeling, L. Zoetekouw, V. Sofia, M. Zappia, and C. Carducci. 2015. "Report of Two Never Treated Adult Sisters with Aromatic L-Amino Acid Decarboxylase Deficiency: A Portrait of the Natural

History of the Disease or an Expanding Phenotype?" *JIMD Rep* 15:39–45.

Lin, Wei, Emmanouil Metzakopian, Yannis E. Mavromatakis, Nan Gao, Nikolaos Balaskas, Hiroshi Sasaki, James Briscoe, Jeffrey A. Whitsett, Martyn Goulding, Klaus H. Kaestner, and Siew Lan Ang. 2009. "Foxa1 and Foxa2 Function Both Upstream of and Cooperatively with Lmx1a and Lmx1b in a Feedforward Loop Promoting Mesodiencephalic Dopaminergic Neuron Development." *Dev. Biol.* 333(2):386–96.

Little, Daniel, Robin Ketteler, Paul Gissen, and Michael J. Devine. 2019. "Using Stem Cell-Derived Neurons in Drug Screening for Neurological Diseases." *Neurobiology of Aging* 78:130–41.

Livide, Gabriella, Tommaso Patriarchi, Mariangela Amenduni, Sonia Amabile, Dag Yasui, Eleonora Calcagno, Caterina Lo Rizzo, Giulia De Falco, Cristina Ulivieri, Francesca Ariani, Francesca Mari, Maria Antonietta Mencarelli, Johannes Wilhelm Hell, Alessandra Renieri, and Ilaria Meloni. 2015. "GluD1 Is a Common Altered Player in Neuronal Differentiation from Both MECP2-Mutated and CDKL5-Mutated IPS Cells." *European Journal of Human Genetics* 23(2):195–201.

Lovenberg, W., H. Weissbach, and S. Udenfriend. 1962. "Aromatic L-Amino Acid Decarboxylase." *J Biol Chem.* 237(1):89–93.

Lu, J., X. Zhong, H. Liu, L. Hao, C. T. Huang, M. A. Sherafat, J. Jones, M. Ayala, L. Li, and S. C. Zhang. 2016. "Generation of Serotonin Neurons from Human Pluripotent Stem Cells." *Nat Biotechnol* 34:89–94.

Mani, M. and TA Ryan. 2009. "Live Imaging of Synaptic Vesicle Release and Retrieval in Dopaminergic Neurons." *Frontiers in Neural Circuits* 3(June):1–9.

La Manno, G., D. Gyllborg, S. Codeluppi, K. Nishimura, C. Salto, A. Zeisel, L. E. Borm, S. R. Stott, E. M. Toledo, J. C. Villaescusa, P. Lonnerberg, J. Ryge, R. A. Barker, E. Arenas, and S. Linnarsson. 2016. "Molecular Diversity of Midbrain

Development in Mouse, Human, and Stem Cells." *Cell* 167:566-580.e19.

Marchand, R. and L. J. Poirier. 1983. "Isthmic Origin of Neurons of the Rat Substantia Nigra." *Neuroscience* 9:373–81.

Marti, Elisa, David A. Bumcrot, Ritsuko Takada, and Andrew P. Mcmahon. 1995. "Requirement of 19K Form of Sonic Hedgehog for Induction of Distinct Ventral Cell Types in CNS Explants." *Nature* 375:322–25.

Mayshar, Yoav, Uri Ben-David, Neta Lavon, Juan Carlos Biancotti, Benjamin Yakir, Amander T. Clark, Kathrin Plath, William E. Lowry, and Nissim Benvenisty. 2010. "Identification and Classification of Chromosomal Aberrations in Human Induced Pluripotent Stem Cells." *Cell Stem Cell* 7(4):521–31.

McMahon, Harvey T., Markus Missler, Cai Li, and Thomas C. Südhof. 1995. "Complexins: Cytosolic Proteins That Regulate SNAP Receptor Function." *Cell* 83(1):111–19.

Miller, G. M. 2011. "The Emerging Role of Trace Amine Associated Receptor 1 in the Functional Regulation of Monoamine Transporters and Dopaminergic Activity." *J Neurochem.* 116(2):164–76.

Miller, Justine D., Yosif M. Ganat, Sarah Kishinevsky, Robert L. Bowman, Becky Liu, Edmund Y. Tu, Pankaj K. Mandal, Elsa Vera, Jae-won Shim, Sonja Kriks, Tony Taldone, Noemi Fusaki, Mark J. Tomishima, Dimitri Krainc, Teresa A. Milner, Derrick J. Rossi, and Lorenz Studer. 2013. "Human IPSC-Based Modeling of Late-Onset Disease via Progerin-Induced Aging." *Stem Cell* 13(6):691–705.

Millet, S., Campbell K., D. J. Epstein, K. Losos, E. Harris, and A. L. Joyner. 1999. "A Role for Gbx2 in Repression of Otx2 and Positioning the Mid / Hindbrain Organizer." *Nature* (401):161–64.

Mills, Philippa B., Robert A. H. Surtees, Michael P. Champion, Clare E. Beesley, Neil Dalton, Peter J. Scamber, Simon J. R. Heales, Anthony Briddon, Irene

Scheimberg, Georg F. Hoffmann, Johannes Zschocke, and Peter T. Clayton. 2005. “Neonatal Epileptic Encephalopathy Caused by Mutations in the PNPO Gene Encoding Pyridox(Am)Ine 5′-Phosphate Oxidase.” *Human Molecular Genetics* 14(8):1077–86.

Missale, C., SR Nash, SW Robinson, M. Jaber, and MG Caron. 1988. “Dopamine Receptors: From Structure to Function.” *Physiological Reviews* 78(1):189–225.

Montioli, R., M. Dindo, A. Giorgetti, S. Piccoli, B. Cellini, and C. B. Voltattorni. 2014. “A Comprehensive Picture of the Mutations Associated with Aromatic Amino Acid Decarboxylase Deficiency: From Molecular Mechanisms to Therapy Implications.” *Hum Mol Genet* 23:5429–40.

Montioli, R., E. Oppici, B. Cellini, A. Roncador, M. Dindo, and C. B. Voltattorni. 2013. “S250F Variant Associated with Aromatic Amino Acid Decarboxylase Deficiency: Molecular Defects and Intracellular Rescue by Pyridoxine.” *Hum Mol Genet* 22:1615–24.

Montioli, R., A. Paiardini, M. A. Kurian, M. Dindo, G. Rossignoli, S. J. Heales, S. Pope, C. B. Voltattorni, and M. Bertoldi. 2016. “The Novel R347g Pathogenic Mutation of Aromatic Amino Acid Decarboxylase Provides Additional Molecular Insights into Enzyme Catalysis and Deficiency.” *Biochim Biophys Acta* 1864:676–82.

Moriyama, Y. and N. Nelson. 1987. “The Purified ATPase from Chromaffin Granule Membranes Is an Anion-Dependent Proton Pump.” *Journal of Biological Chemistry* 262(19):9175–80.

Muotri, Alysson R., Maria C. N. Marchetto, Nicole G. Coufal, Ruth Oefner, Gene Yeo, Kinichi Nakashima, and Fred H. Gage. 2010. “L1 Retrotransposition in Neurons Is Modulated by MeCP2.” *Nature* 468(7322):443–46.

Muramatsu, S., K. Fujimoto, S. Kato, H. Mizukami, S. Asari, K. Ikeguchi, T. Kawakami, M. Urabe, A. Kume, T. Sato, E. Watanabe, K. Ozawa, and I. Nakano.

2010. “A Phase I Study of Aromatic L-Amino Acid Decarboxylase Gene Therapy for Parkinson’s Disease.” *Mol Ther* 18:1731–35.

Nayler, Sam, Magtouf Gatei, Sergei Kozlov, Richard Gatti, Jessica C. Mar, Christine A. Wells, Martin Lavin, and Ernst Wolvetang. 2012. “Induced Pluripotent Stem Cells from Ataxia-Telangiectasia Recapitulate the Cellular Phenotype.” *Stem Cells Translational Medicine* 1(7):523–35.

Nayler, Sam P., Joseph E. Powell, Darya P. Vanichkina, Othmar Korn, Christine A. Wells, Refik Kanjhan, Jian Sun, Ryan J. Taft, Martin F. Lavin, and Ernst J. Wolvetang. 2017. “Human IPSC-Derived Cerebellar Neurons from a Patient with Ataxia-Telangiectasia Reveal Disrupted Gene Regulatory Networks.” *Frontiers in Cellular Neuroscience* 11(October):1–15.

Nelander, J., J. B. Hebsgaard, and M. Parmar. 2009. “Organization of the Human Embryonic Ventral Mesencephalon.” *Gene Expr Patterns* 9:555–61.

Ng, J., A. Papandreou, S. J. Heales, and M. A. Kurian. 2015. “Monoamine Neurotransmitter Disorders--Clinical Advances and Future Perspectives.” *Nat Rev Neurol* 11(10):567–84.

Nguyen, HN, B. Byers, B. Cord, A. Shcheglovitov, J. Byrne, P. Gujar, K. Kee, B. Schüle, RE Dolmetsch, W. Langston, TD Palmer, and RR Pera. 2011. “LRRK2 Mutant IPSC-Derived DA Neurons Demonstrate Increased Susceptibility to Oxidative Stress.” *Cell Stem Cell.* 8(3):267–80.

Nicholas, Cory R., Jiadong Chen, Yunshuo Tang, Derek G. Southwell, Nadine Chalmers, Daniel Vogt, Christine M. Arnold, Ying Jiun J. Chen, Edouard G. Stanley, Andrew G. Elefanty, Yoshiki Sasai, Arturo Alvarez-Buylla, John L. R. Rubenstein, and Arnold R. Kriegstein. 2013. “Functional Maturation of HPSC-Derived Forebrain Interneurons Requires an Extended Timeline and Mimics Human Neural Development.” *Cell Stem Cell* 12(5):573–86.

Niclis, Jonathan C., Anita Pinar, John M. Haynes, Walaa Alsanie, Robert Jenny,

Mirella Dottori, and David S. Cram. 2013. “Characterization of Forebrain Neurons Derived from Late-Onset Huntington’s Disease Human Embryonic Stem Cell Lines.” *Frontiers in Cellular Neuroscience* 7:1–13.

Nutt, Samuel E., Eun Ah Chang, Steven T. Suhr, Laura O. Schlosser, Sarah E. Mondello, Chet T. Moritz, Jose B. Cibelli, and Philip J. Horner. 2013. “Caudalized Human IPSC-Derived Neural Progenitor Cells Produce Neurons and Glia but Fail to Restore Function in an Early Chronic Spinal Cord Injury Model.” *Experimental Neurology* 248:491–503.

Ohm, G. 1827. *Die GalvanischeKette: Methematisch Bearbeitet*. Berlin, Germany: TH Tiemann.

Okita, K., M. Nakagawa, H. Hyenjong, T. Ichisaka, and S. Yamanaka. 2008. “Generation of Mouse Induced Pluripotent Stem Cells without Viral Vectors.” *Science* 322:949–53.

Onali, Pierluigi, Maria C. Olianas, and Gian Luigi Gessa. 1984. “Selective Blockade of Dopamine D-1 Receptors by SCH 23390 Discloses Striatal Dopamine D-2 Receptors Mediating the Inhibition of Adenylate Cyclase in Rats.” *European Journal of Pharmacology* 99(1):127–28.

Ono, Y., T. Nakatani, Y. Sakamoto, E. Mizuhara, Y. Minaki, M. Kumai, A. Hamaguchi, M. Nishimura, Y. Inoue, H. Hayashi, J. Takahashi, and T. Imai. 2007. “Differences in Neurogenic Potential in Floor Plate Cells along an Anteroposterior Location: Midbrain Dopaminergic Neurons Originate from Mesencephalic Floor Plate Cells.” *Development* 134:3213–25.

Ono, Yuichi, Tomoya Nakatani, Yasuko Minaki, and Minoru Kumai. 2010. “The Basic Helix-Loop-Helix Transcription Factor Nato3 Controls Neurogenic Activity in Mesencephalic Floor Plate Cells.” *Development* 137:1897–1906.

Pickel, V. M., J. Chan, and S. R. Sesack. 1992. “Cellular Basis for Interactions between Catecholaminergic Afferents and Neurons Containing Leu-enkephalin-like

Immunoreactivity in Rat Caudate-putamen Nuclei." *Journal of Neuroscience Research* 31(2):212–30.

Placzek, M. and J. Briscoe. 2005. "The Floor Plate: Multiple Cells, Multiple Signals." *Nat Rev Neurosci* 6:230–40.

Pons, R., B. Ford, C. A. Chiriboga, P. T. Clayton, V. Hinton, K. Hyland, R. Sharma, and D. C. De Vivo. 2004. "Aromatic L-Amino Acid Decarboxylase Deficiency: Clinical Features, Treatment, and Prognosis." *Neurology* 62(7):1058–65.

Prakash, Nilima, Claude Brodski, Thorsten Naserke, Eduardo Puelles, Robindra Gogoi, Anita Hall, Markus Panhuysen, Diego Echevarria, Lori Sussel, DM Daniela M. Vogt DM Weisenhorn, Salvador Martinez, Ernest Arenas, Antonio Simeone, and Wolfgang Wurst. 2006. "A Wnt1-Regulated Genetic Network Controls the Identity and Fate of Midbrain-Dopaminergic Progenitors in Vivo." *Development* 133(1):89–98.

Raley-Susman, Kathleen M., Edward J. Cragoe, Robert M. Sapolsky, and Ron R. Kopito. 1991. "Regulation of Intracellular PH in Cultured Hippocampal Neurons by an Amiloride-Insensitive Na+/H+ Exchanger." *Journal of Biological Chemistry* 266(5):2739–45.

Reid, W. D., L. Volicer, H. Smookler, M. A. Beaven, and B. B. Brodie. 1968. "Brain Amines and Temperature Regulation." *Pharmacology* 1:329–44.

Reim, Kerstin, Michael Mansour, Frederique Varoqueaux, Harvey T. McMahon, Thomas C. Südhof, Nils Brose, and Christian Rosenmund. 2001. "Complexins Regulate a Late Step in Ca2+-Dependent Neurotransmitter Release." *Cell* 104(1):71–81.

Reyes, Stefanie, Yuhong Fu, Kay Double, Lachlan Thompson, Deniz Kirik, George Paxinos, and Glenda M. Halliday. 2012. "GIRK2 Expression in Dopamine Neurons of the Substantia Nigra and Ventral Tegmental Area." *J Comp Neurol* 520:2591–2607.

Rhinn, Muriel, Andrée Dierich, William Shawlot, Richard R. Behringer, and Marianne Le Meur. 1998. “Sequential Roles for Otx2 in Visceral Endoderm and Neuroectoderm for Forebrain and Midbrain Induction and Specification.” *Development* 856:845–56.

Roelink, H., J. A. Porter, C. Chiang, and Y. Tanabe. 1995. “Floor Plate and Motor Neuron Induction by Different Concentrations of the Amino-Terminal Cleavage Product of Sonic Hedgehog Autoproteolysis.” *Cell* 81:445–55.

Rubí, Blanca and Pierre Maechler. 2010. “Minireview : New Roles for Peripheral Dopamine on Metabolic Control and Tumor Growth : Let ’ s Seek the Balance.” *Endocrinology*. 151:5570–81.

Ryan, Scott D., Nima Dolatabadi, Shing Fai Chan, Xiaofei Zhang, Mohd Waseem Akhtar, James Parker, Frank Soldner, Carmen R. Sunico, Saumya Nagar, Maria Talantova, Brian Lee, Kevin Lopez, Anthony Nutter, Bing Shan, Elena Molokanova, Yaoyang Zhang, Xuemei Han, Tomohiro Nakamura, Eliezer Masliah, John R. Yates, Nobuki Nakanishi, Aleksander Y. Andreyev, Shu Ichi Okamoto, Rudolf Jaenisch, R. Ambasudhan, and Stuart A. Lipton. 2013. “Isogenic Human IPSC Parkinson’s Model Shows Nitrosative Stress-Induced Dysfunction in MEF2-PGC1α Transcription.” *Cell* 155(6):1351.

Santos, Renata, Krishna C. Vadodaria, Baptiste N. Jaeger, Arianna Mei, Sabrina Lefcochilos-Fogelquist, Ana P. D. Mendes, Galina Erikson, Maxim Shokhirev, Lynne Randolph-Moore, Callie Fredlender, Sonia Dave, Ruth Oefner, Conor Fitzpatrick, Monique Pena, Jerika J. Barron, Manching Ku, Ahmet M. Denli, Bilal E. Kerman, Patrick Charnay, John R. Kelsoe, Maria C. Marchetto, and Fred H. Gage. 2017. “Differentiation of Inflammation-Responsive Astrocytes from Glial Progenitors Generated from Human Induced Pluripotent Stem Cells.” *Stem Cell Reports* 8(6):1757–69.

Sasaki, Hiroshi, Chi-chung Hui, Masato Nakafuku, and Hisato Kondoh. 1997. “A Binding Site for Gli Proteins Is Essential for HNF-3β Floor Plate Enhancer

Activity in Transgenics and Can Respond to Shh in Vitro." *Development* 1322:1313–22.

Schwiening, C. J. and W. F. Boron. 1994. "Regulation of Intracellular PH in Pyramidal Neurones from the Rat Hippocampus by Na(+)-dependent Cl(-)-HCO3- Exchange." *The Journal of Physiology* 475(1):59–67.

Seibler, Philip, Lena F. Burbulla, Marija Dulovic, Simone Zittel, Johanne Heine, Thomas Schmidt, Franziska Rudolph, Ana Westenberger, Aleksandar Rakovic, Dimitri Krainc, and Christine Klein. 2018. "Iron Overload Is Accompanied by Mitochondrial and Lysosomal Dysfunction in WDR45 Mutant Cells." *Brain* 141:3052–64.

Sheridan, Steven D., Kraig M. Theriault, Surya A. Reis, Fen Zhou, Jon M. Madison, Laurence Daheron, Jeanne F. Loring, and Stephen J. Haggarty. 2011. "Epigenetic Characterization of the FMR1 Gene and Aberrant Neurodevelopment in Human Induced Pluripotent Stem Cell Models of Fragile X Syndrome." *PLoS ONE* 6(10).

Shi, Yan, Caroline Desponts, Jeong Tae Do, Heung Sik Hahm, Hans R. Schöler, and Sheng L. B. Shi2008 Ding. 2008. "Induction of Pluripotent Stem Cells from Mouse Embryonic Fibroblasts by Oct4 and Klf4 with Small-Molecule Compounds." *Cell Stem Cell* 3(5):568–74.

Shi, Yichen, Peter Kirwan, and Frederick J. Livesey. 2012. "Directed Differentiation of Human Pluripotent Stem Cells to Cerebral Cortex Neurons and Neural Networks." *Nature Protocols* 7(10):1836–46.

Shih, De-Fen F., Chung-Der D. Hsiao, Ming-Yuan Y. Min, Wen-Sung S. Lai, Chianne-Wen W. Yang, Wang-Tso T. Lee, and Shyh-Jye J. Lee. 2013. "Aromatic L-Amino Acid Decarboxylase (AADC) Is Crucial for Brain Development and Motor Functions." *PLoS ONE* 8:e71741.

Shimada, S., S. Kitayama, C. L. Lin, A. Patel, E. Nanthakumar, P. Gregor, M. Kuhar, and G. Uhl. 1991. "Cloning and Expression of a Cocaine-Sensitive Dopamine

Transporter Complementary DNA." *Science* 254(50 mM):576–78.

Smidt, Marten P., Ceriel H. J. Asbreuk, Joke J. Cox, Haixu Chen, Randy L. Johnson, and J. Peter H. Burbach. 2000. "A Second Independent Pathway for Development of Mesencephalic Dopaminergic Neurons Requires Lmx1b." *Nature Neuroscience* 3:337–41.

Söllner, Thomas, Sidney W. Whiteheart, Michael Brunner, Hediye Erdjument Bromage, Scott Geromanos, Paul Tempst, and James E. Rothman. 1993. "SNAP Receptors Implicated in Vesicle Targeting and Fusion." *Nature* 362:318–24.

Squire, S., B. Darwin, F. Bloom, S. du Lac, and A. Ghosh. 2008. *Fundamental Neuroscience*. Burlington, MA: Elsevier.

Stott, Simon R. W., Emmanouil Metzakopian, Wei Lin, Klaus H. Kaestner, Rene Hen, and Siew-lan Ang. 2013. "Foxa1 and Foxa2 Are Required for the Maintenance of Dopaminergic Properties in Ventral Midbrain Neurons at Late Embryonic Stages." *J. Neurosci* 33:8022–34.

Strasser, B., J. M. Gostner, and D. Fuchs. 2016. "Mood, Food, and Cognition: Role of Tryptophan and Serotonin." *Curr Opin Clin Nutr Metab Care* 19:55–61.

Südhof, Thomas C. 2004. "The Synaptic Vesicle Cycle." *Annual Review of Neuroscience* 27(1):509–47.

Takahashi, K., K. Tanabe, M. Ohnuki, M. Narita, T. Ichisaka, K. Tomoda, and S. Yamanaka. 2007. "Induction of Pluripotent Stem Cells from Adult Human Fibroblasts by Defined Factors." *Cell* 131(5):861–72.

Takahashi, Kazutoshi and Shinya Yamanaka. 2016. "A Decade of Transcription Factor-Mediated Reprogramming to Pluripotency." *Nat Rev Mol Cell Biol.* 17(3):183–93.

Tang, Xin, Julie Kim, Li Zhou, Eric Wengert, Lei Zhang, Zheng Wu, Cassiano

Carromeu, Alysson R. Muotri, Maria C. N. Marchetto, Fred H. Gage, and Gong Chen. 2016. “KCC2 Rescues Functional Deficits in Human Neurons Derived from Patients with Rett Syndrome.” *Proceedings of the National Academy of Sciences* 113(3):751–56.

Tay, S. K., K. S. Poh, K. Hyland, Y. W. Pang, H. T. Ong, P. S. Low, and D. L. Goh. 2007. “Unusually Mild Phenotype of AADC Deficiency in 2 Siblings.” *Mol Genet Metab* 91:374–78.

Thomson, J. A., J. ItsKovitz-Eldor, S. S. Shapiro, M. A. Waknitz, J. J. Swierhiel, V. S. Marshall, J. M. Jones, J. A. Thomson, J. Itskovitz-Eldor, S. S. Shapiro, M. A. Waknitz, J. J. Swiergiel, V. S. Marshall, and J. M. Jones. 1998. “Embryonic Stem Cell Lines Derived from Human Blastocysts.” *Science* 282(5391):1145–47.

Tissari, A. H., P. S. Schonhofer, D. F. Bogdanski, and B. B. Brodie. 1969. “Mechanism of Biogenic Amine Transport. II. Relationship between Na+ and the Mechanism of Ouabain Blockade of the Accumulation of Serotonin and Noradrenalin by Synaptosomes.” *Molecular Pharmacology* 5:593–604.

Toulouse, A. and A. M. Sullivan. 2008. “Progress in Parkinson’s Disease-Where Do We Stand?” *Prog Neurobiol* 85:376–92.

Trilck, M., R1 Hübner, and MJ Frech. 2016. *Generation and Neuronal Differentiation of Patient-Specific Induced Pluripotent Stem Cells Derived from Niemann-Pick Type C1 Fibroblasts*.

Trilck, Michaela, Rayk Hübner, Philip Seibler, Christine Klein, Arndt Rolfs, and Moritz J. Frech. 2013. “Niemann-Pick Type C1 Patient-Specific Induced Pluripotent Stem Cells Display Disease Specific Hallmarks.” *Orphanet Journal of Rare Diseases* 8:144.

Trilck, Michaela, Franziska Peter, Chaonan Zheng, Marcus Frank, Kostantin Dobrenis, Hermann Mascher, Arndt Rolfs, and Moritz J. Frech. 2017. “Diversity of Glycosphingolipid GM2 and Cholesterol Accumulation in NPC1 Patient-

Specific IPSC-Derived Neurons." *Brain Research* 1657:52–61.

Tu, Jiajie, Dandan Cao, Lu Li, Hoi Hung Cheung, and Wai Yee Chan. 2018. "MicroRNA Profiling during Directed Differentiation of Cortical Interneurons from Human-Induced Pluripotent Stem Cells." *FEBS Open Bio* 8(4):502–12.

Tzschentke, T. M. and W. J. Schmidt. 2000. "Functional Relationship among Medial Prefrontal Cortex, Nucleus Accumbens, and Ventral Tegmental Area in Locomotion and Reward." *Crit Rev Neurobiol* 14:131–42.

Urbach, Achia, Ori Bar-Nur, George Q. Daley, and Nissim Benvenisty. 2010. "Differential Modeling of Fragile X Syndrome by Human Embryonic Stem Cells and Induced Pluripotent Stem Cells." *Cell Stem Cell* 6(5):407–11.

Veenvliet, Jesse V, Maria T. M. Alves, Willemieke M. Kouwenhoven, Lars Von Oerthel, Jamie L. Lim, Annemarie J. A. Van Der Linden, Marian J. A. Groot Koerkamp, Frank C. P. Holstege, Marten P. Smidt, Jesse V Veenvliet, Maria T. M. Alves, Willemieke M. Kouwenhoven, Lars Von Oerthel, Jamie L. Lim, Annemarie J. A. Van Der Linden, Marian J. A. Groot Koerkamp, Frank C. P. Holstege, and Marten P. Smidt. 2013. "Specification of Dopaminergic Subsets Involves Interplay of En1 and Pitx3." *Development* 140:3373–84.

Verbeek, M. M., P. B. Geurtz, M. A. Willemsen, and R. A. Wevers. 2007. "Aromatic L-Amino Acid Decarboxylase Enzyme Activity in Deficient Patients and Heterozygotes." *Mol Genet Metab* 90:363–69.

Vincent, Andrea M., Michelle TenBroeke, and Kenneth Maiese. 1999. "Neuronal Intracellular PH Directly Mediates Nitric Oxide-Induced Programmed Cell Death." *Journal of Neurobiology* 40(2):171–84.

Vink, Conrad A., John R. Counsell, Dany P. Perocheau, Rajvinder Karda, Suzanne M. K. Buckley, Martijn H. Brugman, Melanie Galla, Axel Schambach, Tristan R. McKay, Simon N. Waddington, and Steven J. Howe. 2017. "Eliminating HIV-1 Packaging Sequences from Lentiviral Vector Proviruses Enhances Safety and

Expedites Gene Transfer for Gene Therapy." *Molecular Therapy* 25(8):1790–1804.

Volpicelli, Floriana, Massimiliano Caiazzo, Dario Greco, Claudia Consales, Luigi Leone, Carla Perrone-capano, Luca Colucci D. Amato, and Umberto Porzio. 2007. "Bdnf Gene Is a Downstream Target of Nurr1 Transcription Factor in Rat Midbrain Neurons in Vitro." *J. Neurochem* 102:441–53.

Wassarman, Karen Montzka, Mark Lewandoski, Kenneth Campbell, Alexandra L. Joyner, John L. R. Rubenstein, Salvador Martinez, and Gail R. Martin. 1997. "Specification of the Anterior Hindbrain and Establishment of a Normal Mid / Hindbrain Organizer Is Dependent on Gbx2 Gene Function." *Development* 2934:2923–34.

Wassenberg, Tessa, Marta Molero-luis, Kathrin Jeltsch, Georg F. Hoffmann, Birgit Assmann, Nenad Blau, Angeles Garcia-cazorla, Rafael Artuch, Roser Pons, Toni S. Pearson, Vincenco Leuzzi, Mario Mastrangelo, Phillip L. Pearl, Wang Tso Lee, Manju A. Kurian, Simon Heales, Lisa Flint, Marcel Verbeek, Michèl Willemsen, and Thomas Opladen. 2017. "Consensus Guideline for the Diagnosis and Treatment of Aromatic L-Amino Acid Decarboxylase (AADC) Deficiency." *Orphanet Journal of Rare Diseases* 1–21.

Williams, Emily Cunningham, Xiaofen Zhong, Ahmed Mohamed, Ronghui Li, Yan Liu, Qiping Dong, Gene E. Ananiev, Jonathan Chern Choongmok, Benjamin Ray Lin, Jianfeng Lu, Cassandra Chiao, Rachel Cherney, Hongda Li, Su Chun Zhang, and Qiang Chang. 2014. "Mutant Astrocytes Differentiated from Rett Syndrome Patients-Specific IPSCs Have Adverse Effects on Wildtype Neurons." *Human Molecular Genetics* 23(11):2968–80.

Wojcik, Sonja M. and Nils Brose. 2007. "Regulation of Membrane Fusion in Synaptic Excitation-Secretion Coupling: Speed and Accuracy Matter." *Neuron* 55(1):11–24.

Xie, X. S. and D. K. Stone. 1986. “Isolation and Reconstitution of the Clathrin-Coated Vesicle Proton Translocating Complex.” *Journal of Biological Chemistry* 261(6):2492–95.

Xu, Xiaohong, Ying Lei, Jie Luo, Jamie Wang, Shu Zhang, Xiu Juan Yang, Mu Sun, Emile Nuwaysir, Guohuang Fan, Jing Zhao, Lei Lei, and Zhong Zhong. 2013. “Prevention of β-Amyloid Induced Toxicity in Human IPS Cell-Derived Neurons by Inhibition of Cyclin-Dependent Kinases and Associated Cell Cycle Events.” *Stem Cell Research* 10(2):213–27.

Yagi, Takuya, Daisuke Ito, Yohei Okada, Wado Akamatsu, Yoshihiro Nihei, Takahito Yoshizaki, Shinya Yamanaka, Hideyuki Okano, and Norihiro Suzuki. 2011. “Modeling Familial Alzheimer’s Disease with Induced Pluripotent Stem Cells.” *Human Molecular Genetics* 20(23):4530–39.

Yamashita, Atsuko, Satinder K. Singh, Toshimitsu Kawate, Yan Jin, and Eric Gouaux. 2005. “Crystal Structure of a Bacterial Homologue of Na+/Cl- Dependent Neurotransmitter Transporters.” *Nature* 437(7056):215–23.

Yang, N., S. Chanda, S. Marro, YH Ng, JA Janas, D. Haag, CE Ang, Y. Tang, Q. Flores, M. Mall, O. Wapinski, M. Li, H. Ahlenius, JL Rubenstein, HY Chang, AA Buylla, TC Südhof, and M. Wernig. 2017. “Generation of Pure GABAergic Neurons by Transcription Factor Programming.” *Nature Methods* 14(6):621–28.

Zhang, X., JM Beaulieu, TD Sotnikova, RR Gainetdinov, and MG Caron. 2004. “Tryptophan Hydroxylase-2 Controls Brain Serotonin Synthesis.” *Science* 305:217.

Zhang, Zhen-Ning, Beatriz C. Freitas, Hao Qian, Jacques Lux, Allan Acab, Cleber A. Trujillo, Roberto H. Herai, Viet Anh Nguyen Huu, Jessica H. Wen, Shivanjali Joshi-Barr, Jerome V. Karpiak, Adam J. Engler, Xiang-Dong Fu, Alysson R. Muotri, and Adah Almutairi. 2016. “Layered Hydrogels Accelerate IPSC-Derived Neuronal Maturation and Reveal Migration Defects Caused by MeCP2

Dysfunction." *Proceedings of the National Academy of Sciences* 113(12):3185–90.

Zhou, W. and C. R. Freed. 2009. "Adenoviral Gene Delivery Can Reprogram Human Fibroblasts to Induced Pluripotent Stem Cells." *Stem Cells* 27:2667–74.

Zirra, Alexandra, Sarah Wiethoff, and Rickie Patani. 2016. "Neural Conversion and Patterning of Human Pluripotent Stem Cells: A Developmental Perspective." *Stem Cells International* 2016:1–14.